

Technische Universität Kaiserslautern

Fachbereich Chemie

Characterization of Mononuclear and Oligonuclear Transition Metal Complexes in Isolation

Am Fachbereich Chemie der Technischen Universität Kaiserslautern
zur Erlangung des akademischen Grades
"Doktor der Naturwissenschaften"

genehmigte

Dissertation
(D386)

vorgelegt von
Dipl.-Chem. Maximilian Gaffga

Betreuer: Prof. Dr. G. Niedner-Schatteburg

Tag der wissenschaftlichen Aussprache 17. Dezember 2015
Technische Universität Kaiserslautern

Der experimentelle Teil der vorliegenden Arbeit wurde in der Zeit von Oktober 2012 bis Juli 2015 im Fachbereich Chemie der Technischen Universität Kaiserslautern unter der Betreuung von Prof. Dr. G. Niedner-Schatteburg angefertigt.

Datum des Antrags zur Eröffnung des Promotionsverfahrens: 13.08.2015

Promotionskommission:

Vorsitzender: Prof. Dr. W. R. Thiel

1. Berichterstatter: Prof. Dr. G. Niedner-Schatteburg

2. Berichterstatter: Prof. Dr. M. Gerhards

Isabel

*„Nur wenige wissen, wie viel man wissen muss,
um zu wissen, wie wenig man weiß.“*

Werner Heisenberg

Abstract

In this thesis, collision-induced dissociation (CID) studies serve to elucidate relative stabilities and to determine bond strengths within a given structure type of transition metal complexes. The infrared multi photon dissociation (IRMPD) spectroscopy combined with density functional theory (DFT) allow for structural analysis and provide insights into the coordination sphere of transition metal centers. The used combination of CID and IRMPD experiments is a powerful tool to obtain a detailed and comprehensive characterization and understanding of interactions between transition metals and organic ligands. The compounds' spectrum comprises mono- or oligonuclear transition metal complexes containing iron, palladium, and ruthenium as well as lanthanide containing single molecule magnets (SMM). The presented investigations on the different transition metal complexes reveal manifold effects for each species leading to valuable results. A fundamental understanding of metal to ligand interactions is mandatory for the development of new and better organometallic complexes with catalytic, optical or magnetic properties.

Content

| | |
|--|-----------|
| 1. Introduction | 1 |
| 2. Experimental Setup and Methods..... | 7 |
| 2.1 Experimental Setup | 7 |
| 2.1.1 ElectroSpray Ionization (ESI) Source | 7 |
| 2.1.2 Optical Parametric Oscillator / Amplifier (OPO/OPA)..... | 8 |
| 2.1.3 Quadrupole Ion Trap (QIT) Mass Spectrometer | 12 |
| 2.2 Methods..... | 18 |
| 2.2.1 InfraRed MultiPhoton Dissociation (IRMPD)..... | 18 |
| 2.2.2 Collision-Induced Dissociation (CID) | 19 |
| 2.2.3 Computational Methods | 22 |
| 2.3 References | 25 |
| 3. Multi State Mediated Rearrangement and FeCl₂ Elimination in Dinuclear FePd Complexes | 29 |
| 3.1 Preamble..... | 29 |
| 3.2 Abstract..... | 30 |
| 3.3 Introduction | 30 |
| 3.4 Experimental and theoretical methods..... | 33 |
| 3.4.1 Synthesis of compounds 1 and 2..... | 33 |
| 3.4.2 Experimental methods | 33 |
| 3.4.3 Theoretical methods | 35 |
| 3.5 Results and discussion | 36 |
| 3.5.1 Characterization of compounds 1, 2 and 3 | 36 |
| 3.5.2 Collision-induced dissociation (CID) studies | 38 |
| 3.5.3 IRMPD studies and concomitant DFT calculations..... | 42 |
| 3.5.4 Multi state profiles along the reaction coordinate of FeCl ₂ elimination in the CH ₃ CN complex 3a | 50 |
| 3.6 Summary and conclusion..... | 53 |
| 3.7 References | 55 |

| | | |
|-----------|---|------------|
| 3.8 | Supporting Information to Multi State Mediated Rearrangement and FeCl ₂ Elimination in Dinuclear FePd Complexes | 59 |
| 4. | Isomer Discrimination in a Pd-NHC Complex by Collisional and by IR Induced Activation | 83 |
| 4.1 | Preamble..... | 83 |
| 4.2 | Abstract..... | 84 |
| 4.3 | Introduction | 84 |
| 4.4 | Experimental setup and theoretical methods..... | 87 |
| 4.4.1 | Experimental setup | 87 |
| 4.4.2 | Theoretical methods | 89 |
| 4.5 | Results and discussion | 89 |
| 4.5.1 | Mass spectrometric analysis and identification..... | 89 |
| 4.5.2 | Collision-induced dissociation (CID) studies | 89 |
| 4.5.3 | IRMPD studies combined with DFT calculations..... | 94 |
| 4.5.4 | Delay dependent two color IRMPD spectroscopy | 98 |
| 4.5.5 | Identification of isomer specific fragmentation behavior | 102 |
| 4.5.6 | The influence of the ligands: replacing MeCN by pyridine | 105 |
| 4.6 | Summary and conclusion..... | 111 |
| 4.7 | References | 113 |
| 4.8 | Supporting Information to Isomer Discrimination in a Pd-NHC Complex by Collisional and IR Light Induced Activation | 116 |
| 5. | The Influence of Side Groups on the Activation Barrier of [Cl₃Pd(MIP)R]⁻ Complexes: a CID, IRMPD and DFT Study | 127 |
| 5.1 | Preamble..... | 127 |
| 5.2 | Abstract..... | 128 |
| 5.3 | Introduction | 128 |
| 5.4 | Experimental setup and theoretical methods..... | 130 |
| 5.4.1 | Experimental setup | 130 |
| 5.4.2 | Theoretical methods | 132 |
| 5.5 | Results and discussion | 133 |
| 5.5.1 | Mass spectrometric analysis and identification..... | 133 |
| 5.5.2 | IRMPD spectroscopy and structure determination | 133 |
| 5.5.3 | Energy dependent collisional-induced dissociation (CID) studies | 139 |

| | | |
|-----------|--|------------|
| 5.6 | Summary and conclusion..... | 150 |
| 5.7 | References | 152 |
| 5.8 | Supporting Information to The Influence of Side Groups on the Activation Barrier of $[\text{Cl}_3\text{Pd}(\text{MIP})\text{R}]^-$ Complexes: a CID, IRMPD and DFT Study | 155 |
| 6. | IRMPD Spectroscopy and CID Studies on Iron- / Lanthanide based Single Molecule Magnets | 163 |
| 6.1 | Preamble..... | 163 |
| 6.2 | Abstract..... | 164 |
| 6.3 | Introduction | 164 |
| 6.4 | Experimental setup and methods | 165 |
| 6.5 | Results and discussion | 166 |
| 6.5.1 | Structure type definition | 166 |
| 6.5.2 | Structure determination by means of the crystal structure | 167 |
| 6.5.3 | Collision-induced dissociation experiments..... | 170 |
| 6.5.4 | IRMPD spectroscopic investigations | 175 |
| 6.6 | Summary and conclusion..... | 181 |
| 6.7 | References | 183 |
| 7. | IR Spectroscopic Investigations of Electronic Excited States in a Ruthenium Complex..... | 185 |
| 7.1 | Preamble..... | 185 |
| 7.2 | Abstract..... | 186 |
| 7.3 | Introduction | 186 |
| 7.4 | Experimental setup and theoretical methods..... | 188 |
| 7.4.1 | Experimental setup | 188 |
| 7.4.2 | Theoretical methods | 190 |
| 7.5 | Results and discussion | 190 |
| 7.5.1 | Mass spectrometric analysis and identification..... | 190 |
| 7.5.2 | Collision-induced dissociation studies (CID) | 191 |
| 7.5.3 | IRMPD spectroscopy and structure determination | 194 |
| 7.5.4 | Identification of coexisting isomers | 204 |
| 7.5.5 | Electronic Excited States | 205 |
| 7.6 | Summary and conclusion..... | 209 |
| 7.7 | References | 211 |

| | | |
|------------|--|------------|
| 7.8 | Supporting Information to IR Spectroscopic Investigations of Electronic Excited States in a Ruthenium Complex..... | 214 |
| 8. | Summary and Conclusion | 223 |
| 9. | Zusammenfassung und Schlussfolgerung..... | 229 |
| 10. | Publications and Contributions to Conferences | 235 |

Abbreviations

| | |
|-----------------------|--|
| AC | Alternating Current |
| AE | Appearance Energies |
| COM | Center of Mass |
| Cp | Cyclopentadienyl |
| DC | Direct Current |
| CID | Collision-Induced Dissociation |
| Cym | Cymene |
| DFM | Difference Frequency Mixing |
| DFT | Density Functional Theory |
| PIB | 2,2'-[(Prop-2-ynyl)imino] bisethanolat |
| ESI | ElectroSpray Ionization |
| Et | Ethyl |
| fwhm | Full Width at Half Maximum |
| IRMPD | InfrRed Multi Photon Dissociation |
| IVR | Intra-molecular Vibrational Redistribution |
| KTA | Potassium Titanyl Arsenate |
| KTP | Potassium Titanyl Phosphate |
| Me | Methyl |
| MeCN | Acetonitrile |
| MIP | Mesityl-1H-imidazolyl-pyridine |
| MS | Mass Spectrometry |
| Nd ³⁺ :YAG | Neodymium-doped Yttrium Aluminium Garnet |
| OPA | Optical Parametric Amplifier |
| OPO | Optical Parametric Oscillator |
| Piv | Pivalic acid |
| QIT | Quadrupole Ion Trap |
| SMM | Single Molecule Magnets |
| TD-DFT | Time Dependent Density Functional Theory |
| TEA | Triethanolamine |

1. Introduction

Mass spectrometric investigation on isolated ionic compounds finds a large variety of applications.^[1-4] Several established techniques serve to produce ionic species needed for mass analysis. Hereby, the electrospray ionization (ESI) emerged as a valuable and beneficial technique for transferring intact ions into vacuum.^[5] The ESI source is capable to facilitate the transfer of a wide range of compounds, starting from biomolecules^[6-8] up to organometallic species^[9-12], and it makes those accessible for subsequent spectroscopic characterizations if desired. The ESI mass spectrometry established as a versatile tool for mechanistic studies in organic and organometallic chemistry.^[13-16]

Metal containing compounds such as transition metal complexes are of interest due to their catalytic activities mediating important reactions, e.g. C-H or C-C activations in the gas phase.^[17-21] Advances in ligand synthesis allow for the generation of an increasing variety of catalysts. The ESI technique enables the investigation of reaction mixtures, thereby monitoring reactants, products and intermediates and studying properties of the intermediates and their reactivity. These investigations on catalytic active compounds can yield detailed information about elementary reaction steps within a given catalytic cycle.^[22-27] Beside the catalytic activity, transition metal complexes can possess optical properties of significance. Such features often arise from metal to ligand interactions and are closely related to the structure of the complex and the coordination sphere of the metal centers.^[28-30] Certain metal complexes may serve as dyes that convert sunlight into electrical power, and they may be used as antennas in dye-sensitized solar cells.^[31, 32] Hereby, the absorption of light involves a metal to ligand interaction, referred to as charge transfers.^[31] Another highly interesting property of well designed complexes is the so called single molecule magnetism. Here, the magnetic properties are based on the contained metals and their interaction with the surrounding ligands, which may lead to highly interesting magnetic properties on a molecular scale.^[33, 34] Single Molecule Magnets (SMM) may provide for a unique combination of magnetic properties on a molecular level which are assumed intrinsic properties of a sole molecule. The investigation and the associated comprehension of metal to ligand interaction are of fundamental importance achieving insights into the connection between metals and ligands.

Within this thesis metal complexes are investigated by collision-induced dissociation (CID) experiments and infrared multi photon dissociation (IRMPD) spectroscopy aiming at a more detailed understanding of metal to ligand interactions. The selected compounds comprise mono- or oligonuclear transition metals complexes containing iron, palladium and ruthenium as well as lanthanide based SMMs.

Collisional activation by a neutral gas and the corresponding fragmentation behavior allows for structural analysis and is referred to as collision-induced dissociation (CID).^[35-38] This technique had a high impact on mass spectrometry^[39, 40] and finds application in the identification and structural elucidation of a manifold of molecules especially in biology.^[41-44] Furthermore, CID has become a widely used and reviewed technique for the structural analysis of organometallic complexes^[45-48] as well as metal cluster.^[49, 50] The process exhibits insights into characteristic fragmentation patterns and provides information about the stability of the precursor ions.^[51-53] CID serves as a powerful tool to determine bond strengths or binding energies of ligands to metal centers and thus it is capable of elucidating metal to ligand interactions. Next to the CID technique, infrared multi photon dissociation (IRMPD) spectroscopy can be used to obtain insights into binding motifs and to gain information about the structural composition of metal complexes. The IRMPD technique relies on a fragmentation of the ion of interest. It involves sequential absorption of infrared photons by trapped ions which causes a gradual increase in the internal energy until a dissociation threshold is reached.^[54, 55] Hereby, the IRMPD technique has proven a versatile tool to record IR spectra of a great diversity of metal complexes.^[56-60] In conjunction with an electrospray ionization source IRMPD allows for the monitoring and recording of IR spectra of reaction intermediates and offers, e.g., a close view into processes within a catalytic cycle.^[61-63] A detailed structural interpretation of IRMPD spectra requires a comparison to computed IR spectra of adequate geometries.^[64] A capable and efficient approach for that purpose implies comparing IRMPD spectra to harmonic frequency as computed by the density functional theory (DFT). A structural determination may be achieved by combining the IRMPD spectroscopy and DFT computations.^[65]

Within this thesis, the combination of the presented techniques (CID and IRMPD) serves for a comprehensive characterization and understanding of interactions between transition metals and organic ligands such as catalytic activity, charge transfers or single molecule

magnetism. These investigations on metal-organic complexes may be helpful for the development and design of novel catalysts or for compounds of versatile applications.

The thesis comprises a general introduction (chapter 1), an experimental setup and methods part (chapter 2), five results parts (chapters 3-7), and a summary and conclusion part (chapters 8 and 9). Each chapter of the results part is prepared as a manuscript for publication containing a “preamble” that unambiguously states the individual contributions to the presented work. Chapter 3 deals with a multi-state rearrangement and the consequent FeCl_2 elimination in a dinuclear FePd complex in dependence of the coordinated solvent molecule causing a coordination change in the binding motif of the Pd center. Chapter 4 reports on the characterization and distinction of coexisting isomers in a mononuclear Pd-NHC complex by the use of collisional and two-color IR induced activation. Chapter 5 presents the utilization of CID studies to determine activation barriers and the influence of the different side groups in a Pd-MIP complex. Chapter 6 exhibits the influence of the used Ln (lanthanide) metal centers on the IRMPD spectra and activation thresholds for two different types of Fe and Ln based single molecule magnets. Chapter 7 displays the optical properties of three Ru complexes in the mid- and near-IR region. The complexes reveal low lying electronic vibrational excitations which are compared to TD-DFT derived absorption spectra.

References

- [1] G. L. Glish and R. W. Vachet, *Nature Reviews Drug Discovery*, **2003**, 2, 140-150.
- [2] R. G. Cooks, K. L. Busch and G. L. Glish, *Science*, **1983**, 222, 273-291.
- [3] W. N. Delgass and R. G. Cooks, *Science*, **1987**, 235, 545-553.
- [4] R. Lobinski, D. Schaumlöffel and J. Szpunar, *Mass Spectrometry Reviews*, **2006**, 25, 255-289.
- [5] J. B. Fenn, M. Mann, C. K. Meng, S. F. Wong and C. M. Whitehouse, *Mass Spectrometry Reviews*, **1990**, 9, 37-70.
- [6] J. B. Fenn, M. Mann, C. K. Meng, S. F. Wong and C. M. Whitehouse, *Science*, **1989**, 246, 64-71.
- [7] I. Jardine, *Nature*, **1990**, 345, 747-748.
- [8] M. Mann, *Organic Mass Spectrometry*, **1990**, 25, 575-587.
- [9] V. Katta, S. K. Chowdhury and B. T. Chait, *Journal of the American Chemical Society*, **1990**, 112, 5348-5349.
- [10] E. M. Sible, S. P. Brimmer and J. A. Leary, *Journal of the American Society for Mass Spectrometry*, **1997**, 8, 32-42.
- [11] V. B. Di Marco and G. G. Bombi, *Mass Spectrometry Reviews*, **2006**, 25, 347-379.
- [12] M. Kohler and J. A. Leary, *International Journal of Mass Spectrometry and Ion Processes*, **1997**, 162, 17-34.
- [13] K. Bock, J. E. Feil, K. Karaghiosoff and K. Koszinowski, *Chemistry-a European Journal*, **2015**, 21, 5548-5560.
- [14] R. A. J. O'Hair, *International Journal of Mass Spectrometry*, **2015**, 377, 121-129.
- [15] K. L. Vikse, Z. Ahmadi and J. S. McIndoe, *Coordination Chemistry Reviews*, **2014**, 279, 96-114.
- [16] M. Arndt, K. S. M. Salih, A. Fromm, L. J. Goossen, F. Menges and G. Niedner-Schatteburg, *Journal of the American Chemical Society*, **2011**, 133, 7428-7449.
- [17] P. A. M. Vankoppen, J. Brodbeltlustig, M. T. Bowers, D. V. Dearden, J. L. Beauchamp, E. R. Fisher and P. B. Armentrout, *Journal of the American Chemical Society*, **1991**, 113, 2359-2369.
- [18] D. Schroder and H. Schwarz, *Angewandte Chemie-International Edition in English*, **1995**, 34, 1973-1995.

-
- [19] A. M. C. Wittborn, M. Costas, M. R. A. Blomberg and P. E. M. Siegbahn, *Journal of Chemical Physics*, **1997**, 107, 4318-4328.
- [20] D. J. Zhang, R. X. Wang and R. X. Zhu, *Australian Journal of Chemistry*, **2005**, 58, 82-85.
- [21] R. Z. Hinrichs, J. J. Schroden and H. F. Davis, *Journal of Physical Chemistry A*, **2008**, 112, 3010-3019.
- [22] D. A. Plattner, *International Journal of Mass Spectrometry*, **2001**, 207, 125-144.
- [23] J. Wassenaar, E. Jansen, W. J. van Zeist, F. M. Bickelhaupt, M. A. Siegler, A. L. Spek and J. N. H. Reek, *Nature Chemistry*, **2010**, 2, 417-421.
- [24] R. A. J. O'Hair and G. N. Khairallah, *Journal of Cluster Science*, **2004**, 15, 331-363.
- [25] H. Schwarz, *Angewandte Chemie-International Edition*, **2011**, 50, 10096-10115.
- [26] B. L. Tjelta and P. B. Armentrout, *Journal of the American Chemical Society*, **1996**, 118, 9652-9660.
- [27] W. B. Tolman, *Angewandte Chemie-International Edition*, **2010**, 49, 1018-1024.
- [28] S. Ardo and G. J. Meyer, *Chemical Society Reviews*, **2009**, 38, 115-164.
- [29] S. Di Bella, *Chemical Society Reviews*, **2001**, 30, 355-366.
- [30] C. E. Powell and M. G. Humphrey, *Coordination Chemistry Reviews*, **2004**, 248, 725-756.
- [31] N. Robertson, *Angewandte Chemie-International Edition*, **2006**, 45, 2338-2345.
- [32] A. S. Polo, M. K. Itokazu and N. Y. M. Iha, *Coordination Chemistry Reviews*, **2004**, 248, 1343-1361.
- [33] D. Gatteschi, Sessoli, R., Villain, J., *Molecular Nanomagnets*, Oxford University Press, **2006**.
- [34] S. Gao, *Molecular Nanomagnets and Related Phenomena*, Springer, **2015**.
- [35] McLaffer.Fw, P. F. Bente, R. Kornfeld, S. C. Tsai and I. Howe, *Journal of the American Chemical Society*, **1973**, 95, 2120-2129.
- [36] McLaffer.Fw, R. Kornfeld, W. F. Haddon, K. Levsen, I. Sakai, P. F. Bente, S. C. Tsai and Schuddem.Hd, *Journal of the American Chemical Society*, **1973**, 95, 3886-3892.
- [37] E. deHoffmann, *Journal of Mass Spectrometry*, **1996**, 31, 129-137.
- [38] R. G. Cooks, *Journal of Mass Spectrometry*, **1995**, 30, 1215-1221.
- [39] K. R. Jennings, *International Journal of Mass Spectrometry*, **2000**, 200, 479-493.
- [40] K. Biemann and H. A. Scoble, *Science*, **1987**, 237, 992-998.
- [41] R. Aebersold and D. R. Goodlett, *Chemical Reviews*, **2001**, 101, 269-295.
-

- [42] K. Biemann, *Methods in Enzymology*, **1990**, 193, 455-479.
- [43] I. A. Papayannopoulos, *Mass Spectrometry Reviews*, **1995**, 14, 49-73.
- [44] E. Nordhoff, F. Kirpekar and P. Roepstorff, *Mass Spectrometry Reviews*, **1996**, 15, 67-138.
- [45] K. Eller and H. Schwarz, *Chemical Reviews*, **1991**, 91, 1121-1177.
- [46] D. C. Parent and S. L. Anderson, *Chemical Reviews*, **1992**, 92, 1541-1565.
- [47] B. S. Freiser, *Journal of Mass Spectrometry*, **1996**, 31, 703-715.
- [48] M. T. Rodgers and P. B. Armentrout, *Mass Spectrometry Reviews*, **2000**, 19, 215-247.
- [49] A. W. Castleman and K. H. Bowen, *Journal of Physical Chemistry*, **1996**, 100, 12911-12944.
- [50] A. Grushow and K. M. Ervin, *Journal of Chemical Physics*, **1997**, 106, 9580-9593.
- [51] F. Falvo, L. Fiebig, F. Dreiocker, R. Wang, P. B. Armentrout and M. Schafer, *International Journal of Mass Spectrometry*, **2012**, 330, 124-133.
- [52] M. R. Sievers, L. M. Jarvis and P. B. Armentrout, *Journal of the American Chemical Society*, **1998**, 120, 1891-1899.
- [53] Y. M. Chen and P. B. Armentrout, *Chemical Physics Letters*, **1993**, 210, 123-128.
- [54] T. D. Fridgen, *Mass Spectrometry Reviews*, **2009**, 28, 586-607.
- [55] J. R. Eyler, *Mass Spectrometry Reviews*, **2009**, 28, 448-467.
- [56] D. T. Moore, J. Oomens, J. R. Eyler, G. von Helden, G. Meijer and R. C. Dunbar, *Journal of the American Chemical Society*, **2005**, 127, 7243-7254.
- [57] J. Lang, M. Gaffga, F. Menges and G. Niedner-Schatteburg, *Physical Chemistry Chemical Physics*, **2014**, 16, 17417-17421.
- [58] Y. Nosenko, F. Menges, C. Riehn and G. Niedner-Schatteburg, *Physical Chemistry Chemical Physics*, **2013**, 15, 8171-8178.
- [59] L. MacAleese and P. Maitre, *Mass Spectrometry Reviews*, **2007**, 26, 583-605.
- [60] A. Lagutschenkov, U. J. Lorenz and O. Dopfer, *International Journal of Mass Spectrometry*, **2011**, 308, 316-329.
- [61] A. Skriba, J. Schulz and J. Roithova, *Organometallics*, **2014**, 33, 6868-6878.
- [62] A. Tsybizova and J. Roithová, *Mass Spectrometry Reviews*, **2015**, DOI: 10.1002/mas.21464, n/a-n/a.
- [63] N. C. Polfer and J. Oomens, *Physical Chemistry Chemical Physics*, **2007**, 9, 3804-3817.
- [64] N. C. Polfer, *Chemical Society Reviews*, **2011**, 40, 2211-2221.
- [65] J. Roithova and D. Schroder, *Coordination Chemistry Reviews*, **2009**, 253, 666-677.

2. Experimental Setup and Methods

2.1 Experimental Setup

2.1.1 ElectroSpray Ionization (ESI) Source

The ElectroSpray Ionization (ESI) source allows for the transfer of dissolved ions into the gas phase nearly without fragmentation. The basic principle of this method has been developed by *Dole et al.* (1986).^[1] In 2002 *Fenn* was awarded with the Nobel Prize for the development of its first application.^[2-5] The combination of this soft ionization method with a mass spectrometer has become a powerful tool for a wide range of applications (Fig. 1). Initially, the ESI technique was utilized in the biology for the analysis of biomolecules, e.g. peptides, proteins, and nucleic acids.^[6-9] During the last decades the publication of several reviews and books demonstrated the impact of the ESI technique on mass spectrometric analysis.^[10-13] The ESI technique established itself as a valuable application for the characterization of metal containing compounds and for the monitoring of reaction solutions.^[14-16]

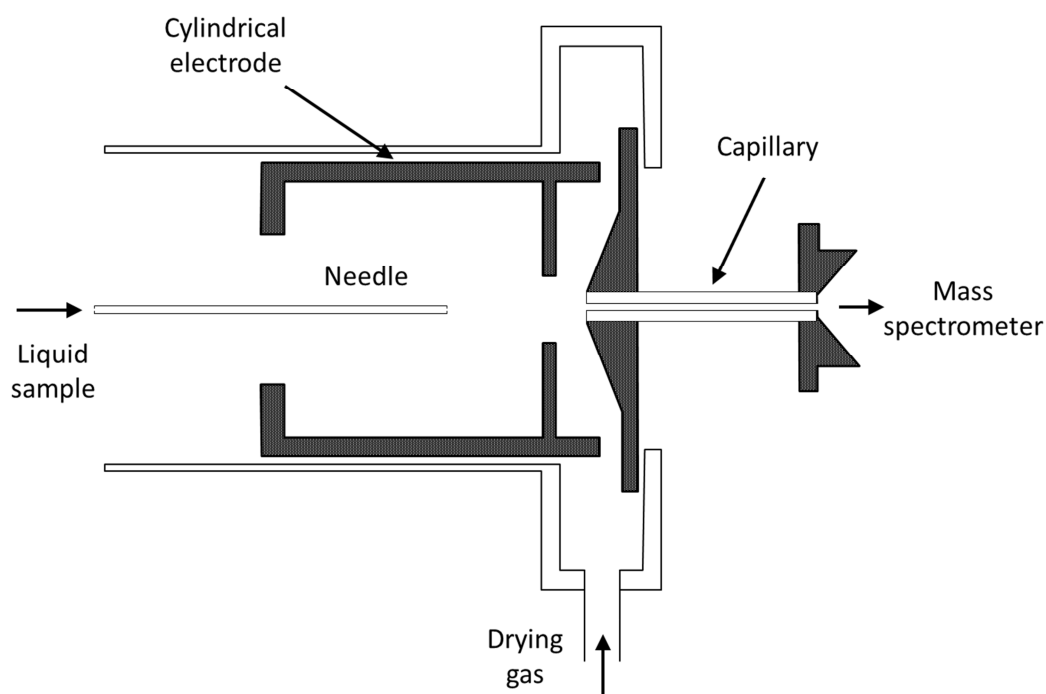


Figure 1: Scheme of an electrospray ionization source.^[2]

The ESI process performs as follows: a field gradient (3 – 6 kV) between a spray needle (containing the solvated ions) and the entrance of a mass spectrometer allows for charge accumulation at the liquid surface at the end of the tube. The electrostatic field favors ions of one polarity at the droplet surface. A nebulizing gas (nitrogen), flowing along the needle, leads to a stream of small particles. A heated drying gas (nitrogen, 200 – 350 °C depending on the application), flowing against the droplet stream, removes the remaining solvent molecules and releases naked ions. Then, the naked ions enter the vacuum chamber of the mass spectrometer. The entrance of all used instruments contains a glass capillary ($\varnothing = 0.5$ mm, length between 15 and 20 cm) which is coated with platinum at both ends. An electrostatic gradient, next to the pressure gradient, serves as an additional driving force to transfer the ions into the vacuum chamber of the mass spectrometer. The exact mechanism of ion release and solvent removal, comprising the charged residue and ion evaporation mechanisms, is still disputed in the literature.^[17,18] Suitable solvents for the ESI process stabilize ions and exhibit low boiling points, e.g. water, methanol, acetonitrile, dimethylsulfoxide or mixtures of those.

2.1.2 Optical Parametric Oscillator / Amplifier (OPO/OPA)

An optical parametric oscillator (OPO) is a coherent light source similar to a laser. It uses a laser resonator, and it is based on optical gain from parametric amplification in a nonlinear crystal rather than from stimulated emission.^[19,20] Nonlinear crystals provide for the generation of second-harmonic frequencies (or higher order).^[21] The OPO converts an intense laser wave of one frequency into two output waves called signal and idler. The signal wave represents the wave with higher frequency. The wavelength of the signal and idler waves depends on the refraction index of the crystal. Changing the angle of the crystal according to the axis of the incident light influences the refraction index and allows for the continuous scanning of the outgoing waves.^[22] An optical parametric amplifier (OPA) intensifies the output of the OPO. The main attraction of OPO/OPAs is that signal and idler wavelengths, which are determined by a phase-matching condition, can be varied in wide ranges.^[22] Thus, it is possible to access wavelengths which are difficult or impossible to

obtain from any laser, and wide wavelength tunability is also often possible. This makes OPO/OPA laser systems extremely valuable for laser spectroscopy. However, any OPO/OPA laser system requires a pump source with high optical intensity and relatively high spatial coherence. For spectroscopic measurements high resolution is necessary. In order to minimize the bandwidth, two conditions have to be considered: Firstly, seeded lasers, in which the oscillator build-up of only one mode within the laser is favored, should be used.^[23] Secondly, the use of an optical grating within the OPO setup may also reduce the bandwidth of the laser light.^[24]

Within this work, two *Dean Guyer* OPO/OPA (LaserVision) laser systems have been used: a “narrowband” OPO/OPA system (Fig. 2) and a “broadband” OPO/OPA system. Both systems differ in their OPO resonators. The broadband OPO contains two potassium titanyl phosphate (KTP) crystals, while the narrowband system only uses one and also involves an optical grating to reduce the bandwidth of the laser light.

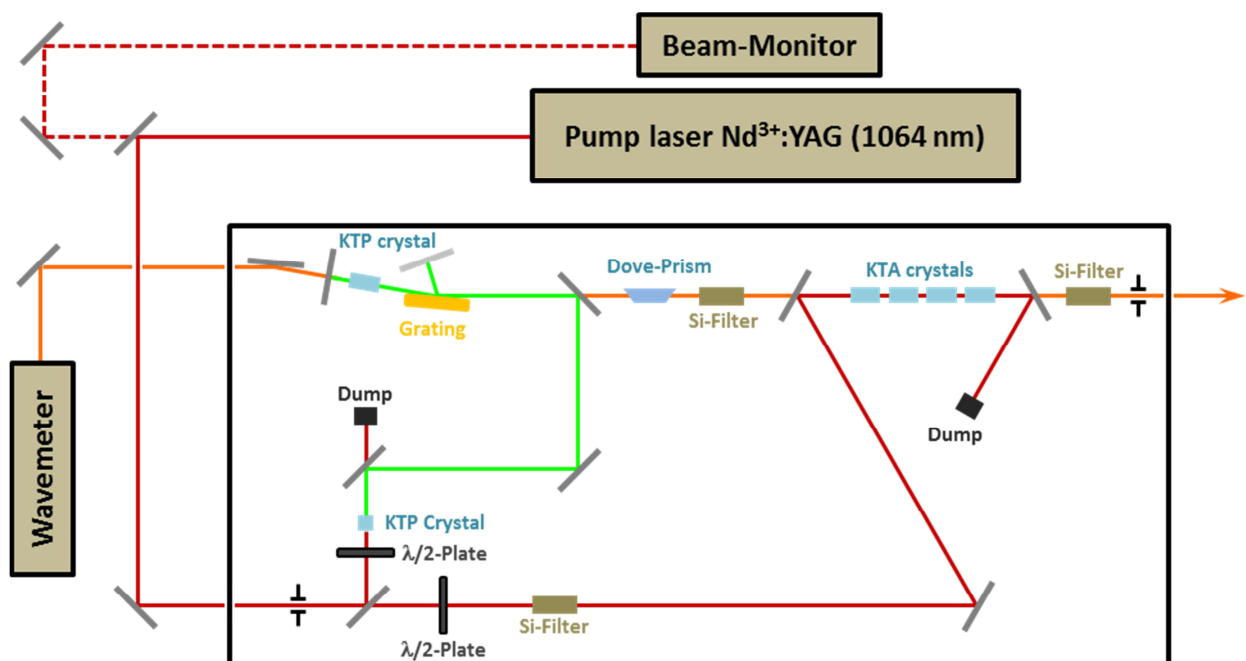


Figure 2: Scheme of the Dean Guyer LaserVision narrowband OPO/OPA laser system.^[25]

Two pulsed injection seeded Nd^{3+} :YAG lasers (Continuum-PL8000; 10 Hz), generating 1064 nm light, were used as pumping sources for the two OPO/OPA systems. A beam splitter separates the incoming pump beam into two beam lines. One third of the original intensity is frequency doubled (532 nm), and the resulting wave is coupled into the OPO resonator. The resonator, containing two potassium titanyl phosphate (KTP) crystals, converts the 532 nm wave into a signal $\nu_{1,s}$ and an idler $\nu_{1,i}$ wave. A silicon filter separates the higher energetic signal $\nu_{1,s}$ wave, while the remaining idler $\nu_{1,i}$ wave is recombined with the residual two thirds of the original 1064 nm pump wave. This recombination takes place within the four potassium titanyl arsenate (KTA) crystals of the OPA stage of the system. During the amplification process, the pumping wave ν_{1064} is converted into a signal $\nu_{2,s}$ and an idler $\nu_{2,i}$ wave. The signal $\nu_{2,s}$ wave has the same wavelength as the idler $\nu_{1,i}$ wave. Since these two wave exhibit different polarizations, a suitable filter can be used to separate them. Table 1 shows the different polarizations of the used and resulting waves.

Table 1: Beam polarization after the different optical elements within the OPO/OPA laser system (ν = vertical, h = horizontal) according to Fig. 2.^[26]

| optical element | in | out |
|---------------------------|-----------------------------------|--|
| OPO $\lambda/2$ -plate | ν_{1064} (h) | ν_{1064} (v) |
| SHG KTP | ν_{1064} (v) | ν_{532} (v) |
| OPO KTP | ν_{532} (v) | ν_{1s} (h) & ν_{1i} (v) |
| dove prism and wave plate | ν_{1s} (h) & ν_{1i} (v) | ν_{1s} (v) & ν_{1i} (h) |
| Si filter 1 | ν_{1s} (v) & ν_{1i} (h) | ν_{1s} (h) = ν_{2s} (h) |
| OPA $\lambda/2$ -plate | ν_{1064} (h) | ν_{1064} (v) |
| OPA KTA | ν_{1064} (v) & ν_{2s} (h) | ν_{1064} (v) & ν_{2s} (h) & ν_{2i} (v) |
| Si filter 2 | ν_{2s} (h) & ν_{2i} (v) | ν_{2s} (h) or ν_{2i} (v) |
| AgGaSe ₂ | ν_{2s} (h) & ν_{2i} (v) | ν_{DFM} (v) |

The wavelength of the resulting idler $\nu_{2,i}$ is in the range from 2200 – 4700 cm^{-1} , the resulting signal $\nu_{2,s}$ exhibits a wavelength in the range from 4700 – 7400 cm^{-1} . Difference frequency mixing (DFM) of these two waves within a AgGaSe₂ crystal enables access to a wavelengths range from 800 – 2200 cm^{-1} .^[27] The OPO/OPA output provides energy up to 15 mJ/pulse. Using the DFM, the power is much lower (approximately 1 – 2.5 mJ/pulse). The intensity of

the OPO/OPA output can be controlled by a variable attenuator (cf. Fig. 5, $\lambda/2$ -plates) in the light path of the linear polarized ν_{1064} beam which is then coupled into the OPA crystals. The $\lambda/2$ -plates blocks the beam at an adjustment angle of 0° and allows for maximum intensity at a position of 45° .

Standard IRMPD measurement conditions:

Two LaserVision KTP/KTA optical parametric oscillator/amplifier systems (Fig. 3) pumped by two 10 Hz injection seeded Nd^{3+} :YAG lasers provide tunable IR radiation in the range from $800 - 7400 \text{ cm}^{-1}$ (bandwidth: broadband system: $\delta\nu = 0.9 \text{ cm}^{-1}$, narrowband system: $\delta\nu = 0.3 \text{ cm}^{-1}$; pulse length: $\delta t = 7 \text{ ns}$).

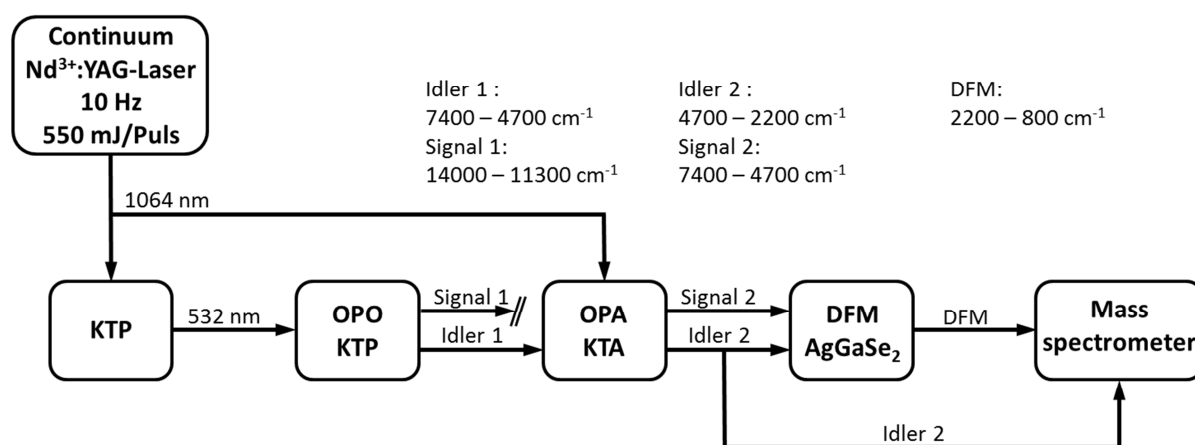


Figure 3: Schematic drawing of the LaserVision KTP/KTA OPO/OPA laser system revealing the stepwise frequency conversion process.

We use one OPO laser for scanning and recording (IR_{scan}) the IRMPD spectrum, and optionally the second OPO laser (IR_{fix}) serves as an additional photon source in order to generate a sufficient amount of fragmentation. Hereby, the second laser is set to a fixed vibrational resonance frequency. The use of a delay generator (Stanford Research System: DG645) allows for a variation of the time delay between the two laser pulses. The IR frequency was calibrated by a wave meter (Bristol Instruments: 821B-NIR, resp. Toptica

Photonics: HighFinesse IRII-WS7). During the IRMPD measurements, we recorded the laser power curve in parallel using either an energy or power meter head.

2.1.3 Quadrupole Ion Trap (QIT) Mass Spectrometer

Paul and *Steinwedel* patented the quadrupole ion trap, commonly known as Paul trap, in 1960 and paved the way for a versatile instrument with a wide applicability.^[28-30] The ion trap operates analogously to a linear quadrupole but in three dimensions rather than two. It consists of three hyperbolic electrodes: two end-caps and one ring electrode (Fig. 4).

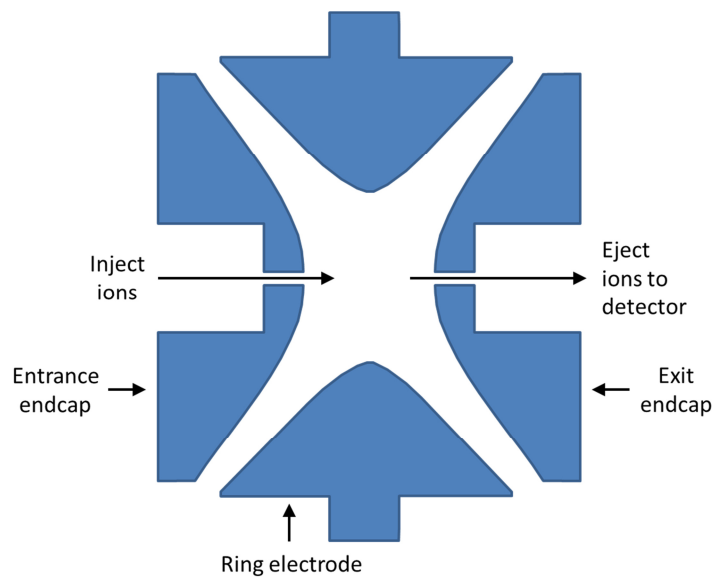


Figure 4: Cross-sectional view of the quadrupole ion trap.^[31]

A quadrupole ion trap uses certain combinations of alternating current (AC) and direct current (DC) voltages allowing for the storage of ions in vacuum. An overlap of these potentials creates a three-dimensional trapping field. The electric fields affect the motion and the trajectory stabilities of the ions in the trap. The movement of an ion in the electric trapping field is described by a second-order differential equation and its solution was firstly described and named after *Mathieu*.^[32] The trapping field exerts a restoring force which

pushes the ions back to the center of the trap. A buffer gas (typically helium), present in the ion trap, increases the trapping efficiency of the QIT and raises the partial pressure to approximately 10^{-3} mbar.^[33] The ions lose excess kinetic energy, impeding the trapping due to collisions with the gas molecules, and they can be more effectively trapped. Both, sensitivity and resolution benefit from the presence of the buffer gas.^[34] By varying the AC and DC voltages, the ion stability can be manipulated, i.e. ions with a certain mass to charge (m/z) ratio have stable trajectories, whereas ions with other m/z ratios do not have stable orbits within the QIT and get lost. This variation allows the ejection of the trapped ions and the isolation of certain m/z ratios.^[33,35] The technique of resonance excitation provides a common method for collisional activation.^[36-39] Since ions of all masses are trapped inside the QIT mass, detection is performed by stepwise changing the amplitude of either the direct or the alternating voltage. This leads to the consecutive loss of stability criteria of the ions, and they leave the trap hitting a detector.

Within this work, two QIT mass spectrometers were used. Both are equipped with an electrospray ionization source (cf. chapter 2.1.2).

The Bruker Esquire 6000 setup:

The first mass spectrometer is the Bruker Esquire 6000 instrument used to perform Collision-Induced Dissociation (CID) studies. After creation in the ESI source, the ions pass the transfer capillary, enter the vacuum chamber of the Bruker Esquire 6000 mass spectrometer and are accelerated towards a skimmer (Fig. 5).

Two linear on axis installed octopoles guide the ions through two differentially pumped vacuum chambers guiding the ion beam into the trap. Here, the ions can be accumulated and stored until detection. Inside the trap, the presence of helium ($\sim 3 \cdot 10^{-3}$ mbar) decelerates the ions simplifying their trapping and allowing to perform collision-induced dissociation experiments by application of an accelerating potential.

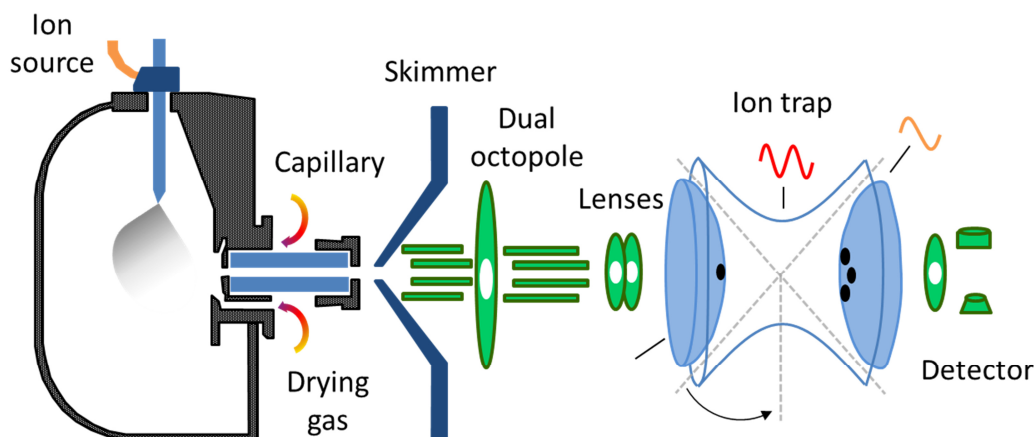


Figure 5: Scheme of the Bruker Esquire 6000 mass spectrometer.^[40]

Standard measurement conditions for the Esquire 6000 instrument:

We used the normal resolution scan mode ($0.3 \text{ fwhm} / \frac{m}{z}$) with a scan speed of $13000 \frac{m}{z \cdot s}$. By the use of a syringe pump sample solutions at concentrations of approximately $1 \cdot 10^{-4} \text{ M}$ were continuously infused into the ESI chamber at a flow rate of $2 \mu\text{L}/\text{min}$. The solutions were sprayed at a nebulizer pressure of 4 psi with the electrospray needle held at 4.5 kV. Nitrogen is used as drying gas at a flow rate of 3.0 L/min at 300 °C. Helium is used as a buffer gas with a partial pressure of approximately $3 \cdot 10^{-3} \text{ mbar}$. The Bruker Esquire Control 5.3 software controlled the instrument, and the data analysis was realized using the Bruker Data Analysis 4.0 software.

The Bruker amaZon SL setup:

The second mass spectrometer used is the Bruker amaZon SL instrument. It has been used to record InfraRed MultiPhoton Dissociation (IRMPD) spectra. A modification of the amazon SL mass spectrometer implemented IR-transparent windows (BaF_2) in the vacuum housing ensures access to the trap. A breadboard serves as a mount for the optical elements. Two holes through the ring electrode allow the IR beam to enter, to irradiate the ions, and to leave the center of the trap. The holes' diameter at the outer surface is 6 mm and it is reduced to 2 mm on the inner surface of the ring electrode. Furthermore, a holding for two mirrors was installed at the support rods of the trap in order to mount two mirrors. One

mirror is positioned directly under the holes of the ring electrode in a 45° angle. The second mirror locates adjacent to the first mirror in a 45° angle as well allowing the redirection of the laser beam out of the vacuum chamber (Fig. 6).

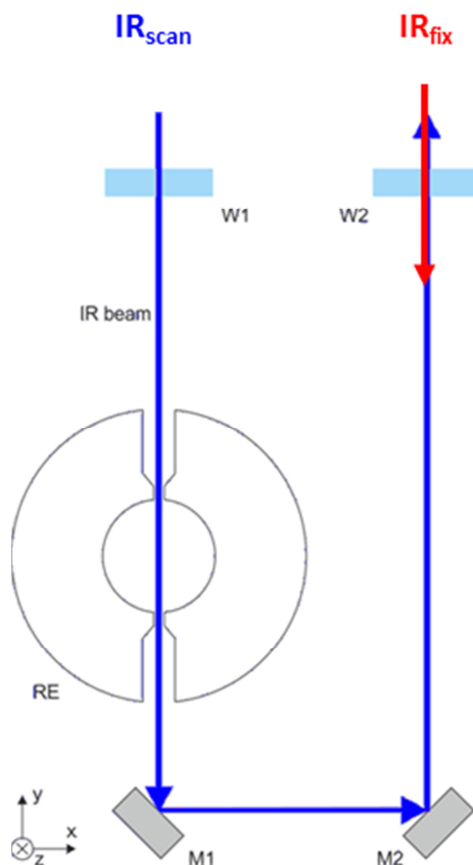


Figure 6: Scheme of the modified ring electrode (RE). IR_{scan} and IR_{fix} laser beams can pass the trap through two BaF_2 windows ($W1$ and $W2$) guided by two mirrors ($M1$ and $M2$).

The optical elements on top of the vacuum chamber (not shown in Fig. 6) comprise of two apertures for laser beam alignment, several mirrors for redirecting the beam including a plain mirror, and a concave mirror, placed on a magnet mount plate above the ion the trap, in order to allow for a quick change of the two types of mirrors. The plain mirror is used for measurements with IR frequencies above 2200 cm^{-1} . A plan-convex CaF_2 ($f = 50\text{ cm}$) lens focuses the laser beam ($2200 - 7500\text{ cm}^{-1}$) into the trap. In order to measure within the spectral range of $1000 - 2200\text{ cm}^{-1}$, the lens is removed due to the self-absorption of CaF_2 .

Instead, a concave mirror ($f = 15$ cm) on top of the vacuum chamber serves to focus the IR laser beam.

The *Bruker Daltonics GmbH* modified the instrument software in order to allow for a synchronization of the duty cycle of the mass spectrometer to the 10 Hz trigger signal of the pump laser. A home-made connector to the auxiliary interface of the instrument allows for the transfer of the laser flash lamp sync. trigger output to the mass spectrometer trigger input. In this mode, the instrument waits for a trigger signal during the fragmentation time of an MS^n step until it starts scanning the trapped precursor and fragment ions. The fragmentation time within the Bruker Trap Control software serves as a value to present an exact number of laser pulses irradiating the ions inside the trap. An electrical shutter, controlled by a trigger signal from the mass spectrometer, allows for an irradiation within $MS^n > 2$ steps. The shutter remains closed unless the instrument sends a TTL pulse lasting as long as the appendant MS^n step.

After passing the trap, the remaining IR laser beam hits an energy or power meter head, connected to the mass spectrometer via an auxiliary adapter. This allows for compiling the analog output of a power or energy meter using the analog digital converter of the mass spectrometer. The analog signal serves as a reference to the laser frequency dependent photon flux within the measurements.

After creation in the ESI source, the ions pass the transfer capillary, enter the vacuum chamber of the Bruker amaZon SL mass spectrometer, and are accelerated towards a dual ion funnel (Fig. 7).

The off axis installed dual funnel gathers the ions and focuses the ion beam on the octopole axis. Because of its off axis position, the funnel avoids the transport of “dirt” molecules towards the high vacuum region guaranteeing a good vacuum gradient. After passing two octopoles the ions are focused into the ion trap. Here, the ions can be accumulated and stored until detection. Helium is used as a buffer gas with a partial pressure of about $3 \cdot 10^{-3}$ mbar. The modified ring electrode of the ion trap allows for IRMPD spectroscopy of the trapped ions.

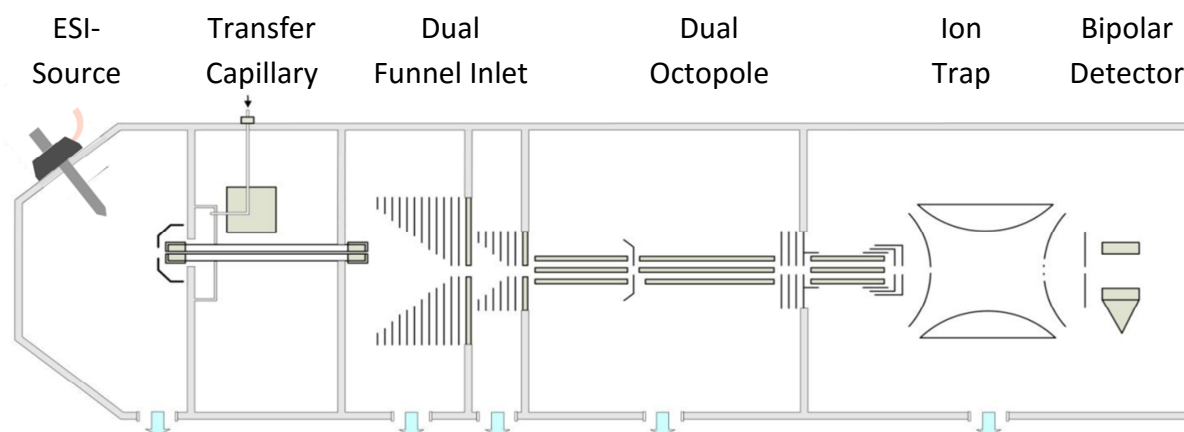


Figure 7: Scheme of the Bruker amaZon SL mass spectrometer.^[41]
 Note the additional dual funnel inlet which is not available at the Esquire 6000 instrument (cf. Fig. 5).

Standard measurement conditions for the amaZon SL instrument:

We use the normal resolution scan mode ($0.3 \text{ fwhm} / \frac{m}{z}$) with a scan speed of $32500 \frac{m}{z \cdot s}$. By the use of a syringe pump, the sample solutions were continuously infused into the ESI chamber at concentrations of approximately $1 \cdot 10^{-4} \text{ M}$ and a flow rate of $2 \mu\text{L}/\text{min}$. The solutions were sprayed at a nebulizer pressure of 4 psi with the electrospray needle held at 4.5 kV. Nitrogen is used as drying gas at a flow rate of 3.0 L/min at 220 °C. Helium is used as a buffer gas with a partial pressure of approximately $3 \cdot 10^{-3} \text{ mbar}$. The Bruker Trap Control 7.0 software controlled the instrument and the data analysis was realized using the Bruker Data Analysis 4.0 software.

2.2 Methods

2.2.1 InfraRed MultiPhoton Dissociation (IRMPD)

The first use of tunable lasers to induce fragmentation by irradiation of trapped ions was done by *Beauchamp et al.* in 1978 within a Penning trap of a Fourier transform ion cyclotron resonance (FTICR) mass spectrometer.^[42] The application of IRMPD spectroscopy using QIT instruments followed.^[43,44] This combination presents the advantage of a small spherically-shaped cloud of trapped ions which can improve the overlap of the ion cloud with the focal point of the laser beam.^[45]

A tunable infrared laser irradiates a mass-selected ion of interest. If the laser frequency is in resonance with a vibrational mode of the molecule, the ion may absorb one or several IR photons exceeding its dissociation threshold. Overcoming of the dissociation thresholds result in fragmentation processes. The mass spectrometer detects the resulting dissociation of the ion leading to a change in the mass-to-charge (m/z) ratio. The dissociation yield as a function of the laser wavelength is related to the vibrational spectrum of the ion. IRMPD spectroscopy, also known as action spectroscopy, is an indirect method of measuring the IR spectra of ions where the light causes a change in the molecule.

Two models have been debated illustrating the photon absorption process. Within the first model, dissociation occurs by absorbing photon energy into one single mode and ladder-climbing in this mode. This coherent “ladder-climbing” mechanism in a single vibrational potential well would be impeded by the “anharmonicity bottleneck” which causes the laser to gradually run out of resonance as the molecule is excited.^[46] On the other hand, mechanistically, the absorption of multiple photons is thought to be a non-coherent process^[47], where the energy absorbed by the ion is quickly dissipated into the bath of vibrational degrees of freedom of the molecule by intra-molecular vibrational redistribution (IVR) (Fig. 8).^[48,49] Photon absorption takes place at a fundamental vibrational frequency.^[50] Each sequential step of absorption raises the internal energy of the ion until the dissociation threshold is exceeded, and leads to fragmentation. The energy is stored in the bath of vibrational degrees of freedom of the molecule which means that light absorption leads to a heating of the ions. In contrast to a ladder-climbing process, the anharmonicity bottleneck is avoided as a result of the IVR.^[48]

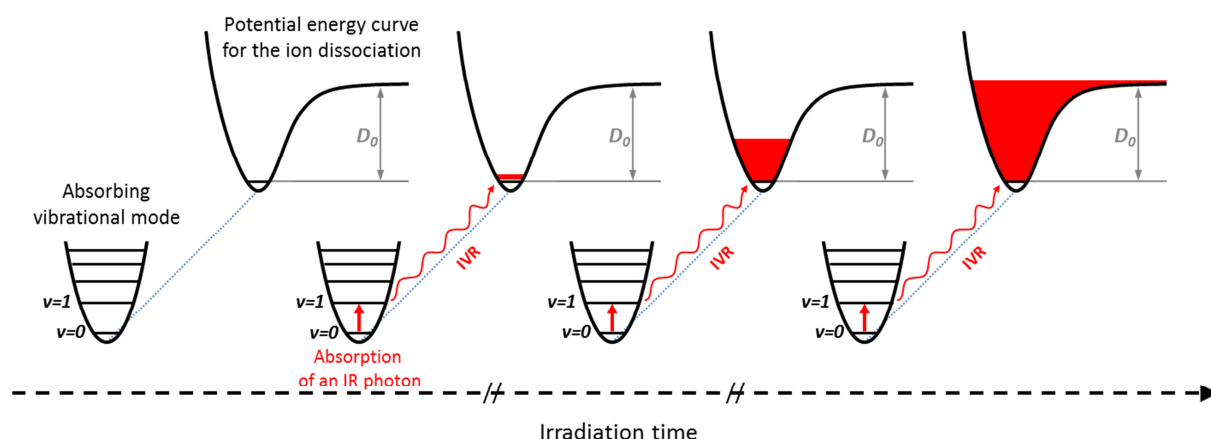


Figure 8: Schematic representation of the mechanism of infrared multi-photon dissociation (IRMPD).^[49]

The second model appears much more reasonable, since the experimental observations often reveal fragmentation occurring within the dissociation path exhibiting low bond strengths instead of within the excited mode itself.

Within this work, IRMPD measurements were performed using the modified Bruker amaZon SL mass spectrometer (cf. chapter 2.1.3).

2.2.2 Collision-Induced Dissociation (CID)

Dissociation of ions and mass detection of the fragments serves as a powerful approach to gather structural information of a molecule. Collisions with a neutral gas provide another activation method to induce fragmentation, referred to as collision-induced dissociation (CID).^[51,52] This process exhibits insights in characteristic fragmentation pattern and provides information on the stability of the precursor ions or binding strengths.^[53-56]

The application of a DC potential, in addition to the trapping potential, will excite the trapped precursor ions causing them to undergo collisions with the buffer gas (helium) in the ion trap. The collisional energy is transferred into internal degrees of freedom. Exceeding a threshold level leads to fragmentation of the precursor ion. The applied collision potential is proportional to an energy value in the lab frame (E_{LAB}^{rel}) in arbitrary units. The transferred

energy amount of a single collision depends on the velocity and the masses of the collision gas and the ion of interest. Therefore, a center-of-mass transformation insures the comparability of relative excitation energies (E_{COM}^{rel}) of molecules with different masses. The E_{COM}^{rel} energy value is the theoretical amount of energy that can be absorbed during collisional activation as a fraction of E_{LAB}^{rel} and can be calculated by:

$$E_{COM}^{rel} = \frac{m_{He}}{m_{He}+m_{ion}} \cdot E_{LAB}^{rel} \quad (1)$$

m_{He} : molecular mass of the He gas

m_{ion} : isotopically averaged mass of the precursor ion

The variation of excitation magnitudes in a stepwise fashion until complete dissociation of the ion of interest allows for the recording of CID appearance curves. For every voltage step, the relative intensities of the precursor and fragment ions of a distinct number of mass are averaged, resulting in a curve of sigmoid shape (Fig. 9).

Normalized relative ($I_{i,norm}^{fr}$) and total fragmentation yields (I_{tot}^{fr}) were calculated according to the following equations:

$$I_{i,norm}^{fr}(E_{LAB}^{rel}) = \frac{I_i^{fr}(E_{LAB}^{rel})}{\sum_i I_i^{fr}(E_{LAB}^{rel}) + \sum_i I_i^p(E_{LAB}^{rel})} \quad (2)$$

$$I_{tot}^{fr}(E_{LAB}^{rel}) = \sum_i I_{i,norm}^{fr}(E_{LAB}^{rel}) \quad (3)$$

In the center-of-mass frame, E_{LAB}^{rel} converts to E_{COM}^{rel} . Fragmentation amplitude dependent CID spectra were fitted by sigmoid fit functions using a least-squares criterion:

$$I_{fit}^{fr}(E_{COM}^{rel}) = \frac{a_i}{(1+e^{(E_{50}-E)B_i})} \quad (4)$$

$$I_{fit}^p(E_{COM}^{rel}) = \frac{a_i}{(1+e^{-(E_{50}-E)B_i})} \quad (5)$$

Here, a_i denotes the branching ratio of the particular product ion ($\sum a_i = 1$), E_{50} is the voltage at which the sigmoid function has reached half of its maximum, E is the fragmentation amplitude, and B describes the slope of the sigmoid curve. Due to the correlation of fragmentation voltage and appearance energies, it is assumed that the breakdown curves allow for the estimation of binding energies of the different complex ions. The phenomenological appearance energy values (AE) are derived from a numerical linear

extrapolation of the rise of the sigmoid fit function at E_{50} to the baseline. The line passes through $y = E_{50}$ and the corresponding abscissa value.^[57-59]

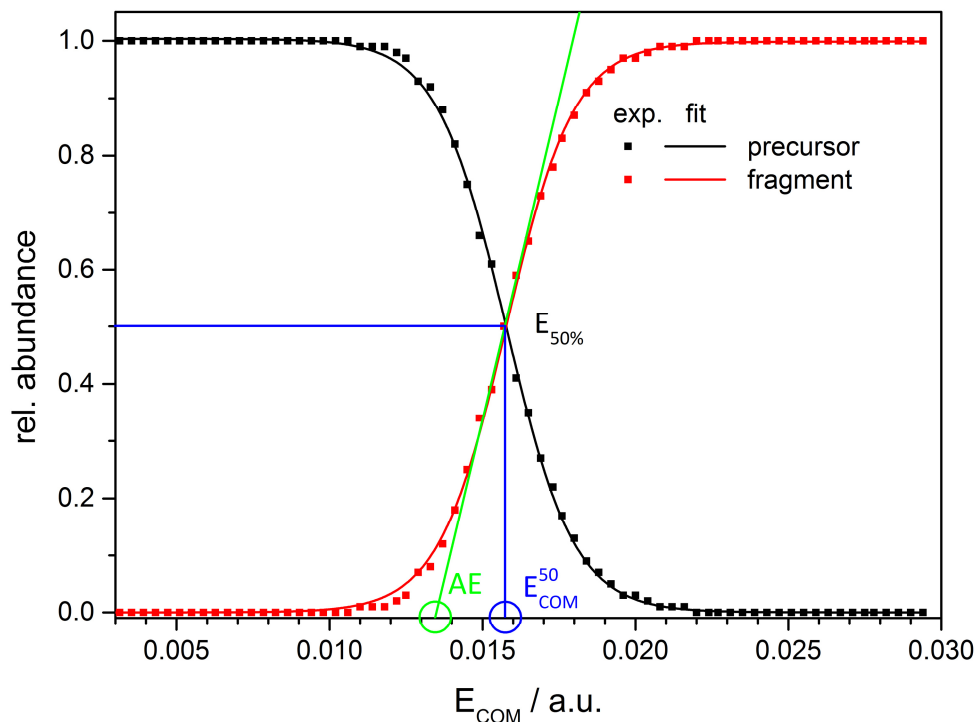


Figure 9: Example of a CID breakdown diagram as a function of the center-of-mass corrected fragmentation amplitude E_{COM} . The dots represent the experimental data, the black and red lines are sigmoid fit functions. The green line was derived from the slope of the sigmoid fit function at E_{COM}^{50} . Positions of the E_{COM}^{50} (blue) and AE (green) values are marked with circles.

This procedure allows for a determination of the phenomenological E_{COM}^{50} values (Fig. 8, blue circle) and the appearance energies (AE) (Fig. 8, green circle). The determination of CID curves and thus, derived bond stabilities succeeds by comparing an energy value that has to be used to yield 50% fragmentation efficiency (E_{COM}^{50}) or the deduced AE value. The use of so called “thermometer ions” to calibrate the internal energy scale of the mass spectrometer allows for the correlation of E_{COM}^{50} and AE values with activation energies derived from *ab initio* computations. This approach provides access to binding energies.^[58,60-64]

As shown by *Lifshitz*^[65] and as reviewed by *Schroeder et al.*^[58], the phenomenological *AE* values should deliver better results than the E_{COM}^{50} values. The consideration of the *AE* values reduces the influence of kinetic effects on the derivation of the underlying intrinsic thermochemistry. Specifically for a simple bond cleavage, the rise of the fragment ion from their threshold is determined by the density of states of the precursor ion, which is a size effect. Larger ions should dissociate more slowly, thus the resulting CID appearance curve is flatter. Therefore, the E_{COM}^{50} values are shifted to larger values. In the determination of the *AE* values, the extrapolation to the baseline does not eliminate but lowers the effect of the slope on the energetics value derived from E_{COM}^{50} .^[58] Furthermore, the rise of the sigmoid fit function is an indication for the transition state which is passed during the fragmentation process. Like all chemical reactions, the unimolecular decomposition of ions is subject to thermodynamic versus kinetic reaction control: the kinetic product forms faster, whereas the thermodynamic product is more stable. A flat slope arises from a tight transition (thermodynamic) state, while a steep slope points out a loose transition (kinetic) state. An activated complex with strict steric requirements is referred to as a tight complex, whereas the transition state without such requirements is called a loose complex. The tight complex needs more energy to dissociate and this leads to a flatter slope, while the loose complex is weakly bonded resulting in steep slopes.^[66,67]

Within this work, CID experiments were performed using the Bruker Esquire 6000 mass spectrometer (cf. chapter 2.1.3).

2.2.3 Computational Methods

A detailed structural interpretation of IRMPD spectra requires a comparison to theoretical linear IR absorption spectra of suspected geometries. A common approach is the comparison of IRMPD spectra to harmonic frequency computations at the density functional theory (DFT) level of theory. For that purpose, the harmonic spectra are scaled in order to compensate for anharmonicities.^[68]

A structural determination succeeds in performing calculations with different start geometries, since this method only finds the minimum structure within the given start geometry. A comparison of the final energy values allows for the determination of a global minimum structure.

DFT has become a widely used method for determining a molecule's ground state energy based on the distribution of the electron density.^[69-72] The DFT calculation allows for the energy optimization of a molecule's geometry in order to reach the lowest energy within given convergence criteria without a previous calculation of the many-electron wave function.^[73]

Kohn and Hohenberg formulated the fundamental theorem for the density functional theory. In 1998, they received the Nobel Prize for chemistry together with *Pople*. (Hohenberg-Kohn-Theorem).^[74] The theorem states that the properties of the ground state of a N electron system depend on the electron density. All molecular properties are functionals of this electron density.

Instead of solving the Schrödinger equation for the whole system, the Kohn-Sham equations examine the whole system as a system of non-interacting electrons generating the same density as any given system of interacting electrons.^[75] The Kohn-Sham wavefunction is a single Slater determinant constructed from a set of orbitals that are the lowest energy solution to

$$\left(-\frac{\hbar^2}{2m}\nabla^2 + v_{eff}(r)\right)\Phi_i(r) = \varepsilon_i\Phi_i(r) \quad (6)$$

with ε_i being the orbital energy of the corresponding Kohn-Sham orbital i .

The density of the whole system reads as follows:

$$\rho(r) = \sum_i^N |\Phi_i(r)|^2 \quad (7)$$

The total energy of a system is defined as:

$$E(\rho) = T_s(\rho) + \int dr v_{ext}(r)\rho(r) + V_H(\rho) + E_{XC}(\rho) \quad (8)$$

with $T_s(\rho)$ being the Kohn-Sham kinetic energy, v_{ext} an external potential including the electron-nuclei interaction, $V_H(\rho)$ the Coulomb energy, and $E_{XC}(\rho)$ the exchange-correlation (XC) energy describing the electron-electron interaction.

The $E_{XC}(\rho)$ term actually combines from an exchange and a correlation term – neither of which is known *a priori*:

$$E_{XC}(\rho) = E_X(\rho) + E_C(\rho) \quad (9)$$

The approximation of $E_{XC}(\rho)$ plays a crucial role within DFT, and it is subject of the used functionals. The use of hybrid methods, combining local density approximations (LDA) and generalized gradient approximations (GGA) with calculating exchange energies according to the Hartree-Fock method, helps to achieve reasonable results.^[76-78]

In the present work, all geometry optimizations and frequency computations were performed using the program packages Gaussian 03 and Gaussian 09.^[79,80] The different specific basis sets and functionals used will be addressed in the relevant chapters. Calculations were gratefully run on the computing clusters of the TU Kaiserslautern, which are under the supervision of the group of Prof. Dr. Ch. Van Wüllen.

2.3 References

- [1] M. Dole, L. L. Mack and R. L. Hines, *Journal of Chemical Physics*, **1968**, 49, 2240-&.
- [2] J. B. Fenn, *Angewandte Chemie-International Edition*, **2003**, 42, 3871-3894.
- [3] J. B. Fenn, M. Mann, C. K. Meng, S. F. Wong and C. M. Whitehouse, *Science*, **1989**, 246, 64-71.
- [4] J. B. Fenn, M. Mann, C. K. Meng, S. F. Wong and C. M. Whitehouse, *Mass Spectrometry Reviews*, **1990**, 9, 37-70.
- [5] M. Yamashita and J. B. Fenn, *Journal of Physical Chemistry*, **1984**, 88, 4451-4459.
- [6] M. Mann, *Organic Mass Spectrometry*, **1990**, 25, 575-587.
- [7] G. Siuzdak, *Proceedings of the National Academy of Sciences of the United States of America*, **1994**, 91, 11290-11297.
- [8] M. Mann, R. C. Hendrickson and A. Pandey, *Annual Review of Biochemistry*, **2001**, 70, 437-473.
- [9] W. J. Griffiths, A. P. Jonsson, S. Y. Liu, D. K. Rai and Y. Q. Wang, *Biochemical Journal*, **2001**, 355, 545-561.
- [10] J. F. de la Mora, G. J. Van Berkel, C. G. Enke, R. B. Cole, M. Martinez-Sanchez and J. B. Fenn, *Journal of Mass Spectrometry*, **2000**, 35, 939-952.
- [11] N. B. Cech and C. G. Enke, *Mass Spectrometry Reviews*, **2001**, 20, 362-387.
- [12] A. P. Snyder, *Biomolecular and Biotechnological applications of electrospray ionization mass spectrometry*, American Chemical Society, **1996**.
- [13] R. B. Cole, *Electrospray Ionization Mass Spectrometry: Fundamentals, Instrumentation and Applications*, Wiley VCH, **1997**.
- [14] D. A. Plattner, *International Journal of Mass Spectrometry*, **2001**, 207, 125-144.
- [15] A. Skriba, J. Schulz and J. Roithova, *Organometallics*, **2014**, 33, 6868-6878.
- [16] Stewart, II, *Spectrochimica Acta Part B-Atomic Spectroscopy*, **1999**, 54, 1649-1695.
- [17] P. Kebarle and L. Tang, *Analytical Chemistry*, **1993**, 65, A972-A986.
- [18] A. Gomez and K. Q. Tang, *Physics of Fluids*, **1994**, 6, 404-414.
- [19] R. L. Byer and R. L. Herbst, *Parametric oscillation and mixing*, Springer-Verlag, **1977**.
- [20] Giordmai.Ja and R. C. Miller, *Physical Review Letters*, **1965**, 14, 973-&.
- [21] P. A. Franken, G. Weinreich, C. W. Peters and A. E. Hill, *Physical Review Letters*, **1961**, 7, 118-&.

- [22] R. C. Eckardt, C. D. Nabors, W. J. Kozlovsky and R. L. Byer, *Journal of the Optical Society of America B-Optical Physics*, **1991**, 8, 646-667.
- [23] J. G. Haub, M. J. Johnson, B. J. Orr and R. Wallenstein, *Applied Physics Letters*, **1991**, 58, 1718-1720.
- [24] W. R. Bosenberg and D. R. Guyer, *Journal of the Optical Society of America B-Optical Physics*, **1993**, 10, 1716-1722.
- [25] C. Merkert, Dr. rer. nat., Technische Universität Kaiserslautern, **2014**.
- [26] F. Menges, Dr. rer. nat., Technische Universität Kaiserslautern, **2013**.
- [27] M. Gerhards, *Optics Communications*, **2004**, 241, 493-497.
- [28] W. Paul and H. Steinwedel, *Zeitschrift Fur Naturforschung Section a-a Journal of Physical Sciences*, **1953**, 8, 448-450.
- [29] *USA Pat.*, 2939952, **1960**.
- [30] R. E. March, *Journal of Mass Spectrometry*, **1997**, 32, 351-369.
- [31] A. H. Payne and G. L. Glish, in *Biological Mass Spectrometry*, ed. A. L. Burlingame, Elsevier Academic Press Inc, San Diego, **2005**, vol. 402, pp. 109-148.
- [32] E. Hohn, *McLachlan, NW - Theory and Application of Mathieu Functions*, **1966**.
- [33] G. C. Stafford, P. E. Kelley, J. E. P. Syka, W. E. Reynolds and J. F. J. Todd, *International Journal of Mass Spectrometry and Ion Processes*, **1984**, 60, 85-98.
- [34] J. N. Louris, J. W. Amy, T. Y. Ridley and R. G. Cooks, *International Journal of Mass Spectrometry and Ion Processes*, **1989**, 88, 97-111.
- [35] R. E. Kaiser, Louris, J.N., Amy, J.W., Cooks, R.G. , *Rapid Commun. Mass Spectrom.*, **1989**, 3, 225-229.
- [36] M. Splendore, F. A. Londry, R. E. March, R. J. S. Morrison, P. Perrier and J. Andre, *International Journal of Mass Spectrometry and Ion Processes*, **1996**, 156, 11-29.
- [37] J. D. Williams, R. G. Cooks, J. E. P. Syka, P. H. Hemberger and N. S. Nogar, *Journal of the American Society for Mass Spectrometry*, **1993**, 4, 792-797.
- [38] M. J. Charles, S. A. McLuckey and G. L. Glish, *Journal of the American Society for Mass Spectrometry*, **1994**, 5, 1031-1041.
- [39] R. E. March, A. W. McMahon, E. T. Allinson, F. A. Londry, R. L. Alfred, J. F. J. Todd and F. Vedel, *International Journal of Mass Spectrometry and Ion Processes*, **1990**, 99, 109-124.
- [40] Bruker Daltonics GmbH, **2005**.

- [41] Bruker Daltonics GmbH, **2009**.
- [42] R. L. Woodin, D. S. Bomse and J. L. Beauchamp, *Journal of the American Chemical Society*, **1978**, 100, 3248-3250.
- [43] J. S. Brodbelt and J. J. Wilson, *Mass Spectrometry Reviews*, **2009**, 28, 390-424.
- [44] L. Sleno and D. A. Volmer, *Journal of Mass Spectrometry*, **2004**, 39, 1091-1112.
- [45] A. Simon, L. MacAleese, P. Maitre, J. Lemaire and T. B. McMahon, *Journal of the American Chemical Society*, **2007**, 129, 2829-2840.
- [46] N. C. Polfer and J. Oomens, *Mass Spectrometry Reviews*, **2009**, 28, 468-494.
- [47] D. W. Lupo and M. Quack, *Chemical Reviews*, **1987**, 87, 181-216.
- [48] N. C. Polfer, *Chemical Society Reviews*, **2011**, 40, 2211-2221.
- [49] J. Roithova, *Chemical Society Reviews*, **2012**, 41, 547-559.
- [50] E. R. Grant, P. A. Schulz, A. S. Sudbo, Y. R. Shen and Y. T. Lee, *Physical Review Letters*, **1978**, 40, 115-118.
- [51] McLaffer.Fw, P. F. Bente, R. Kornfeld, S. C. Tsai and I. Howe, *Journal of the American Chemical Society*, **1973**, 95, 2120-2129.
- [52] McLaffer.Fw, R. Kornfeld, W. F. Haddon, K. Levsen, I. Sakai, P. F. Bente, S. C. Tsai and Schuddem.Hd, *Journal of the American Chemical Society*, **1973**, 95, 3886-3892.
- [53] L. Batiste and P. Chen, *Journal of the American Chemical Society*, **2014**, 136, 9296-9307.
- [54] L. A. Hammad, G. Gerdes and P. Chen, *Organometallics*, **2005**, 24, 1907-1913.
- [55] M. Li, S. R. Liu and P. B. Armentrout, *Journal of Chemical Physics*, **2009**, 131.
- [56] M. R. Sievers, L. M. Jarvis and P. B. Armentrout, *Journal of the American Chemical Society*, **1998**, 120, 1891-1899.
- [57] P. Gruene, C. Trage, D. Schroder and H. Schwarz, *European Journal of Inorganic Chemistry*, **2006**, DOI: 10.1002/ejic.200600587, 4546-4552.
- [58] E. L. Zins, C. Pepe and D. Schroder, *Journal of Mass Spectrometry*, **2010**, 45, 1253-1260.
- [59] G. Bouchoux, J. Y. Salpin and D. Leblanc, *International Journal of Mass Spectrometry and Ion Processes*, **1996**, 153, 37-48.
- [60] K. V. Barylyuk, K. Chingin, R. M. Balabin and R. Zenobi, *Journal of the American Society for Mass Spectrometry*, **2010**, 21, 172-177.

- [61] E. L. Zins, C. Pepe, D. Rondeau, S. Rochut, N. Galland and J. C. Tabet, *Journal of Mass Spectrometry*, **2009**, 44, 12-17.
- [62] E. L. Zins, D. Rondeau, P. Karoyan, C. Fosse, S. Rochut and C. Pepe, *Journal of Mass Spectrometry*, **2009**, 44, 1668-1675.
- [63] C. Collette and E. De Pauw, *Rapid Communications in Mass Spectrometry*, **1998**, 12, 165-170.
- [64] C. Collette, L. Drahos, E. De Pauw and K. Vekey, *Rapid Communications in Mass Spectrometry*, **1998**, 12, 1673-1678.
- [65] C. Lifshitz, *European Journal of Mass Spectrometry*, **2002**, 8, 85-98.
- [66] C. Lifshitz, Laskin, J., *Principles of Mass Spectrometry Applied to Biomolecules*, John Wiley & Sons, **2006**.
- [67] E. V. Anslyn, Dougherty, D.A., *Modern Physical Organic Chemistry*, Macmillan Education, **2005**.
- [68] J. P. Merrick, D. Moran and L. Radom, *Journal of Physical Chemistry A*, **2007**, 111, 11683-11700.
- [69] K. Capelle, *Brazilian Journal of Physics*, **2006**, 36, 1318-1343.
- [70] A. Szabo, Ostlund, N.S., *Modern Quantum Chemistry: Introduction to Advanced Electronic Structure Theory*, Mineola, N.Y.: Dover Pubn Inc, **1996**.
- [71] W. Koch, Holthausen, M.C., *A Chemist's Guide to Density Functional Theory*, Weinheim: Wiley VCH, **2001**.
- [72] D. S. Sholl, Steckel, J.A., *Density Functional Theory: A Practical Introduction*, Wiley-Interscience, **2009**.
- [73] W. Kohn, A. D. Becke and R. G. Parr, *Journal of Physical Chemistry*, **1996**, 100, 12974-12980.
- [74] P. Hohenberg and W. Kohn, *Physical Review B*, **1964**, 136, B864-+.
- [75] W. Kohn and L. J. Sham, *Physical Review*, **1965**, 140, 1133-&.
- [76] S. Grimme, *Journal of Computational Chemistry*, **2004**, 25, 1463-1473.
- [77] S. Grimme, *Journal of Computational Chemistry*, **2006**, 27, 1787-1799.
- [78] J. P. Perdew, J. A. Chevary, S. H. Vosko, K. A. Jackson, M. R. Pederson, D. J. Singh and C. Fiolhais, *Physical Review B*, **1992**, 46, 6671-6687.
- [79] M. J. T. Frisch, *et al.*, Gaussian, Inc., Wallingford CT, Revision C.02 edn., **2004**.
- [80] M. J. T. Frisch, *et al.*, Gaussian, Inc., Wallingford CT, Revision D.01 edn., **2009**.

3. Multi State Mediated Rearrangement and FeCl₂ Elimination in Dinuclear FePd Complexes

Maximilian Gaffga, Isabel Munstein, Patrick Müller, Johannes Lang, Werner R. Thiel and
Gereon Niedner-Schatteburg

*Fachbereich Chemie und Forschungszentrum OPTIMAS, Technische Universität
Kaiserslautern, 67663 Kaiserslautern, Germany*

3.1 Preamble

The following chapter has been accepted for publication by the Journal of Physical Chemistry with the title: "Multi State Mediated Rearrangement and FeCl₂ Elimination in Dinuclear FePd Complexes". Measurements, data evaluation, structural and energetic calculations were performed by myself. I received experimental support by Patrick Müller. Johannes Lang helped with discussions. The synthesis of the complexes was done by Isabel Munstein. The basic manuscript was written by myself and modified by Gereon Niedner-Schatteburg.

3.2 Abstract

Mass spectrometric, spectroscopic and computational characterization of a novel bifunctional iron-palladium complex proves a change of coordination upon solvation. Collisional excitation reveals FeCl₂ and HCl elimination in a solvent modulated competition. Hereby, *syn* and *anti* isomers, identified by theoretical calculations favour and disfavour FeCl₂ elimination, respectively. The FeCl₂ elimination likely proceeds by chlorido and Cp ligand exchange amongst the metallic centers in a concerted, ballet like manner. A multitude of stationary points were identified along the computed multistep reaction coordinates of the three conceivable spin states. The quintet state shows a static Jahn-Teller type relaxation by a tilt away of the Cp ligand at the iron center. The direct singlet-quintet spin cross over is an unprecedented assumption, leaving behind the triplet state as a spectator without involvement. The FeCl₂ elimination would decrease catalytic activity. It is kinetically hindered within a range of applicable temperatures in conceivable technical applications.

3.3 Introduction

The ability of transition metal complexes to catalytically activate different bonds (e.g. C-H or C-C) has made them indispensable tools in modern synthesis.^[1-3] Due to a profound mechanistic basis that had been established for homogeneous transformations during the last decades, the selection of the right element for a certain catalytic reaction became obvious. In contrast, the selection of the right ligand system is a much less knowledge-based process, since the details of the electronic and steric cooperation of the ligand and the metal site are still not completely understood. Therefore it is an important issue to develop novel ligand structures and to investigate their interactions with catalytically active metal sites.

The nature of the donor site (electronic impact), the substituents at the donor site (steric impact) and the structure of the ligand backbone (chelating ligands, stereochemistry) are the essential issues for ligand design. In this context, organometallic complexes being part of the ligand system itself have turned out to be versatile structural motifs to achieve ligand properties that cannot be realized by purely organic structures at all. Generally, stable 18

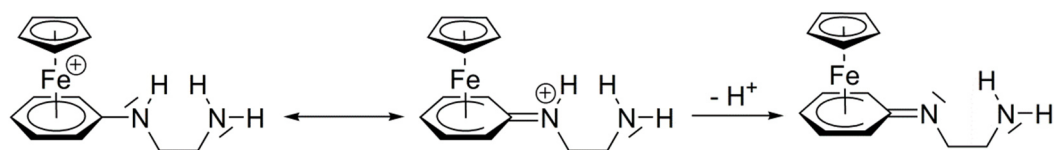
valence electron complexes are used for this purpose being able to survive the conditions of catalytic reactions. The probably most frequently found organometallic structures in such systems are based on ferrocene.^[4, 5] Ferrocene is a stable, quite inexpensive compound for which a multitude of transformations has been established since its discovery in 1951.^[6-8] This allows the introduction of multiple donor sites on each of the cyclopentadienide (Cp) rings. On the other hand, ferrocenes allows switching the activity of the catalytic site by oxidation of the iron(II) center to iron(III) (ferrocenium).^[9-14] Substitution in 1- and 1' position leads to chelating ligands with the ferrocene motif in the rear of the metal site, which on one hand results in special bite angles due to the fixed Cp-Cp distance. 1,1'-Bisdiphenylphosphinoferrocene, being often used for C-C-coupling reactions is the paradigm for such a type of ligand.^[4, 15, 16] In contrast, functionalization of the same Cp ring in 1- and 2- position with two different substituents results in ferrocenes possessing planar chirality which have gained lots of applications in stereoselective catalysis.^{[17-22][23-25]}

Formal substitution of one of the ferrocene Cp anions by a neutral six-membered arene ring results in $[\eta^5\text{-CpFe}(\eta^6\text{-arene})]^+$ complexes being isoelectronic to ferrocene but carrying a positive charge. The first member of this family had been discovered shortly after the invention of ferrocene.^[26, 27] While the Cp rings of ferrocene are electron-rich, the arene motif in $[\eta^5\text{-CpFe}(\eta^6\text{-arene})]^+$ becomes electron poor. This allows to undertake a further functionalization of the arene ring by simple nucleophilic aromatic substitution reactions as long as a chloro arene ring is coordinated to iron. $[\eta^5\text{-CpFe}(\eta^6\text{-C}_6\text{H}_5\text{Cl})]^+$ and *ortho*-, *meta*-, resp. *para*-substituted $[\eta^5\text{-CpFe}(\eta^6\text{-C}_6\text{H}_4\text{Cl}_2)]^+$ are accessible from ferrocene by AlCl₃ promoted reactions with the corresponding chloro benzene derivative in reasonable yields.^[28] While a whole bunch of compounds has been generated from these precursors by S_NAr reactions,^[29-33] to the best of our knowledge, no ligand with a $[\eta^5\text{-CpFe}(\eta^6\text{-arene})]^+$ motif linked to a donor site has been described up to now.

We considered it necessary to strive for the synthesis of such a compound, and we concluded to characterize it by classical tools of molecular chemistry and by advanced techniques of physical chemistry alike. Such a combined approach allows for elucidation of otherwise inaccessible molecular phenomena: Spin state changes of the transition metal centers likely modulates the product formation along reaction path ways, e.g. of

dissociation. Such effects are known as a multi state reactivity scenario, which has been illustrated by numerous studies of various compounds before.^[34]

Here, we report the synthesis of the chelating ligand $[\eta^5\text{-CpFe}(\eta^6\text{-C}_6\text{H}_5\text{NH}(\text{CH}_2)_2\text{NH}_2)]^+$ (**1**), its coordination to PdCl₂ and a series of dynamic, spectroscopic and computational studies on the activation of the CpFe bond of this compound. An important issue of this structure is the poorly donating, arene bound nitrogen donor, making this compound a novel type of a so-called hemilabile ligand, which easily opens up a coordination site at a (catalytically active) metal center. This special property is due to the delocalization of the free electron pair at the nitrogen atom into the arene ring being described by a second mesomeric structure including a pentadienide ligand and an exocyclic iminium cation (Scheme 1). The charge distribution of this second mesomeric form makes the generation of an imine donor by splitting of a proton feasible.



Scheme 1: Charge distribution in the cation **1**⁺.

Our dynamic and spectroscopic characterization arose through Infrared Multi Photon Dissociation (IRMPD) spectroscopy^[35, 36] or Collision-Induced Dissociation (CID) experiments^[37, 38] of the mass-selected ions in order to elucidate the interaction between ligand and metal center, both in conjunction with high level Density Functional Theory (DFT) structure computations. The coupling of these methods provides powerful tools to investigate chemical structures in the gas phase and indirectly allows obtain infrared spectra of selected ions by fragmentation. In combination with theoretical DFT calculations it is perfectly suitable to characterize the chemical structure of transition metal-ligand complexes in the gas phase.^[39-42]

3.4 Experimental and theoretical methods

3.4.1 Synthesis of compounds **1** and **2**

We performed the synthesis of (η^6 -*N*-(2-Aminoethyl)aniline)(η^5 -cyclopentadienide)iron(II) hexafluorophosphate (**1**) as follows: 0.30 g (0.34 mL, 5.0 mmol) of freshly distilled ethylenediamine was added dropwise to a solution of 378 mg (1.0 mmol) (η^6 -chlorobenzene)(η^5 -cyclopentadienide)iron(II) hexafluorophosphate^[28] dissolved in 20 mL of dichloromethane. The reaction mixture was stirred for 30 min at room temp.. 2 mL of a saturated aqueous solution of ammonium hexafluorophosphate were added and the mixture was stirred for 5 min. The organic phase was washed first with 5 mL of an aqueous solution of K₂CO₃ and then twice with 5 mL of water and subsequently dried over MgSO₄. Removing the solvent under vacuum resulted in 360 mg (90 %) of **1** as an orange-red solid. For further characterization of **1** see supplementary material (Texts T1 and T2, and Scheme S1 in supplementary material).

We performed the synthesis of [(η^6 -*N*-(2-(Aminoethyl)aniline)(η^5 -cyclopentadienide)iron(II)]dichloridopalladium(II)hexafluorophosphate (**2**) as follows: A solution of 201 mg (0.5 mmol) of **1** in 20 mL of dichloromethane was added dropwise to a solution of 194 mg of di(benzonitrile)palladium(II) chloride (0.50 mmol) in 10 mL of dichloromethane. The reaction mixture was stirred for 16 h at room temp.. The precipitated solid was filtered off, washed with 2 mL of dichloromethane and dried under vacuum to yield 254 mg (88 %) of **2** as an ochre solid. For further characterization of **2** see supplementary material (Text T2).

3.4.2 Experimental methods

Electrospray ionization mass spectra (ESI-MS) were recorded with two ion trap instruments (Bruker Esquire 6000 for CID and Bruker amaZonSL for IRMPD measurements). The scan speed was 13000 $\frac{m}{z \cdot s}$ in normal resolution scan mode (0.3 fwhm / $\frac{m}{z}$); the scan range was at least 70 to 1500 m/z . The sample solutions of complex **2** in CH₃CN (a), CH₃CN:DMF 9:1 (b) and CH₃CN:DMSO 9:1 (c) at concentrations of approximately 1 x 10⁻⁴ M were continuously infused into the ESI chamber at a flow rate of 2 μ l/min by a syringe pump. We use nitrogen

as drying gas at a flow rate of 3.0 to 4.0 L/min at 220 °C up to 300 °C and sprayed the solutions at a nebulizer pressure of 3 to 4 psi with the electrospray needle held at 4.5 kV. We held constant the transfer parameters to the Paul trap of the mass spectrometer, and we used helium as the buffer gas with a partial pressure of about 3×10^{-3} mbar inside the ion trap. BrukerEsquireControl 5.3 (Esquire) and BrukerTrapControl 7.0 (amaZonSL) software controlled the instrument, and we carried out the data analysis using the Data Analysis 4.0 software.

Collision-induced dissociation (CID) appearance curves were recorded with varying excitation magnitude from 0.0 to 1.5. Note that the well defined excitation amplitudes lead to *a priori* unknown excitation energies of the stored ions. The corresponding scaling factor varies by the very nature of the stored ions, and it is subject of ongoing investigations.^[37] In the present case, we utilize a relative energy scale in the the lab frame (E_{lab}^{rel}) in arbitrary units. These excitation energies were increased in a stepwise fashion until complete dissociation of the ion of interest was observed. Normalized relative and total fragmentation yields were calculated according to the following equations:

$$I_{i,norm}^{fr}(E_{lab}^{rel}) = \frac{I_i^{fr}(E_{lab}^{rel})}{\sum_i I_i^{fr}(E_{lab}^{rel}) + \sum_i I_i^p(E_{lab}^{rel})} \quad (1a)$$

$$I_{tot}^{fr}(E_{lab}^{rel}) = \sum_i I_{i,norm}^{fr}(E_{lab}^{rel}) \quad (1b)$$

We calculated center of mass transformed relative excitation energies (E_{COM}^{rel}) by:

$$E_{COM}^{rel} = \frac{m_{He}}{m_{He} + m_{ion}} \cdot E_{LAB}^{rel} \quad (2)$$

where m_{ion} indicates the isotopically averaged mass of the molecular cation under investigation.

A KTP/KTA optical parametric oscillator/amplifier (OPO/OPA, LaserVision) system pumped with a pulsed 10 Hz injection seeded Nd³⁺:YAG laser (PL8000, Continuum) was used as a source of tunable IR radiation ($\delta\bar{\nu} = 0.9 \text{ cm}^{-1}$, $\delta t = 7 \text{ ns}$) for recording the vibrational spectra. Spectra within the frequency range of 2600 – 3700 cm^{-1} were recorded by application of the OPA idler wave ($\leq 10 \text{ mJ}$ per pulse). Spectra within the range of 1200 – 2100 cm^{-1} were recorded by difference frequency mixing (DFM) in a AgGaSe₂ crystal of the OPA signal and idler waves ($\leq 2 \text{ mJ}$ per pulse). The idler beam was focused by a 50 cm CaF₂ lens. The DF

radiation was focused tighter, by a 90° off-axis parabolic silver mirror with an effective focal length of 15 cm. The IR pulse energy was recorded by a power meter sensor that obtained the applied photon beam after exiting the ions inside the mass spectrometer through a second window. From the recorded fragment and parent ion intensities we determine an IRMPD yield (Y) as:

$$Y = \frac{\sum_i I_i^{fr}}{\sum_i I_i^{fr} + \sum_i I_i^p} \quad (3)$$

The applied IR frequencies were calibrated by a wave meter (Bristol Instruments: 821 Pulsed Laser Wavelength Meter) to a theoretical accuracy of $\pm 0.02 \text{ cm}^{-1}$ which is beyond the spectral bandwidth of the utilized IR photon beams by more than an order of magnitude. Note that IRMPD yields scale in an intrinsically nonlinear way with the applied IR photon flux.^[35, 43-46] Therefore we refrained from any normalization.

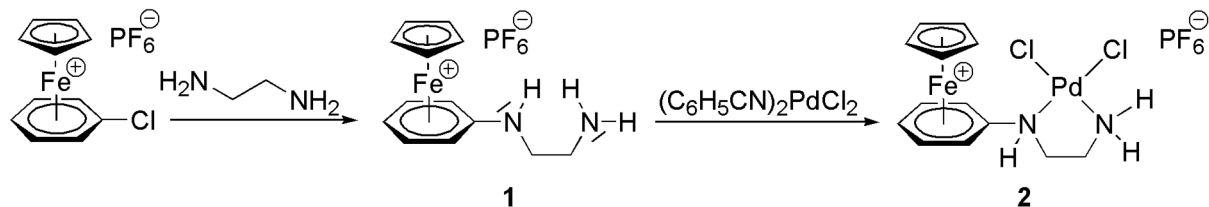
3.4.3 Theoretical methods

We conducted electronic structure calculations at the B3LYP^[47-50] /cc-pVDZ^[51-53] level of theory with Stuttgart RSC 1997^[54, 55] effective core potential representing the iron and palladium atoms as implemented in the Gaussian 09 program package.^[56] We searched for fully optimized molecular structures of the most stable isomers as a function of multiplicities, for linear IR absorption spectra, and for stable points and transition states along the reaction path for the FeCl₂ elimination in the case of **3a**. Standard convergence criteria were applied. Harmonic vibrational frequencies were scaled by a linear lump sum scaling factor of 0.97 as suggested elsewhere.^[57]

3.5 Results and discussion

3.5.1 Characterization of compounds 1, 2 and 3

Reacting $[(\eta^5\text{-Cp})\text{Fe}(\eta^6\text{-C}_6\text{H}_5\text{Cl})]\text{PF}_6$, which was synthesized according to a published procedure, with an excess of ethylene diamine resulted in the formation of the cationic *N,N'*-ligand **1** in 90% yield (Scheme 2). The NMR spectra of compound **1** clearly prove the expected structure: besides the resonances of the Cp ligand (^1H NMR: 4.85; ^{13}C NMR: 76.7 ppm) there are three resonances in the ^1H NMR (6.12, 5.99, 5.80 ppm) as well as four in the ^{13}C NMR (127.7, 87.1, 81.8, 69.2 ppm) spectrum, all of them shifted to higher field compared to the precursor $[(\eta^5\text{-Cp})\text{Fe}(\eta^6\text{-C}_6\text{H}_5\text{Cl})]\text{PF}_6$ that can be assigned to the η^6 -coordinating aniline derivative. More important, there are the resonances of the ethylene linker (^1H NMR: 3.19, 2.90; ^{13}C NMR: 47.0, 41.7 ppm) and the ^1H NMR signals of the two amine units, one at low field (NH: 5.29), the other in the high field region (NH₂: 1.92 ppm), according to the different hybridization of two amines.

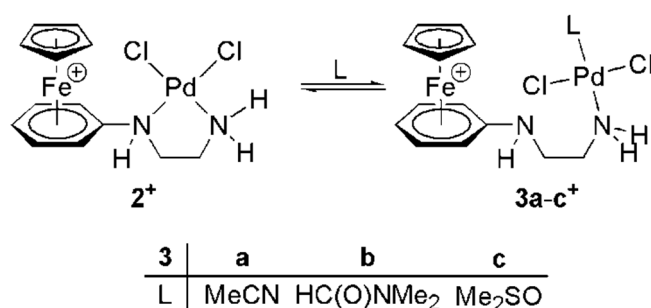


Scheme 2: Synthesis of compounds **1** and **2**.

In the FT-IR-ATR spectrum of the solid compound **1**, there are three well separated absorptions at 3392 (NH) and 3222 (asym. NH₂), resp. 3120 cm⁻¹ (sym. NH₂) that can be assigned to the amino functions of the molecule. The strongest peak in the ESI mass spectrum confirms the mass of the cation $[\text{C}_{13}\text{H}_{17}\text{FeN}_2]^+$ ($m/z = 256.8$).

Compound **1** is well soluble in polar organic solvents, allowing to apply it as an *N,N'*-chelating ligand to coordinate to transition metal sites. As a model type substrate we used dibenzonitrile palladium(II) dichloride that delivers a PdCl₂ fragment by cleavage of the labile benzonitrile ligands (Scheme 2). The heterobimetallic compound **2** is thus formed in almost 90% yields. While the $[\text{CpFe}(\text{arene})]^+$ moiety is not very much influenced by the *N,N'*-donation,

there are pronounced changes in the NMR spectra of the ligand backbone: the ¹H NMR resonances assigned to this part of the molecule are generally shifted to lower field. This effect is most pronounced for the NHCH₂ protons and the NH₂ function. The multiplicity of the NH₂CH₂ pattern (**2**: virtual quintet) increases with respect to the precursor **1** (triplet) indicating a decrease of fluxionality at that site of the molecule. The ¹³C NMR resonances of the ethylene chain are both observed at approx. 44.5 ppm. These data clearly prove a stable coordination of both nitrogen atoms of the ethylenediamine chain to the palladium(II) center in acetonitrile solution.



Scheme 3: Molecular structure of the iron palladium complex **2** and of observed microsolvation species **3a - 3c** together with solvent species $X=CH_3CN$ (**a**), DMF (**b**) and DMSO (**c**). Note the change of palladium coordination sphere upon solvation: The diamine Pd coordination changes from η^2 to η^1 .

This situation changes under the conditions of ESI mass spectrometry: here the solvated cations $[(\eta^5\text{-Cp})\text{Fe}(\eta^6\text{-C}_6\text{H}_5\text{NHCH}_2\text{CH}_2\text{NH}_2\text{-PdCl}_2\text{-L})]^+$ (**3a - 3c**; **3a**: L = MeCN, **3b**: L = HC(O)NMe₂, **3c**: Me₂SO) are observed to a small extent. We then assign structures as shown in Scheme 3 with the terminal NH₂ group staying coordinated to the palladium(II) site.

3.5.2 Collision-induced dissociation (CID) studies

We have recorded fragmentation yields of mass-selected parent ions **2** and **3a - 3c** by gradually increasing the activation magnitude up to complete depletion of the parent ions (Fig. 1).

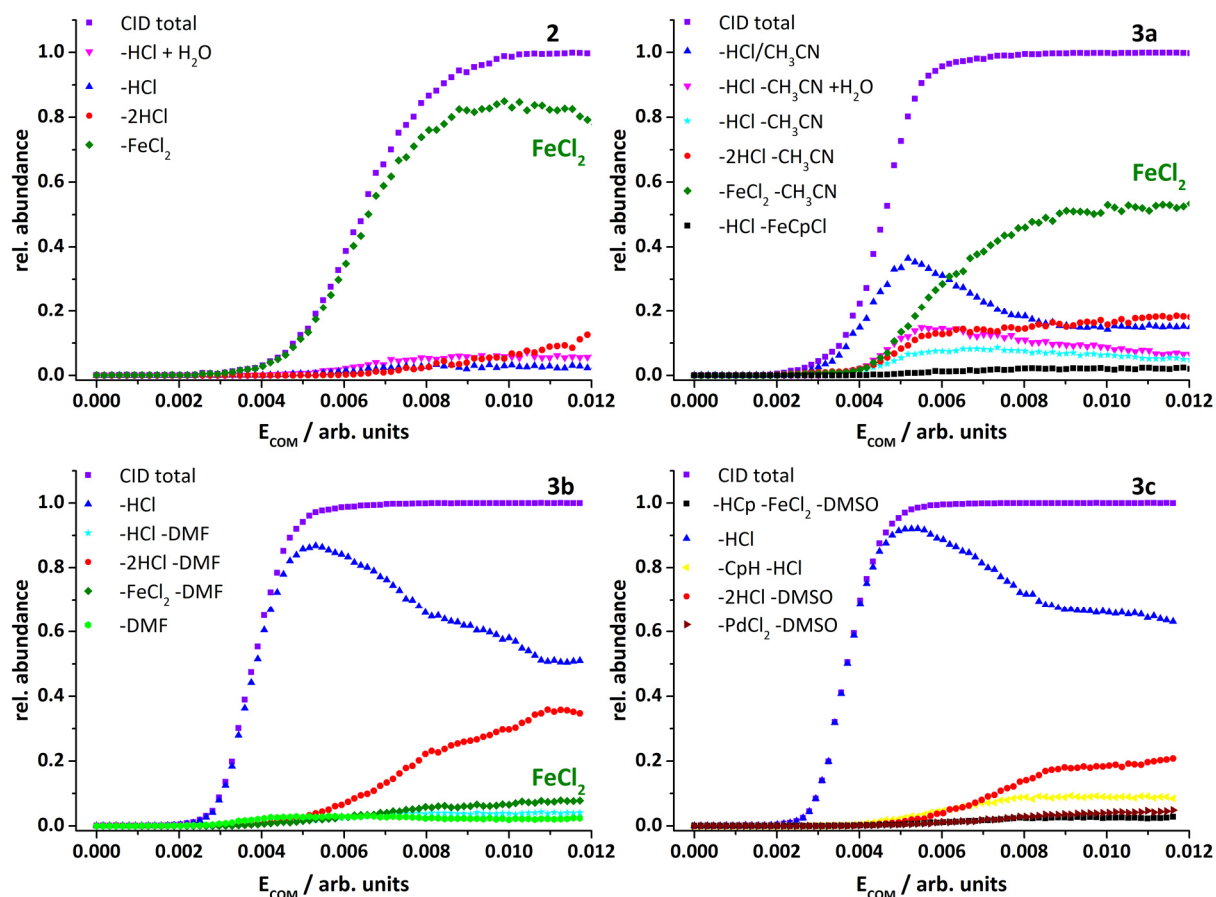


Figure 1: Normalized CID fragment yields of the complex **2** and of observed micro solvation species **3a - 3c** as function of relative excitation energy E_{com} . Note the solvent dependent change in intensity of the $FeCl_2$ elimination channel.

The thus obtained energy-dependent fragmentation yields (formerly known as breakdown curves) reveal varying intensities of up to six fragment ions. The solvent-free complex **2** surprisingly expels $FeCl_2$ with large preference at any level of excitation (green diamonds). Note that an elimination of cyclopentadienyl anion (Cp) moiety off Pd was not observed at all. It is well known, and we have confirmed by swift DFT calculations, that the $FeCl_2$

formation exceeds that of PdCl₂ by 319 kJ/mol. Therefore an exoergic FeCl₂ formation thus provides for a strong thermodynamic driving force of fragmentation (Table S1).

The situation changes as soon as strongly coordinating solvents came into play. For the CH₃CN coordinating complex **3a** behaves differently at low excitation energies (Fig. 1). The dominant fragmentation channel at low excitation energies is the elimination of either HCl and/or CH₃CN (blue triangle), which gives rise to overlapping isotopic patterns that can not be separated unambiguously. Upon increasing the excitation energy another fragmentation channel becomes dominant, which is the concerted elimination of FeCl₂ and CH₃CN (green diamonds). Note that once more the elimination of CpH is not observed. The dominant fragmentation channel of the DMF and DMSO coordinated complexes **3b** and **3c** is the elimination of HCl. It rises at the expense of FeCl₂ elimination, which diminishes in the case of **3b** and vanishes in the case of **3c**. Note that HCl elimination from **3b** and **3c** occurs without loss of solvent (DMF and DMSO, resp.). HCl elimination is weak in the cases of the complex **2** or of the CH₃CN coordinated complex **3a**. Some further fragmentation channels are minor (Table 1).

Table 1: Observed fragmentation channels of complexes **2** and **3a** - **3c**. They are listed in their relative order of appearance. Dominating channels are highlighted in bold.

| complex | neutral loss | | | | | |
|-----------|--------------------------|---------------------|--------------------------|---|-----------------------------|-----------------------------------|
| 2 | -FeCl₂ | -2HCl | -HCl + H ₂ O | -HCl | | |
| 3a | -FeCl₂ | -2HCl | -HCl/CH ₃ CN | -HCl - CH ₃ CN + H ₂ O | -HCl - CH ₃ CN | -HCl -FeCpCl |
| | -CH₃CN | -CH ₃ CN | | | | |
| 3b | -HCl | -2HCl - DMF | -FeCl ₂ - DMF | -HCl - DMF | -DMF | |
| 3c | -HCl | -2HCl -DMSO | -CpH - HCl | -HCl - DMSO | -PdCl ₂ -DMSO | -HCp - FeCl ₂ -DMSO |

Nevertheless it is highly unexpected to observe a likely loss of FeCl₂ from complexes that comprise of joint units of an 18 VE FeCp(arene) fragment and a 16 VE (N)₂PdCl₂ moiety instead of simply expelling HCl, CpH or PdCl₂. This is the more so as the Cp anion remains in the complexes upon FeCl₂ elimination. Such observation indicates the occurrence of an

activated concerted rearrangement prior to dissociation, which may be followed conveniently these days through appropriate calculations (cf. chapter 3.4 in the following).

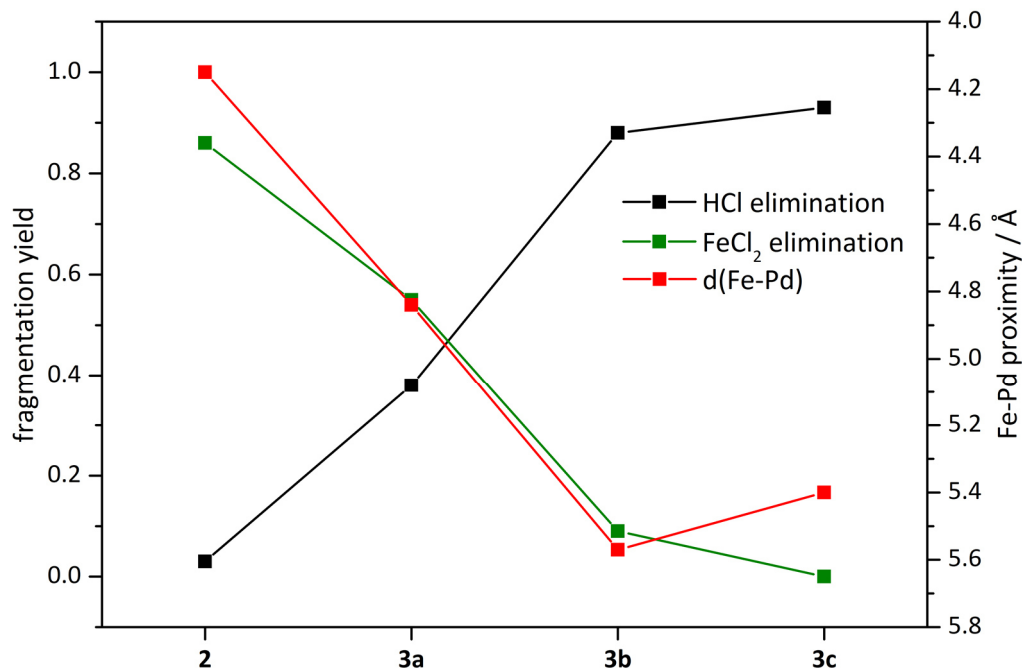


Figure 2: Maximum observed yields of the FeCl₂ (green) and of the HCl (black) fragmentation channels for the complex **2** and for the observed micro solvation species **3a** - **3c**. Note that the binding energy of the solvents CH₃CN, DMF, DMSO to **2** in **3a**, **3b**, **3c** increases from left to right.

HCl elimination and FeCl₂ elimination seem to compete. The competition is confirmed by the visualization of the maximum fragmentation yields in **2** and **3a** - **3c** (Fig. 2). Coordination of a solvent molecule inhibits the FeCl₂ elimination and favors HCl elimination. Obviously the donor strength of the solvent allows tuning the fragmentation channels: the better donating the solvent, the less pronounced is the splitting of FeCl₂ and the more dominant becomes splitting of HCl. The latter effect can easily be explained by the transfer of electron density from the solvent molecule to the Pd site, making the Pd-Cl bond to become weaker and thus the chlorido ligand more basic, which allows the deprotonation of one of the amine sites leaving an amido ligand coordinated to Pd. The concomitant structural relaxation will be

elucidated in conjunction with the discussion of IRMPD spectra (cf. chapter 3.3. in the following). Here we inspect the obtained Fe-Pd proximities and find close correlation with FeCl₂ yields (cf. Fig. 2). An increase in solvation energy seems to hinder FeCl₂ elimination in favor of HCl elimination (cf. Table 2). Note that the competing fragmentation channel (HCl elimination) operates without the necessity of prior solvent detachment. In effect, the very nature of the attached solvent modulates the branching ratio of the competing FeCl₂ and HCl eliminations.

Table 2: Calculated binding energies of attached solvent molecules in complexes **3a**, **3b**, and **3c**.

| complex | solvent molecule | binding energy / kJ/mol |
|-----------|--------------------|-------------------------|
| 3a | CH ₃ CN | 143 |
| 3b | DMF | 165 |
| 3c | DMSO | 198 |

In IRMPD experiments (discussed in the following chapter) the applied IR photonic excitation leads to fragment patterns that are similar to those of CID experiments, as e.g. in prior studies of other compounds by ourselves.^[58] In the present case of **3a**, **3b**, **3c** an IR photonic excitation preferentially yield fragment patterns that are similar to CIR patterns at about $E_{COM}^{rel} = 0.01 \text{ a.u.}$. If we would apply previous scaling factors as obtained by prior work on so called thermometer ions^[59], we would correlate this relative excitation energy E_{COM}^{rel} to an absolute value of $E_{COM} \approx 80 \text{ kJ/mol}$. Cross check with the known solvent binding energies (Table 2) reveals that such value of fragmentation threshold would be too small by about a factor of 2. Recent work rationalized system size dependent correction factors for the ion number of degrees of freedom.^[60] It is thus likely that similar correction would apply in our present case as well. We refrain, however, from dwelling on this issue further at present stage.

3.5.3 IRMPD studies and concomitant DFT calculations

The IRMPD spectrum of the complex **2** (Fig. 3) exhibits three bands in the region of 3380 to 3260 cm⁻¹ and several weak bands between 3230 and 2920 cm⁻¹. In the fingerprint range there is a single strong absorption at 1540 cm⁻¹. One would expect to see IR active C=C ring modes in the fingerprint range around 1500 cm⁻¹, weak aliphatic and aromatic CH stretching modes around 2920 cm⁻¹ and 3230 cm⁻¹, and NH and NH₂ stretching vibrations around 3350 cm⁻¹. These expectations are nicely matched by the recorded observations.

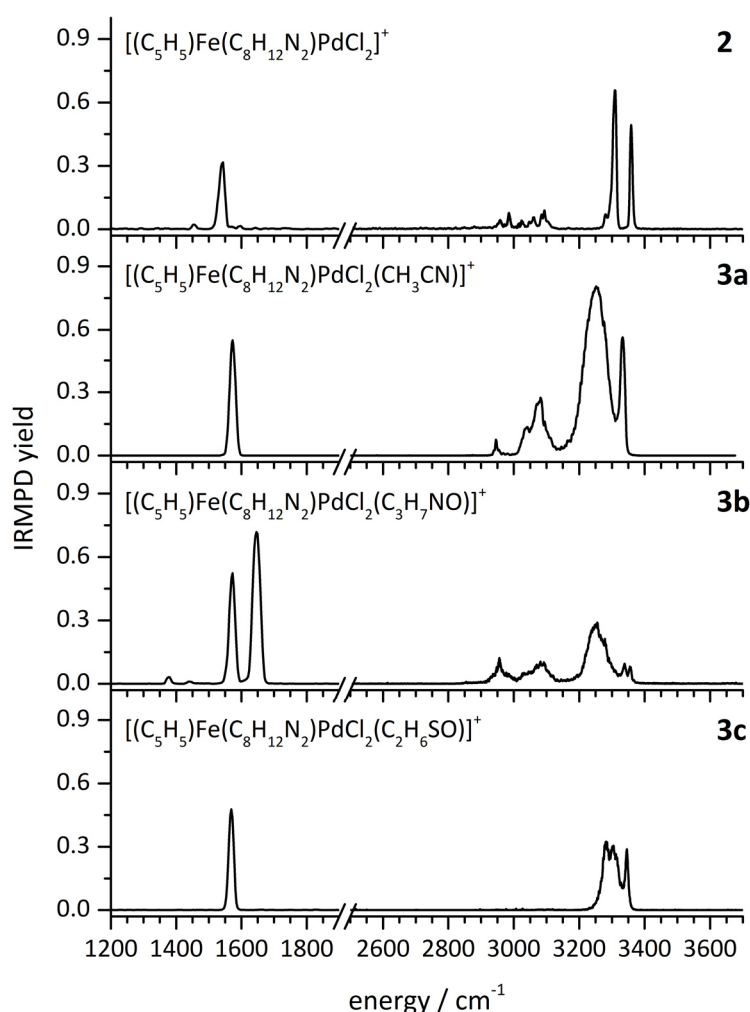


Figure 3: IRMPD spectra of the complex **2** and of the observed micro solvation species **3a** - **3c**. Note the solvent specific broadening and enhancement of NH₂ vibrations due to NH-Cl hydrogen bonding (see text).

The IRMPD spectrum of the CH₃CN coordinated complex **3a** reveals a major spectral change from the complex **2**. There is a significant shift, enhancement and broadening of NH stretching bands around 3250 cm⁻¹. There is also some enhancement and broadening in the CH stretching region. There is a sharp band at 1570 cm⁻¹ in **3a** which is blue shifted from **2** by 30 cm⁻¹.

The IRMPD spectrum of the DMF coordinated complex **3b** looks much like **3a**; somewhat weaker intense in the stretching region. There is an additional band at 1650 cm⁻¹ and a weak bands at 1440 and 1375 cm⁻¹ originate from the CO chromophore in DMF.

The DMSO coordinated complex **3c** exhibits no recordable signal from CH stretching modes. The NH stretching modes are weaker than for **3b**. There is one broad centered at 3295 cm⁻¹ and one sharp band at 3350 cm⁻¹. The single band in the fingerprint region coincident with the blueshifted bands of **3a** and **3b**. Thus all three solvent coordinated complexes **3a** - **3c** share some kind of electronic rearrangement that leads to a strong IR active band around 1565 cm⁻¹. It locates 30 cm⁻¹ to the blue of a somewhat less strong band at 1540 cm⁻¹ in the complex **2** which seems to resemble an aryl C=C stretching mode. It remains open, whether the **3a** - **3c** bands and the **2** band originate from the same type of vibration.

For further elucidation we computed energetics and geometries of likely structures of complexes **2**, **3a** - **3c** by DFT at given level of theory (cf. chapter on theoretical methods). Structure geometries exhibiting a Fe-Cl coordination are questionable due to an instability of 120 kJ/mol. We apply a Newman projection for classification and visualization of computed rotamers (see insets to Fig. 4). Other than e.g. in alkane stereochemistry, the present complexes consist of two subunits of C₂ and C₃ symmetry each. We adopt a *syn* and *anti* nomenclature for the 0° and 120° rotamers of the dihedral angle α (between C¹C²N³C⁴) in the cases of all complexes **2**, **3a** - **3c**. For further characterization we varied this dihedral angle, and we performed full structural relaxation at fixed dihedral angles in steps of 15° in order to obtain optimized geometries and their relative energies (Fig.4). All complexes reveal a total and a local minimum at 0° (*syn*) and 120° (*anti*). Complex **2** shows the highest rotational barrier, which might be due to the close proximity of the Fe and Pd bearing sub units within the complex. The solvent molecule attached complexes **3a** - **3c** exhibit smaller barriers, which might be due to the increased distance between the sub units. The rotational barrier in complex **3a** is low (10 kJ/mol), while the barriers of the complexes **3b** and **3c** are

higher, 15 and 20 kJ/mol. We will show in the following that the FeCl₂ elimination likely takes place from the *syn* isomer (see chapter 3.4). The relative population of *syn* to *anti* isomers thus determines the relative FeCl₂ yield as compared to the alternative HCl expulsion, which might occur from either rotational conformer.

In **2** the high barrier slows down rotational isomerization. Nevertheless, it is fast (ms) compared to the experimental time scale (s). Equilibrium populations favor *syn* and diminish *anti* to less than 2%. Thus FeCl₂ elimination should diminish in favor of HCl expulsion – as observed (cf. Fig. 2).

Solvent attachment stabilizes *anti* in **3a** and **3b**, and it destabilizes *anti* in **3c**; the rotational barrier is reduced in all of these cases. *Anti* population increases – FeCl₂ elimination diminishes (cf. Fig. 2), since it is only possible after solvent abstraction and rearrangement of the molecule (see chapter 3.3). Therefore FeCl₂ elimination for **3a** - **3c** is anti-proportional to the solvents binding energies (cf. table 2), and it correlates with the Fe-Pd proximity (see Fig. 2).

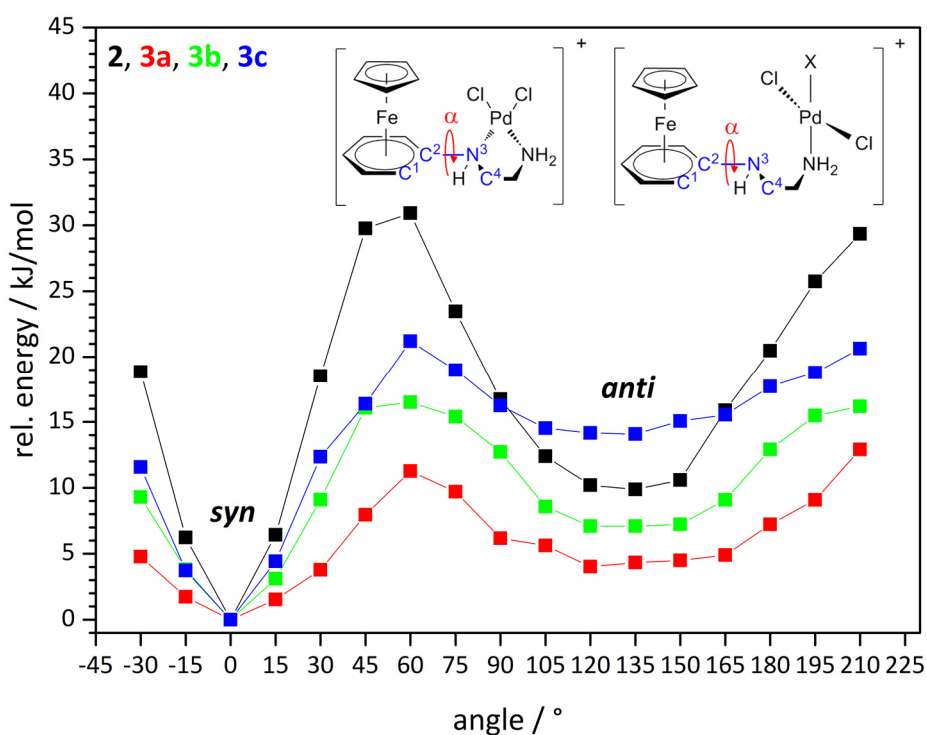


Figure 4: Computed relative energies of rotational conformers of the complexes **2**, **3a** - **3c** by variation of the dihedral angle $\alpha(C^1C^2N^3C^4)$.

The electronic structure calculations provide for structures and linear IR absorption spectra of the likely, most stable isomers of complex **2** and of the solvent coordinated complexes **3a** - **3c**. Comparison with IRMPD spectra leads to further insights.

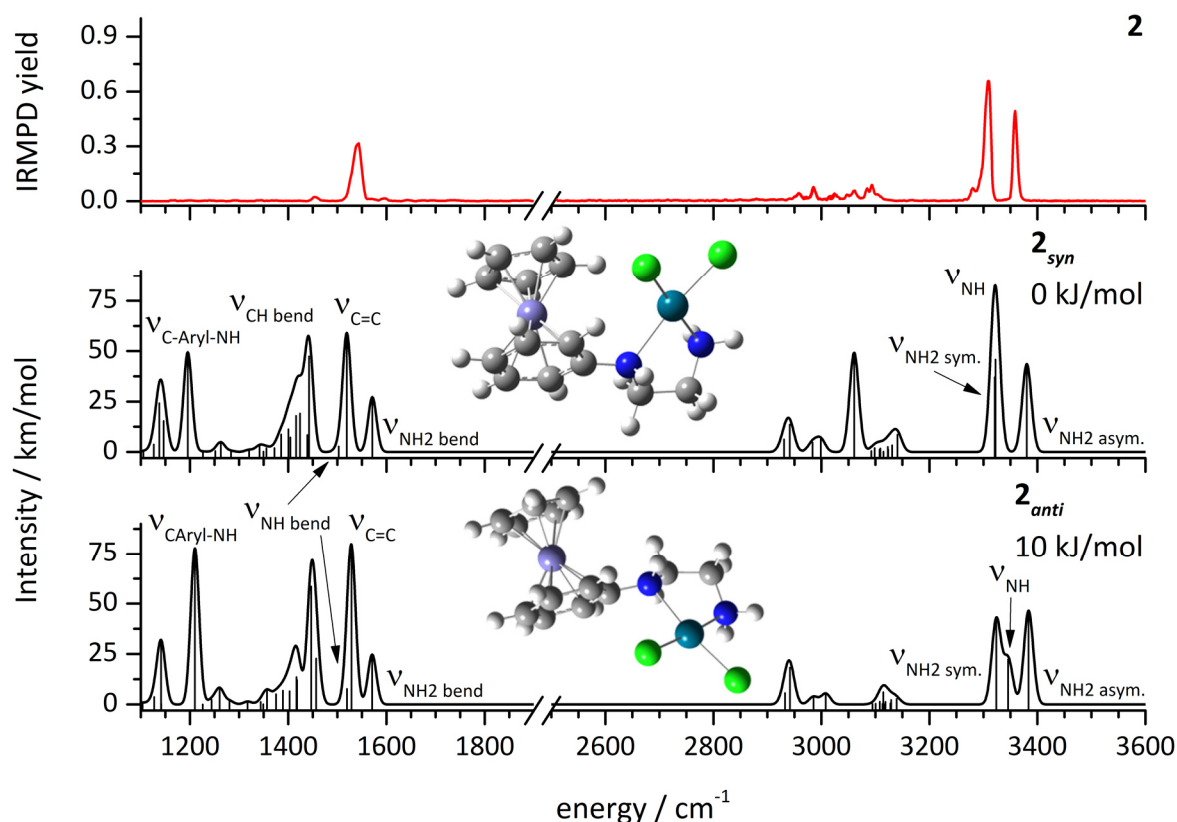


Figure 5: IRMPD spectrum of the complex **2** in comparison to the DFT predicted IR absorption spectra of the two most stable isomers **2_{syn}** and **2_{anti}**. Both isomers provide for a conceivable interpretation of the experimental spectrum.

In the case of the complex **2** the two rotational isomers **2_{syn}** and **2_{anti}** differ by 10 kJ/mol in favor of conformer **2_{syn}** (cf. insets in Fig. 4). In both isomers the Pd cation coordinates square planar to the NH and NH₂ functional groups and to the two chlorido ligands. Both isomers reveal linear IR absorption spectra that are well in line with the experimental IRMPD spectrum. All recorded features are well reproduced, and the above presumed assignments confirmed. Note that there must not be a close correspondence in intensities. It is well known that IRMPD intensities vary from those of absorption spectra.^[35, 43-46]

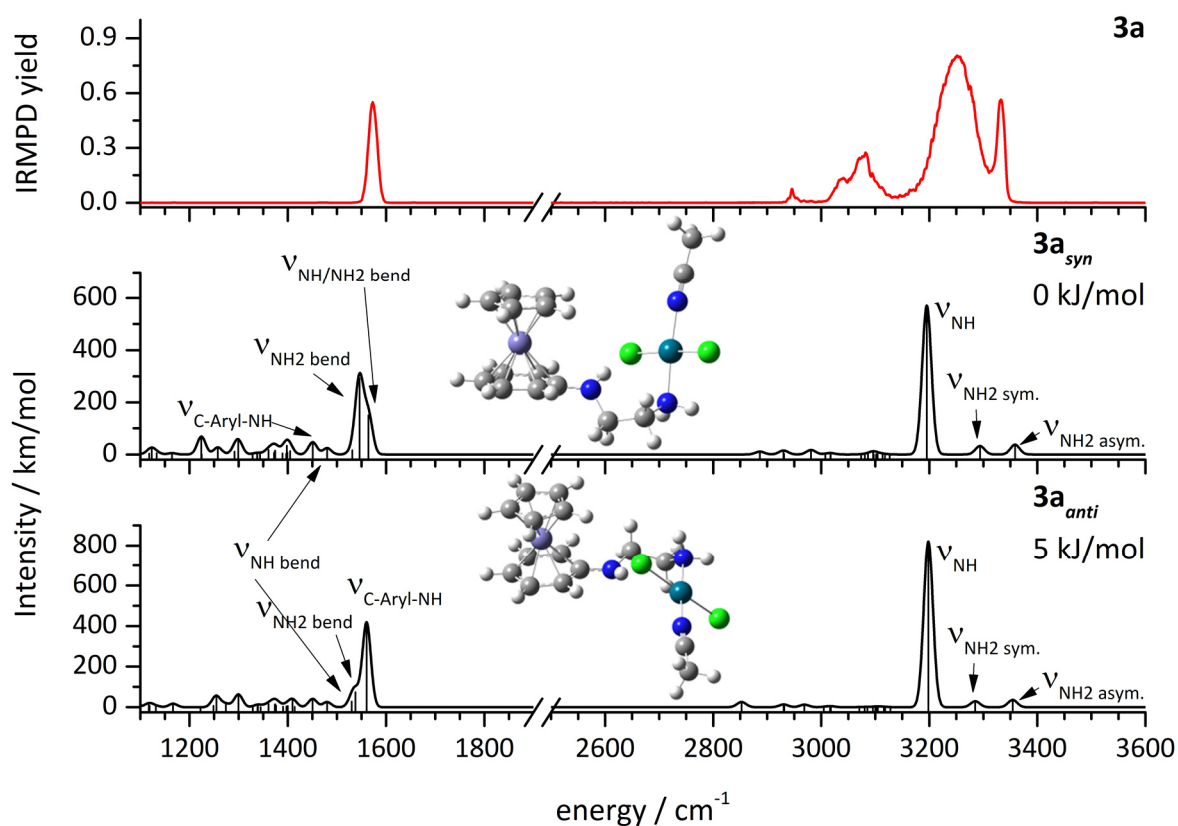


Figure 6: IRMPD spectrum of the complex **3a** in comparison to the DFT predicted IR absorption spectra of the two most stable isomers **3a_{syn}** and **3a_{anti}**. The scaled harmonic eigen modes of NH and NH₂ stretching vibrations fail to explain the experimental pattern.

In the CH₃CN coordinated complex **3a** the two rotational isomers **3a_{syn}** and **3a_{anti}** differ by 5 kJ/mol (cf. insets in Fig. 6) in favor of the conformer **3a_{syn}** - much in line with the findings on the complex **2**. In both isomers the Pd cation has lost NH coordination in favor of CH₃CN attachment. As opposed to di-chlorido *syn* arrangement in **2**, the solvent changes the ligand arrangement in **3a** to *trans* configuration. In both isomers the Pd cation coordinates square planar to the NH₂ functional group, the CH₃CN solvent and to the two chlorido ligands.

The linear IR absorption spectra of both isomers **3a_{syn}** and **3a_{anti}** reveal sharp features throughout. We assign the sharp IRMPD band at 3330 cm⁻¹ to the asymmetric NH₂ stretching mode as predicted by the calculations of isomers **3a_{syn}** and **3a_{anti}**. The computed spectra fail to predict the observed broadening of the recorded bands between 3000 and 3300 cm⁻¹. This effect seems to originate from effects beyond the predictions of linear IR absorptions in harmonic approximation.

Table 3: NH-Cl hydrogen bond lengths and corresponding NH stretching frequencies.

| complex | isomer | d(NH-Cl) / Å | $\nu_{\text{NH calc}} / \text{cm}^{-1}$ | $\nu_{\text{NH exp.}} / \text{cm}^{-1}$ |
|-----------|--------------------------|--------------|---|---|
| 2 | 2_{syn} | - | 3320 | 3308 |
| | 2_{anti} | - | 3347 | |
| 3a | 3a_{syn} | 2.26 | 3195 | 3351 |
| | 3a_{anti} | 2.28 | 3195 | |
| 3b | 3b_{syn} | 2.25 | 3218 | 3350 |
| | 3b_{anti} | 2.23 | 3220 | |
| 3c | 3c_{syn} | 2.32 | 3275 | 3290 |
| | 3c_{anti} | 2.21 | 3205 | |

Upon close inspection it becomes obvious that the solvent attachment to **2** causes subsequent structural changes beyond the coordinative rearrangement of the Pd center in **3a**, **3b**, and **3c**. An additional hydrogen bond forms between the secondary amine NH and the proximate chlorido ligand (d(NH-Cl): 2.26 Å in isomer **3a_{syn}** and 2.28 Å in isomer **3a_{anti}**, cf. Tab. 3). Due to this NH-Cl hydrogen bond, the calculated value of the NH stretching mode red shifts to 3195 cm⁻¹ (in **3a_{syn}**), this value suffering from well-known anharmonic uncertainty in as much as any according hydrogen bond. Moreover this band is expected to broaden significantly as indeed observed at 3250 cm⁻¹. Adjacent CH stretching modes may couple and broaden thereby explaining the observed humps around 3075 cm⁻¹. It is gratifying to see that the predicted increase from **2** to **3a** in IR line strength of ν_{NH} (80 to 600 km/mol) at 3195 cm⁻¹ seems to reflect in the enhancement of integrated area of the 3250 cm⁻¹ hump in the IRMPD spectrum. There is no forcing evidence that a conceivable NH stretch bend-overtone Fermi resonance contributes. Anharmonic calculations (by VPT2, cf. supplement) point to a frequency mismatch.

The calculations reveal the very nature of the 1575 cm⁻¹ IRMPD band. It is of NH/NH₂ bending character with a possible contribution of CN stretching by isomer **3a_{anti}**. For sure, it does not contain contributions of aryl C=C ring breathing modes which redshift to 1390 cm⁻¹ through coordination. The remaining weak IRMPD bands between 2900 and 3050 cm⁻¹ are well predicted by various aliphatic and aryl C-H stretching modes in both isomers **3a_{syn}** and **3a_{anti}**.

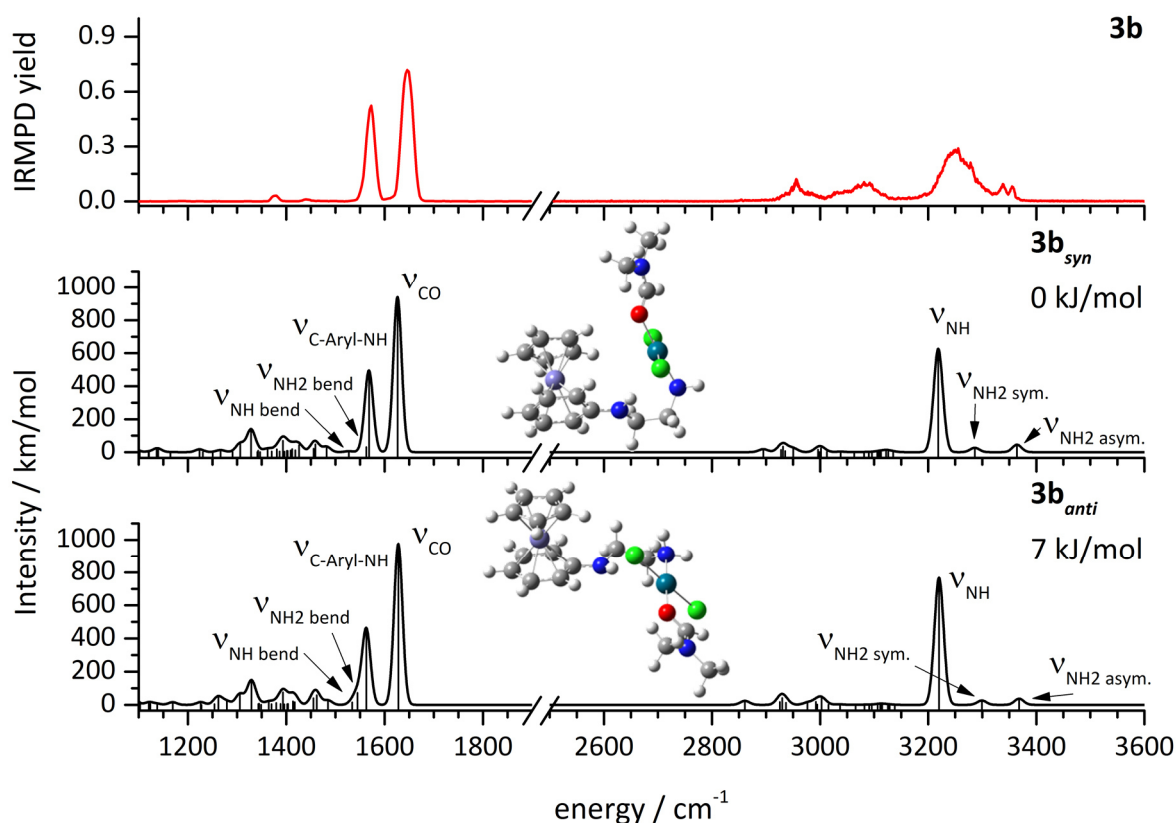


Figure 7: IRMPD spectrum of the complex **3b** in comparison to the DFT predicted IR absorption spectra of the two most stable isomers **3b_{syn}** and **3b_{anti}**. The scaled harmonic eigen modes of NH and NH₂ stretching vibrations fail to explain the experimental pattern.

In the DMF coordinated complex **3b** the two rotational isomers **3b_{syn}** and **3b_{anti}** differ by 7 kJ/mol (cf. insets in Fig. 7) in favor of the *syn* conformer **3b_{syn}** - much in line with the findings on the complex **2** and the CH₃CN coordinating complex **3a**. All structural motifs in **3b** correspond to those of **3a** as discussed above.

The calculated IR spectra of both isomers of **3b** show the typical NH and NH₂ stretching vibrations in close resemblance to **3a**. The experimental evidence for a NH-Cl hydrogen bond in **3b** holds through observation of the broad hump around 3250 cm⁻¹ as before in **3a**. However, the total IRMPD intensities diminish in **3b** by a factor of 2 with respect to **3a**. In contrast the calculated IR intensities of the secondary amine NH stretching mode vary little (about 600 km/mol in both cases). We thus attribute the drop in IRMPD intensity of the NH stretching band in **3b** to a suspected change in fragmentation efficiency. Due to the carbonyl group of DMF there is a C=O stretching vibration around 1625 cm⁻¹ for both isomers **3b_{syn}**

and **3b_{anti}**. The coordination of the carbonyl group at the Pd cation leads to a red shift of about 120 cm⁻¹ with respect to free CO in similar structures. Other spectral features in **3b** resemble those of **3a**.

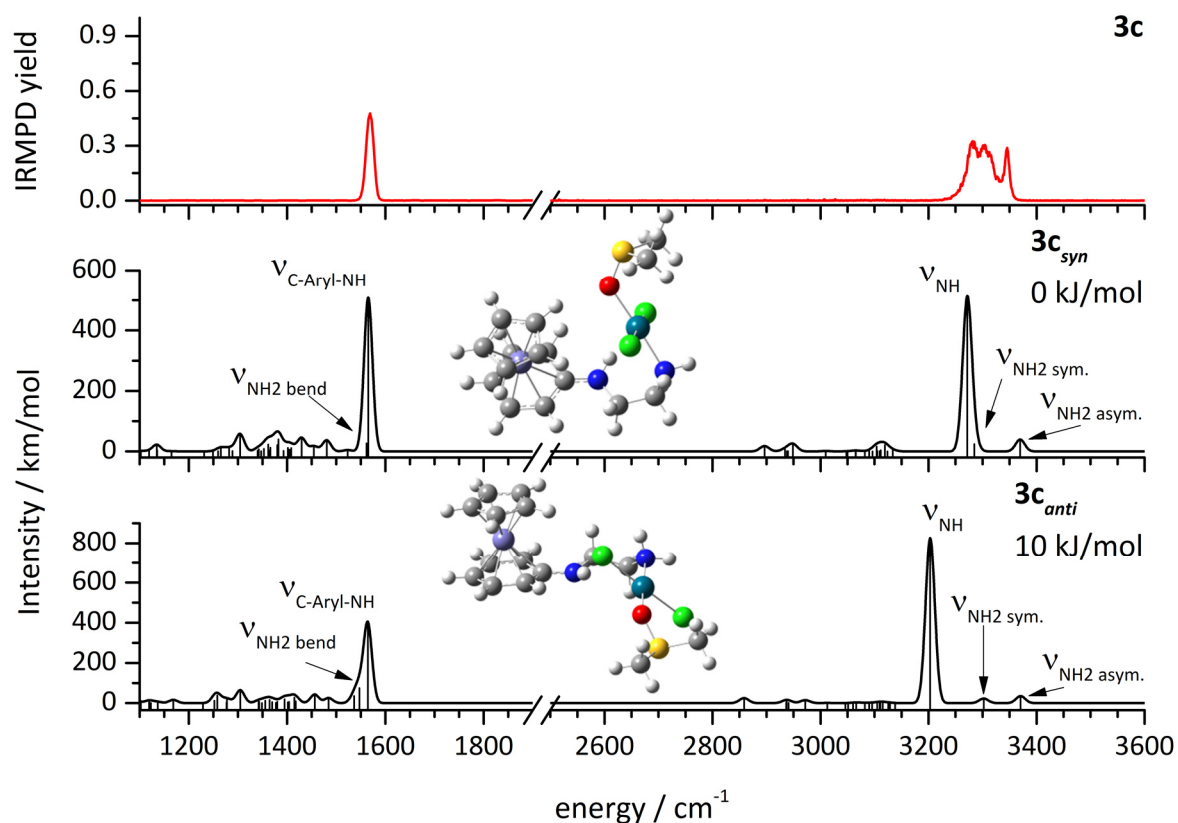


Figure 8: IRMPD spectrum of the complex **3c** in comparison to the DFT predicted IR absorption spectra of the two most stable isomers **3c_{syn}** and **3c_{anti}**. The scaled harmonic eigen modes of NH and NH₂ stretching vibrations fail to explain the experimental pattern.

In the DMSO coordinated complex **3c** the two rotational isomers **3c_{syn}** and **3c_{anti}** differ by 13 kJ/mol (cf. insets in Fig. 8) in favor of the *syn* conformer **3c_{syn}** - much in line with the findings on the complex **2** and the other complexes **3a** and **3b**. All structural motifs in **3c** correspond to those of **3a** and **3b** as discussed above.

The calculations reveal a hydrogen bond between the NH functional group and a chlorido ligand that is significantly longer (+ 0.06 Å, cf. Table 3) in case of the *syn* isomer **3c_{syn}**, and thereby weaker, than the corresponding hydrogen bonds in the *syn* isomers **3a_{syn}** and **3b_{syn}**.

In accord with this finding both the calculated IR absorption spectrum of isomer **3c_{syn}** and the measured IRMPD spectrum reveal a NH stretching band that is by about 50 cm⁻¹ less red shifted than the corresponding bands of complexes **3a** and **3b**. It seems as if the less stable isomer **3c_{ant}**, which would reveal itself through a short NH-Cl hydrogen bond and a concomitant vibrational band more to the red, is not manifest by the experimental IRMPD spectrum. In summary, we assign the recorded band at 3345 cm⁻¹ in **3c** to the asymmetric NH₂ stretching vibration, and the split band with the two maxima at 3305 and 3280 cm⁻¹ to the symmetric NH₂ and the NH stretching vibrations.

3.5.4 Multi state profiles along the reaction coordinate of FeCl₂ elimination in the CH₃CN complex **3a**

The FeCl₂ elimination deserves further attention. It is far from obvious how the Cp anion detaches from its coordination site, setting free the Fe center for release by (or after) acceptance of two chlorido ligands off their prior Pd host.

We chose to exemplify this complex multistep dissociation/fragmentation dynamic of the counterintuitive FeCl₂ elimination process by calculating the energy profiles of the **3a_{syn}** complex along the reaction coordinate(s), taking conceivably contributing spin state multiplicities explicitly into account (Fig. 9).

We found it necessary to take into account the high and low spin states of the open shell Fe(II) cation. This leads to quintet (high spin) and singlet (low spin) multiplicities, and to a conceivable intermediate triplet state. We neglect unlikely high spin states of the Pd(II) cation where a 4d⁸ configuration in square planar coordination stabilizes a singlet state by ligand field splitting. We scale the obtained total energies to the *syn* isomer ¹**3a_{syn}** where the index "1" indicates its singlet ground state. We found the eventual FeCl₂ elimination to proceed through a chain of four consecutive rearrangements, and we identified stationary points (Minima and transitions states) along this reaction coordinate (cf. Fig. 9). We chose a designation of the found minima by "A", "B", "C", "D", and "E" in order to achieve an unambiguous designation and for reasons of simplicity. By "TS A/B" we denote the transition states in between of minima A and B etc.. Note that A in singlet (blue), triplet (green) or

quintet (red) spin states equals $^1\mathbf{3a}_{syn}$, $^3\mathbf{3a}_{syn}$, or $^5\mathbf{3a}_{syn}$, and accordingly for the other minima (cf. blue, red or green curves in Fig. 9). We provide for viewgraphs of the minimum and transition state structures of the lowest spin state along the FeCl₂ elimination path (singlet in the beginning and quintet to the end).

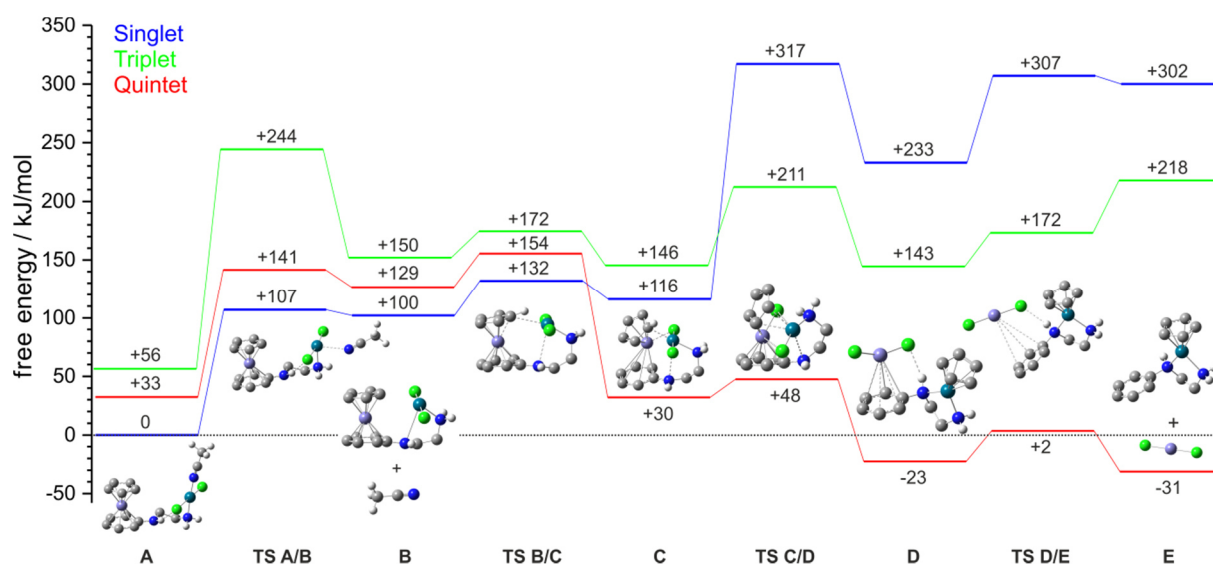


Figure 9: Normalized energetics of stationary points along the reaction coordinate of the FeCl₂ elimination within singlet (blue), triplet (green) and quintet (red) spin states, indicated values in kJ/mol. Depicted structures of stationary points refer to those of the lowest spin state which change along the reaction coordinate from singlet to quintet. For purpose of clarity, aliphatic and aromatic H atoms were omitted, except in CH₃CN. Note that the very structures of the calculated stationary points vary in some dihedral angles by multiplicity (cf. Figs. S2 – S4 in the supporting information), while in any case the primary and secondary structural motifs persist.

Note that structures of any stationary point vary by the spin state. Namely, in $^1\mathbf{A}$ and $^3\mathbf{A}$, the Cp and aryl ligands at the Fe center are opposite to each in an almost perfect sandwich arrangement (Cp-Fe-aryl angle of 178° and 177° for $^1\mathbf{A}$ and $^3\mathbf{A}$, respectively). The computed quintet state $^5\mathbf{A}$ exhibits a tilted-sandwich structure (Cp-Fe-aryl angle of 171°, cf. Fig. S4 in the supporting information).

We rationalize this significant change in geometry via inspection of the orbital energies in a ferrocene like Cp-Fe-aryl structure **4**, which is void of the diamine-Pd-Cl₂ group (cf. calculated MO energies in Fig. S5 in the supporting information). The Fe d orbitals split via the distorted octahedral ligand field of the Cp and aryl ligands. We find in ascending order two (almost) degenerate e_2' orbitals, a sole a_1' , and two almost degenerate e_1'' orbitals. This equates to non-degenerate singlet and triplet ground states, $(e_2')^4(a_1')^2$ and $(e_2')^4(a_1')^1(a_1'')^1$ in similar geometries **14** and **34**, respectively. A quintet state in a linear Cp-Fe-aryl geometry would imply an orbital occupations $(e_2')^3(a_1')^1(a_1'')^1(b_1')^1$ that enforce, however, a symmetry reduction through Jahn-Teller distortion, and effectively lifts the orbital degeneracy into a $(a_2')^2(b_2')^1(a_1')^1(a_1'')^1(b_1')^1$ configuration. Indeed **54** is tilted to 172° – much as observed in the tilted-sandwich structure of **5A**. Thereby we have found a rationalization of seemingly unusual ordering in computed stabilities: $E_{\text{tot}}^{\text{OK}}(\mathbf{1A}) < E_{\text{tot}}^{\text{OK}}(\mathbf{5A}) < E_{\text{tot}}^{\text{OK}}(\mathbf{3A})$, explained through the sandwich relaxation/tilt in the quintet state.

With this insight we are ready to progress further along the reaction coordinate as depicted in Fig. 9. The triplet state remains high along all of this reaction coordinate, and it does not couple to the singlet or quintet states. We thus need not to discuss it further. Endothermic elimination of the acetonitrile ligand from **1A** to **1B** and from **5A** to **5B** proceed almost barrierless via transition states **1TS A/B** and **5TS A/B**. There is some relaxation in dihedral angles with little energy gain, and the Pd center acquires a vacant coordination site. This vacancy receives electron density from the adjacent electron rich Cp ligand in **1B** (Fig. 9) while the Cp ligand tilts away from Pd in **5B** (Fig. S4). The latter quintet case leaves space for favourable approach to Fe of the two chlorido ligands from Pd while the former singlet case runs into a Pd-C bond in **1C** that needs to re-open before chlorido migration enables through **1TS C/D** at high enthalpic expenses (+ 116 to + 317 kJ/mol). The **5B** may run via a low barrier **5TS B/C** transition state into a **5C** structure that reveals close Fe-Pd proximity (**5C**: $d(\text{Fe-Pd})=2.86 \text{ \AA}$, $d(\text{Pd-C})=2.38 \text{ \AA}$; **5TS B/C**: $d(\text{Fe-Pd})=3.26 \text{ \AA}$, $d(\text{Pd-C})=2.47 \text{ \AA}$), other than **1C** (**1C**: $d(\text{Fe-Pd})=3.30 \text{ \AA}$, $d(\text{Pd-C})=2.40 \text{ \AA}$; **1TS B/C**: $d(\text{Fe-Pd})=3.35 \text{ \AA}$, $d(\text{Pd-C})=2.49 \text{ \AA}$). Thereby, **5C** becomes most favourable since the ligand field splitting in the high spin Fe, as induced by the chloride ligands, is smaller than the splitting of the cyclopentadienyl anion.^[61] Thereby, the singlet and quintet diabatic potential surfaces cross on the way from **TS B/C** to **C**. The assumption of an adiabatic progression along the reaction path would thus imply a direct singlet-quintet spin cross over – seemingly without a direct involvement of the higher triplet

state. The concomitant spin flips of two electrons (likely d electrons at Fe) need to occur in concert – an unprecedented assumption, to the best of our knowledge.

Assuming further progression of reaction on the low lying singlet surface the remainder of the multistep FeCl₂ is obvious. The close Fe-Pd proximity in presence of a tilt away Cp ligand allows for easy exchange/switch of the two chlorido ligands from Pd to Fe (⁵C via ⁵TS C/D to ⁵D) in concert with opposite Cp exchange from Fe to Pd – conveniently migrating above the Fe(Cl₂)Pd plane without steric hinderance. Moderate reorganization via ⁵TS D/E allows for exothermic FeCl₂ expulsion towards ⁵E which comprises ⁵FeCl₂ and a singlet Pd fragment cation – in accord with the IRMPD MS detection.

3.6 Summary and conclusion

We have presented a novel bifunctional iron-palladium catalyst. Mass spectrometric characterization revealed ready solvent attachment. Computed structures show a coordination change of the Pd atom in favour of solvent attachment. Upon collisional excitation these solvent attached complexes (**3a**, **3b**, **3c**) may loose the attached solvent, may loose HCl, may loose both in concert, or may loose – most notably – FeCl₂ and solvent in concert. A solvent modulated Fe-Pd proximity coincides, and seems to favour, FeCl₂ elimination. Our IRMPD studies reveal competing HCl/FeCl₂ elimination with branching ratios much alike the CID ones. The solvent modulated formation of NH-Cl hydrogen bonds help to verify computed structures and isomers. The identified *syn* and *anti* isomers favour and disfavour FeCl₂ elimination, respectively.

The DFT calculations reveal a multitude of stationary points along the multistep reaction coordinates of the three conceivable spin states. The quintet state shows a static Jahn-Teller type relaxation by a tilt away of the Cp ligand at the iron center. Thereby, the quintet stabilizes below the triplet state, and amidst the rearrangements towards FeCl₂ elimination this quintet state steeply drops below the initially most stable singlet state – namely by further enhancing the Cp ligand tilt at the iron center. The remainder of rearrangements likely proceed by the quintet state, allowing for chlorido and Cp ligand exchange amongst the

metallic centers in opposite directions in a concerted, ballet like manner. The assumption of an adiabatic progression along the reaction path would thus imply a direct singlet-quintet spin cross over – seemingly without a direct involvement of the higher triplet state. The concomittant spin flips of two electrons (likely d electrons at Fe) need to occur in concert. Unless alternate – yet currently unknown – structures prevail, such an unprecedented assumption would ask for further elucidation and verification by sound high level quantum chemical modelling of structures and dynamics, taking into account a likely multi reference character of transition state structures. Such treatment is much beyond the scope of the current study.

The elucidated coordination change upon solvent attachment at the Pd center nicely reveals a likely structure with conceivable catalytic activity. Electron rich hydrocarbon molecules may easily swap for the solvent and proceed towards further steps of activation.

The exoergic elimination of FeCl₂ would result in a deactivation of the catalytic activity of the complex. It is kinetically hindered by a barrier of 132 kJ/mol which limits the range of applicable temperatures in conceivable technical applications.

3.7 References

- [1] O. Daugulis, *C-H Activation*, **2010**, 292, 57-84.
- [2] S. Rana, A. Modak, S. Maity, T. Patra and D. Maiti, in *Progress in Inorganic Chemistry, Vol 59*, ed. K. D. Karlin, John Wiley & Sons Inc, Hoboken, **2014**, vol. 59, pp. 1-188.
- [3] B. Cornils, *Angewandte Chemie-International Edition*, **2013**, 52, 9079-9079.
- [4] Chichester, *Ferrocenes: Ligands, Materials and Biomolecules*, John Wiley & Sons, **2008**.
- [5] H. Togni, *Ferrocenes: Homogeneous Catalysis, Organic Synthesis, Materials Science*, Wiley-VCH, **1995**.
- [6] T. J. Kealy and P. L. Pauson, *Nature*, **1951**, 168, 1039-1040.
- [7] E. O. Fischer and W. Pfab, *Zeitschrift Fur Naturforschung Section B-a Journal of Chemical Sciences*, **1952**, 7, 377-379.
- [8] S. A. Miller, J. A. Tebboth and J. F. Tremaine, *Journal of the Chemical Society*, **1952**, DOI: 10.1039/jr9520000632, 632-635.
- [9] P. Neumann, H. Dib, A. M. Caminade and E. Hey-Hawkins, *Angewandte Chemie-International Edition*, **2015**, 54, 311-314.
- [10] R. Savka, S. Foro, M. Gallei, M. Rehahn and H. Plenio, *Chemistry-a European Journal*, **2013**, 19, 10655-10662.
- [11] K. Arumugam, C. D. Varnado, S. Sproules, V. M. Lynch and C. W. Bielawski, *Chemistry-a European Journal*, **2013**, 19, 10866-10875.
- [12] G. Y. Liu, H. Y. He and J. H. Wang, *Advanced Synthesis & Catalysis*, **2009**, 351, 1610-1620.
- [13] C. K. A. Gregson, V. C. Gibson, N. J. Long, E. L. Marshall, P. J. Oxford and A. J. P. White, *Journal of the American Chemical Society*, **2006**, 128, 7410-7411.
- [14] C. S. Slone, C. A. Mirkin, G. P. A. Yap, I. A. Guzei and A. L. Rheingold, *Journal of the American Chemical Society*, **1997**, 119, 10743-10753.
- [15] D. J. Young, S. W. Chien and T. S. A. Hor, *Dalton Transactions*, **2012**, 41, 12655-12665.
- [16] G. Bandoli and A. Dolmella, *Coordination Chemistry Reviews*, **2000**, 209, 161-196.
- [17] S. Toma, J. Csizmadiova, M. Meciarova and R. Sebesta, *Dalton Transactions*, **2014**, 43, 16557-16579.
- [18] N. A. Butt, D. L. Liu and W. B. Zhang, *Synlett*, **2014**, 25, 615-630.
- [19] D. Schaarschmidt and H. Lang, *Organometallics*, **2013**, 32, 5668-5704.

- [20] H. Dai, *Chiral Ferrocenes in Asymmetric Catalysis* Wiley-VCH, **2010**.
- [21] R. Gomez Arrayas, J. Adrio and J. C. Carretero, *Angewandte Chemie (International ed. in English)*, **2006**, 45.
- [22] H. U. Blaser, B. Pugin, F. Spindler and M. Thommen, *Accounts of Chemical Research*, **2007**, 40, 1240-1250.
- [23] S. H. Eitel, M. Bauer, D. Schweinfurth, N. Deibel, B. Sarkar, H. Kelm, H. J. Kruger, W. Frey and R. Peters, *Journal of the American Chemical Society*, **2012**, 134, 4683-4693.
- [24] D. E. Fischer, Z. Q. Xin and R. Peters, *Angewandte Chemie-International Edition*, **2007**, 46, 7704-7707.
- [25] S. Jautze, P. Seiler and R. Peters, *Angewandte Chemie-International Edition*, **2007**, 46, 1260-1264.
- [26] M. L. H. Green, L. Pratt and G. Wilkinson, *Journal of the Chemical Society*, **1960**, DOI: 10.1039/jr9600000989, 989-997.
- [27] A. N. Nesmeyanov, N. A. Volkenau and I. N. Bolesova, *Tetrahedron Letters*, **1963**, 1725-1729.
- [28] I. U. Khand, P. L. Pauson and W. E. Watts, *Journal of the Chemical Society C-Organic*, **1968**, DOI: 10.1039/j39680002261, 2261-&.
- [29] A. S. Abdelaziz, Y. Lei and C. R. Dedenus, *Polyhedron*, **1995**, 14, 1585-1591.
- [30] N. Raouafi, N. Belhadj, K. Boujlel, A. Ourari, C. Amatore, E. Maisonhaute and B. Schollhorn, *Tetrahedron Letters*, **2009**, 50, 1720-1722.
- [31] A. S. Abd-El-Aziz, E. K. Todd and T. H. Afifi, *Macromolecular Rapid Communications*, **2002**, 23, 113-117.
- [32] A. S. Abdelaziz, C. R. Dedenus and H. M. Hutton, *Canadian Journal of Chemistry-Revue Canadienne De Chimie*, **1995**, 73, 289-295.
- [33] R. G. Sutherland, R. L. Chowdhury, A. Piorko and C. C. Lee, *Journal of Organic Chemistry*, **1987**, 52, 4618-4620.
- [34] D. Schroder, S. Shaik and H. Schwarz, *Accounts of Chemical Research*, **2000**, 33, 139-145.
- [35] N. C. Polfer, *Chemical Society Reviews*, **2011**, 40, 2211-2221.
- [36] L. MacAleese and P. Maitre, *Mass Spectrometry Reviews*, **2007**, 26, 583-605.

- [37] F. Menges, C. Riehn and G. Niedner-Schatteburg, *Zeitschrift Fur Physikalische Chemie-International Journal of Research in Physical Chemistry & Chemical Physics*, **2011**, 225, 595-609.
- [38] R. H. Schultz, K. C. Crellin and P. B. Armentrout, *Journal of the American Chemical Society*, **1991**, 113, 8590-8601.
- [39] N. C. Polfer, J. Oomens and R. C. Dunbar, *Physical Chemistry Chemical Physics*, **2006**, 8, 2744-2751.
- [40] J. Lang, M. Gaffga, F. Menges and G. Niedner-Schatteburg, *Physical Chemistry Chemical Physics*, **2014**, 16, 17417-17421.
- [41] A. Fedorov, E. P. A. Couzijn, N. S. Nagornova, O. V. Boyarkin, T. R. Rizzo and P. Chen, *Journal of the American Chemical Society*, **2010**, 132, 13789-13798.
- [42] S. Chakraborty and O. Dopfer, *Chemphyschem*, **2011**, 12, 1999-2008.
- [43] A. Skriba, J. Schulz and J. Roithova, *Organometallics*, **2014**, 33, 6868-6878.
- [44] G. von Helden, J. Oomens, B. G. Sartakov and G. Meijer, *International Journal of Mass Spectrometry*, **2006**, 254, 1-19.
- [45] J. Roithova, *Chemical Society Reviews*, **2012**, 41, 547-559.
- [46] T. D. Fridgen, *Mass Spectrometry Reviews*, **2009**, 28, 586-607.
- [47] A. D. Becke, *Physical Review A*, **1988**, 38, 3098-3100.
- [48] A. D. Becke, *Journal of Chemical Physics*, **1993**, 98, 5648-5652.
- [49] B. Miehlich, A. Savin, H. Stoll and H. Preuss, *Chemical Physics Letters*, **1989**, 157, 200-206.
- [50] C. T. Lee, W. T. Yang and R. G. Parr, *Physical Review B*, **1988**, 37, 785-789.
- [51] T. H. Dunning, *Journal of Chemical Physics*, **1989**, 90, 1007-1023.
- [52] D. E. Woon and T. H. Dunning, *Journal of Chemical Physics*, **1993**, 98, 1358-1371.
- [53] D. E. Woon and T. H. Dunning, *Journal of Chemical Physics*, **1993**, 99, 3730-3737.
- [54] D. Andrae, U. Haussermann, M. Dolg, H. Stoll and H. Preuss, *Theoretica Chimica Acta*, **1991**, 78, 247-266.
- [55] M. Dolg, U. Wedig, H. Stoll and H. Preuss, *Journal of Chemical Physics*, **1987**, 86, 866-872.
- [56] M. J. T. Frisch, *et al.*, **2009**, Revision D.01 Wallingford CT. 2009.
- [57] NIST Standard Reference Database 101, <http://cccbdb.nist.gov/vibscalejust.asp>.

- [58] Y. Nosenko, F. Menges, C. Riehn and G. Niedner-Schatteburg, *Physical Chemistry Chemical Physics*, **2013**, 15, 8171-8178.
- [59] F. Menges, Dr. rer. nat. Doctoral, TU Kaiserslautern, **2013**.
- [60] N. Vinokur and V. Ryzhov, *Journal of Mass Spectrometry*, **2004**, 39, 1268-1274.
- [61] Holleman-Wieberg, *Lehrbuch der anorganischen Chemie*, de Gruyter, **1995**.

3.8 Supporting Information to Multi State Mediated Rearrangement and FeCl₂ Elimination in Dinuclear FePd Complexes

Maximilian Gaffga, Isabel Munstein, Patrick Müller, Johannes Lang, Werner R. Thiel and Gereon Niedner-Schatteburg

*Fachbereich Chemie und Forschungszentrum OPTIMAS, Technische Universität
Kaiserslautern, 67663 Kaiserslautern, Germany*

Table of content

Text T1: *General remarks on synthetic procedures*

Scheme S1: *Assignment of NMR resonances*

Text T1: *Characterization of compound 1*

Text T2: *Characterization of compound 2*

Table S1: *Information about bond length and bond angles of FeCl₂ and PdCl₂.*

Figure S1: *Comparison of harmonic and anharmonic calculations.*

Figure S2: *Normalized energetics of stationary points along the reaction coordinate of the FeCl₂ elimination within the singlet spin state.*

Figure S3: *Normalized energetics of stationary points along the reaction coordinate of the FeCl₂ elimination within the triplet spin state.*

Figure S4: *Normalized energetics of stationary points along the reaction coordinate of the FeCl₂ elimination within the quintet spin state.*

Figure S5: *Ligand field splitting of the 3d orbitals of the Fe(II) cation in ¹3, ³3 and ⁵3 sub unit.*

Figure S6: *ESI mass spectra of complex 2.*

Figure S7: *ESI mass spectrum of complex 3a.*

Figure S8: *ESI mass spectrum of complex 3b.*

Figure S9: ESI mass spectrum of complex **3c**.

Figure S10: CID mass spectrum of **2** including simulations of the isotopic patterns of resulting fragment ions.

Figure S11: CID mass spectrum of **3a** including simulations of the isotopic patterns of resulting fragment ions.

Figure S12: CID mass spectrum of **3b** including simulations of the isotopic patterns of resulting fragment ions.

Figure S13: CID mass spectrum of **3c** including simulations of the isotopic patterns of resulting fragment ions.

Figure S14: Structural isomers of complex **2**.

Figure S15: Structural isomers of complex **3a**.

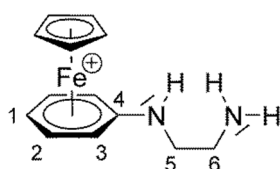
Figure S16: Structural isomers of complex **3b**.

Figure S17: Structural isomers of complex **3c**.

Figure S18: Geometry optimization of complex **3c** for NH-Cl hydrogen bonded starting geometries.

Text T1: General remarks on synthetic procedures.

Solvents were dried by standard methods. Reagents were purchased from ACROS, Alfa Aesar or Sigma-Aldrich and used without further purification, unless otherwise noted. [η^5 -CpFe(η^6 -C₆H₅Cl)]PF₆ was synthesized from ferrocene and chlorobenzene in the presence of aluminiumtrichloride according to a published procedure.[Ref 8 in the paper] The NMR spectra were recorded with a Bruker DPX 400 spectrometer, the assignment of the resonances is according to Scheme S1.



Scheme S1: Assignment of the NMR resonances.

Text T1: Characterization of compound **1**, (η^6 -N-(2-Aminoethyl)aniline)(η^5 -cyclopentadienide)iron(II) hexafluorophosphate.

¹H NMR (400 MHz, d₃ acetonitrile): δ = 5.95 (t, ³J_{HH} = 6.4 Hz, 2 H, H-2), 5.85 (t, ³J_{HH} = 5.8 Hz, 1 H, H-1), 5.62 (d, ³J_{HH} = 6.4 Hz, 2 H, H-3), 5.29 (br, 1 H, NH), 4.85 (s, 5 H, H-Cp), 3.19 (dt, 2 \times ³J_{HH} = 5.7 Hz, 2 H, H-5), 2.90 (t, ³J_{HH} = 6.0 Hz, 2 H, H-6) ppm, 1.92 (br, 3.5 H, NH₂ + H₂O from the solvent) ¹³C{¹H} NMR (101 MHz, d₃ acetonitrile): δ = 127.7 (C-4), 87.1 (C-2), 81.8 (C-1), 76.7 (C-Cp), 69.2 (C-3), 47.0 (C-6), 41.7 (C-5) ppm. ³¹P NMR (162 MHz, d₃ acetonitrile): δ = -144.5 (sept, ¹J_{FP} = 707.4 Hz, PF₆) ppm. ¹⁹F NMR (376 MHz, d₃ acetonitrile): δ = -72.6 (d, ¹J_{FP} = 707.4 Hz, PF₆) ppm. IR (ATR): $\bar{\nu}$ = 3392w, 3222w, 3120w, 2940w, 2860w, 1553s, 1489w, 1465m, 1420w, 1392w, 1323w, 1288w, 1164w, 1112w, 1028w, 1012w 943m, 878m, 815vs, 741s, 657s cm⁻¹. Elemental analysis for C₁₃H₁₇F₆FeN₂P (402.1): calcd C 38.83, H 4.26, N 6.97 %; found C 39.07, H 4.34, N 6.65 %. ESI-MS: m/z = 256.8 [C₁₃H₁₇FeN₂]⁺. M.p.: 125 °C.

Text T2: Characterization of compound **2**, [(η^6 -N-2-(Aminoethyl)aniline)(η^5 -cyclopentadienide) iron(II)]dichloridopalladium(II)hexafluorophosphates.

¹H NMR (400 MHz, d₃ acetonitrile): δ = 6.12 (t, ³J_{HH} = 6.8 Hz, 2 H, H-2), 5.99 (t, ³J_{HH} = 6.0 Hz, 1 H, H-1), 5.80 (d, ³J_{HH} = 6.4 Hz, 2 H, H-3), 5.47 (br, 1 H, NH), 5.03 (s, 5 H, H-Cp), 3.74 (pseudo q, ³J_{HH} = 5.9 Hz, 2 H, H-5), 3.62 (br, 2 H, NH₂), 2.80 (dt, ³J_{HH} = 12.0 Hz, 6.0 Hz, 2 H, H-6) ppm. ¹³C{¹H} NMR (101 MHz, d₃ acetonitrile): δ = 126.4 (C-4), 87.1 (C-2), 82.3 (C-1), 77.0 (C-Cp), 69.8 (C-3), 44.9 (C-6), 44.0 (C-5) ppm. ³¹P NMR (162 MHz, d₃ acetonitrile): δ = -144.6 (sept, ¹J_{FP} = 706.3 Hz, PF₆) ppm. ¹⁹F NMR (376 MHz, d₃ acetonitrile): δ = -72.7 (d, ¹J_{FP} = 706.3 Hz, PF₆) ppm. IR (ATR): $\bar{\nu}$ = 3631w, 3308w, 3206w, 3114m, 2987w, 1560m, 1527m, 1461s, 1420m, 1277w, 1220w, 1190m, 1153w, 1052m, 1013m, 823vs, 740s, 672w, 658w cm⁻¹. Elemental analysis for C₁₃H₁₇Cl₂F₆FeN₂PPd (exact mass: 548.91): calcd C 26.95, H 2.96 N 4.83 %; found C 26.12, H 3.02, N 4.63 %. ESI-MS: m/z = 434.8 [C₁₃H₁₇Cl₂FeN₂Pd]⁺.

Table S1: *M-Cl bond length d and Cl-M-Cl bond angles α in dependence of the different spin states (singlet, triplet and quintet) of the metal M ($M=Fe, Pd$).*

| spin state | $\alpha(\text{Cl-Fe-Cl}) / ^\circ$ | $d(\text{Fe-Cl}) / \text{\AA}$ | $\alpha(\text{Cl-Pd-Cl}) / ^\circ$ | $d(\text{Pd-Cl}) / \text{\AA}$ |
|------------|------------------------------------|--------------------------------|------------------------------------|--------------------------------|
| singlet | 159 | 2.07 | 180 | 2.22 |
| triplet | 179 | 2.11 | 180 | 2.23 |
| quintet | 180 | 2.16 | 180 | 2.44 |

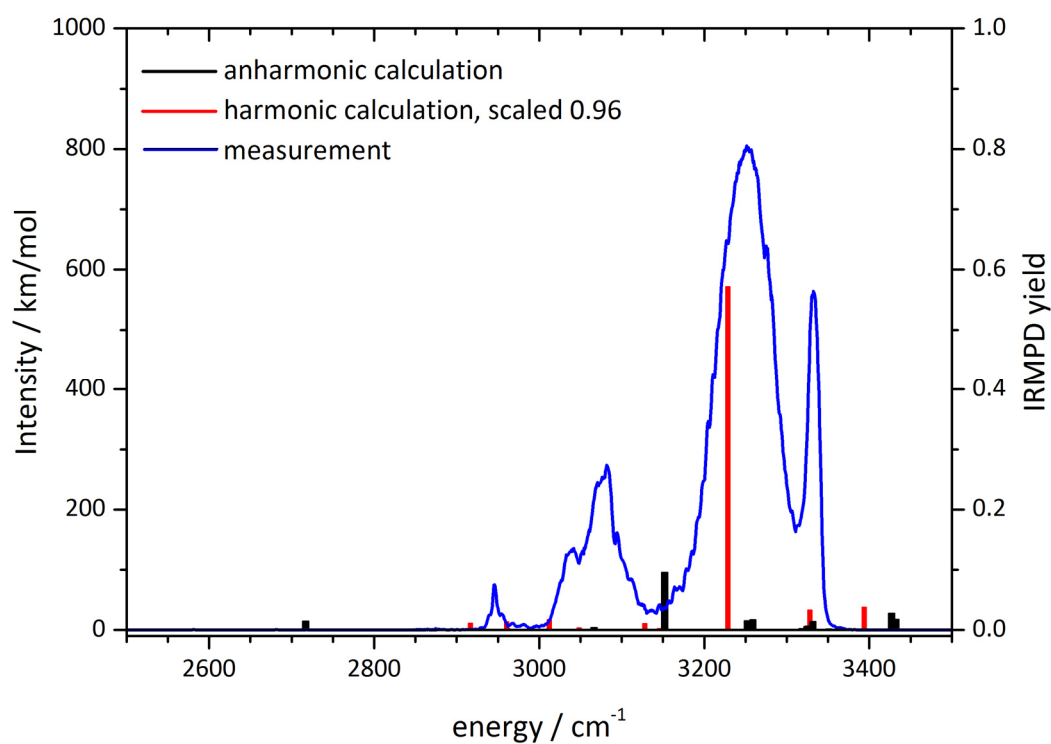


Figure S1: Comparison of anharmonic VPT2 calculations (black line) with scaled harmonic calculations (red line) and with the experimental spectrum (blue line) of complex **3a**.

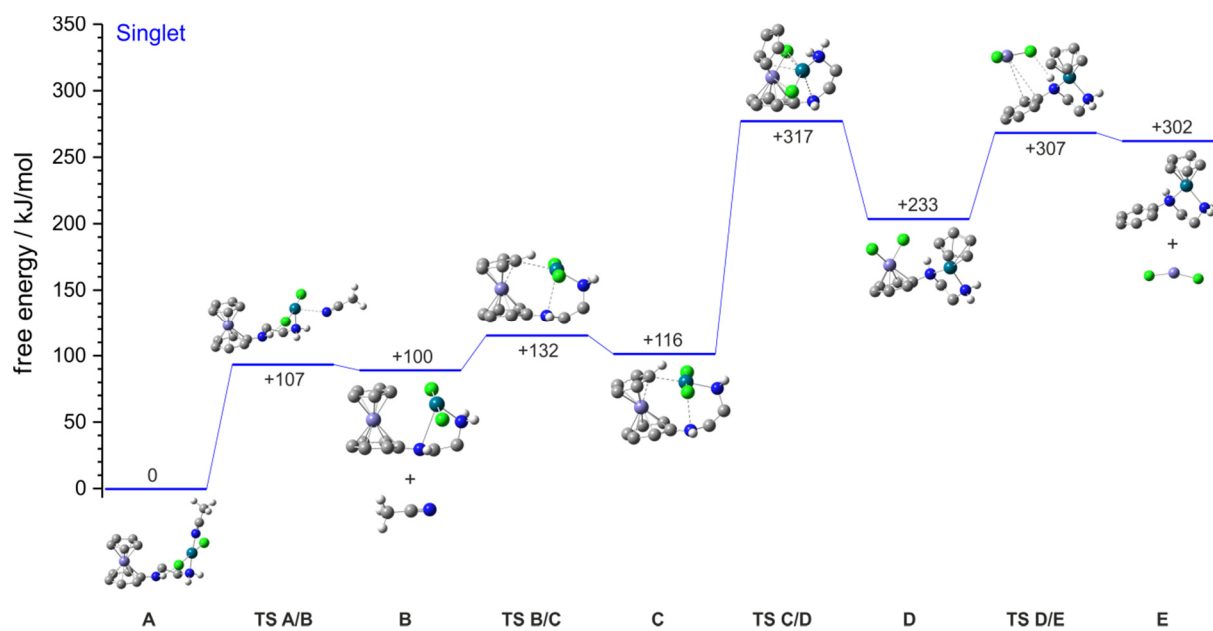


Figure S2: Reaction coordinate of the FeCl₂ elimination by the singlet spin state. All energy values are given in kJ/mol. Some aliphatic hydrogen atoms are omitted for clarity.

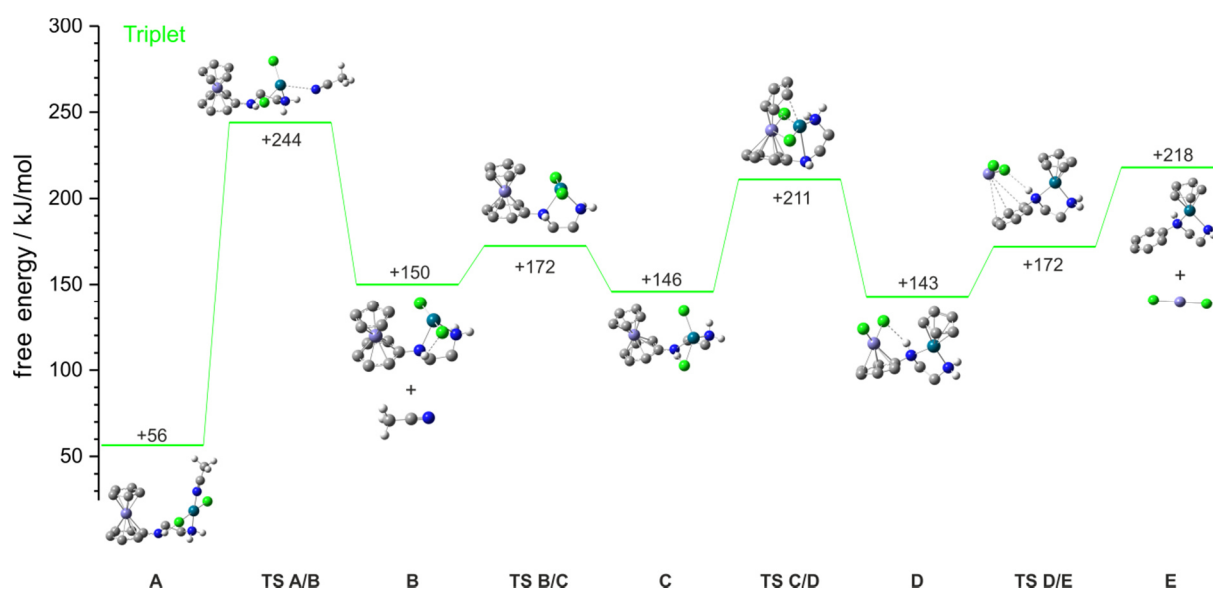


Figure S3: Reaction coordinate of the FeCl₂ elimination by the triplet spin state. The energy scale is relative to the minimum structure in the singlet spin state. All energy values are given in kJ/mol. Some aliphatic hydrogen atoms are omitted for clarity.

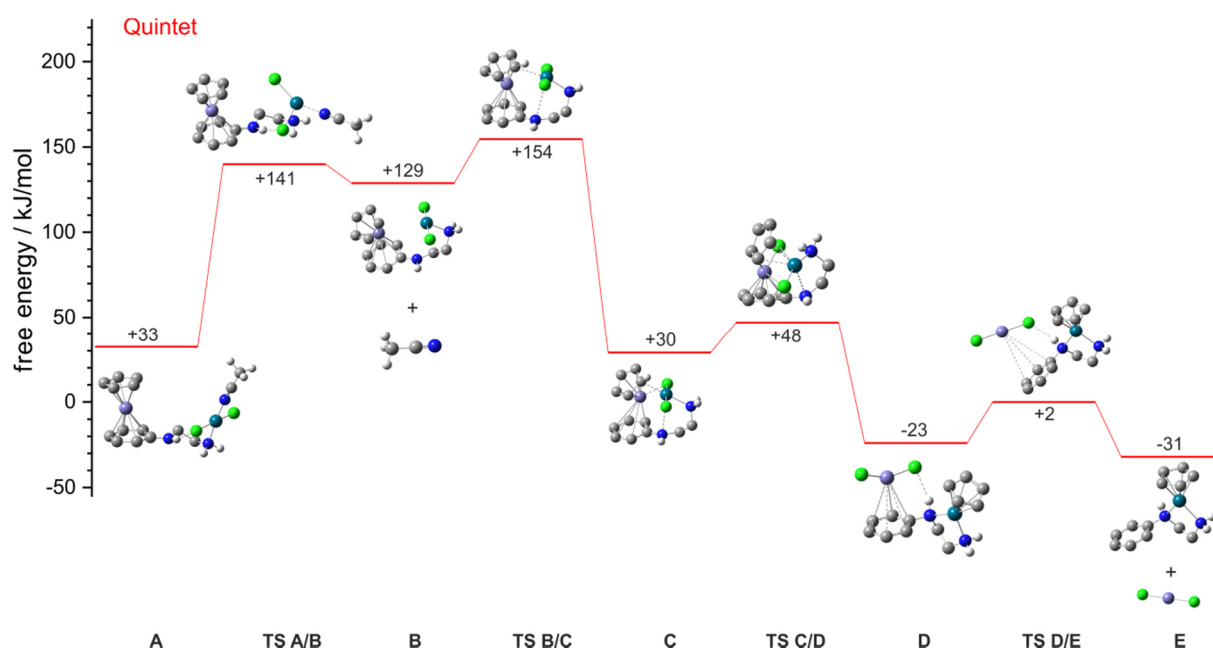


Figure S4: Reaction coordinate of the FeCl₂ elimination by the quintet spin state. The energy scale is relative to the minimum structure in the singlet spin state. All energy values are given in kJ/mol. Some aliphatic hydrogen atoms are omitted for clarity.

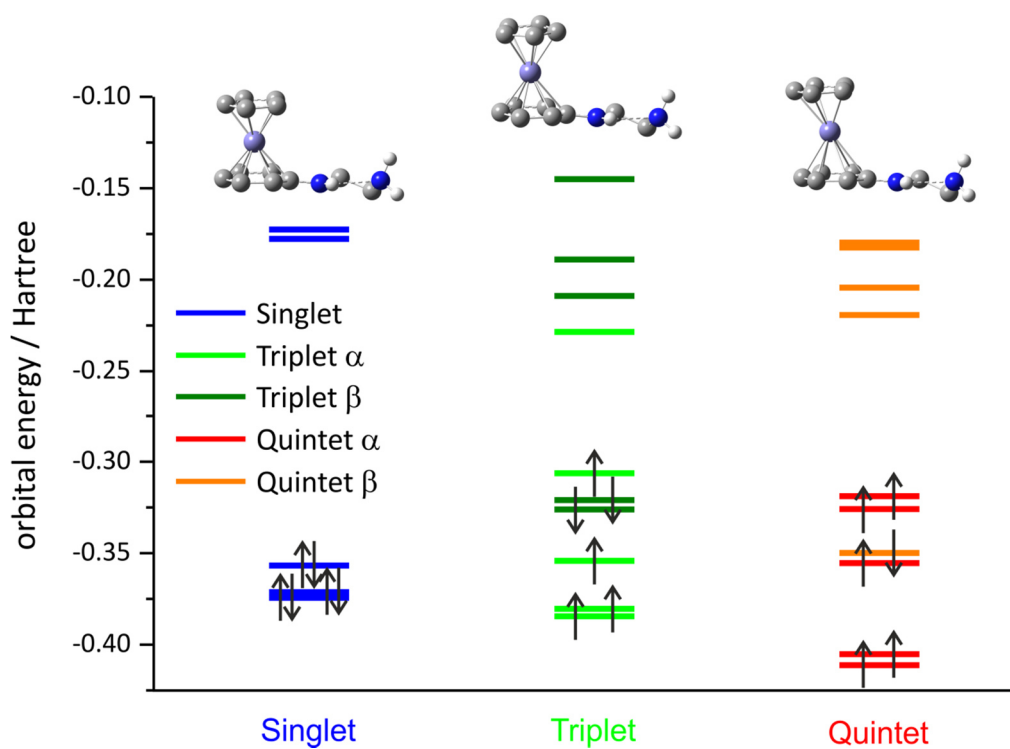


Figure S5: Ligand field splitting of the 3d orbitals and orbital occupation of the iron(II) cation of the Cp-Fe-aryl unit 14 , 34 and 54 in the different spin states. Aliphatic hydrogen atoms are omitted for clarity.

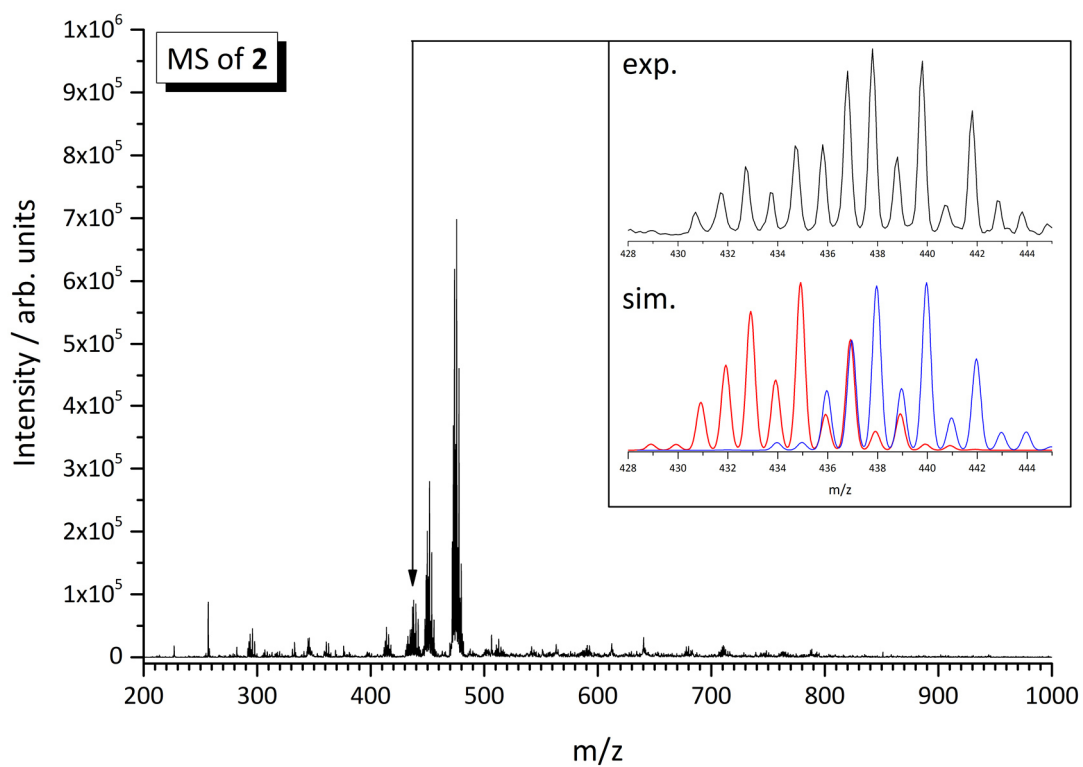


Figure S6: Mass spectrum of the solution of complex **2** including simulation of the isotopic pattern (inset). Note the overlapping isotopic pattern of the complex **2** (red) and **3a-HCl** (blue) mass peaks.

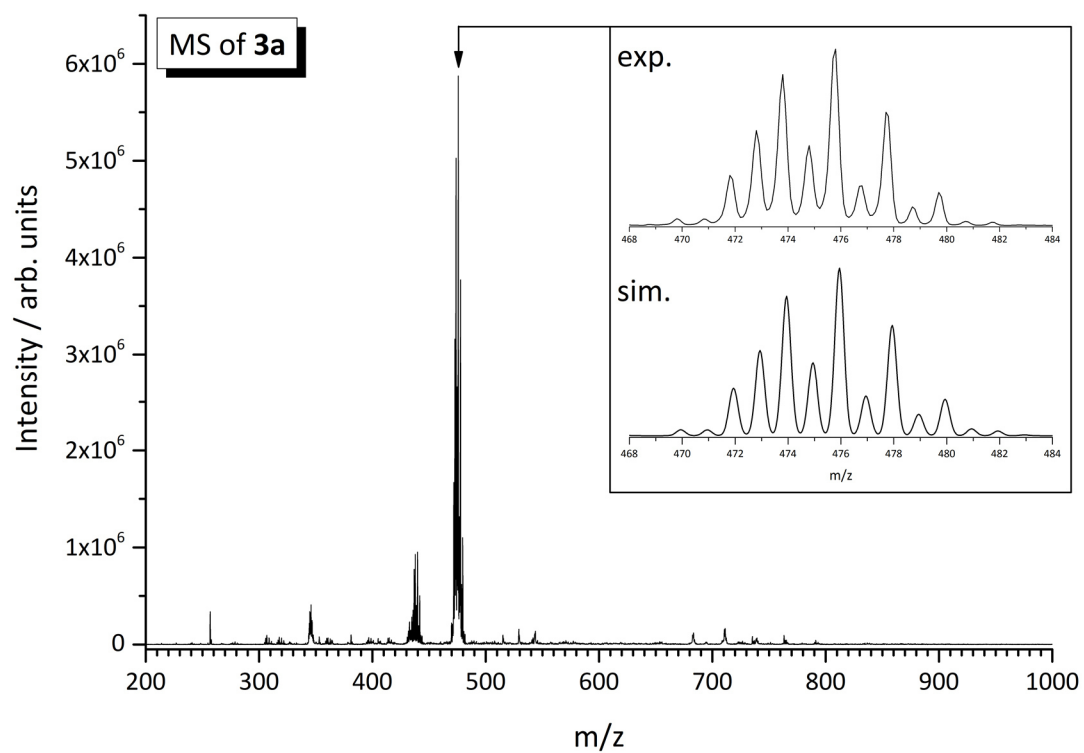


Figure S7: Mass spectrum of the solution of complex **3a** including simulation of the isotopic pattern (inset).

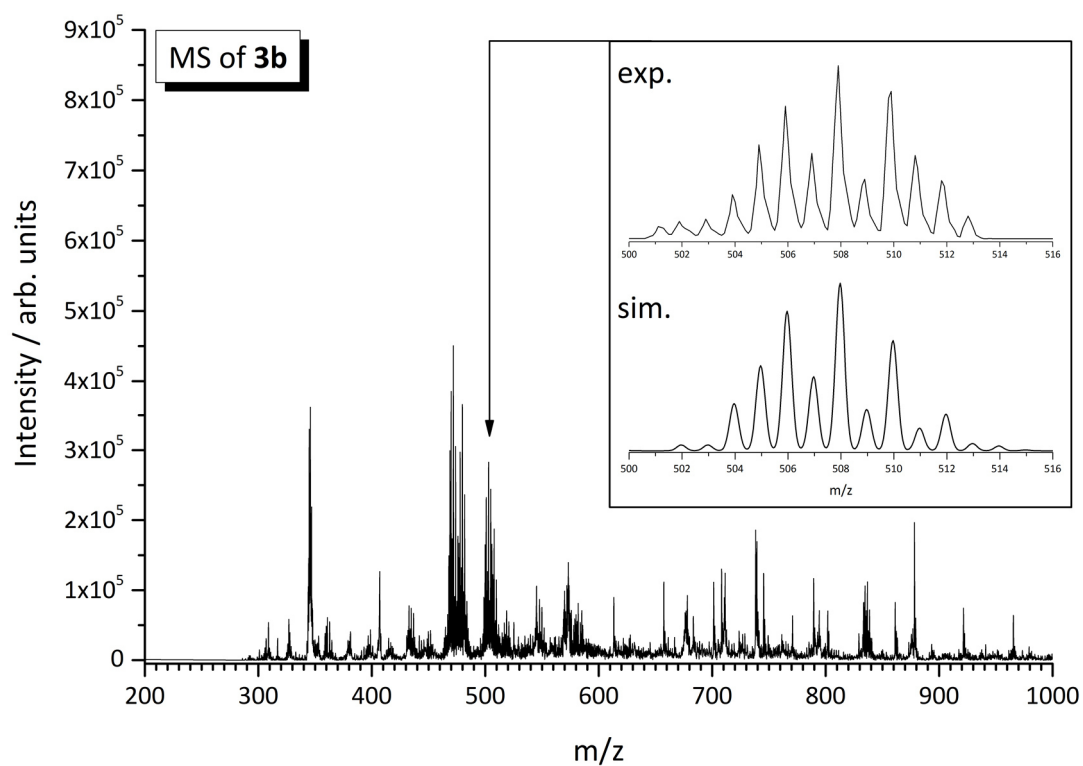


Figure S8: Mass spectrum of the solution of complex **3b** including simulation of the isotopic pattern (inset).

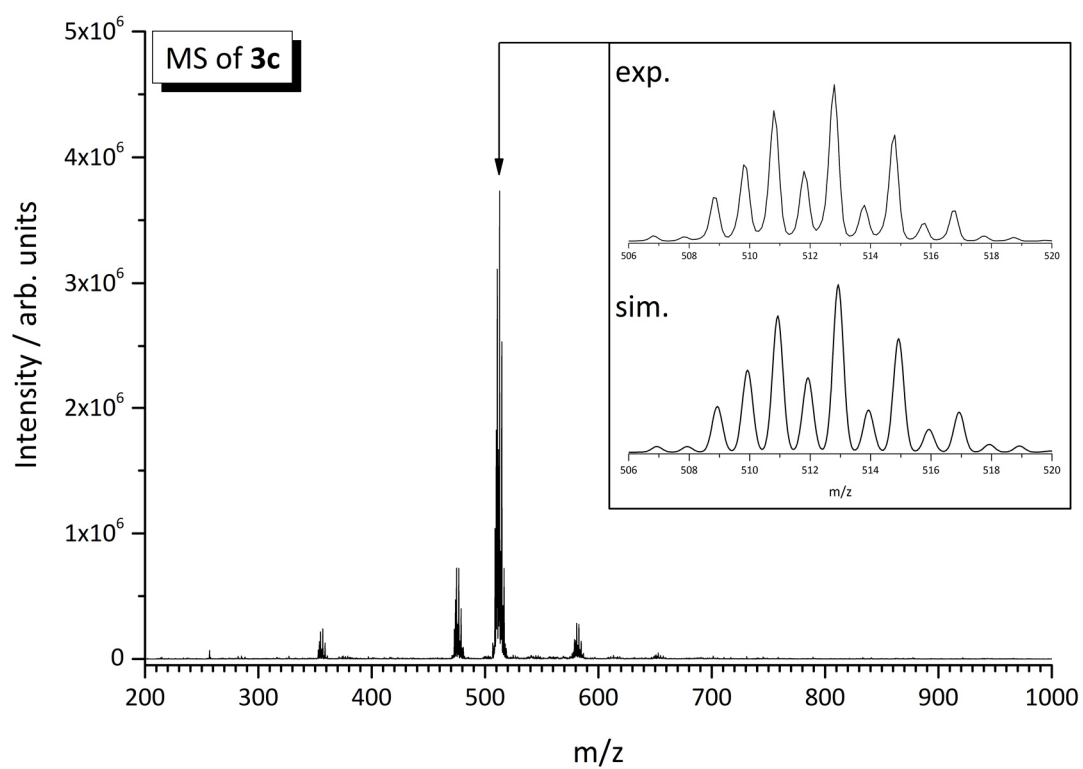


Figure S9: Mass spectrum of the solution of complex **3c** including simulation of the isotopic pattern (inset).

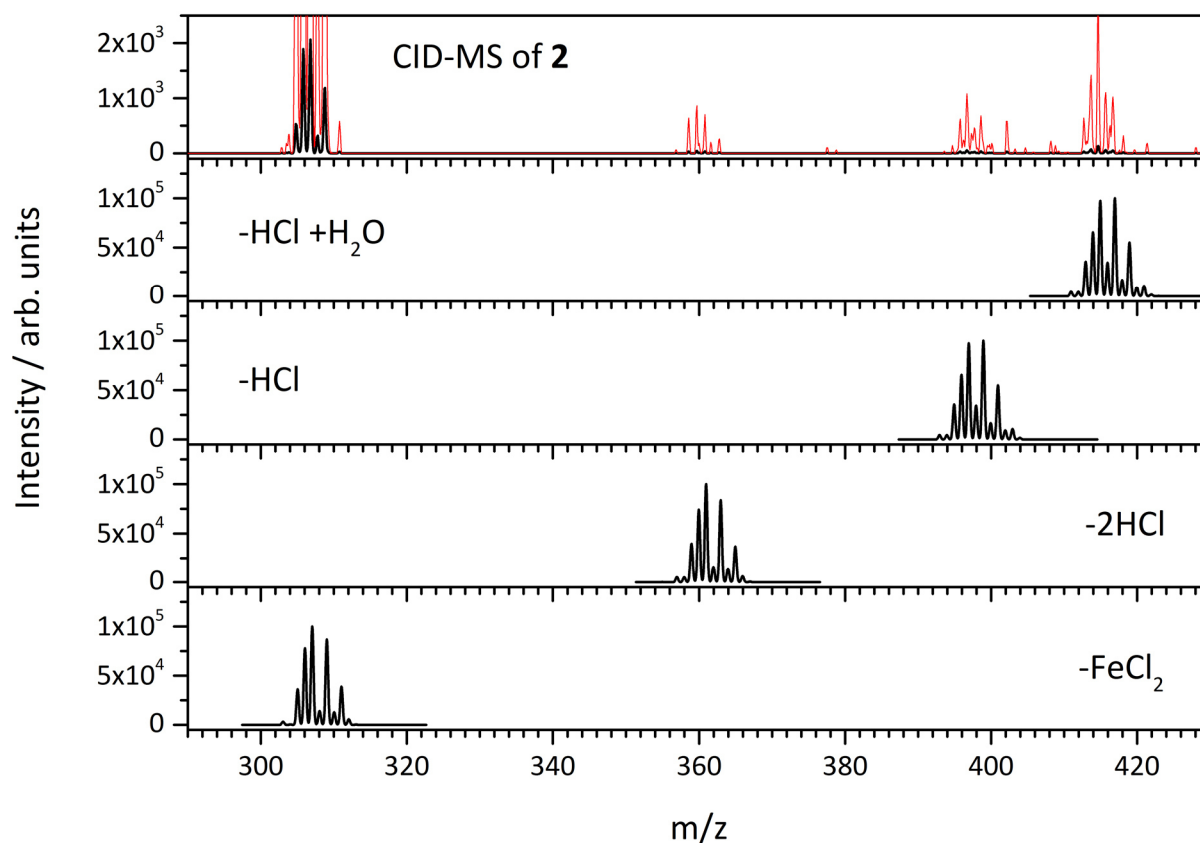


Figure S10: CID mass spectrum of complex **2** (upper graph) taken at $E_{COM} = 0.007$ a.u. and simulations of the isotopic patterns of resulting fragment ions (lower graphs). The CID mass spectrum is multiplied by a factor of 10 (red lines) to exhibit the significant influence of containing Fe on the isotopic pattern.

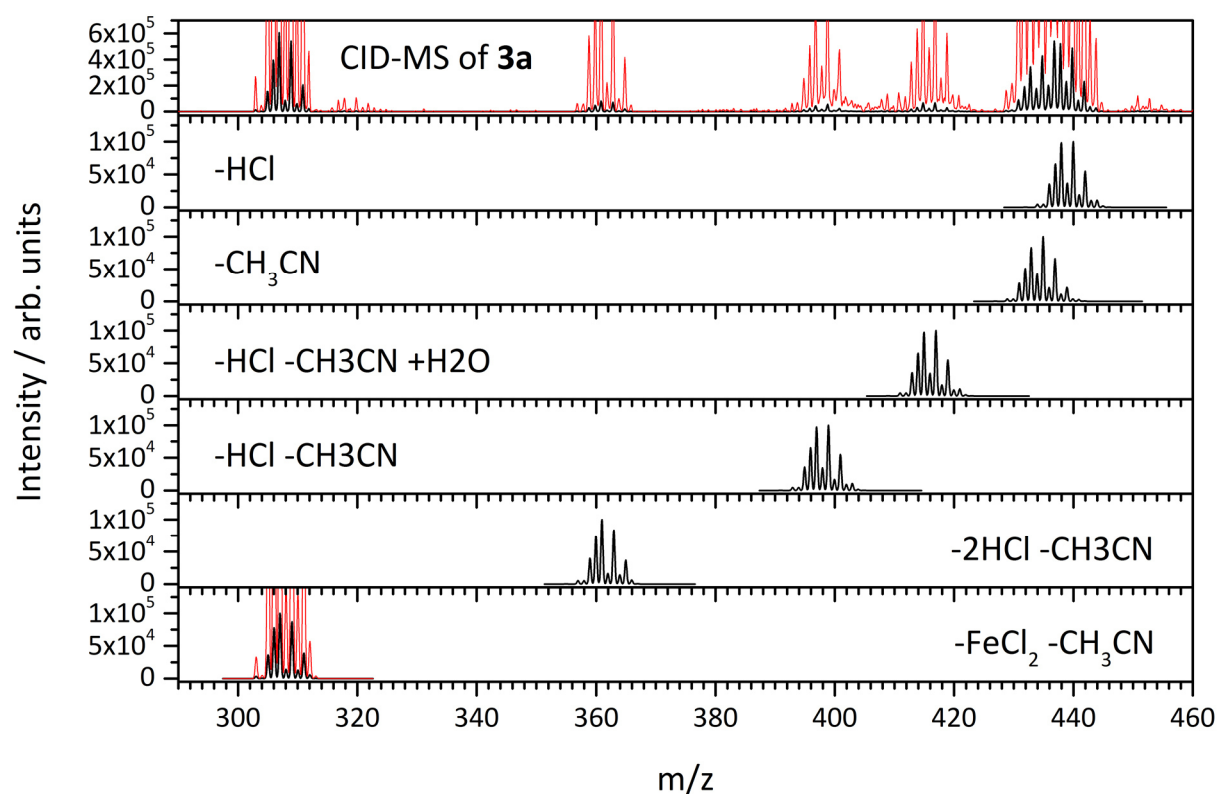


Figure S11: CID mass spectrum of complex **3a** (upper graph) taken at $E_{COM} = 0.005$ a.u. and simulations of the isotopic patterns of resulting fragment ions (lower graphs). The CID mass spectrum and a distinct simulation are multiplied by a factor of 10 (red lines) to exhibit the significant influence of containing Fe on the isotopic pattern.

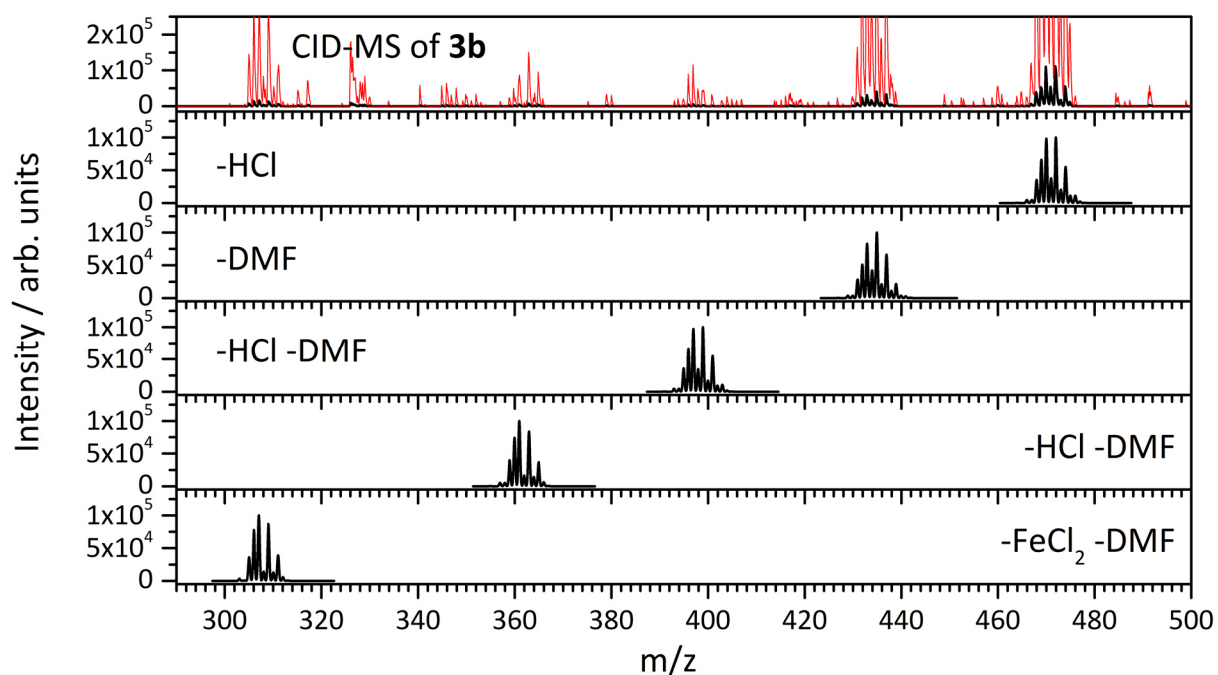


Figure S12: CID mass spectrum of complex **3b** (upper graph) taken at $E_{COM} = 0.005$ a.u. and simulations of the isotopic patterns of resulting fragment ions (lower graphs). The CID mass spectrum is multiplied by a factor of 10 (red lines) to exhibit the significant influence of containing Fe on the isotopic pattern.

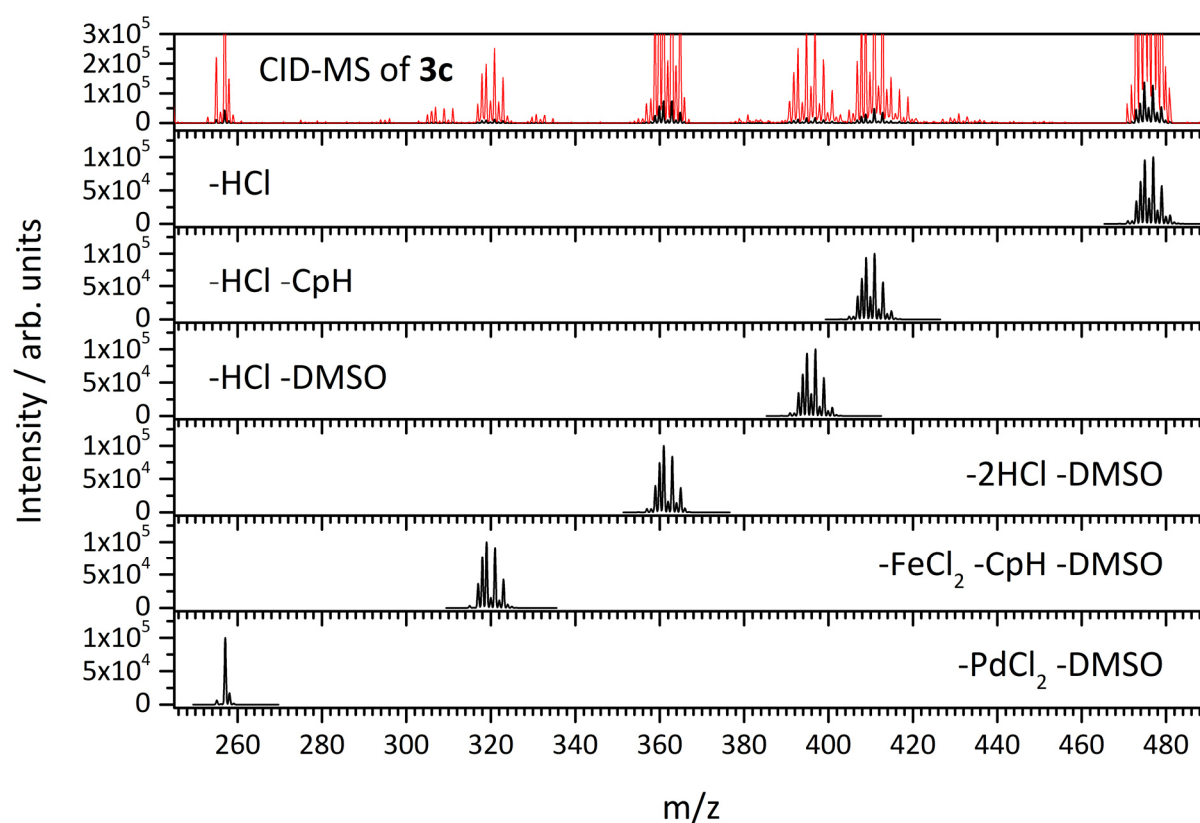


Figure S13: CID mass spectrum of complex **3c** (upper graph) taken at $E_{COM} = 0.005$ a.u. and simulations of the isotopic patterns of resulting fragment ions (lower graphs). The CID mass spectrum is multiplied by a factor of 10 (red lines).

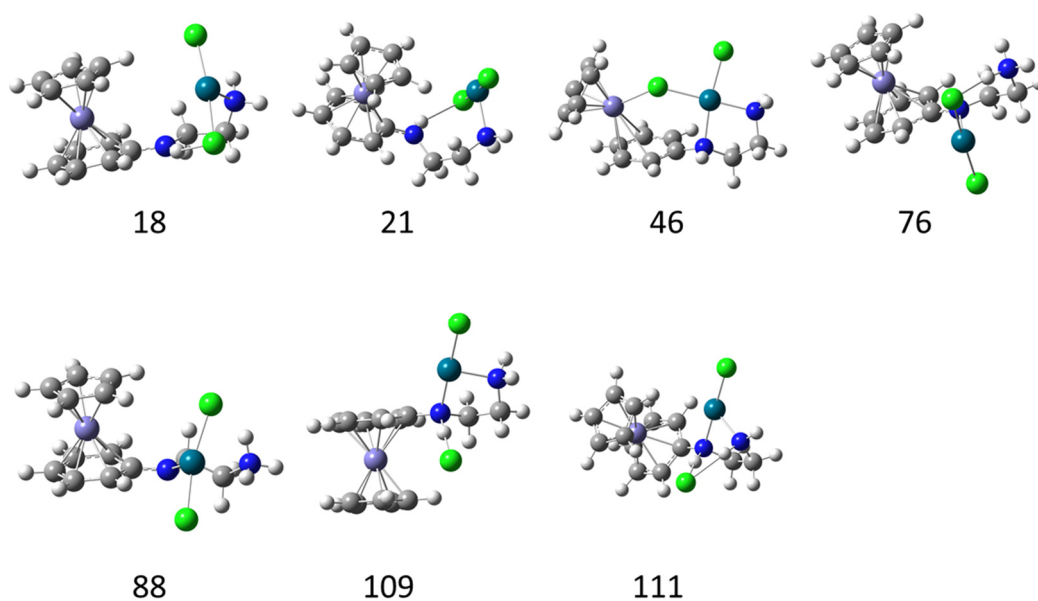


Figure S14: Structural isomers of complex **2**. The energy values are relative to the minimum structure of the most stable isomer **2_{syn}** and are given in kJ/mol.

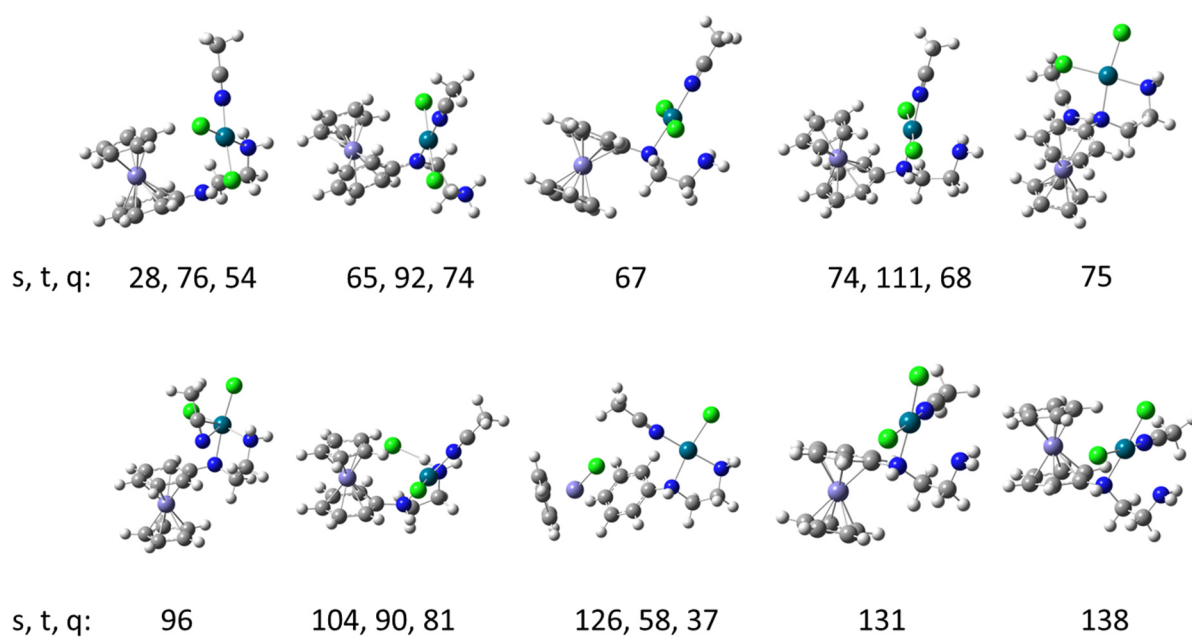


Figure S15: Structural isomers of complex **3a** including relative energy values for the corresponding spin states (*s*: singlet, *t*: triplet, *q*: quintet). The energy values are relative to the minimum structure of the most stable isomer **3a_{syn}** and are given in kJ/mol.

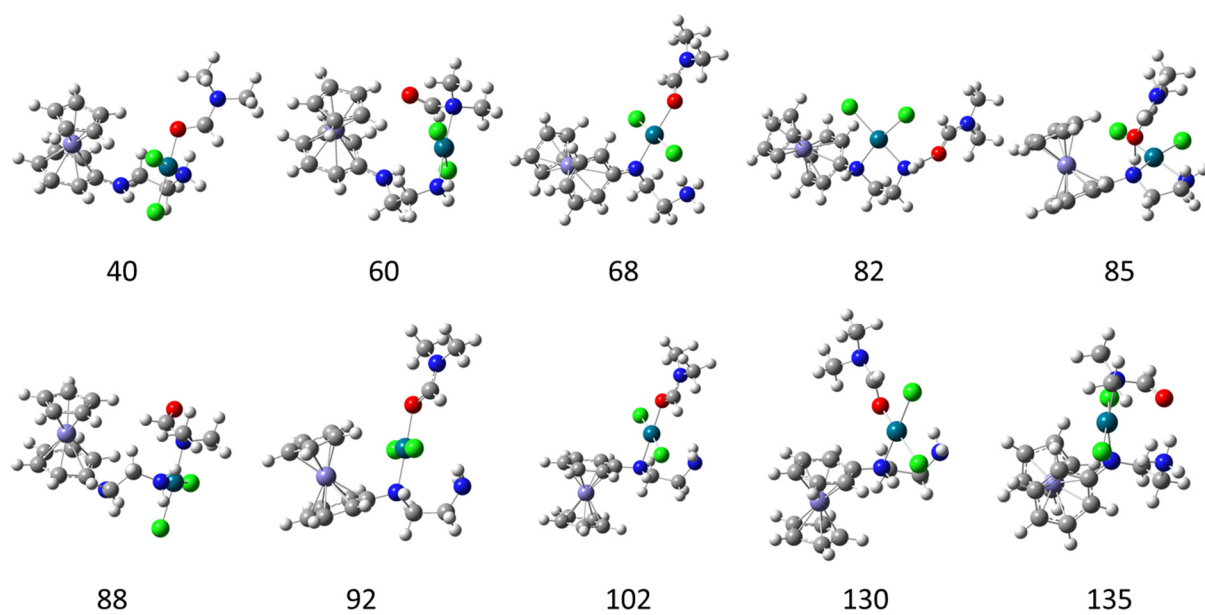


Figure S16: Structural isomers of complex **3b**. The energy values are relative to the minimum structure of the most stable isomer **3b_{syn}** and are given in kJ/mol.

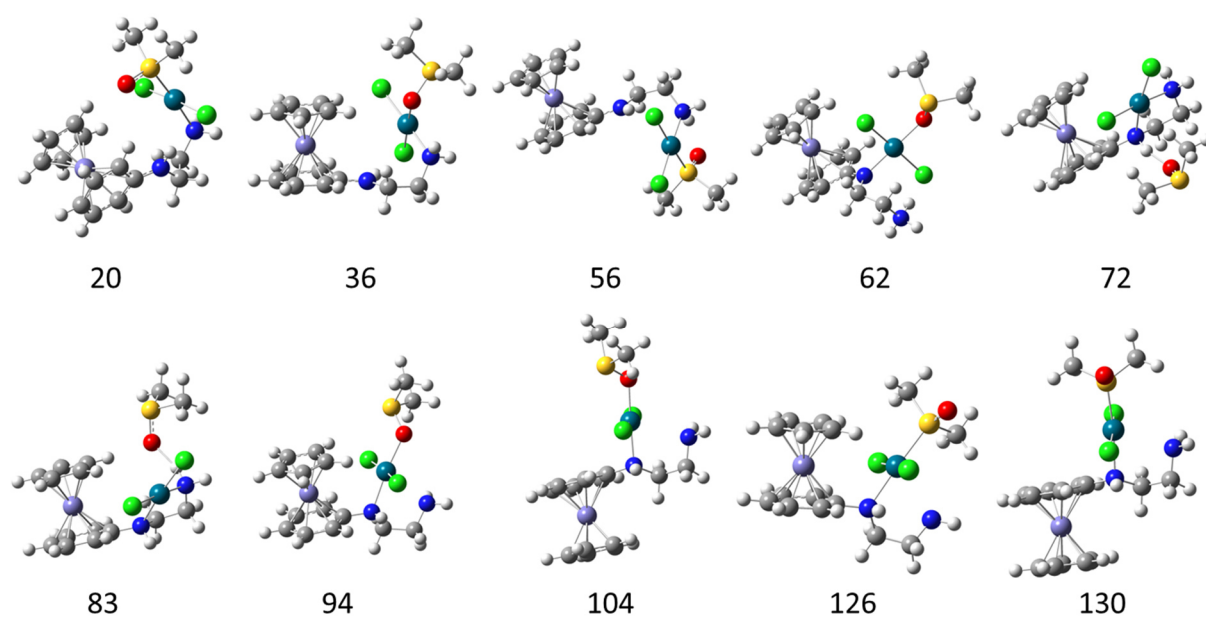


Figure S17: Structural isomers of complex **3c**. The energy values are relative to the minimum structure of the most stable isomer **3c_{syn}** and are given in kJ/mol.

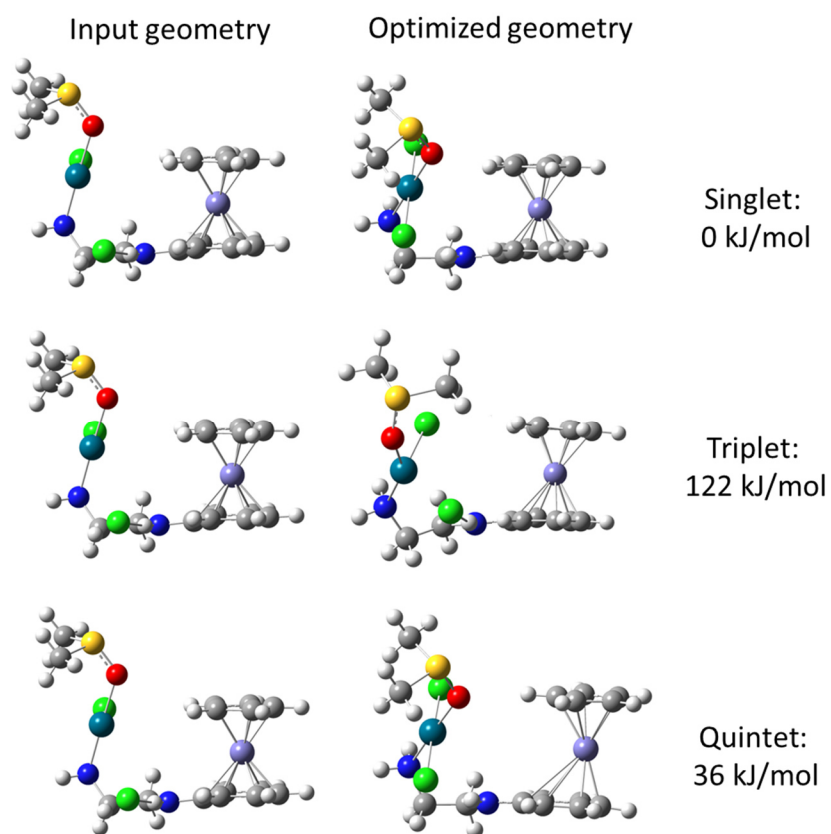


Figure S18: Starting points and geometry optimized structures of the complex **3c** for NH-Cl hydrogen bonded input structures.

4. Isomer Discrimination in a Pd-NHC Complex by Collisional and by IR Induced Activation

Maximilian Gaffga, Agnes Fizia, Werner R. Thiel and Gereon Niedner-Schatteburg

Fachbereich Chemie und Forschungszentrum OPTIMAS, Technische Universität

Kaiserslautern, 67663 Kaiserslautern, Germany

4.1 Preamble

The following chapter was prepared as a manuscript for publication. It is not submitted so far. All presented measurements, data evaluation, computations and all of the preparation of the manuscript itself were performed by myself. I received experimental support by Joachim Hewer, and I exchanged ideas with my colleagues Matthias Tombers and Johannes Lang. Gereon Niedner-Schatteburg helped by discussions. Agnes Fizia of the Thiels group synthesized the compounds.

4.2 Abstract

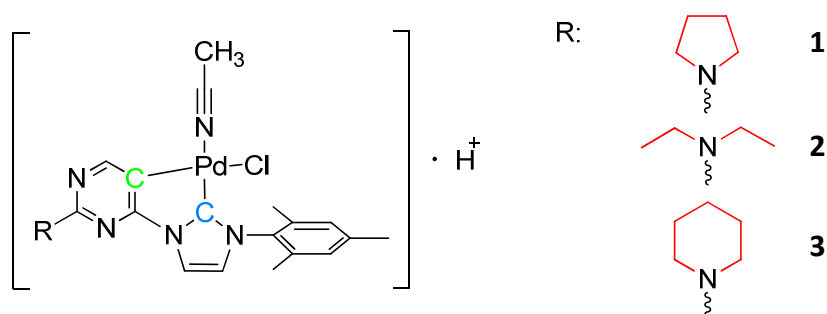
We present collision-induced dissociation (CID) and infrared multi photon dissociation (IRMPD) investigations on three derivatives of a palladium (II) complex. The CID studies reveal evidence of two coexisting isomers. The comparison of the experimental IRMPD spectra and linear absorption spectra of the computed most stable isomers identifies these two coexistent isomers. The computed structures show a competition of palladium-carbanion and palladium-nitrogen coordination motifs. Mass spectrometric analysis of the individual fragmentation channels of complex **2** exhibits the contributions of the individual fragments to the resulting IRMPD bands. Hereby, different bands reveal different fragmentation channels. Computations ascribe these untypical fragmentation contributions to a rearrangement during the fragmentation process. Two color delayed IRMPD investigations help to distinguish between these isomers. Replacing the MeCN ligand in all structures by pyridine reveals a remarkable change in the behavior during collisional activation and the IRMPD spectra do not show an indication for two coexistent isomers. We conclude that π -stacking stabilization effects inhibit the formation of competing isomers.

4.3 Introduction

The ability of transition metal complexes to activate different bond types (e.g. C-H or C-C) in organic molecules is well known.^[1-3] Therefore, catalysts enable reactions even with thermodynamically very stable reactants, e.g. the conversion of CO₂ into useful products such as methanol.^[4-6] This makes them attractive prospects in modern homogeneous and heterogeneous catalysis.^[7] However, catalytically active complexes often contain expensive and rare transition metals such as palladium.^[8, 9] For these transition metal complexes it is mandatory to obey the atom-economical concept to lower the costs. It is desirable to minimize the number of reaction steps and suppress side products. Hence, a primary goal in modern catalysis is the development of synthetic catalysts containing cheap and non-hazardous metals and with enhanced atom economy.^[10]

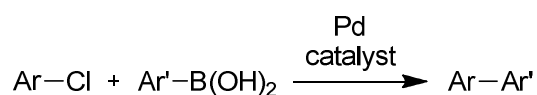
While the right transition metal for a certain catalytic reaction is often well known, selecting the right ligand system is a more demanding task. The details of the electronic and steric cooperation of the ligand and the metal site are not completely understood. Therefore, it is an important issue to design novel ligand structures and to investigate their interactions with catalytically active metal sites. To develop new catalysts obeying the atom economical concept, it is of considerable interest to understand the elementary reactions within a given catalytic cycle.^[11]

Herein, we present three derivatives **1**, **2** and **3** of a novel palladium *N*-heterocyclic carbene (NHC) complex differing in their substituent R as a model system to investigate the ligand metal interactions (Scheme 1). NHCs are heterocyclic species containing a carbene carbon (blue) and at least one nitrogen atom within the ring structure.^[12]



Scheme 1: Molecular structure of the palladium(II) complexes **1**, **2** and **3**. Note that the palladium(II) coordinates at the carbene (blue) and the carbanion (green) functional group of the NHC ligand. The three derivatives differ in the functional group of the tertiary amine (red). For mass spectrometry analysis the neutral complex is protonated.

Palladium is a well known catalytically active center in cross-coupling chemistry.^[13, 14] The Suzuki-Coupling reaction is one of the most important and widely used cross-coupling reactions. The palladium-catalyzed cross-coupling reaction between different types of organoboron compounds and various organic electrophiles including halides in the presence of base provides a powerful and general methodology for the formation of carbon-carbon bonds (Scheme 2).^[15] The Suzuki-Coupling reaction is widely used to synthesize poly-olefins, styrenes and substituted biphenyls.^[16-18]



Scheme 2: Pd-catalyzed cross-coupling reaction of an aryl boron with an aryl chloride forming a biaryl compound.^[19]

We use the electrospray ionization technique (ESI) to transfer these complexes to the gas phase.^[20, 21] The infrared multi photon dissociation (IRMPD) spectroscopy of mass-selected ions in the gas phase is a powerful tool to investigate chemical structures. We use this kind of spectroscopy coupled with a mass spectrometer applying a so called action type spectroscopy.^[22-25] Mass spectrometric analysis reveals that protonation of the complexes takes place and leads to singly positive charged complex ions. This protonation leads to coexisting structural isomers. State of the art two-color double resonance studies serve to perform isomer selective characterizations of various gas phase complexes.^[26-31] The IRMPD technique in combination with density functional theory (DFT) computations is highly suitable to characterize the chemical structure of transition metal-ligand complexes in the gas phase.^[32-35] Next to the IRMPD technique, collision-induced dissociation (CID) experiments can be used to obtain insights about binding motifs and provide information about the structural composition of these complexes.^[36, 37] CID appearance curves may be useful for distinguishing isomeric species.^[38] We conduct these methods to elucidate the chemical structure and the fragmentation behavior in preparation of subsequently catalytic studies.

4.4 Experimental setup and theoretical methods

4.4.1 Experimental setup

The presented electrospray ionization mass spectrometry (ESI-MS) was performed with two ion trap instruments (Bruker Esquire 6000 for CID and amaZonSL for IRMPD measurements). The investigated cations were produced in the positive electrospray ionization mode. The scan speed was $13000 \frac{m}{z \cdot s}$ in normal resolution scan mode ($0.3 \text{ fwhm} / \frac{m}{z}$). The scan range was at least 70 to $1500 \frac{m}{z}$. Sample solutions of complex **1**, **2** and **3** in acetonitrile (MeCN) at concentrations of approximately $1 \times 10^{-4} \text{ M}$ were continuously infused into the ESI chamber at a flow rate of $2 \mu\text{l}/\text{min}$ using an automatical syringe pump. We used nitrogen as drying gas at a flow rate of 3.0 to 4.0 l/min heated to 220 and 300 °C. We sprayed the solutions at a nebulizer gas pressure of 3 to 4 psi with the electrospray needle held at 4.5 kV. We used Helium as a buffer gas with a partial pressure of about $3 \times 10^{-3} \text{ mbar}$ inside the ion trap. BrukerEsquireControl 5.3 (Esquire) and BrukerTrapControl 7.0 (amaZonSL) software controlled the instrument and we performed data analysis using the Data Analysis 4.0 software.

Collision induced dissociation (CID) appearance curves were recorded with varying excitation magnitude from 0.0 to 1.5 corresponding to an excitation energy scale in the lab frame (E_{LAB}).^[36] These excitation energies were increased in a stepwise fashion until complete dissociation of the ion of interest was observed. Normalized relative and total fragmentation yields were calculated according to:

$$I_{i,norm}^{fr}(E_{LAB}) = \frac{I_i^{fr}(E_{LAB})}{\sum_i I_i^{fr}(E_{LAB}) + \sum_i I_i^p(E_{LAB})} \quad (1a)$$

$$I_{tot}^{fr}(E_{LAB}) = \sum_i I_{i,norm}^{fr}(E_{LAB}) \quad (1b)$$

Center of mass transformed relative excitation energies (E_{COM}) were calculated from the internal amplitudes as following in order to allow for comparability:

$$E_{COM} = \frac{m_{He}}{m_{He} + m_{ion}} \cdot E_{LAB} \quad (2)$$

m_{ion} was chosen according to the most abundant mass peak of the molecule.

An optical parametric oscillator/amplifier (OPO/OPA, LaserVision) laser system pumped with a pulsed (10 Hz) injection seeded Nd³⁺:YAG laser (PL8000, Continuum) was used as a source of tunable IR radiation ($\delta\bar{\nu} = 0.9 \text{ cm}^{-1}$, $\delta t = 7 \text{ ns}$) to record the vibrational spectra (IR_{scan}). The OPA idler wave ($\leq 10 \text{ mJ}$ per pulse) was used to record spectra within the spectral range of 2600 – 3700 cm⁻¹. The difference frequency (DF) between the OPA signal and idler waves generated in a AgGaSe₂ crystal was used for the energy range of 1200 – 2100 cm⁻¹ ($\leq 2 \text{ mJ}$ per pulse). After passing through the ion trap chamber, the IR beam was directed onto a power meter sensor to record the laser power during the measurement. The idler beam was focused by a 50 cm CaF₂ lens. The DF radiation was focused tighter by a 90° off-axis parabolic silver mirror with an effective focal length of 15 cm. The two-color IRMPD was facilitated using a second OPO/OPA laser system set to a fixed frequency (IR_{fix}). The idler output of the IR_{fix} laser system was focused by a 75 cm CaF₂ lens being aligned counter-propagating with respect to the scanning laser IR_{scan}. The time delay between the fixed IR and the scanning IR pulses was varied in the range of -100 and +100 ns and is determined by:

$$\Delta t = t_{\text{fix}} - t_{\text{scan}} \quad (3)$$

Negative time delay Δt indicates that the IR_{fix} laser irradiates the ions before the IR_{scan} laser. A positive Δt indicates that the IR_{scan} irradiates the ion first and the IR_{fix} serves as an additional energy source.

The IR spectra were recorded as ion chromatograms while continuously scanning the IR wavelength. The IRMPD yield (Y) was determined as:

$$Y = \frac{\sum_i I_i^{fr}}{\sum_i I_i^{fr} + \sum_i I_i^p} \quad (4)$$

The IR frequency was calibrated by a wavemeter (Bristol Instruments: 821 Pulsed Laser Wavelength Meter) to a theoretical accuracy of $\pm 0.02 \text{ cm}^{-1}$, which is beyond the spectral bandwidth of the utilized IR photon beams by more than one order of magnitude. IRMPD yields scale in an intrinsically nonlinear way with the applied IR photon flux. Therefore, we refrained from any photon flux normalization.

4.4.2 Theoretical methods

We conducted electronic structure calculations at the B3LYP^[39-42]/cc-pVDZ^[43-45] level of theory using the Stuttgart RSC 1997^[46, 47] effective core potential to represent palladium atom as implemented in the Gaussian 09 program package.^[48] We searched for fully optimized molecular structures of the most stable isomers found and for linear IR absorption spectra. The SCF density convergence criterion needed to relax to 10^{-8} . Harmonic vibrational frequencies were scaled by a linear lump-sum factor of 0.97 as suggested elsewhere.^[49]

4.5 Results and discussion

4.5.1 Mass spectrometric analysis and identification

The main peaks of the ESI mass spectra obtained from MeCN solutions of the complexes **1**, **2** and **3** are located at $\frac{m}{z} = 517$, $\frac{m}{z} = 519$, and $\frac{m}{z} = 531$ (most abundant mass) in the positive ion mode. These mass peaks correspond to the singly protonated complexes **1**, **2** and **3**: $[(R-C_{17}H_{18}N_5)Pd(Cl)]^+$ (R=C₄H₈N, C₄H₁₀N and C₅H₁₀N) unambiguously confirmed by simulations of their isotopic patterns. Collision-induced dissociation studies reveal the elimination of HCl, MeCN and the simultaneous elimination of HCl and MeCN (Fig. S1 – S3 in the supporting information).

4.5.2 Collision-induced dissociation (CID) studies

We have recorded fragmentation yields of the mass-selected parent ions **1**, **2** and **3** by gradually increasing the activation magnitude up to complete depletion of the parent ions (Fig. 1). Hereby, the dots represent the relative fragmentations as a function of the activation magnitude E_{COM} . The CID appearance curves of all three complexes do not show a single sigmoidal rise. The curves of all complexes exhibit a “step” around $E_{COM} = 0.004$ a.u.. At this energy value the rise flattens and after the kink it rises again. Such curve shapes may arise from two structural isomers coexisting with different fragmentation energies.^[11]

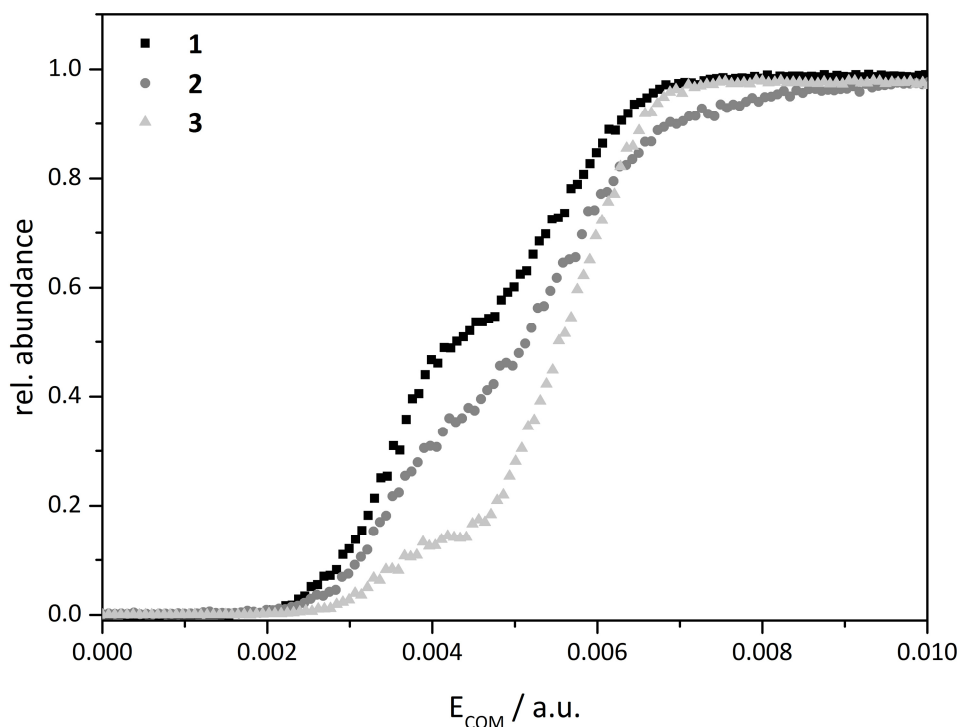


Figure 1: CID appearance curves of the three palladium complexes **1** (squares), **2** (dots) and **3** (triangles).

These curves are assembled from two curves caused by the different structural isomers. This behavior indicates that the isomers differ in the energy needed to dissociate. The rise of the sigmoid fit function indicates the nature of the transition state of fragmentation. Like all chemical reactions, the unimolecular decomposition of isolated ions is subject to thermodynamic versus kinetic reaction control: the kinetic product forms faster, whereas the thermodynamic product is more stable.^[50, 51] A flat slope arises from a tight transition (thermodynamic) state, while a steep slope points out a loose transition (kinetic) state. An activated complex with strict steric requirements is referred to as a tight complex, whereas the transition state without such requirements is called a loose complex. The tight complex needs more energy to dissociate and this leads to a flatter slope, while the loose complex is weakly bonded resulting in steep slopes.^[52-55] In order to make assessments about the transition states of the individual isomers, the curves of the isomers have to be considered separately. Therefore, we extrapolate the rise of the sigmoid fit function of each isomer at the corresponding E_{50} value of the different isomers to the baseline (Fig. 2).

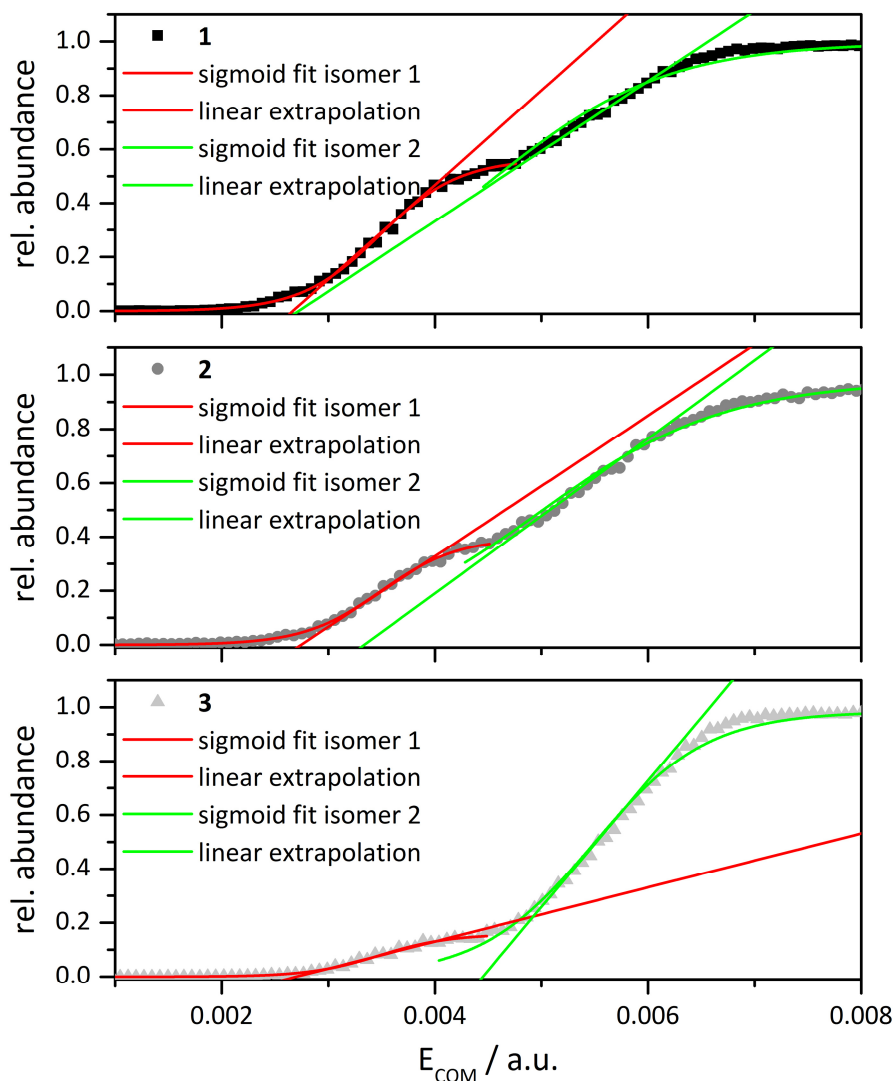


Figure 2: CID appearance curves of **1** (squares), **2** (dots) and **3** (triangles). The red curves represent isomer one, the green curves represent isomer two. Each isomer is fitted by a sigmoid fit function for analysis.

The red curves correspond to the first isomer and the green curves correspond to the second isomer of the complexes **1**, **2** and **3**. The second isomer of complex **1** reveals a flatter slope than the first isomer. This means that a tighter transition state is passed during the fragmentation process. The curves' slopes of both isomers of complex **2** are more or less equal. In the case of complex **3**, the slopes of both curves are considerably different. In comparison to the complexes **1** and **2**, the first isomer reveals the tightest transition state, while the second isomer exhibits the loosest transition state of all. Furthermore, an additional observation is that complex **3** needs the most dissociation energy. It also shows

the strongest difference in the slopes of the two isomers. The second isomer of complex **3** needs the highest dissociation energy and therefore, the appearance curve exhibit the biggest step. Complex **1** fragments at lower energies, complex **2** is an intermediate and complex **3** is the most stable.

The mass spectra taken at $E_{\text{com}}=0.006$ a.u. reveal different fragmentation channels for the three complexes. Figure 3 shows the individual fragmentation channels and their contribution to the total CID curve as a function of the collisional energy. The fragments shown in the mass spectra (Fig. 3, left) and the related appearance curves (Fig. 3, right) are marked in the same color. The orange dots represent the experimental data of the breakdown curve of the parent ion. The red dots are the total CID yield curves. The main fragmentation channels are the elimination of MeCN, HCl or both simultaneously (blue, green and magenta). Complex **2** exhibits the elimination of HCl and the loss of MeCN. We neglect the discrimination of the HCl elimination and the MeCN elimination due to the overlapping isotopic pattern (cyan). Note the attachment of water to the unsaturated palladium metal center after the elimination/loss of a ligand. The water originates from the nebulizing gas and remains within the trap as a slight impurity. Complex **1** shows two elimination processes, the elimination of HCl and the concomitant loss of HCl and MeCN. Water attaches to the HCl and MeCN eliminated complex. As discussed before, the CID curve shows a step at $E_{\text{COM}}=0.004$ a.u.. At lower energy values the CID curve is dominated by an isomer dissociating at lower energy values. At higher energies the elimination of HCl and MeCN rises, which means that the other isomer is responsible for the shape of the CID curve at this point. Only complex **1** shows elimination of HCl and MeCN at the same time without water attachment. This behavior cannot be observed for complex **2** and **3**. All complexes show water attachment after the loss of MeCN due to the unsaturated palladium center. The elimination of HCl does not lead to water attachment at all. For complex **2** is the channel, which occurs at a higher energy level, the elimination of HCl and MeCN with simultaneous water attachment. Complex **3** exhibits two fragmentation channels. It looks as if the elimination of HCl is responsible for the part of the curve before the step (isomer one). After the step, HCl and MeCN elimination with simultaneous water attachment takes place (isomer two).

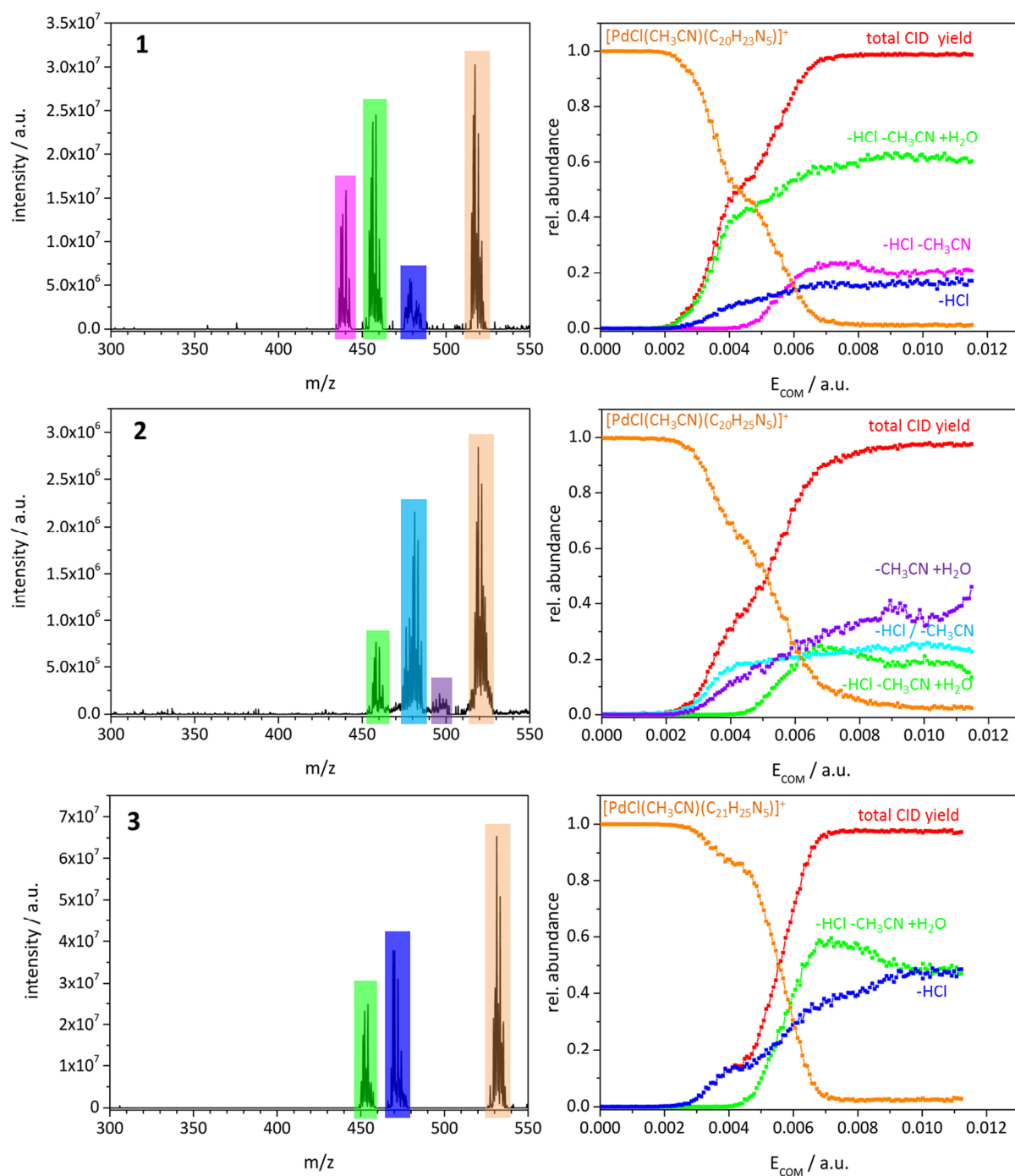


Figure 3: CID mass spectra of the mass-selected precursor complexes **1**, **2** and **3** (left) (taken at $E_{COM} = 0.08$ a.u.) and their breakdown diagrams (right) as a function of the center of mass corrected collision energies E_{COM} . Corresponding fragmentation channels are marked in the same color.

4.5.3 IRMPD studies combined with DFT calculations

The IRMPD spectroscopy provides infrared spectra of isolated mass-selected ions of interest. The IR irradiation induces fragmentation with respect to the photon energy. If the energy of the photon is in resonance with a vibration, absorption of these photons may take place. This technique is multiphotonic, therefore the absorption bands are at correct position but the intensities can be rather different from those of linear absorption spectra. In combination with computed IR spectra, this technique can be used for molecular structure analysis and isomer identification of individual complexes.

A protonation of the neutral complexes **1**, **2** and **3** generates singly positive charged ions. In general, three positions are conceivable for this protonation: the negatively charged carbanion, or either of the two nitrogen atoms of the pyrimidine ring. Therefore, one may conceive two types of binding motifs: Either the palladium cation coordinates to the carbene and to the carbanion, or it coordinates to the carbene and to a nitrogen atom of the pyrimidine. Chloride and an acetonitrile molecule complete the quadratic planar coordination sphere of the palladium.

The experimental IRMPD spectrum of complex **1** exhibits a sharp band at 3450 cm^{-1} (Fig. 4). There are also two sharp bands at 3190 and 3160 cm^{-1} and several strong bands between 2860 and 3060 cm^{-1} . We assign the bands at 3190 and 3160 cm^{-1} to aromatic CH stretching vibrations originating from the CH groups of the pyrimidine and the imidazole. The bands between 2860 and 3060 cm^{-1} are in the typical region of aliphatic CH stretching vibrations. In the fingerprint region ($1400\text{-}1700\text{ cm}^{-1}$) there is a strong absorption at 1595 cm^{-1} and two weak bands at 1550 and 1445 cm^{-1} . One would expect to see IR active C=C ring modes and C-N stretching modes in this spectral region. The comparison of the experimental spectrum with computed absorption spectra reveal that it takes multiple isomers to explain the IRMPD spectrum. A combination of the computed spectra of the two isomers **1a** and **1b** manages to explain the experimental spectrum. These isomers differ in the Pd coordination motif (cf. insets of Fig. 4). Isomer **1a** coordinates the Pd center through a carbene and carbanion and a nitrogen atom of the pyrimidine is protonated. Isomer **1b** shows a Pd-N bond to the pyrimidine ring of the ligand instead of the Pd-carbanion bond. The protonation takes place at the original carbanion functional group. Note the change of ligand proximities and orientations in particular those of chloride and MeCN.

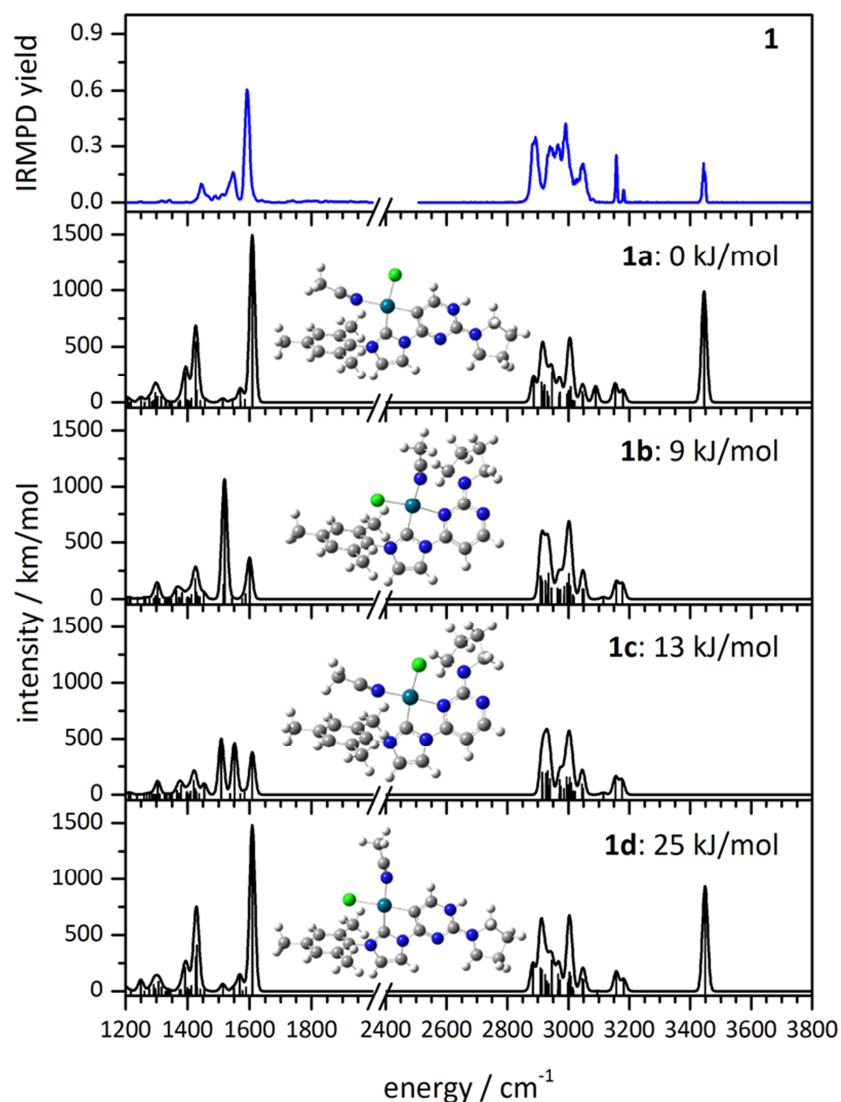


Figure 4: Experimental IRMPD spectrum (blue) of **1** and computed linear absorption spectra (black, level of theory: B3LYP/cc-pVDZ, Stuttgart RSC for palladium, scaled by 0.97) including the computed structures of the four most stable isomers **1a–1d** found. For a better visualization, the frequency intensities between 2800 and 3600 cm^{-1} are multiplied by a factor of 10. The stick spectra are folded with a Gaussian function ($\text{fwhm} = 10 \text{ cm}^{-1}$).

For isomer **1a** the MeCN ligand is above the mesitylene and in isomer **1b** the chloride ligand is above the mesitylene. This coordination change results in an instability of 9 kJ/mol. We assign the band at 3450 cm^{-1} to the NH stretching vibration of isomer **1a**. The bands between 2860 and 3060 cm^{-1} and the two sharp bands at 3190 and 3160 cm^{-1} are covered by both isomers **1a** and **1b** and are likely aliphatic and aromatic CH stretching vibrations.

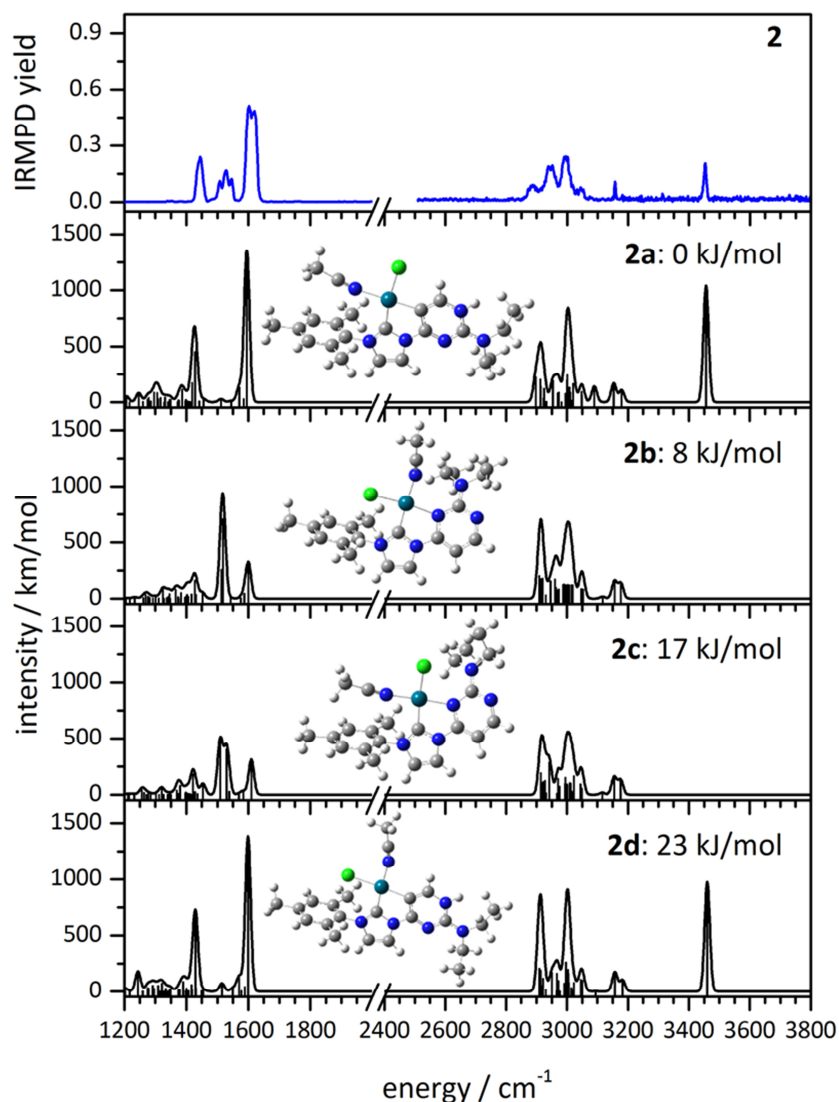


Figure 5: Experimental IRMPD spectrum (blue) of **2** and computed linear absorption spectra (black, level of theory: B3LYP/cc-pVDZ, Stuttgart RSC for palladium, scaled by 0.97) including the computed structures of the four most stable isomers **2a–2d** found. For a better visualization, the frequency intensities between 2800 and 3600 cm^{-1} are multiplied by a factor of 10. The stick spectra are folded with a Gaussian function ($fwhm = 10 \text{ cm}^{-1}$). Note that recorded band around 1530 cm^{-1} suffers from laser instabilities (cf. Fig. S9).

In the fingerprint region one would expect to see C=C and C-N stretching vibrations, which can indeed be explained by the overlapping spectra of **1a** and **1b**. A weighted combination of the computed spectra of the high energy isomers **1c** and **1d** would agree equally well with the experimental IRMPD spectrum. However, these isomers are likely less populated.

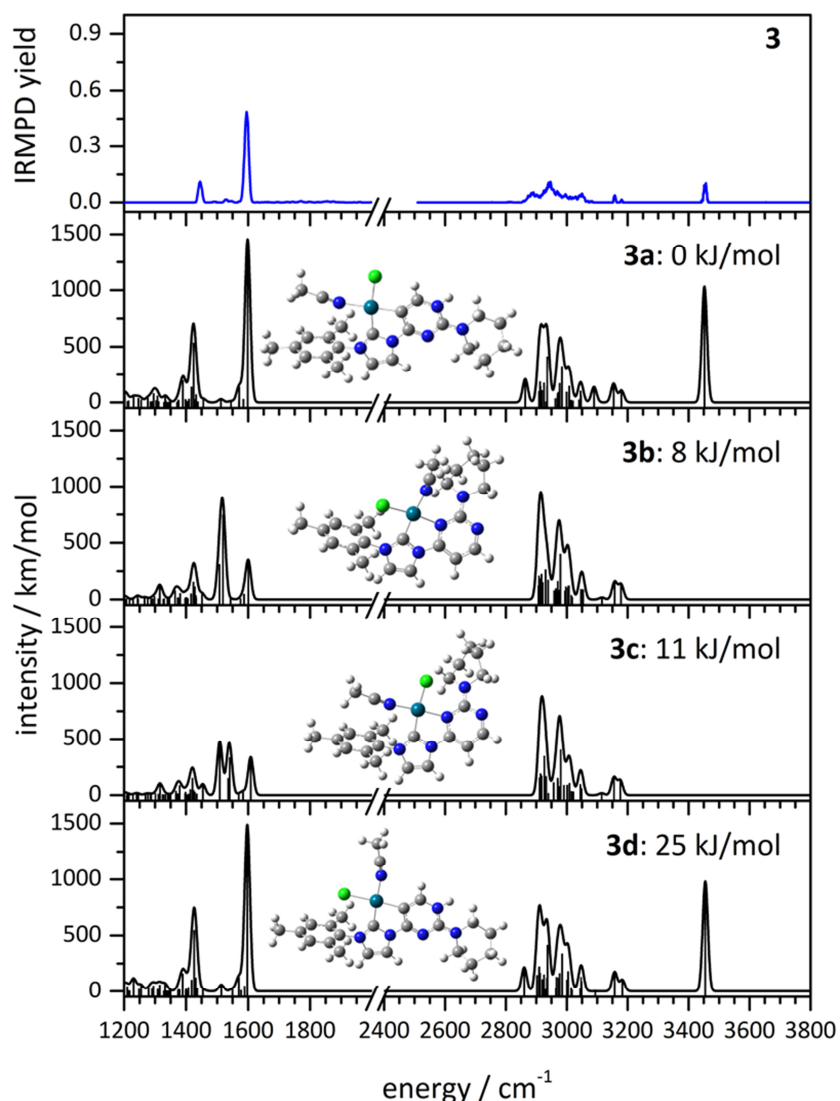


Figure 6: Experimental IRMPD spectrum (blue) of **3** and computed linear absorption spectra (black, level of theory: B3LYP/cc-pVDZ, Stuttgart RSC for palladium, scaled by 0.97) including the computed structures of the four most stable isomers **3a–3d** found. For a better visualization, the frequency intensities between 2800 and 3600 cm⁻¹ are multiplied by a factor of 10. The stick spectra are folded with a Gaussian function (fwhm = 10 cm⁻¹).

In any case the IRMPD spectrum suggests the coexistence of (at least) two isomers, which is in a nice agreement with the findings from the CID experiments. The recorded IRMPD spectrum of complex **2** basically resembles the spectrum of complex **1** (Fig. 5). The two computed isomers **2a** and **2b** suffice to explain the experimental spectrum. The isomers **2c** and **2d** contribute to a smaller extend due to higher enthalpies. The recorded band at

1535 cm^{-1} of complex **2** differs from the corresponding band of complex **1**. Here, the effect of the two isomers is more distinct due to the intense band of **2b**. Seeming fine structure in the recorded band are artifacts (cf Fig. S9 in the supporting information).

The general spectral features of complex **3** are in line with those of the complexes **1** and **2**. There are two differences: (i) stretching vibrations of complex **3** are less intense than those of the complexes **1** and **2** (Fig. 6), (ii) in the fingerprint region of complex **3** there is no band around 1540 cm^{-1} , other than in the spectra of complexes **1** and **2**. Seemingly, isomer **3b** is less populated than the isomers **1b** and **2b**. On the other hand, it is conceivable that the available laser power is not sufficient to fragment the isomer **3b**. Such speculation finds support by the CID findings that **3b** possesses the highest fragmentation threshold as seen in the CID part (cf. chapter 4.5.2). The recorded IRMPD spectrum may result from a single isomer (**3a**) in case of complex **3**, and from overlapping spectra of two isomers (**1a** and **1b**, **2a** and **2b**) in the cases of the complexes **1** and **2**. All recorded features in the IRMPD spectrum of **3** are well reproduced by isomer **3a**. Band assignment follows largely those of **1** and **2**.

4.5.4 Delay dependent two color IRMPD spectroscopy

For further elucidation of the isomer population, we performed two-color IRMPD measurements. We choose complex **2** for these investigations, because complex **2** reveals the most pronounced two isomer population, as detected in the IRMPD spectrum. Therefore, we expect to find a significant two-color effect: our two-color IRMPD technique should induce a shift in the relative isomer populations.^[26] In complex **2**, the stretching band at 3450 cm^{-1} indicates the isomer **2a** explicitly. We use this frequency for the frequency fixed laser pulse (IR_{fix}).

By varying the time delay between the two laser pulses we have recorded time dependent two-color IRMPD spectra (Fig. 7 and Fig. 8). The NH band of complex **2** is fingerprinting isomers **2a** and, much less abundant, **2d**, the IRMPD yield changes with respect to the one-color IRMPD yield in dependence of the time delay between the two laser pulses by using a fixed frequency of 3450 cm^{-1} (Fig. 7).

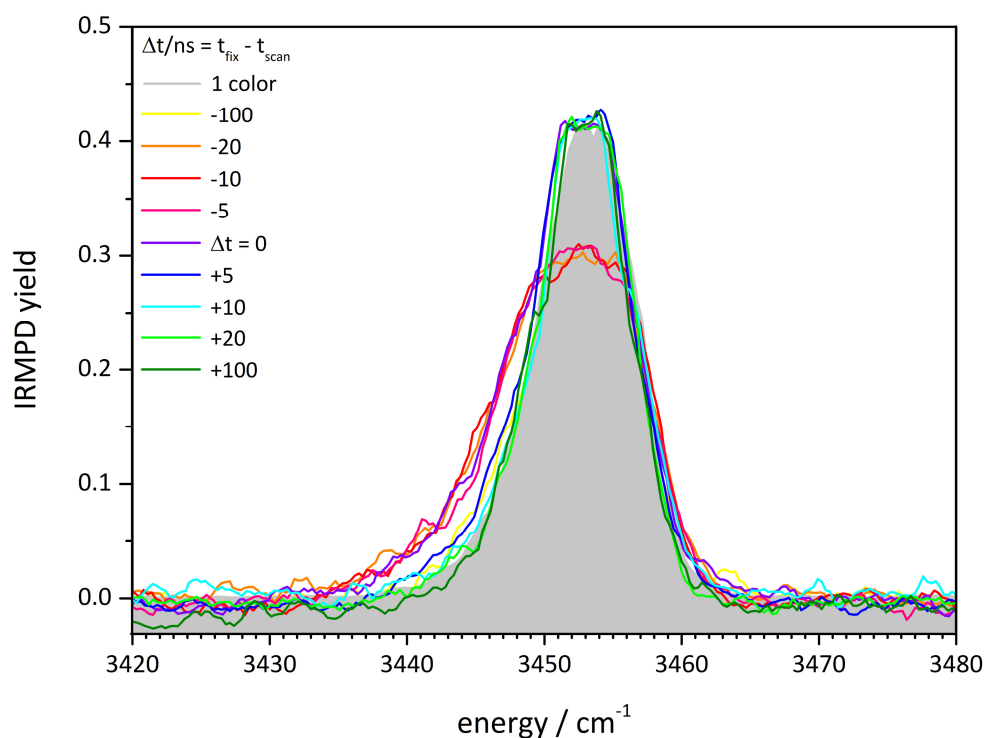


Figure 7: Two color delay dependent IRMPD spectra of complex **2** within the spectral range of 3420-3480 cm^{-1} at a fixed frequency of IR_{fix} at 3450 cm^{-1} . The grey colored area represents the one color spectrum and is given as a point of reference.

We performed measurements with the positive and negative time delay of 0, ± 5 , ± 10 , ± 20 and ± 100 ns. The grey area represents the one color IRMPD experiment and it is given as a point of reference. A negative time delay, indicates that the IR_{fix} laser irradiates before the IR_{scan} . This causes the IRMPD yield to decrease by about 30 % with regard to the one color IRMPD measurement. This decrease does not vary with the length of the negative delay. We interpret this finding as follows: the IR_{fix} laser excites and preheats the isomer **2a**. It is conceivable that particular conversion into **2b** takes place. The NH band diminishes. The IR_{scan} laser probes and fragments the preheated ions resulting in a broadening and decreasing IRMPD band (warm colors: yellow, orange and red). We conclude that: firstly, the IR_{fix} laser pulse heats the complex and induces fragmentation of a certain amount of **2a**. The IR_{fix} laser power is not sufficient enough to fragment all ions of **2a**. The second laser pulse (IR_{scan}) fragments the remaining already preheated ions. In total, all of this leads to an increase in intensity and broadening of the recorded NH stretching band. The red flank of the band broadens because of the vibrational preheating of the ion ensemble by the IR_{fix}

laser pulse prior to the IR_{scan} laser pulse.^[26] For irradiation at the same time (purple) or a positive time delay (cold colors: blue, cyan and green), the IR_{fix} laser serves as an additional energy source. We do not observe any enhancement on this band, although two lasers provide more energy for fragmentation. We infer from this behavior that almost all ions of this isomer are already fragmented by the IR_{scan} laser (“saturation”).

We also performed such two-color measurements in the fingerprint region, within the spectral range of 1350-1750 cm^{-1} (Fig. 8).

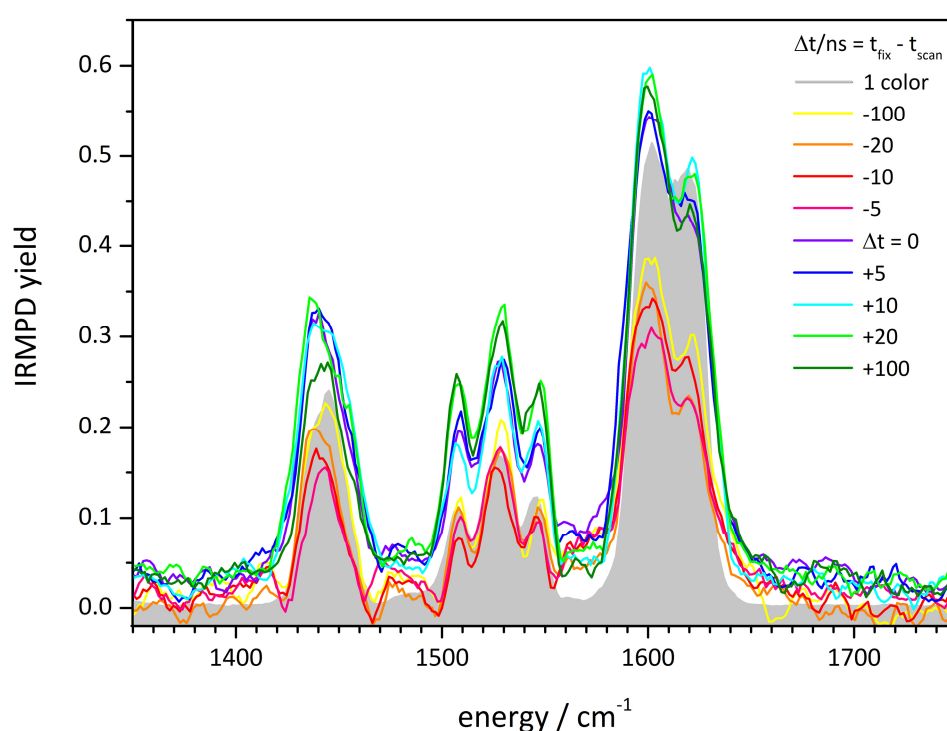


Figure 8: Two-color delay dependent IRMPD spectra of complex 2 within the spectral range of 1350-1750 cm^{-1} at a fixed frequency of IR_{fix} at 3450 cm^{-1} . The grey colored area represents the one color spectrum and is given as a point of reference. Note that the triplet form of the band around 1535 cm^{-1} originates from drops in the laser power curve (Fig. S9 in the supporting information).

We utilize time delays as before and with a fixed frequency of IR_{fix} at 3450 cm^{-1} . The maximum observed IRMPD yields change in dependence of the time delay with regard to the one color experiment (Fig. 9, dashed lines). The IRMPD yield of the bands at 1600 and

1435 cm^{-1} decreases, while it remains the same at the band at 1535 cm^{-1} for a positive time delay (Fig. 8 warm colors: yellow, orange and red). At 1600 and 1435 cm^{-1} , the yield decreases by 10-15 % with respect to the one color experiment. This is another evidence that two isomers **2a** and **2b** have to be taken into account to explain the IRMPD spectrum. The two bands influenced by the IR_{fix} laser belong to the same isomer **2a** as the band of the NH stretching vibration (cf. Fig. 5). The band at 1535 cm^{-1} originates from the second isomer **2b** and it is not influenced by the IR_{fix} laser and the IRMPD yield does not change.

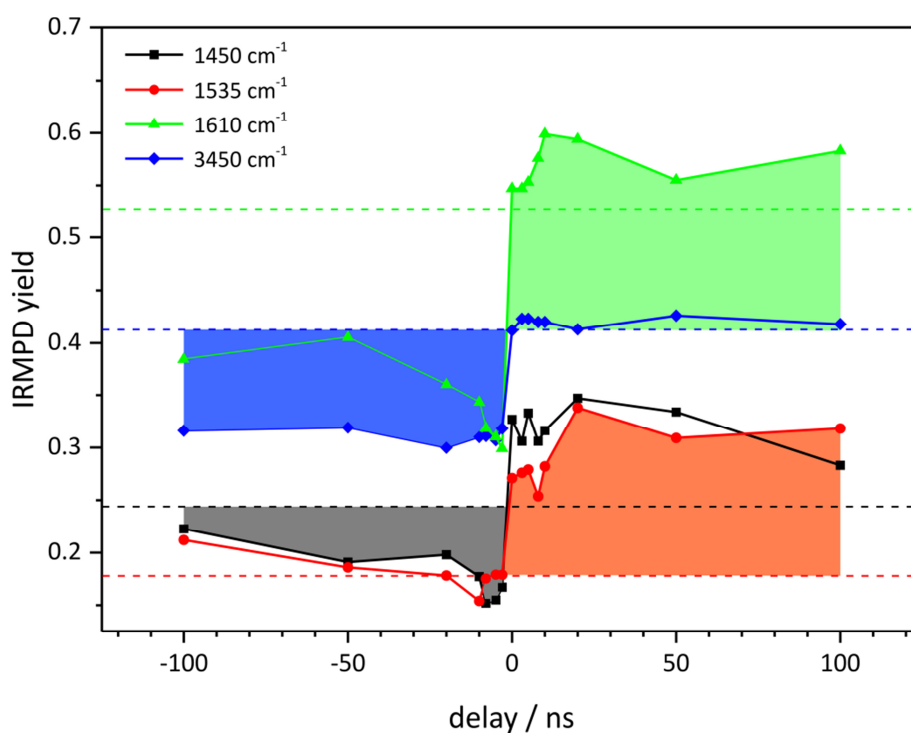


Figure 9: Maximum observed IRMPD yield of the corresponding bands at 1445, 1535, 1600 and 3450 cm^{-1} in dependence of the time delay between IR_{fix} and IR_{scan} . At negative time delays there is a minimum IRMPD yield due to isomer selective hole burning. At positive time delays the IR_{fix} laser acts as an amplifier. The dashed lines represent the value for the IRMPD yield in the case of the one color experiment.

Changing the time delay to positive values leads to an enhancement in IRMPD yield of all bands in the fingerprint region (cold colors: blue, cyan and green). In contrast to the one color IRMPD spectrum, the yield increases by 10-20 %. With the additional second IR_{fix} laser,

there is more power provided for fragmentation and the IR_{fix} laser serves as an additional energy source.

We conclude (i) the observed changes in the two-color IRMPD spectra originating from two coexisting isomers identified as **2a** and **2b** and (ii) our two-color IRMPD technique may be used to distinguish between two isomers. These findings confirm the assumptions of the CID and IRMPD parts (cf. chapter 4.5.2 and 4.5.3). It is likely, yet inconclusive, that the IR_{fix} laser at negative time delays may induce some isomer conversion, **2a** into **2b**. Further experiments at other than the currently utilized IR_{fix} frequency need to verify.

4.5.5 Identification of isomer specific fragmentation behavior

The complexes exhibit different specific fragmentation pathways after collisional activation (Fig. 3). In the IRMPD experiments, the applied IR photonic excitation leads to fragment patterns similar to those of the CID experiments, as seen in previous studies of other compounds.^[56]

To obtain a total IRMPD spectrum, we sum the total intensity of all recorded fragments into a total fragmentation yield (according to equation 4). It is also possible to create fragment specific IRMPD spectra just considering single fragmentation channels. This procedure gives insights into the fragment specific contribution to the bands received by the IR photonic excitation (Fig. 10a). It shows that fragmentation after IR excitation of complex **2** is dominated by the elimination of HCl or MeCN followed by a concomitant attachment of water (magenta colored curve: water attachment; cyan colored curve: no water attachment). The mass spectra at 1610 and 1450 cm⁻¹ show a different fragmentation pattern than the mass spectrum of the specified band at 1535 cm⁻¹ (Fig. 10b-d). Simulations of the isotopic pattern of the mass peaks reveal either HCl or MeCN elimination or both. band at 1535 cm⁻¹ originates exclusively from the elimination of HCl (Fig. 10c; red isotopic pattern).

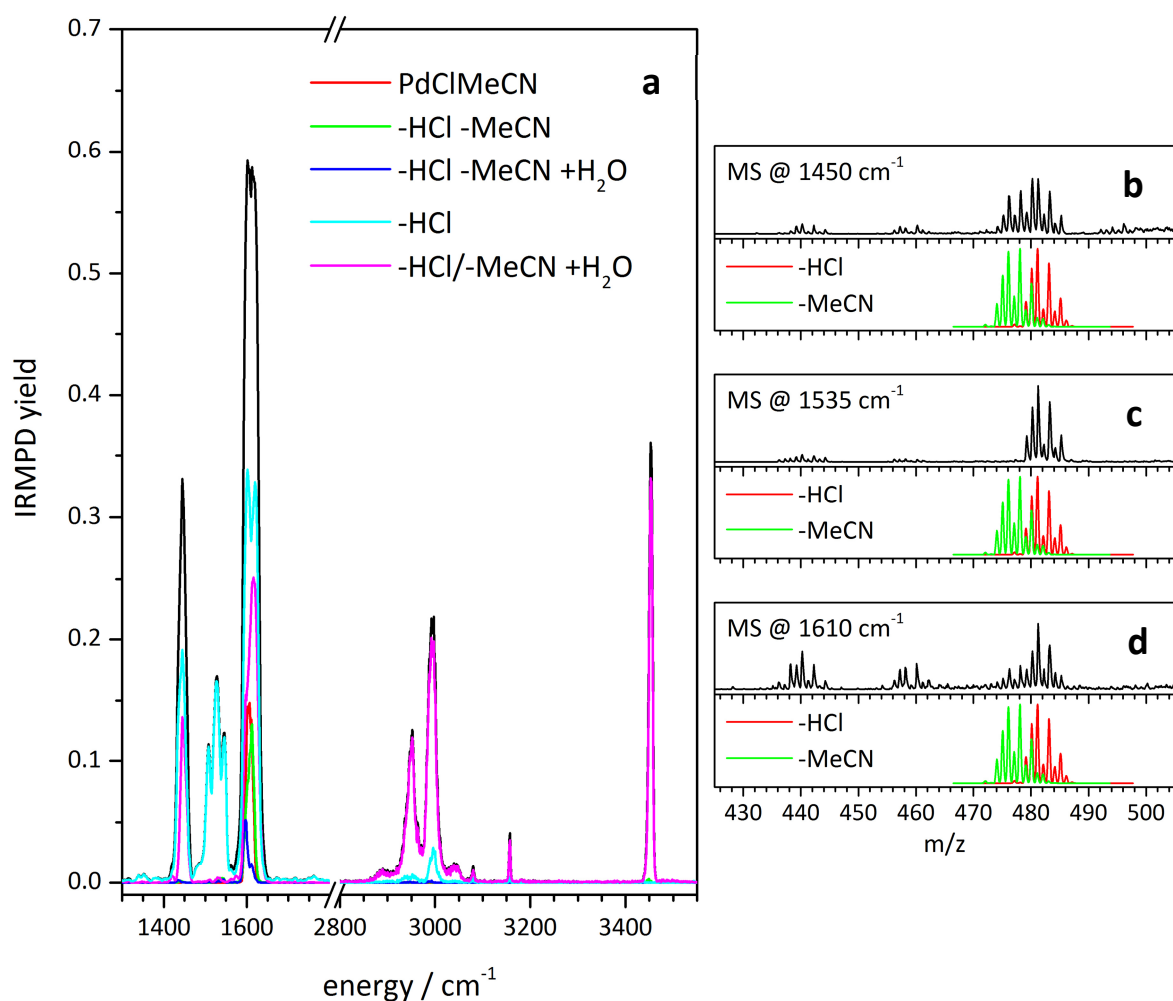
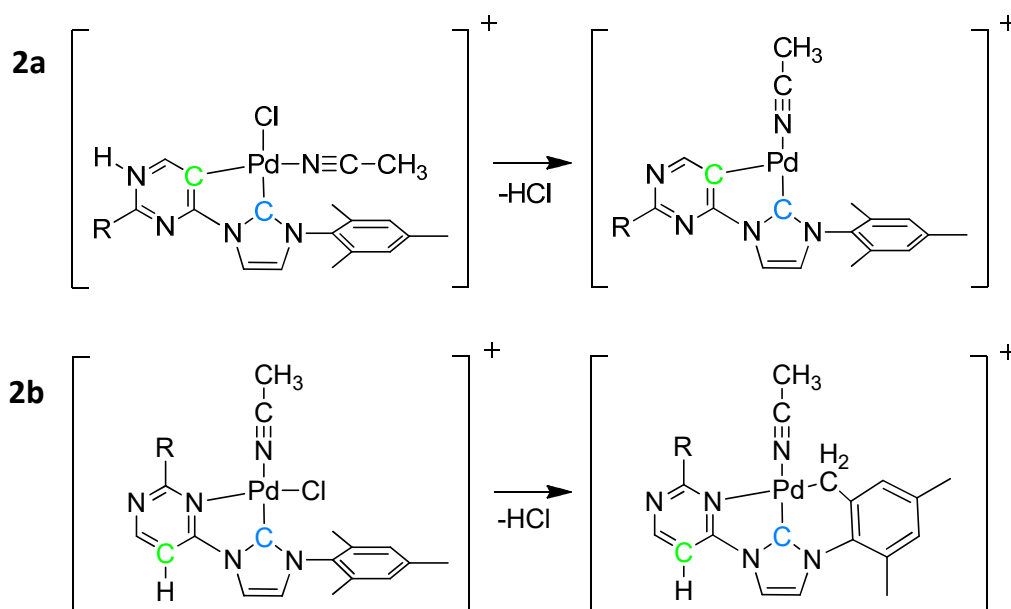


Figure 10: IRMPD spectrum of **2** including the fragment channels which are responsible for the observed bands (a). Mass spectra at 1450 (b), 1535 (c) and 1610 cm^{-1} (d) show the fragmentation behavior at the specified band. By simulations, it can be shown that the elimination of HCl (red) or the elimination of MeCN (green) are responsible for these three bands. Note that only HCl is eliminated at 1535 cm^{-1} and no water attachment takes place.

In general, metal complexes become unsaturated after eliminating ligands. In the gas phase, this unsaturation may be balanced by water attachment, which is present as a slight impurity within the ion trap. The water molecule acts as a new ligand and stabilizes the complex. In the special case of complex **2**, two isomers contribute to the IRMPD spectrum as shown above (cf. Fig. 5). The band at 1535 cm^{-1} clearly belongs to the isomer **2b** and the band at 3450 cm^{-1} to the isomer **2a**. The observed fragmentation behavior leads to the conclusion that two isomers **2a** and **2b** fragment in different ways. On the one hand, the band at

3450 cm^{-1} water attachment takes place. On the other hand, at 1535 cm^{-1} no water attachment is observed. We assume that the isomer **2b** undergoes a rearrangement after the elimination of HCl and this rearrangement inhibits the attachment of water.



Scheme 3: Illustration of the computed most stable product ions after HCl elimination of the two isomers **2a** (above) and **2b** (bottom). The hydrogen atoms for the HCl elimination process originate from the NH group (**2a**) and from the methyl group of the mesitylene (**2b**).

We computed possible structures after HCl elimination. The hydrogen atom needed for the formation of HCl may originate from several sites, i.e. the NH group or CH groups. Scheme 3 shows the most stable structure after HCl elimination of both isomers **2a** and **2b**. Deprotonation of the NH group, in order to form HCl, leads to the most stable product ion found in the case of isomer **2a**. The palladium metal center remains coordinatively unsaturated and water attachment may take place. In the case of isomer **2b**, the deprotonation takes place at the methyl group of the mesitylene. The mesitylene ring rearranges and the remaining CH₂ group forms a new bond to the palladium metal center. This bond formation leads to a square planar coordination sphere of the palladium center and thus inhibits the attachment of water.

The found rearrangement after HCl elimination explains the differences in the mass spectra for 1610, 1535 and 1450 cm^{-1} fragmentation energy (Fig. 10b-d).

Table 1: Zero Kelvin enthalpies $\Delta_{\text{frag}}H^{0K}$ for the elimination of HCl or MeCN of the isomers **2a** and **2b** (in kJ/mol).

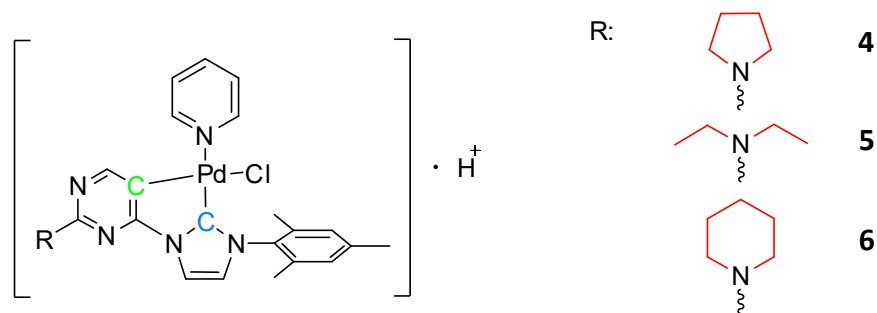
| isomer | - HCl | - MeCN |
|-----------|-------|--------|
| 2a | 138 | 118 |
| 2b | 107 | 91 |

The dissociation energy for the HCl elimination of **2a** exceeds that of **2b** by 31 kJ/mol (Table 1). However, both isomers **2a** and **2b** prefer the elimination of MeCN (20 and 16 kJ/mol). These computed dissociation energies sustain the observations and results of the CID and IRMPD parts.

4.5.6 The influence of the ligands: replacing MeCN by pyridine

Dissolving the complexes in CH_2Cl_2 and adding 100 μl of pyridine to the sample solution leads to the replacement of the MeCN ligand by pyridine (Scheme 4).

The main peaks of the ESI mass spectra of the complexes **4**, **5** and **6** are located at $\frac{m}{z} = 553$, $\frac{m}{z} = 555$ and $\frac{m}{z} = 567$ (most abundant mass). These mass peaks correspond to the singly protonated complexes **4**, **5** and **6**: $[(\text{R}-\text{C}_{20}\text{H}_{20}\text{N}_5)\text{Pd}(\text{Cl})]^+$ ($\text{R}=\text{C}_4\text{H}_8\text{N}$, $\text{C}_4\text{H}_{10}\text{N}$ and $\text{C}_5\text{H}_{10}\text{N}$) unambiguously confirmed by simulations of their isotopic patterns. Upon collisional activation the complexes **4**, **5** and **6** show the loss of HCl, pyridine and the concomitant loss of HCl and pyridine. An additional fragmentation channel is the elimination of a $[\text{PdPyrHCl}]$ unit (Fig. S4 - S6 in the supporting information). The MeCN complexes **1**, **2** and **3** do not show a corresponding fragmentation channel.



Scheme 4: Molecular structure of the palladium(II) NHC complexes **4**, **5** and **6**. Note that the MeCN ligand is exchanged by a pyridine ligand. The palladium(II) coordinates at the carbene (blue) and a carbanion (green) functional group of the NHC ligand. The three derivatives differ in the functional group of the tertiary amine (red). For mass spectrometry analysis, the neutral complex is protonated.

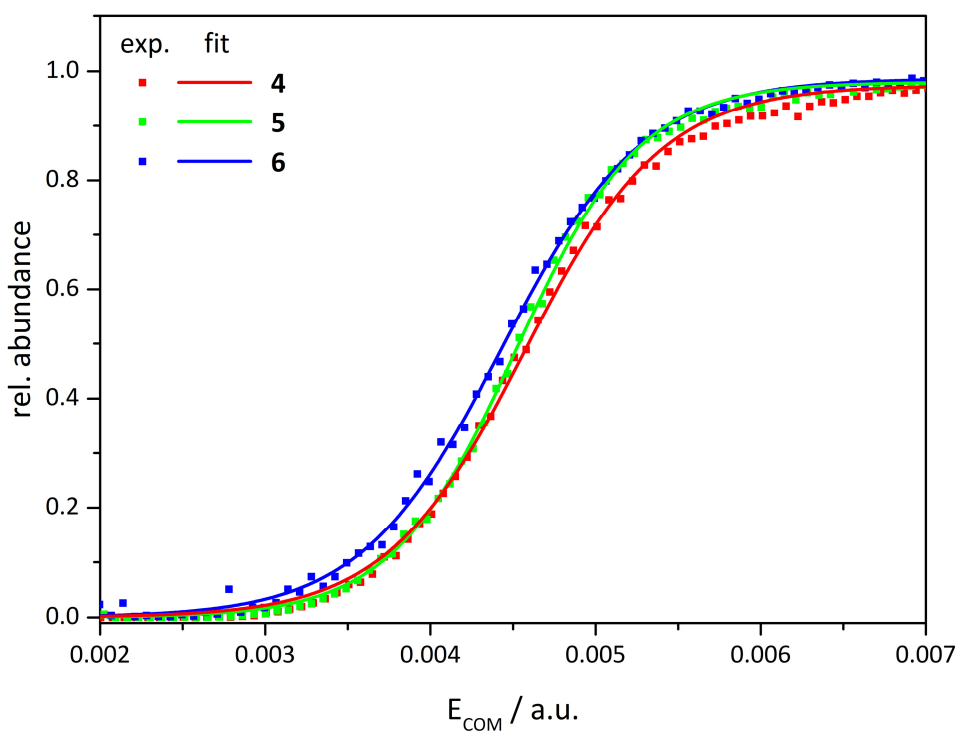


Figure 11: CID appearance curves for the complexes **4**, **5** and **6**. The dots represent the experimental data, the lines are sigmoid fit functions.

The stepwise variation of the activation magnitude delivers CID appearance curves of the mass-selected complexes **4**, **5** and **6** (Fig. 11). The squares represent the experimental data points, the lines are sigmoid fit functions. Complex **6** dissociates at the lowest activation magnitude followed by complex **4** and **5**. The differences in the activation thresholds are rather small. As compared to the findings for the complexes **1**, **2** and **3** (cf. chapter 4.5.2), the appearance curves of the complexes **4**, **5** and **6** do not indicate any presence of two coexisting isomers. The influence of the pyridine ligand is significant and it seems to affect the isomer population and likely stabilizes a single isomer.

The experimental IRMPD spectrum of complex **4** reveals an isolated sharp band at 3445 cm^{-1} , a weak band at 3160 cm^{-1} , another sharp band at 3000 cm^{-1} , several weak bands between 2900 and 3080 cm^{-1} , an asymmetric strong band at 1630 cm^{-1} and two proximate bands at 1420 and 1450 cm^{-1} (Fig. 12). The computed spectra of the isomers **4b** and **4d** are in a good agreement with the experimental IRMPD spectrum. In the computed structure, the Pd coordinates to a chlorido ligand, to the pyridine and to the carbene and the carbanion of the NHC ligand in a square planar geometry. The protonation takes place at a nitrogen atom of the pyrimidine ring. The major difference between the isomers **4b** and **4d** is the relative orientation of the pyridine ligand. In isomer **4b** the pyridine locates close and parallel to the mesitylene ring, which leads to a stabilization by π -stacking effects. Swapping the relative positions of the chlorido ligand and the pyridine aim isomer **4d** leading to a loss of stability by 18 kJ/mol . All recorded IRMPD bands are well reproduced by the spectra of these two isomers. The less stable isomer **4d** possesses no exclusively fingerprint band and it may not populate. Although the relative energy differences are small, the isomers **4a** and **4c** do not prevail either supported by the CID results which seemingly do not indicate the presence of more than one isomer. Both isomers would reveal a more or less strong band around 1520 cm^{-1} , which is not apparent in the experimental IRMPD spectrum. The isomers **4a** and **4c** would exhibit a Pd coordination to a nitrogen atom of the pyrimidine ring instead of a coordination to the carbanion. The protonation would take place at the carbanion.

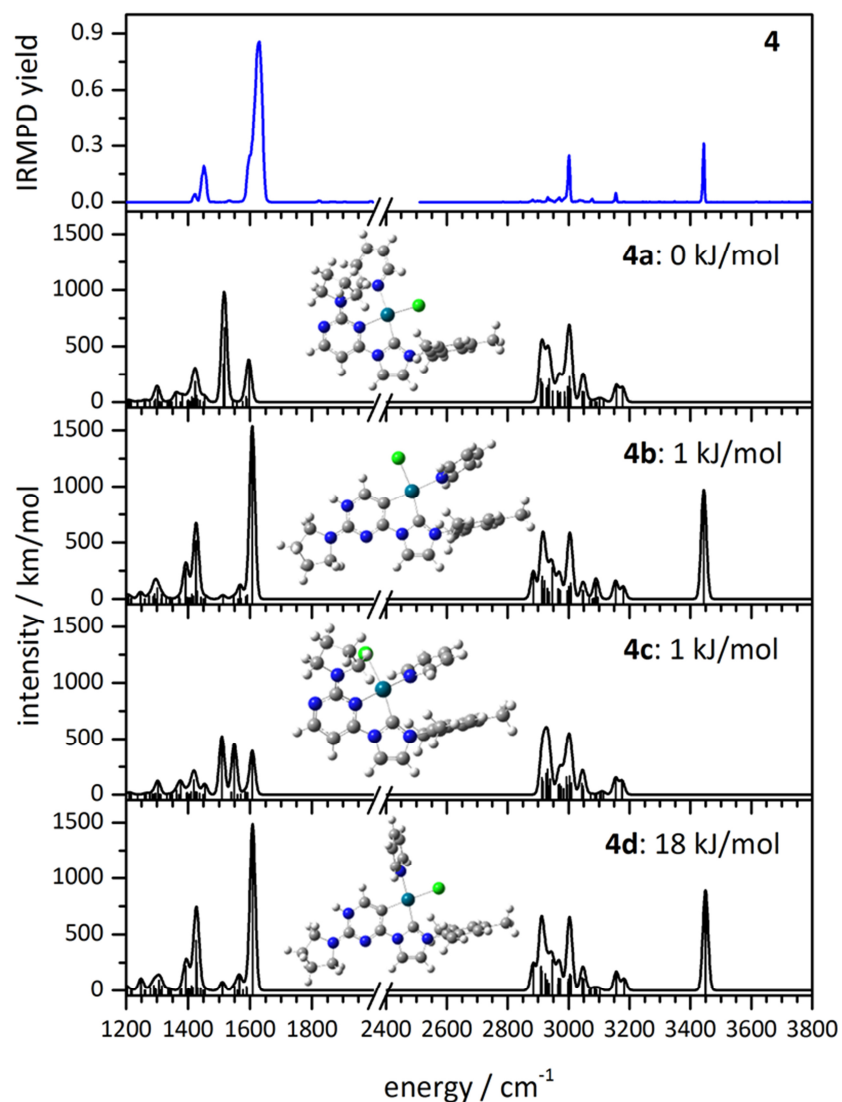


Figure 12: Experimental IRMPD spectrum (blue) of **4** and computed linear absorption spectra (black, level of theory: B3LYP/cc-pVDZ, Stuttgart RSC for palladium, scaled by 0.97) including the computed structures of the four most stable isomers **4a–4d** found. For better visualization, the frequency intensities between 2800 and 3600 cm^{-1} are multiplied by a factor of 10. The stick spectra are folded with a Gaussian function ($\text{fwhm} = 10 \text{ cm}^{-1}$).

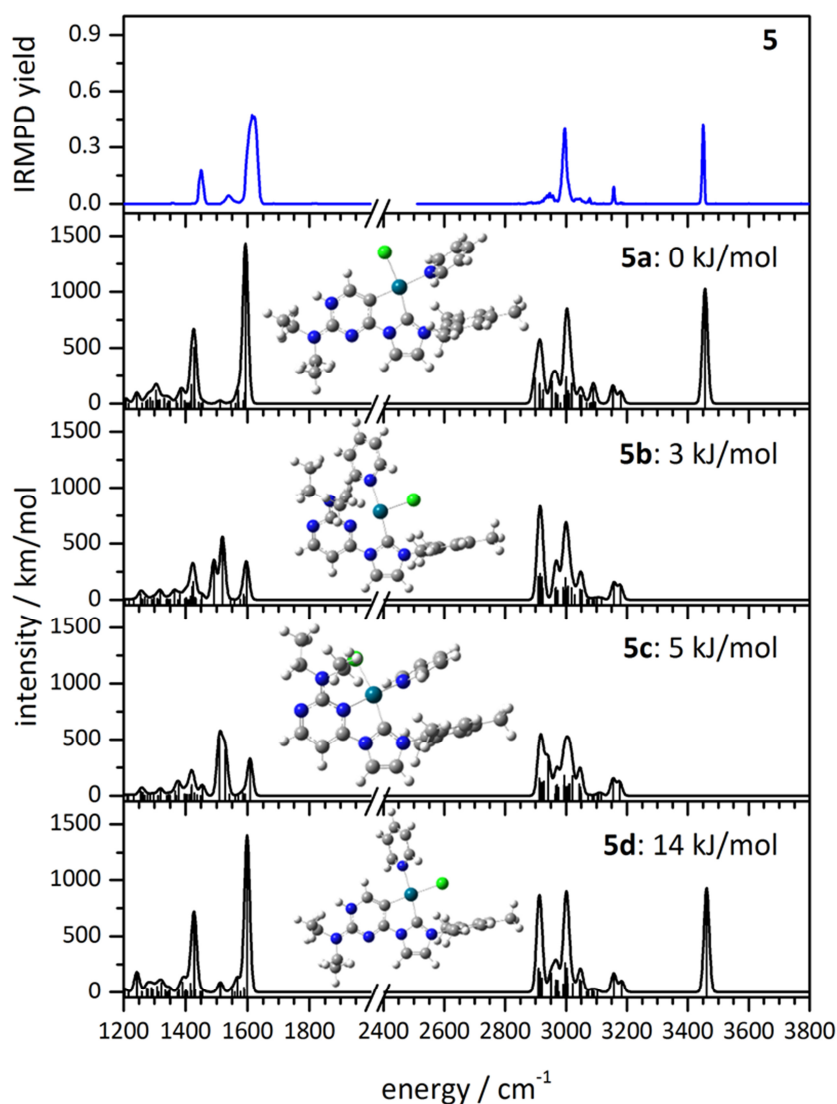


Figure 13: Experimental IRMPD spectrum (blue) of **5** and computed linear absorption spectra (black, level of theory: B3LYP/cc-pVDZ, Stuttgart RSC for palladium, scaled by 0.97) including the computed structures of the four most stable isomers **5a–5d** found. For better visualization, the frequency intensities between 2800 and 3600 cm^{-1} are multiplied by a factor of 10. The stick spectra are folded with a Gaussian function ($\text{fwhm} = 10 \text{ cm}^{-1}$).

The IRMPD spectrum of complex **5** shows almost the same spectral features as the IRMPD spectrum of complex **4** (Fig. 13). There is an additional band at 1540 cm^{-1} , which is not observed in the case of complex **4**. The geometry and the binding motifs of the found isomers **5a – 5d** are similar to the isomers **4a – 4d**. The findings are comparable. The computed spectra of the isomers **5a** and **5d** are well in line with the experimental IRMPD

spectrum. The isomers **5b** and **5c** show bands around 1550 cm^{-1} . Although these bands reproduce the experimental band at 1540 cm^{-1} , the isomers can be neglected due to their band shape. The computed spectra of the isomers **5a** and **5d** also reveal a weak band at 1520 cm^{-1} .

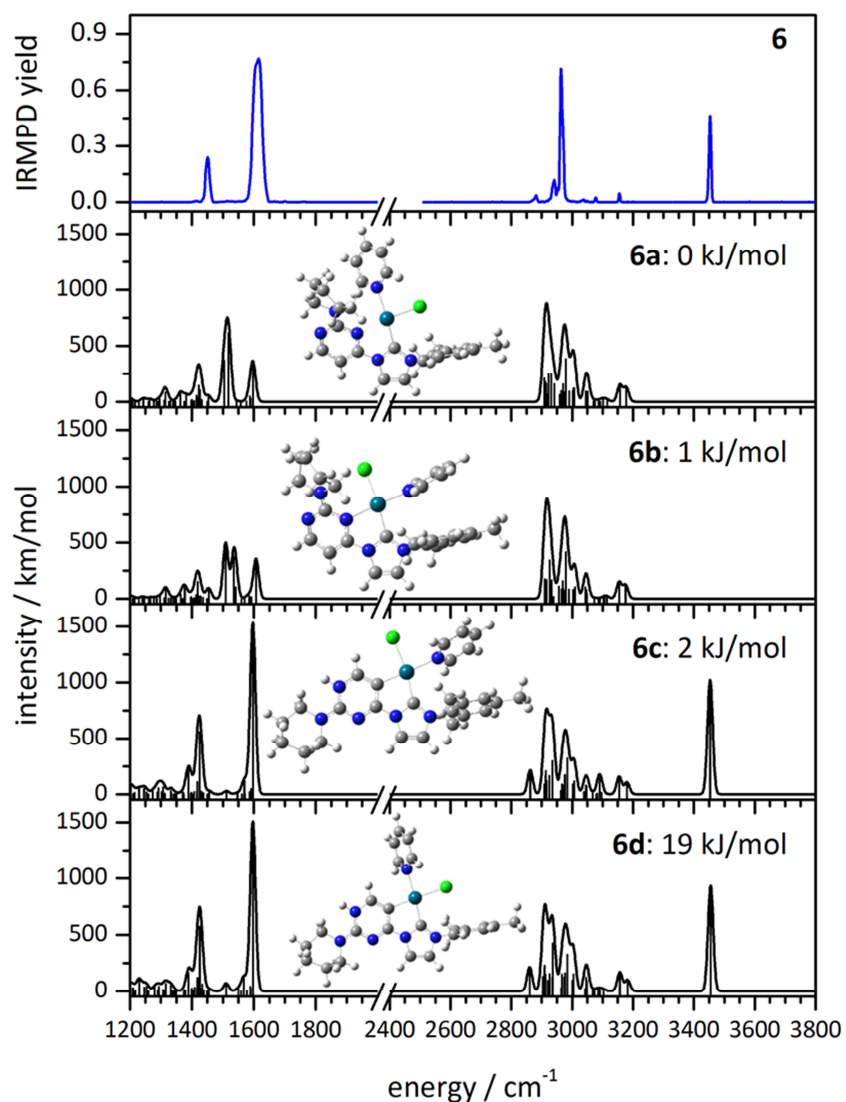


Figure 14: Experimental IRMPD spectrum (blue) of **6** and computed linear absorption spectra (black, level of theory: B3LYP/cc-pVDZ, Stuttgart RSC for palladium, scaled by 0.97) including the computed structures of the four most stable isomers **6a–6d** found. For better visualization, the frequency intensities between 2800 and 3600 cm^{-1} are multiplied by a factor of 10. The stick spectra are folded with a Gaussian function ($\text{fwhm} = 10\text{ cm}^{-1}$).

The experimental IRMPD spectrum of complex **6** exhibits similar spectral features as those in the spectrum of complex **4** (Fig. 14). The findings are alike to the findings of the complexes **4** and **5**. The computed spectrum of isomer **6c** reproduces the experimental IRMPD spectrum. All computed vibrations of isomer **6c** are well in line with the recorded spectral features.

As seen in the CID part, the influence of the pyridine ligand on the IRMPD spectra is remarkable. Compared to the IRMPD results of the MeCN complexes **1**, **2** and **3** the spectra of the pyridine complexes **4**, **5** and **6** do not reveal evidence for two coexisting isomers. The present isomer arises from the stabilizing π -stacking between the pyridine and the mesitylene. Moreover, the pyridine is larger than the MeCN, and thus may lead to an increased amount of steric hindrance.

4.6 Summary and conclusion

We have presented CID and IRMPD investigations on three derivatives of protonated palladium complexes that coordinate MeCN or pyridine. Collision-induced dissociation studies of the MeCN complexes reveal evidence of two coexisting isomers, which are both populated at room temperature. Experimental IRMPD spectra and computed linear absorption spectra of the most stable isomers identify the likely structures of the two coexistent isomers. Protonation takes place at the carbanion function or at the nitrogen atoms of the pyrimidine ring. Depending on the position of the protonation, Pd either coordinates to the carbanion or to the nitrogen atom of the pyrimidine ring. Mass spectrometric analysis of the single fragment channels exhibits the contributions of the individual fragments to the resulting IRMPD bands. Hereby, the band at 1535 cm^{-1} exclusively revealing HCl elimination and no concomitant loss of HCl and MeCN followed by water attachment, remarkable contrast to the other recorded IRMPD bands. Computed structures of the resulting fragments reveal a rearrangement that hinders the attachment of water. A methylene group of the mesitylene takes the vacant Pd coordination site. Two-color IRMPD investigations show isomer selective hole burning in dependence on the time delay between the two laser pulses. According to the time delay, enhancement or decrease of

bands assigned to certain isomers are observed. Photon-induced isomerization is likely taking place.

The replacement of the MeCN ligand by pyridine reveals a remarkably different fragmentation behavior. The IRMPD spectra as well as the CID appearance curves do not show any evidence of two coexisting isomers. The comparison of the experimental IRMPD spectra with computed linear absorption spectra allows for structure determination and identifies the likely sole isomer prevailing. According to the findings of the MeCN containing complexes two possible protonation sites have to be considered. However, the IRMPD spectra of the pyridine containing complexes reveal that the protonation of the carbanion can be neglected. The pyrimidine protonated isomers show a good agreement with the experimental IRMPD spectra. These isomers are stabilized by π -stacking due to the interaction of the pyridine with the mesitylene. Moreover, the considerably size of the pyridine leads to steric hindrances. These two effects inhibit the formation of a second isomer.

4.7 References

- [1] O. Daugulis, *C-H Activation*, **2010**, 292, 57-84.
- [2] S. Rana, A. Modak, S. Maity, T. Patra and D. Maiti, in *Progress in Inorganic Chemistry, Vol 59*, ed. K. D. Karlin, John Wiley & Sons Inc, Hoboken, **2014**, vol. 59, pp. 1-188.
- [3] B. Cornils, *Angewandte Chemie-International Edition*, **2013**, 52, 9079-9079.
- [4] A. Dibenedetto, A. Angelini and P. Stufano, *Journal of Chemical Technology and Biotechnology*, **2014**, 89, 334-353.
- [5] G. A. Olah, *Angewandte Chemie-International Edition*, **2005**, 44, 2636-2639.
- [6] J. H. Lunsford, *Catalysis Today*, **2000**, 63, 165-174.
- [7] J. Pritchard, G. A. Filonenko, R. van Putten, E. J. M. Hensen and E. A. Pidko, *Chemical Society Reviews*, **2015**, 44, 3808-3833.
- [8] C. Torborg and M. Beller, *Advanced Synthesis & Catalysis*, **2009**, 351, 3027-3043.
- [9] A. Zapf and M. Beller, *Topics in Catalysis*, **2002**, 19, 101-109.
- [10] B. M. Trost, *Science*, **1991**, 254, 1471-1477.
- [11] A. Skriba, J. Schulz and J. Roithova, *Organometallics*, **2014**, 33, 6868-6878.
- [12] M. N. Hopkinson, C. Richter, M. Schedler and F. Glorius, *Nature*, **2014**, 510, 485-496.
- [13] C. Seechurn, M. O. Kitching, T. J. Colacot and V. Snieckus, *Angewandte Chemie-International Edition*, **2012**, 51, 5062-5085.
- [14] X. F. Wu, H. Neumann and M. Beller, *Chemical Reviews*, **2013**, 113, 1-35.
- [15] A. Suzuki, *Angewandte Chemie-International Edition*, **2011**, 50, 6722-6737.
- [16] A. Suzuki, *Journal of Organometallic Chemistry*, **1999**, 576, 147-168.
- [17] A. Suzuki, *Pure and Applied Chemistry*, **1991**, 63, 419-422.
- [18] N. Miyaura and A. Suzuki, *Chemical Reviews*, **1995**, 95, 2457-2483.
- [19] G. R. Peh, E. A. B. Kantchev, J. C. Er and J. Y. Ying, *Chemistry-a European Journal*, **2010**, 16, 4010-4017.
- [20] J. B. Fenn, *Angewandte Chemie-International Edition*, **2003**, 42, 3871-3894.
- [21] M. Yamashita and J. B. Fenn, *Journal of Physical Chemistry*, **1984**, 88, 4451-4459.
- [22] N. C. Polfer, *Chemical Society Reviews*, **2011**, 40, 2211-2221.
- [23] L. MacAleese and P. Maitre, *Mass Spectrometry Reviews*, **2007**, 26, 583-605.
- [24] T. D. Fridgen, *Mass Spectrometry Reviews*, **2009**, 28, 586-607.
- [25] G. von Helden, J. Oomens, B. G. Sartakov and G. Meijer, *International Journal of Mass Spectrometry*, **2006**, 254, 1-19.

- [26] J. Lang, M. Gaffga, F. Menges and G. Niedner-Schatteburg, *Physical Chemistry Chemical Physics*, **2014**, 16, 17417-17421.
- [27] K. Tanabe, M. Miyazaki, M. Schmies, A. Patzer, M. Schutz, H. Sekiya, M. Sakai, O. Dopfer and M. Fujii, *Angewandte Chemie-International Edition*, **2012**, 51, 6604-6607.
- [28] N. Heine, M. R. Fagiani, M. Rossi, T. Wende, G. Berden, V. Blum and K. R. Asmis, *Journal of the American Chemical Society*, **2013**, 135, 8266-8273.
- [29] A. Fujii and K. Mizuse, *International Reviews in Physical Chemistry*, **2013**, 32, 266-307.
- [30] T. R. Rizzo, J. A. Stearns and O. V. Boyarkin, *International Reviews in Physical Chemistry*, **2009**, 28, 481-515.
- [31] C. M. Leavitt, A. B. Wolk, J. A. Fournier, M. Z. Kamrath, E. Garand, M. J. Van Stipdonk and M. A. Johnson, *Journal of Physical Chemistry Letters*, **2012**, 3, 1099-1105.
- [32] N. C. Polfer, J. Oomens and R. C. Dunbar, *Physical Chemistry Chemical Physics*, **2006**, 8, 2744-2751.
- [33] A. Fedorov, E. P. A. Couzijn, N. S. Nagornova, O. V. Boyarkin, T. R. Rizzo and P. Chen, *Journal of the American Chemical Society*, **2010**, 132, 13789-13798.
- [34] M. Savoca, T. Wende, L. Jiang, J. Langer, G. Meijer, O. Dopfer and K. R. Asmis, *Journal of Physical Chemistry Letters*, **2011**, 2, 2052-2056.
- [35] S. Chakraborty and O. Dopfer, *Chemphyschem*, **2011**, 12, 1999-2008.
- [36] F. Menges, C. Riehn and G. Niedner-Schatteburg, *Zeitschrift Fur Physikalische Chemie-International Journal of Research in Physical Chemistry & Chemical Physics*, **2011**, 225, 595-609.
- [37] R. H. Schultz, K. C. Crellin and P. B. Armentrout, *Journal of the American Chemical Society*, **1991**, 113, 8590-8601.
- [38] J. M. Wells and S. A. McLuckey, in *Biological Mass Spectrometry*, ed. A. L. Burlingame, Elsevier Academic Press Inc, San Diego, **2005**, vol. 402, pp. 148-185.
- [39] A. D. Becke, *Physical Review A*, **1988**, 38, 3098-3100.
- [40] A. D. Becke, *Journal of Chemical Physics*, **1993**, 98, 5648-5652.
- [41] B. Miehlich, A. Savin, H. Stoll and H. Preuss, *Chemical Physics Letters*, **1989**, 157, 200-206.
- [42] C. T. Lee, W. T. Yang and R. G. Parr, *Physical Review B*, **1988**, 37, 785-789.
- [43] T. H. Dunning, *Journal of Chemical Physics*, **1989**, 90, 1007-1023.
- [44] D. E. Woon and T. H. Dunning, *Journal of Chemical Physics*, **1993**, 98, 1358-1371.

- [45] D. E. Woon and T. H. Dunning, *Journal of Chemical Physics*, **1993**, 99, 3730-3737.
- [46] D. Andrae, U. Haussermann, M. Dolg, H. Stoll and H. Preuss, *Theoretica Chimica Acta*, **1991**, 78, 247-266.
- [47] M. Dolg, U. Wedig, H. Stoll and H. Preuss, *Journal of Chemical Physics*, **1987**, 86, 866-872.
- [48] M. J. T. Frisch, *et al.*, **2009**, Revision D.01 Wallingford CT. 2009.
- [49] NIST Standard Reference Database 101, <http://cccbdb.nist.gov/vibscalejust.asp>.
- [50] J. A. Hipple and E. U. Condon, *Physical Review*, **1945**, 68, 54-55.
- [51] E. V. Anslyn, Dougherty, D.A., *Modern Physical Organic Chemistry*, Macmillan Education, **2005**.
- [52] S. Torker, D. Merki and P. Chen, *Journal of the American Chemical Society*, **2008**, 130, 4808-4814.
- [53] S. Narancic, A. Bach and P. Chen, *Journal of Physical Chemistry A*, **2007**, 111, 7006-7013.
- [54] M. T. Rodgers, K. M. Ervin and P. B. Armentrout, *Journal of Chemical Physics*, **1997**, 106, 4499-4508.
- [55] C. Lifshitz, Laskin, J., *Principles of Mass Spectrometry Applied to Biomolecules; Energy and Entropy Effects in Gas Phase Dissociation of Proteins and Peptides*, John Wiley & Sons, **2006**.
- [56] Y. Nosenko, F. Menges, C. Riehn and G. Niedner-Schatteburg, *Physical Chemistry Chemical Physics*, **2013**, 15, 8171-8178.

4.8 Supporting Information to Isomer Discrimination in a Pd-NHC Complex by Collisional and IR Light Induced Activation

Maximilian Gaffga, Agnes Fizia, Werner R. Thiel and Gereon Niedner-Schatteburg

*Fachbereich Chemie und Forschungszentrum OPTIMAS, Technische Universität
Kaiserslautern, 67663 Kaiserslautern, Germany*

Table of content

Figure S1: CID mass spectrum of complex **1** including simulations of the isotopic patterns.

Figure S2: CID mass spectrum of complex **2** including simulations of the isotopic patterns.

Figure S3: CID mass spectrum of complex **3** including simulations of the isotopic patterns.

Figure S4: CID mass spectrum of complex **4** including simulations of the isotopic patterns.

Figure S5: CID mass spectrum of complex **5** including simulations of the isotopic patterns.

Figure S6: CID mass spectrum of complex **6** including simulations of the isotopic patterns.

Figure S7: IRMPD spectra of the mass-selected precursor complexes **1**, **2** and **3**.

Figure S8: IRMPD spectrum of **2** and the laser power curve in the range of 2700-3600 cm^{-1} .

Figure S9: IRMPD spectrum of **2** and the laser power curve in the range of 1200-1800 cm^{-1} .

Figure S10: IRMPD spectrum in dependence of the fragment channel contribution.

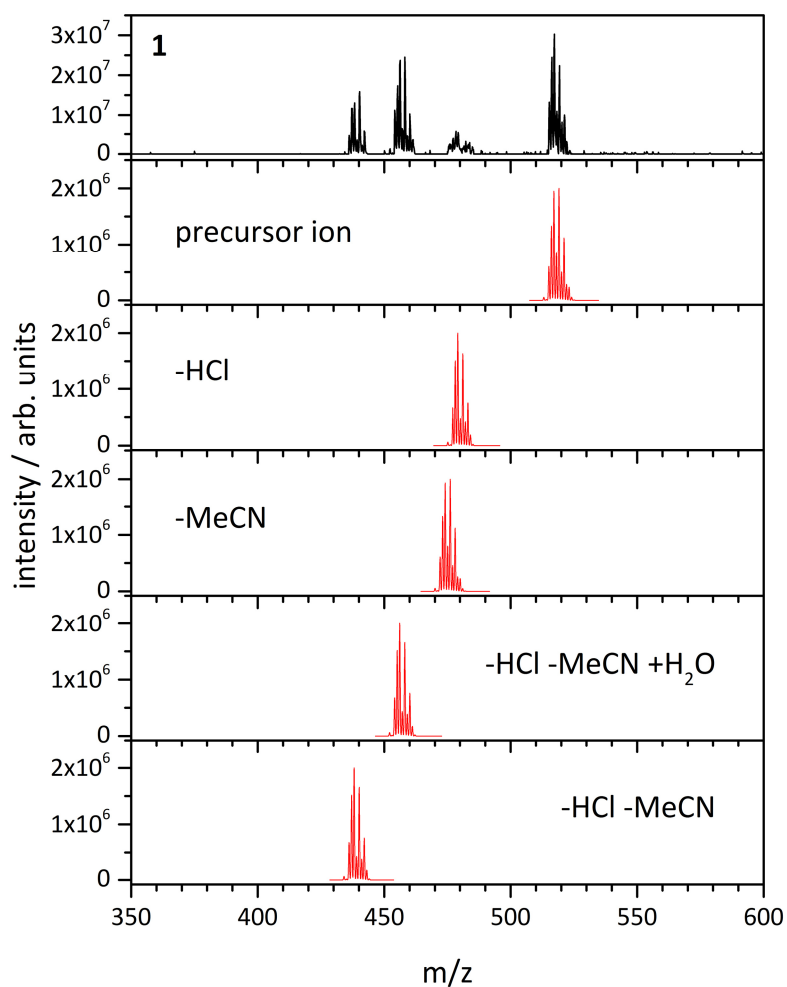


Figure S1: CID mass spectrum of the complex ion **1** (black curve) taken at $E_{COM} = 0.005$ a.u. and simulations of the isotopic pattern of the resulting fragment ions (red curves). The main fragmentation channels are the elimination of HCl, acetonitrile (MeCN) and the concomitant loss of HCl and MeCN.

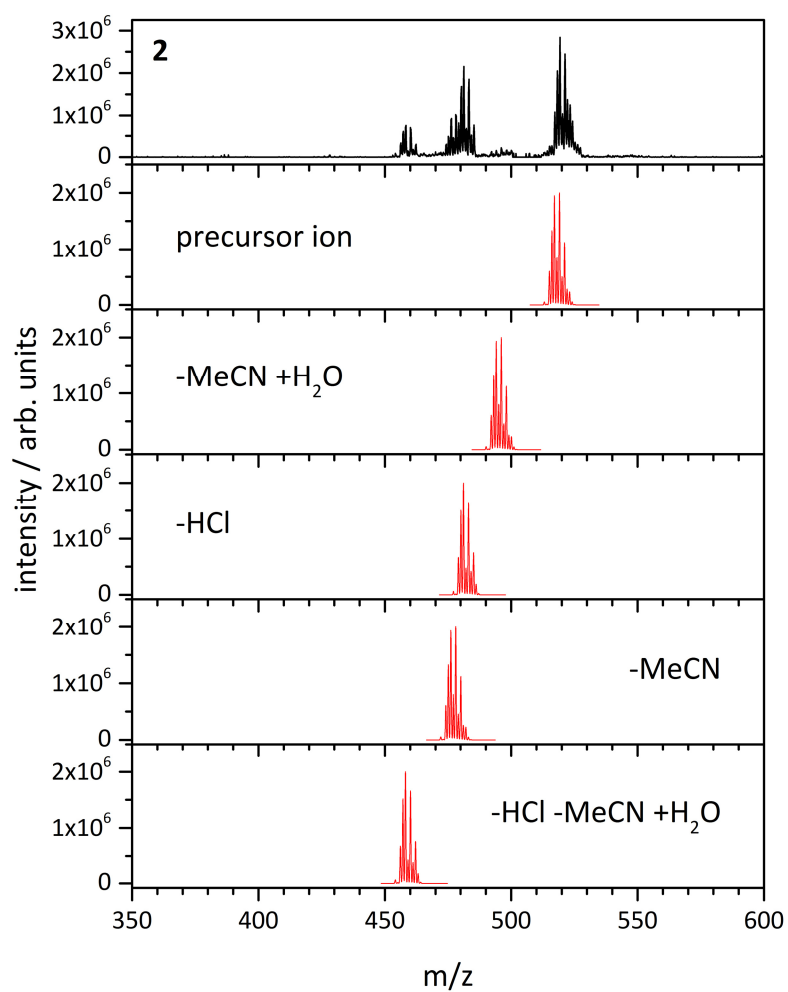


Figure S2: CID mass spectrum of the complex ion **2** (black curve) taken at $E_{COM} = 0.005$ a.u. and simulations of the isotopic pattern of the resulting fragment ions (red curves). The main fragmentation channels are the elimination of HCl, acetonitrile (MeCN) and the concomitant loss of HCl and MeCN.

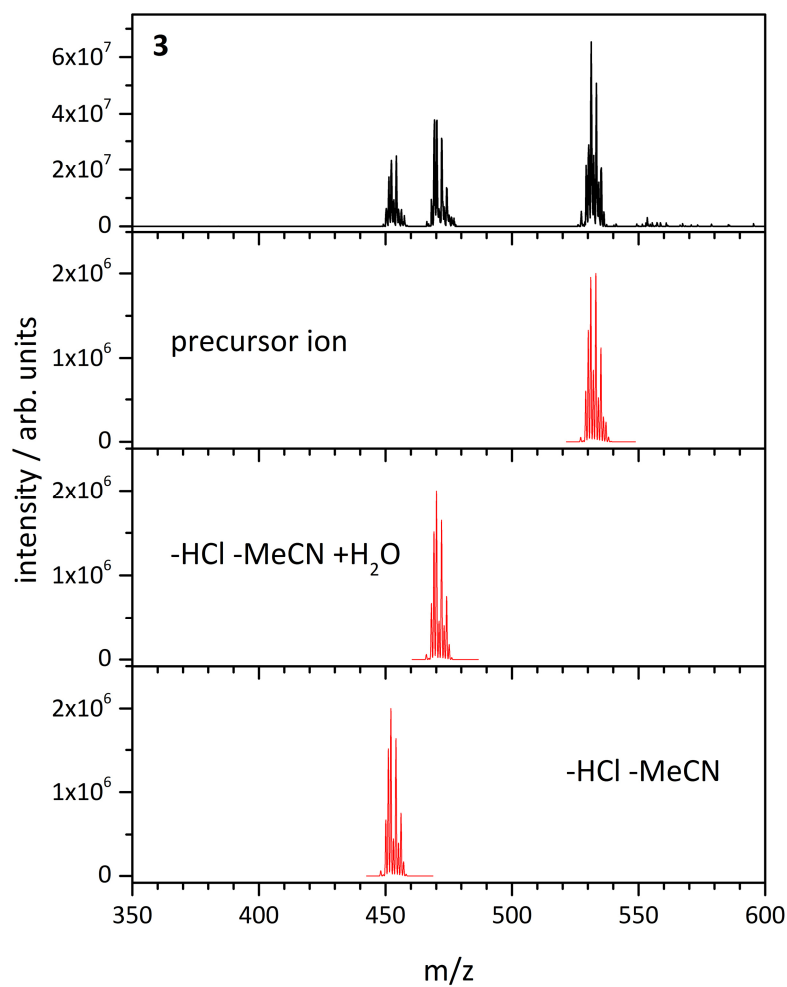


Figure S3: CID mass spectrum of the complex ion **3** (black curve) taken at $E_{COM} = 0.005$ a.u. and simulations of the isotopic pattern of the resulting fragment ions (red curves). The main fragmentation channels are the elimination of HCl, acetonitrile (MeCN) and the concomitant loss of HCl and MeCN.

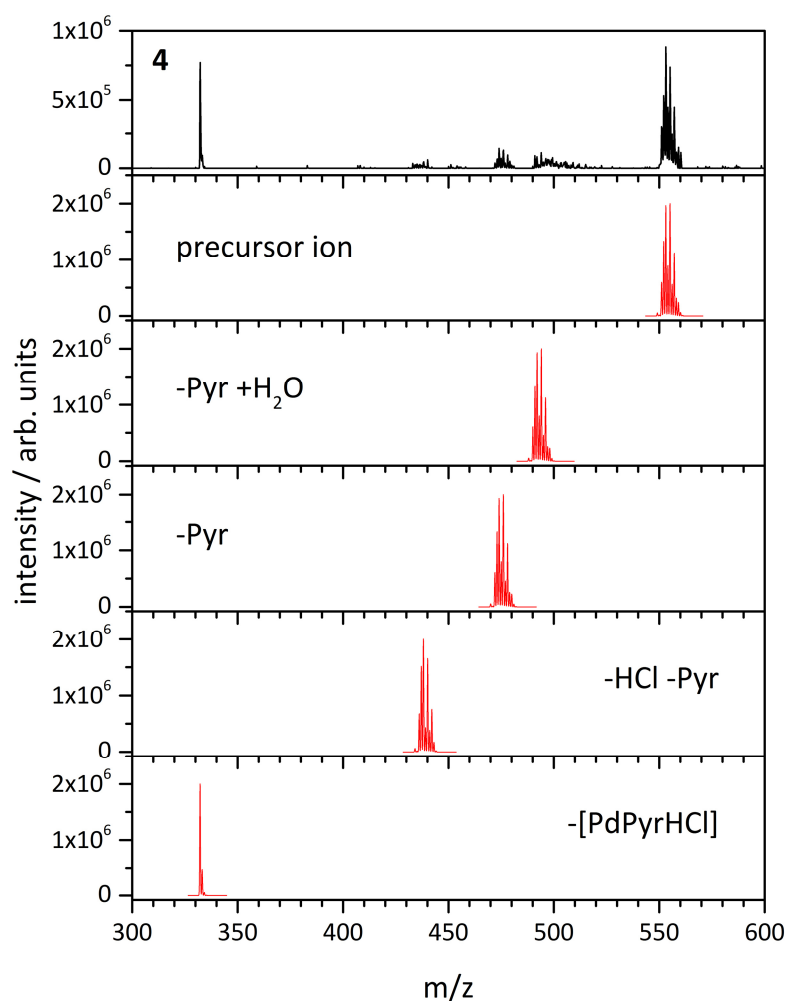


Figure S4: CID mass spectrum of the complex ion **4** (black curve) taken at $E_{COM} = 0.004$ a.u. and simulations of the isotopic pattern of the resulting fragment ions (red curves). The main fragmentation channels are the elimination of HCl, pyridine (Pyr), the concomitant loss of HCl and Pyr and the abstraction of a [PdPyrHCl] unit.

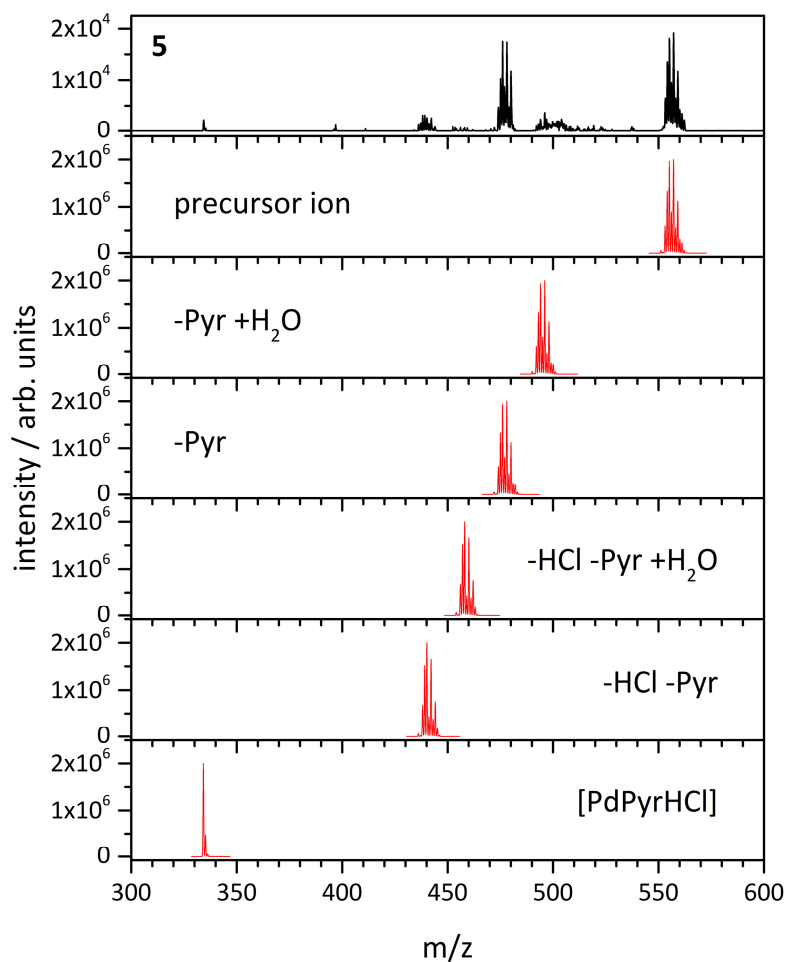


Figure S5: CID mass spectrum of the complex ion **5** (black curve) taken at $E_{COM} = 0.004$ a.u. and simulations of the isotopic pattern of the resulting fragment ions (red curves). The main fragmentation channels are the elimination of HCl, pyridine (Pyr), the concomitant loss of HCl and Pyr and the abstraction of a [PdPyrHCl] unit.

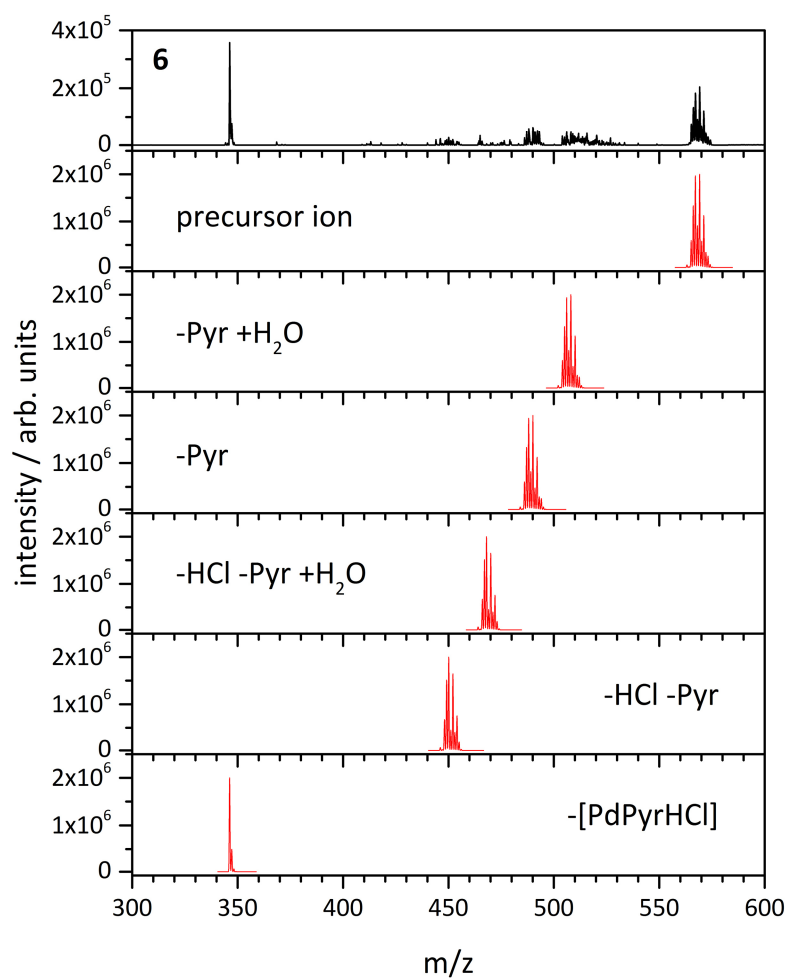


Figure S6: CID mass spectrum of the complex ion **6** (black curve) taken at $E_{COM} = 0.004$ a.u. and simulations of the isotopic pattern of the resulting fragment ions (red curves). The main fragmentation channels are the elimination of HCl, pyridine (Pyr), the concomitant loss of HCl and Pyr and the abstraction of a [PdPyrHCl] unit.

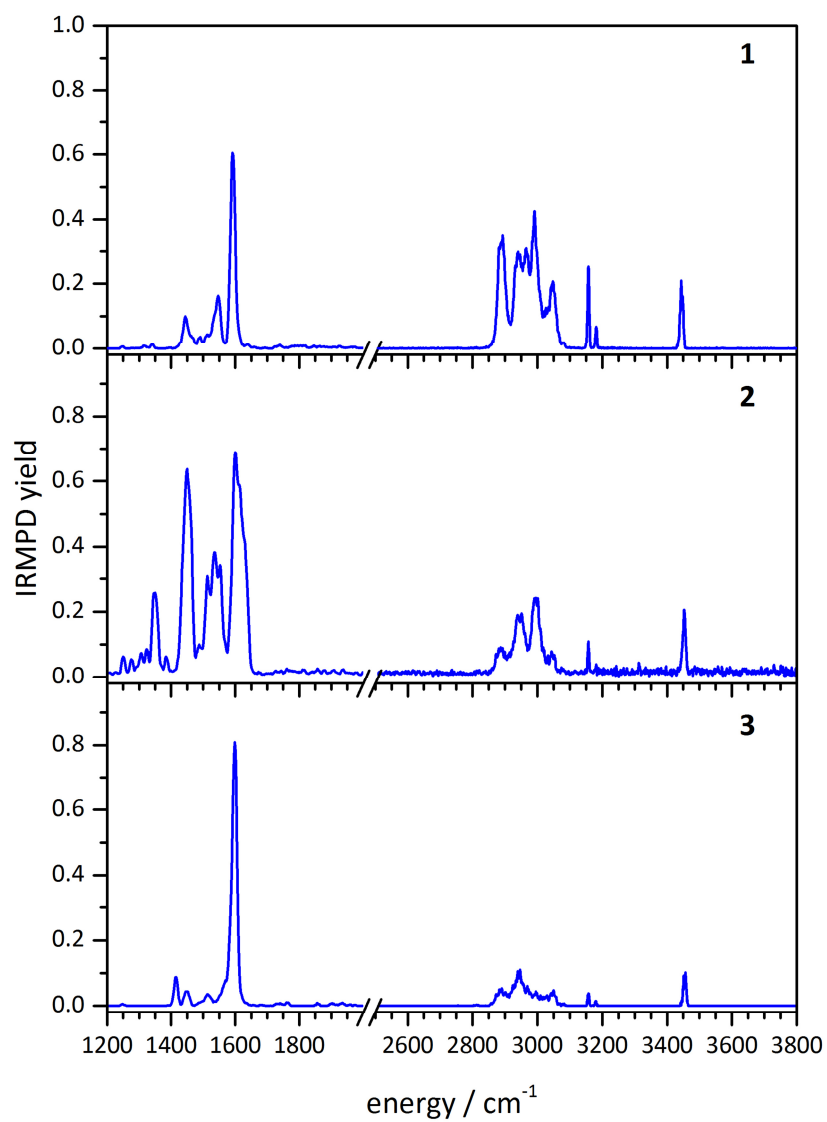


Figure S7: IRMPD spectra of the mass-selected precursor complexes **1**, **2** and **3**.

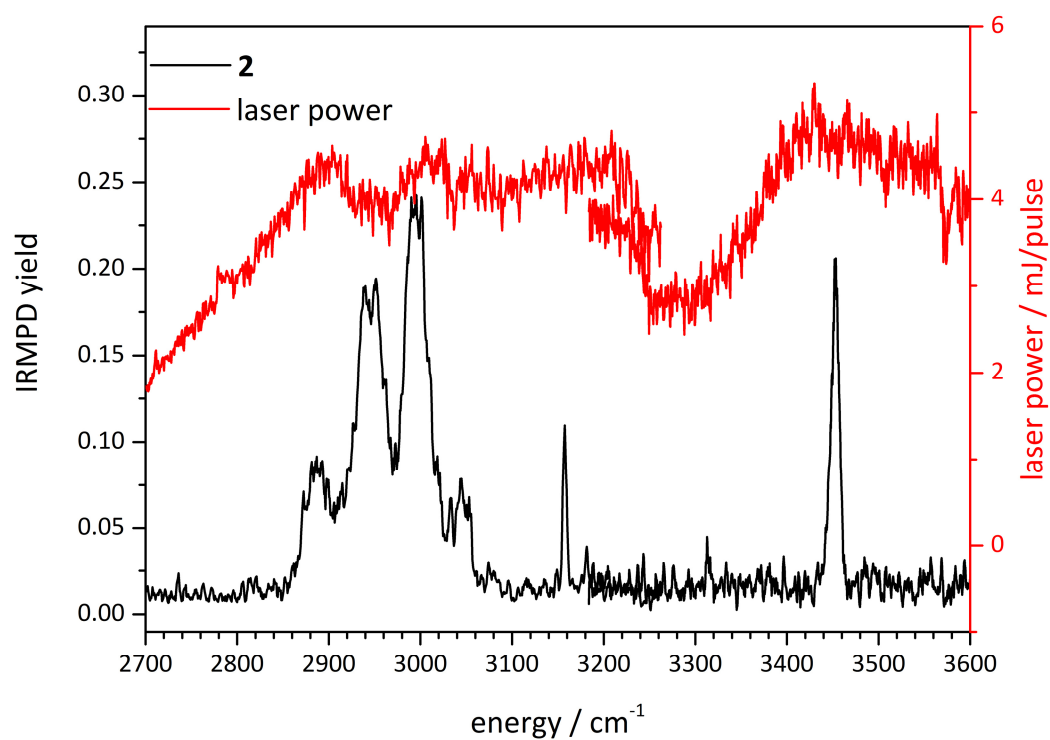


Figure S8: IRMPD spectrum of complex **2** and the laser power curve in the range of 2700-3600 cm⁻¹.

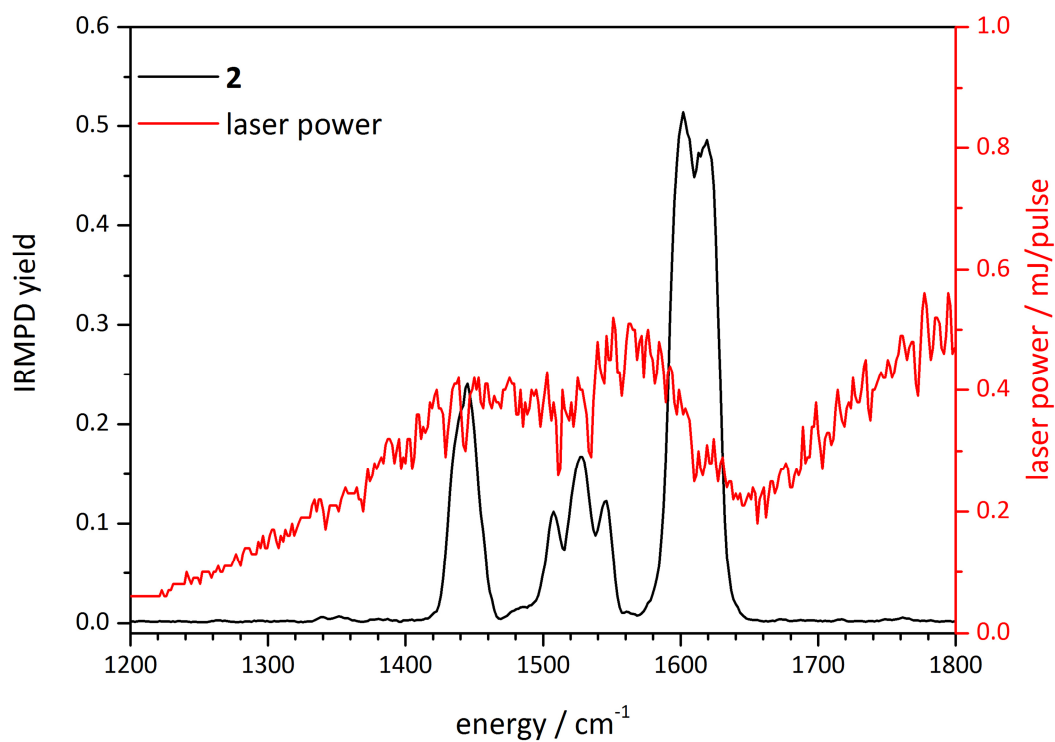


Figure S9: IRMPD spectrum of complex **2** and the laser power curve in the range of 1200-1800 cm⁻¹. Note that the trident shape of the band around 1535 cm⁻¹ originates from drops in the laser intensity.

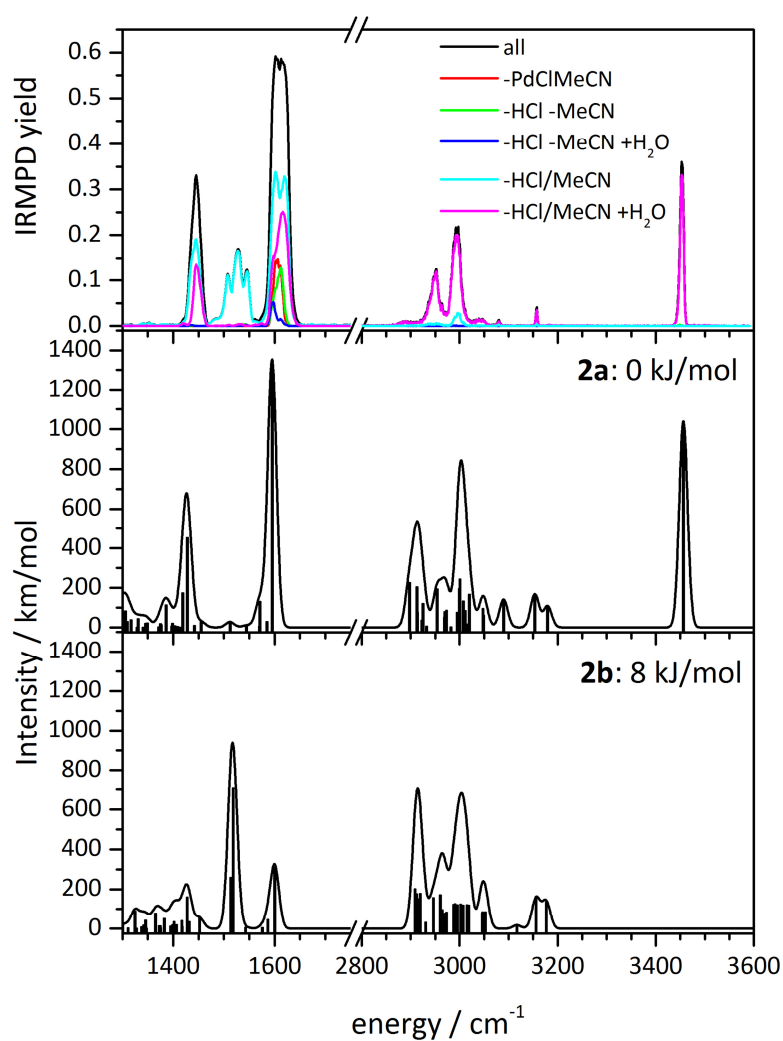


Figure S10: IRMPD spectrum of complex **2** including the fragment channels which are responsible for the observed bands (above) in comparison with the computed IR spectra of the isomers **2a** and **2b** (middle and bottom). The predicted IR spectra (level of theory B3LYP/cc-pVDZ, Stuttgart RSC for palladium) are scaled by a factor of 0.97. Note the isomer **2b** does not show water attachment.

5. The Influence of Side Groups on the Activation Barrier of $[\text{Cl}_3\text{Pd}(\text{MIP})\text{R}]^-$ Complexes: a CID, IRMPD and DFT Study

Maximilian Gaffga, Agnes Fizia, Werner R. Thiel and Gereon Niedner-Schatteburg

Fachbereich Chemie und Forschungszentrum OPTIMAS, Technische Universität

Kaiserslautern, 67663 Kaiserslautern, Germany

5.1 Preamble

The following chapter was prepared as a manuscript for publication. It is not submitted so far. All presented measurements, data evaluation, computations and all of the preparation of the manuscript itself were performed by myself. I received experimental support by Joachim Hewer, and I exchanged ideas with my colleagues Matthias Tombers and Johannes Lang. Gereon Niedner-Schatteburg helped by discussions. Agnes Fizia of the Thiels group synthesized the compounds.

5.2 Abstract

We present three Pd-MIP (mesityl-1H-imidazolyl-pyridine) complexes **1**, **2** and **3**, differing in the substituted side group. Collision-induced dissociation (CID) studies provide for appearance curves and exhibit the influence of the side group. CID appearance curves allow for the estimation of binding energies due to the correlation between the arbitrary fragmentation voltage and the appearance energies. In order to determine binding energies, we use benzylpyridinium ions to calibrate the arbitrary internal energy scale of the mass spectrometer. We consider the benzylium cation (direct bond cleavage) and the tropylium cation (arised from a rearrangement) as fragment ions and determine activation (E_{COM}^{50}) and appearance (AE) energies. The comparison of these energy values with computed Gibbs free dissociation energies shows a good correlation. The thus CID derived dissociation energies of the complex ions are reasonable and correspond to DFT derived Gibbs free energies. We varied the basis set and the DFT functional to achieve the best agreement. This procedure is a simple approach to determine precise dissociation energies of transition metal complexes. The IRMPD spectra in combination with DFT calculations allow for structure determination and give valuable information about the coordination sphere of the transition metal within the complex.

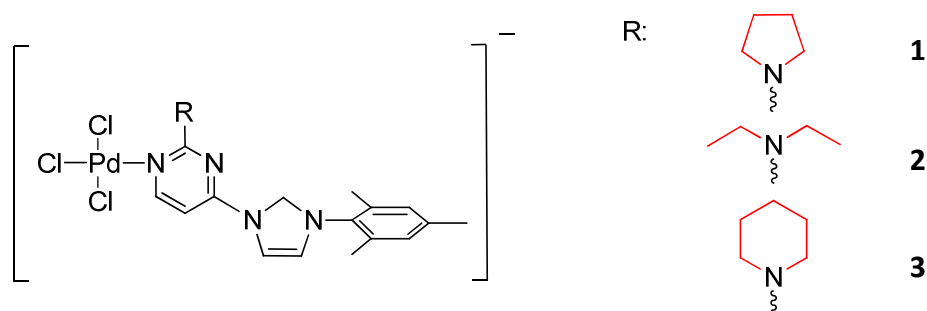
5.3 Introduction

Electrospray ionization mass spectrometry (ESI-MS) is widely used to characterize various transition metal complexes.^[1-4] In the case of ESI-MS, the internal energy of the parent ions may depend on the instrument parameter settings and experimental conditions. For many applications, such as structure determination, differentiation of isomers and MS/MS experiments, it is important to control the ion internal energy since mass spectra are affected by the internal energy deposition in ions.^[5-8]

Collision-induced dissociation experiments (CID) can provide accurate bond dissociation energies.^[9, 10] However, the conversion of the raw threshold dissociation energies from the lab frame (e.g. phenomenological appearance energies AE and activation energies E_{Lab})

into absolute bond energies is not trivial.^[11] The situation is even more complex, if ion trap mass spectrometers are used. RF-excitation of the ions affects the collisional activation of the stored ions. This excitation leads to multiple collisions of the ions with the helium buffer gas present in the trap. Hence, CID experiments are easy to perform in ion trap instruments, but their quantitative analysis and the determination of absolute dissociation energies is difficult. Generally, an internal energy scale of the mass spectrometer defines the dissociation energies.^[12, 13] Therefore, it is necessary to convert the internal energy scale of the mass spectrometer into absolute energy values.^[14]

To calibrate the internal energy scale of a mass spectrometer, substituted benzylpyridinium compounds were used due to (i) their simple fragmentation pattern and (ii) the direct bond cleavage was not accompanied by a significant reverse activation energy process.^[11, 15, 16] The fragmentation pattern of the benzylpyridinium compounds occurs as a direct bond cleavage of the C-N bond between the benzyl and pyridyl subunits and gives rise to neutral pyridine and a substituted benzylium cation.^[17] Depending on the substituents, *Zins et al.* suggested the rearrangement of benzylium cations into stable tropylium cations under ESI-MS conditions.^[11, 18-20] Neutral toluene under gas phase reactivity conditions can be used to examine the presence of benzylium, tropylium or both isomers during the fragmentation of benzylpyridinium compounds. Tropylium cations are unreactive towards toluene, while benzylium cations mediate a formal CH_2^+ .^[18]



Scheme 1: Molecular structure of the negatively charged Pd complexes **1**, **2** and **3**. The three derivatives differ in the functional group of the tertiary amine R (red).

Herein, we present three derivatives **1**, **2** and **3** of a novel Pd complex differing in their substituent R (Scheme 1). We use these complexes as model systems to test the thermometer ion approach determining bond dissociation energies.

This work is part of our ongoing research on the interaction of transition metal centers with organic ligand systems. Therefore, we use ESI-MS and CID studies to investigate the fragmentation behavior.^[21] We apply infrared multi photon dissociation (IRMPD) spectroscopy for the structural characterization of the Pd based complexes **1**, **2** and **3** in the gas phase.^[22, 23] Furthermore, we use the so called thermometer ions, considering benzylium and tropylium cations, to calibrate the internal energy scale of our mass spectrometer. This approach may serve to determine reasonable dissociation energies of these transition metal complexes.

5.4 Experimental setup and theoretical methods

5.4.1 Experimental setup

We recorded electrospray ionization mass spectra (ESI-MS) using two ion trap instruments (Bruker Esquire 6000 for CID studies and Bruker amaZonSL for IRMPD measurements). The scan speed was $13000 \frac{m}{z \cdot s}$ in normal resolution scan mode ($0.3 \text{ fwhm} / \frac{m}{z}$). The concentration of the sample solutions was approximately $1 \times 10^{-4} \text{ M}$ by using acetonitrile (MeCN) as solvent. We continuously injected the solutions into the ESI chamber at a flow rate of $2 \mu\text{l}/\text{min}$ by an automatic syringe pump. We used nitrogen as drying gas at a flow rate of 3.0 to $4.0 \text{ l}/\text{min}$ at $220 \text{ }^\circ\text{C}$ up to $300 \text{ }^\circ\text{C}$ and sprayed the solutions at a nebulizer gas pressure of 3 to 4 psi with the electrospray needle held at 4.5 kV. We held the transfer parameters to the Paul trap constant and we used helium as buffer gas inside the ion trap with a partial pressure of about $3 \times 10^{-3} \text{ mbar}$. BrukerEsquireControl 5.3 (Esquire) and BrukerTrapControl 7.0 (amaZonSL) software controlled the instrument. We carried out the data analysis using the Data Analysis 4.0 software.

Collision-induced dissociation (CID) appearance curves were recorded with varying excitation magnitudes from 0.0 to 1.5 V corresponding to the internal energy scale of the mass

spectrometer.^[21] Note that the well defined excitation amplitudes lead to *a priori* unknown excitation energies of the stored ions. The corresponding scaling factor varies by the very nature of the stored ions and it is subject of ongoing investigations. In the present case, we utilize a relative energy scale in the the lab frame (E_{LAB}^{rel}) in arbitrary units. These excitation energies were increased in a stepwise fashion until complete dissociation of the ion of interest was observed. Normalized relative and total fragmentation yields were calculated according to the following equations:

$$I_{i,norm}^{fr}(E_{LAB}^{rel}) = \frac{I_i^{fr}(E_{LAB}^{rel})}{\sum_i I_i^{fr}(E_{LAB}^{rel}) + \sum_i I_i^p(E_{LAB}^{rel})} \quad (1a)$$

$$I_{tot}^{fr}(E_{LAB}^{rel}) = \sum_i I_{i,norm}^{fr}(E_{LAB}^{rel}) \quad (1b)$$

For reasons of comparability we calculated center of mass transformed relative excitation energies (E_{COM}^{rel}) by:

$$E_{COM}^{rel} = \frac{m_{He}}{m_{He} + m_{ion}} \cdot E_{LAB}^{rel} \quad (2)$$

where m_{ion} indicates the isotopically averaged mass of the molecular cation under investigation.

Fragmentation amplitude dependent CID spectra were fitted by sigmoid fit functions of the type

$$I_{fit}^{fr}(E_{COM}^{rel}) = \frac{a_i}{(1 + e^{(E_{50} - E)B_i})} \quad (3)$$

$$I_{fit}^p(E_{COM}^{rel}) = \frac{a_i}{(1 + e^{-(E_{50} - E)B_i})} \quad (4)$$

using a least-squares criterion. Here, a_i denotes the branching ratio of the particular product ion ($\sum a_i = 1$), E_{50} is the voltage, at which the sigmoid function has reached half of its maximum, E is the fragmentation amplitude and B describes the slope of the sigmoid curve. Due to the correlation of fragmentation voltage and appearance energies, it is assumed that the breakdown curves allow for the estimation of binding energies of the different complex ions. The phenomenological appearance energy values (AE) are derived from a numerical linear extrapolation of the rise of the sigmoid fit function at E_{50} to the baseline. The line passes through $y = E_{50}$ and the corresponding abscissa value.^[24-27]

An optical parametric oscillator/amplifier (OPO/OPA, LaserVision) system pumped with a pulsed 10 Hz injection seeded Nd^{3+} :YAG laser (PL8000, Continuum) was used as a source of tunable IR radiation ($\delta\bar{\nu} = 0.9 \text{ cm}^{-1}$, $\delta t = 7 \text{ ns}$) for recording the vibrational spectra. Spectra within the frequency range of $2600 - 3700 \text{ cm}^{-1}$ were recorded by application of the OPA idler wave ($\leq 10 \text{ mJ}$ per pulse). Spectra within the range of $1200 - 2100 \text{ cm}^{-1}$ were recorded by difference frequency mixing (DFM) in a AgGaSe_2 crystal of the OPA signal and idler waves ($\leq 2 \text{ mJ}$ per pulse). The idler beam was focused by a 50 cm CaF_2 lens. The DF radiation was focused tighter by a 90° off-axis parabolic silver mirror with an effective focal length of 15 cm . The IR pulse energy was recorded by a power meter sensor that obtained the applied photon beam after exiting the ions inside the mass spectrometer through a second window. From the recorded fragment and parent ion intensities, we determine an IRMPD yield (Y) as:

$$Y = \frac{\sum_i I_i^{fr}}{\sum_i I_i^{fr} + \sum_i I_i^p} \quad (3)$$

The applied IR frequencies were calibrated by a wave meter (Bristol Instruments: 821 Pulsed Laser Wavelength Meter) to a theoretical accuracy of $\pm 0.02 \text{ cm}^{-1}$, which is beyond the spectral bandwidth of the utilized IR photon beams by more than an order of magnitude. Note that IRMPD yields scale in an intrinsically nonlinear way with the applied IR photon flux. Therefore, we refrained from any normalization.

5.4.2 Theoretical methods

We conducted electronic structure calculations at the $\text{B3LYP}^{[28-31]}/\text{cc-pVDZ}^{[32-34]}$ level of theory with the Stuttgart RSC 1997^[35, 36] effective core potential, representing the Pd atom as implemented in the Gaussian 09 program package.^[37] We performed full geometry relaxation of the most stable isomers found and for linear IR absorption spectra. The SCF density convergence criterion needed to relax to 10^{-8} . Harmonic vibrational frequencies were scaled by a linear lump-sum scaling factor of 0.97 as suggested elsewhere.^[38] We varied the basis set for H, C, N and Cl (cc-pVDZ, aug-cc-pVDZ, 6-31G, 6-31++G, 6-311G, 6-311G* and 6-311G++(3df,3pd))^[33, 39-45] as well as the DFT functionals (B3LYP, BLYP, B3P86 and B97D)^[28, 46-51] in order to guarantee comparability between the CID derived dissociation

energies and computed dissociation energies. All computed energy values are zero-point corrected.

5.5 Results and discussion

5.5.1 Mass spectrometric analysis and identification

The main peaks of the ESI mass spectra obtained from acetonitrile solution, at concentrations of approximately 1×10^{-4} M, are located at $\frac{m}{z} = 548$, $\frac{m}{z} = 550$, and $\frac{m}{z} = 562$ (most abundant mass peaks) in the negative ion mode. These peaks corresponds to the molecular peaks of the negative charged Pd complexes **1** ($\text{Cl}_3\text{Pd}(\text{C}_{16}\text{H}_{17}\text{N}_4)\text{C}_4\text{H}_8\text{N})^-$, **2** ($\text{Cl}_3\text{Pd}(\text{C}_{16}\text{H}_{17}\text{N}_4)\text{C}_4\text{H}_{10}\text{N})^-$, and **3** ($\text{Cl}_3\text{Pd}(\text{C}_{16}\text{H}_{17}\text{N}_4)\text{C}_5\text{H}_{10}\text{N})^-$, respectively (Fig. S1 in the supporting information). The elemental composition is unequivocally assigned by their isotopic intensity patterns (insets Fig. S1 in the supporting information).

Upon collisional activation all three complexes **1**, **2** and **3** exhibit a mass loss of $\frac{m}{z} = 37$, which corresponds to an elimination of HCl confirmed by simulations of their isotopic pattern (Fig. S1 in the supporting information).

5.5.2 IRMPD spectroscopy and structure determination

We measured IRMPD spectra of the three Pd complexes **1**, **2** and **3** (Fig. 1). The direct comparison of the spectra shows similar band features. Since the change in the side group is given by an additional CH_2 group, the observation is not surprising. The spectra reveal several bands in the region from 2800 to 3100 cm^{-1} , a strong and broad absorption at 1580 cm^{-1} and also several bands between 1350 and 1500 cm^{-1} . All three complexes exhibit a splitting of the band at 1580 cm^{-1} . One would expect to see aliphatic and aromatic CH stretching vibrations in the region from 2800 to 3100 cm^{-1} . Around 1580 cm^{-1} one would

expect C=C ring modes and C-N stretching vibrations. Between 1350 and 1500 cm^{-1} one would expect to see C-C stretching and C-H bending modes.

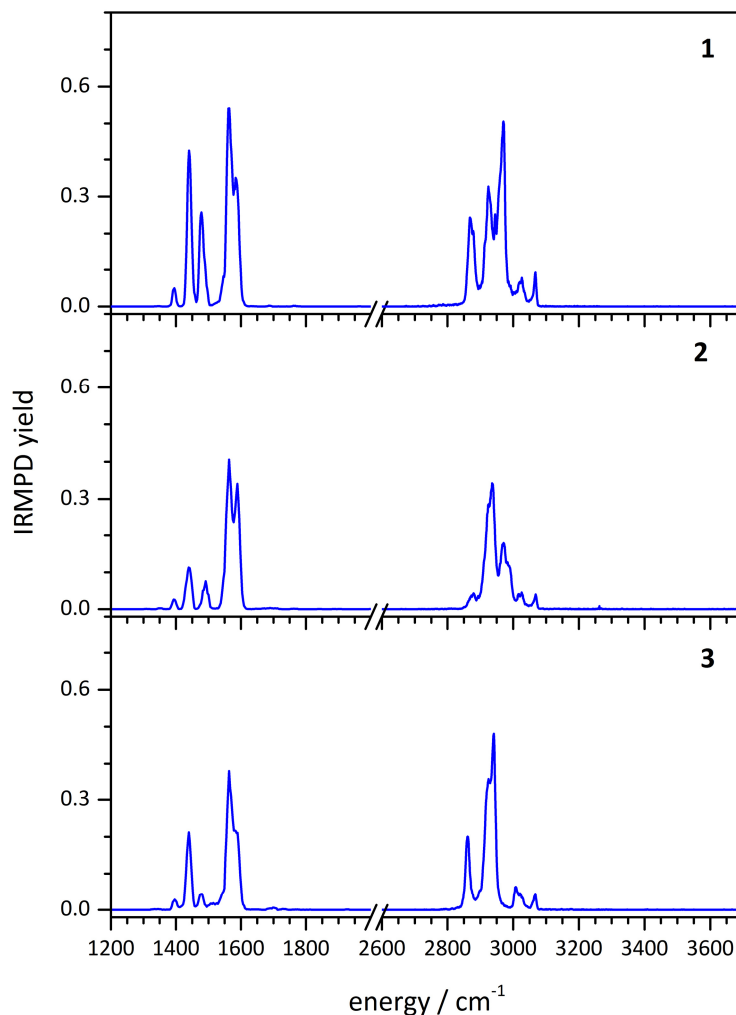


Figure 1: IRMPD spectra of the mass-selected Pd complexes **1**, **2** and **3**.

We present the four most stable isomers found ($< 100\text{ kJ/mol}$, with respect to the most stable isomer) of each complex **1**, **2** and **3** and computed their linear absorption spectra (Fig. 2 – Fig. 4). All found isomers of the complexes **1**, **2** and **3** reveal a square planar binding motif for the Pd cation. The Pd coordinates to one of the nitrogen atoms of the pyrimidine ring and to the three chlorido ligands. The main difference in the isomers structures is the orientation of the pyrimidine ring and the imidazole ring, resulting from a torsion around the

C-N bond. The comparison of the measured IRMPD spectra with computed IR absorption spectra allows for structure determination.

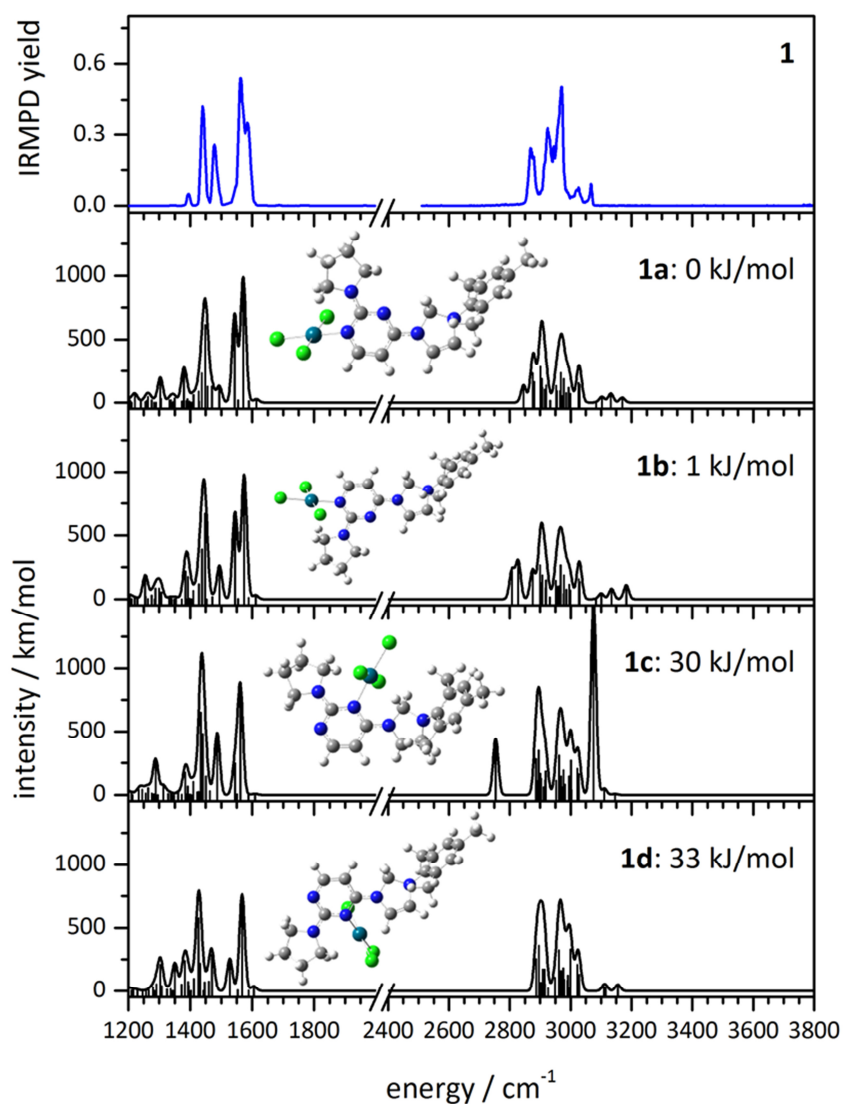


Figure 2: IRMPD spectrum of **1** and computed linear IR absorption spectra (level of theory: B3LYP/cc-pVDZ, Stuttgart RSC for Pd, scaled by 0.97) including the computed structures of the four most stable isomers **1a–1d**. For a better visualization, the frequency intensities between 2800 and 3200 cm⁻¹ are multiplied by a factor of 10. The stick spectra are folded with a Gaussian function (fwhm = 10 cm⁻¹).

All major peaks of the presented IRMPD spectrum of complex **1** are in a good agreement with the computed spectra of all isomers, except for isomer **1c** (Fig. 2). The spectrum of isomer **1c** exhibits two strong additional bands at 2750 and 3080 cm^{-1} , which result from a close proximity of the chlorido ligands to the adjacent CH_2 group of the imidazole ring. These spectral features are not observed in the experimental IRMPD spectrum. Due to this fact and the high relative energies of isomer **1c** and **1d** (~ 30 kJ/mol), these two isomers can be excluded. The spectrum of isomer **1b** reveals a strong absorption at 2820 cm^{-1} , which is not visible in the IRMPD spectrum. Thus, isomer **1b** is less likely and we conclude that the IRMPD spectrum most likely results from isomers **1a**. More definite conclusions would need to rely on a determination of a torsional barrier height. The two strong and energetically close calculated vibrations at 1545 and 1570 cm^{-1} explain the splitting of the observed band at 1580 cm^{-1} . The seeming shift of these calculated bands to smaller energy values originate from the application of a uniform scaling factor.

The spectrum of the isomer **2a** is in a good agreement with the measured IRMPD spectrum (Fig. 3). The isomers **2c** and **2d** can be excluded due to the higher relative energy (25-30 kJ/mol). Also here isomer **2c** reveals two strong additional bands at 2780 and 3100 cm^{-1} . These bands are CH stretching modes of the CH_2 group of the ethyl functional group influenced by the adjacent chlorido ligands. Isomer **2b** can also be excluded due to the strong absorption at 2820 cm^{-1} , which is not present in the experimental IRMPD spectrum. Again, the splitting of the band at 1580 cm^{-1} is well reproduced by the two strong absorptions at 1540 and 1570 cm^{-1} of isomer **2a**. Therefore, we again ascribe our experimental IRMPD spectrum to the computed isomer with the lowest relative energy (**2a**).

The findings are much like the findings of complex **1** and complex **2** (Fig. 4). Again, the isomers **3c** and **3d** can be excluded due to higher energy purposes (~ 38 kJ/mol). The IRMPD spectrum is much in line with the computed spectrum of the isomers **3a** and **3b**. The IR spectra of the isomers **3a** and **3b** are quite similar and therefore, isomer **3b** cannot be excluded. We conclude that the experimental IRMPD spectrum originates from the isomer **3a** and **3b**.

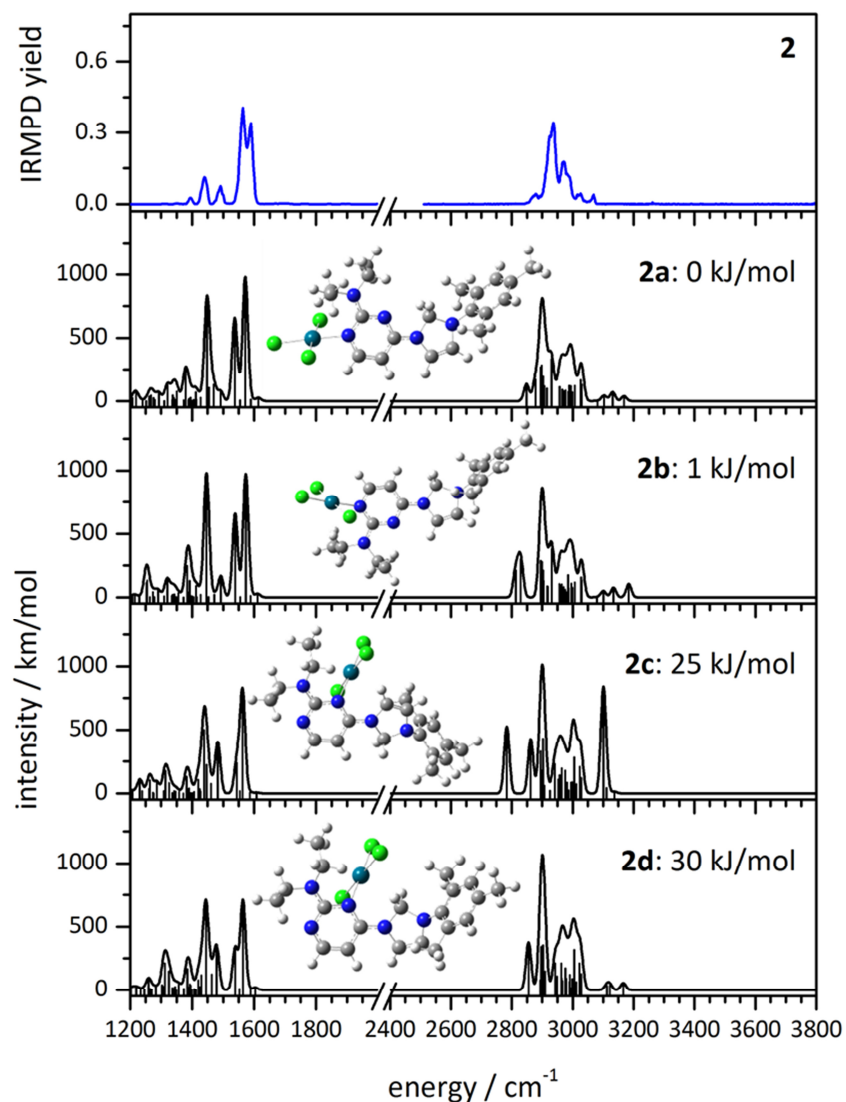


Figure 3: IRMPD spectrum of **2** and computed linear IR absorption spectra (level of theory: B3LYP/cc-pVDZ, Stuttgart RSC for Pd, scaled by 0.97) including the computed structures of the four most stable isomers **2a–2d**. For a better visualization, the frequency intensities between 2800 and 3200 cm^{-1} are multiplied by a factor of 10. The stick spectra are folded with a Gaussian function (fwhm = 10 cm^{-1}).

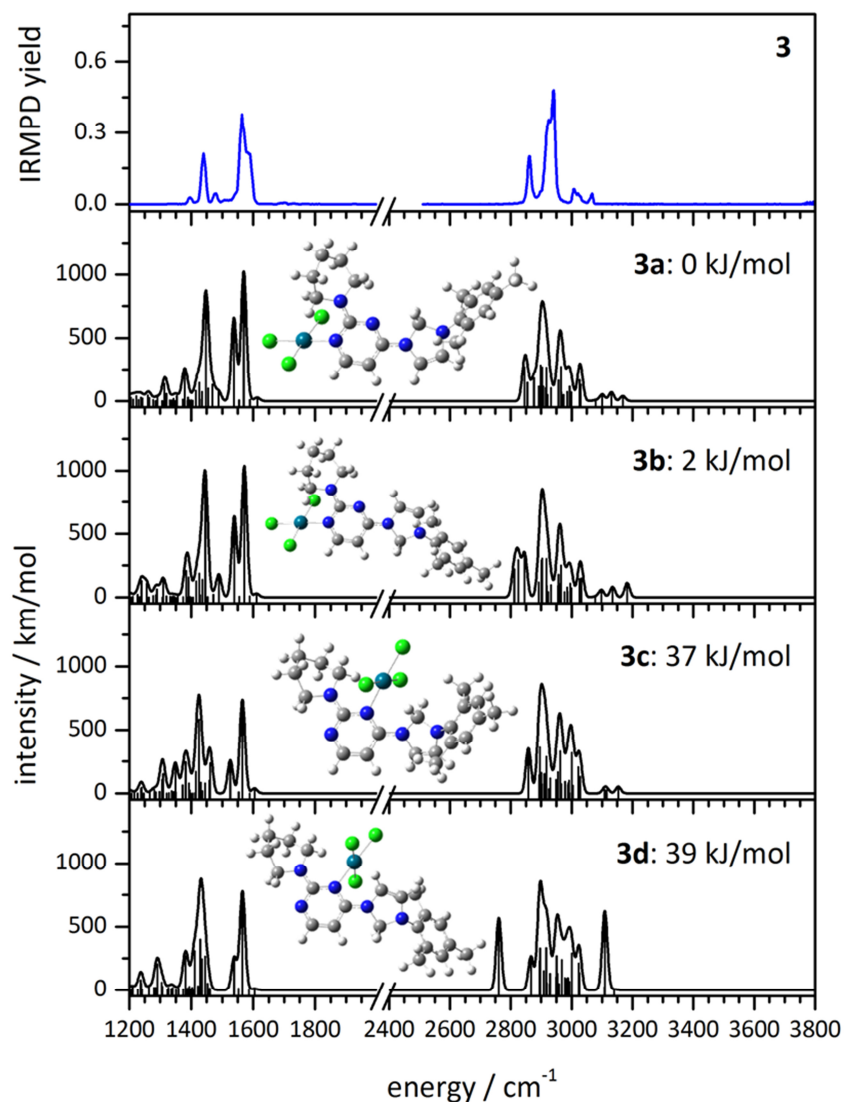


Figure 4: IRMPD spectrum of **3** and computed linear IR absorption spectra (level of theory: B3LYP/cc-pVDZ, Stuttgart RSC for Pd, scaled by 0.97) including the computed structures of the four most stable isomers **3a–3d**. For a better visualization, the frequency intensities between 2800 and 3200 cm^{-1} are multiplied by a factor of 10. The stick spectra are folded with a Gaussian function (fwhm = 10 cm^{-1}).

5.5.3 Energy dependent collisional-induced dissociation (CID) studies

During the collision-induced dissociation process, an additional DC potential accelerates the trapped ions. Due to this acceleration, the ions undergo collisions with the helium buffer gas. The collisions lead to a transfer of kinetic energy to internal degrees of freedom of the ions. If the ions have stored a sufficient amount of energy, dissociation can occur. Depending on the nature of the investigated ion and on the height of the dissociation barrier, the loss of stable neutral molecules (H_2O , NH_3 or CO_2), larger molecules and ionic fragments of the precursor molecule can be observed. By varying the excitation magnitude, CID appearance curves can be recorded.

Collision-induced dissociation studies of electrosprayed complexes in combination with quantum mechanical calculations may provide access to binding energies. It is a pressing issue to gauge the relative CID energy scale for absolute values.

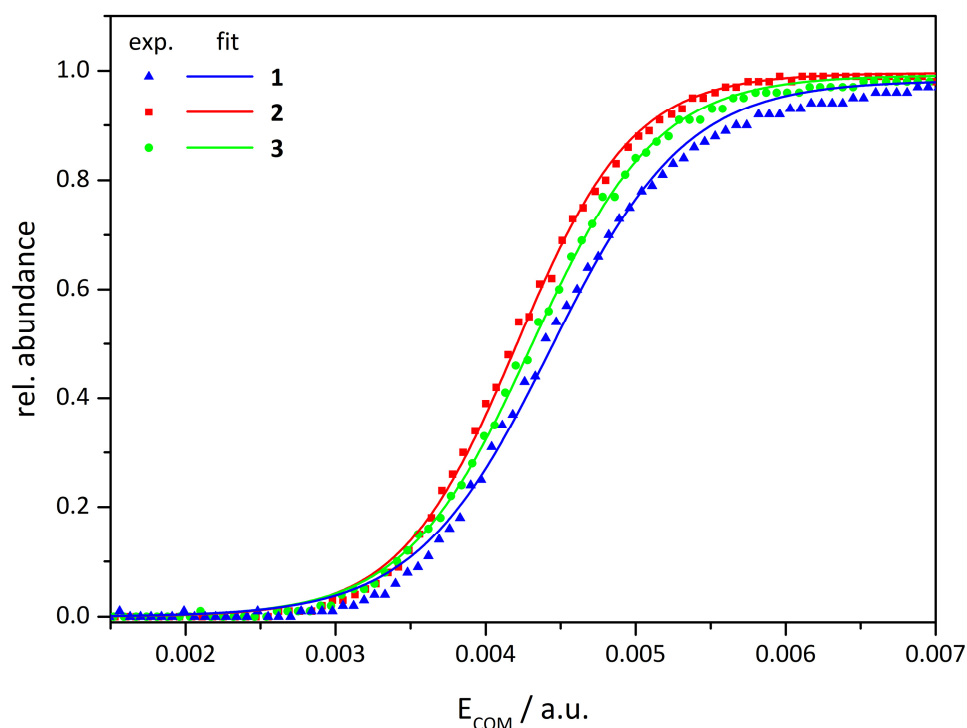
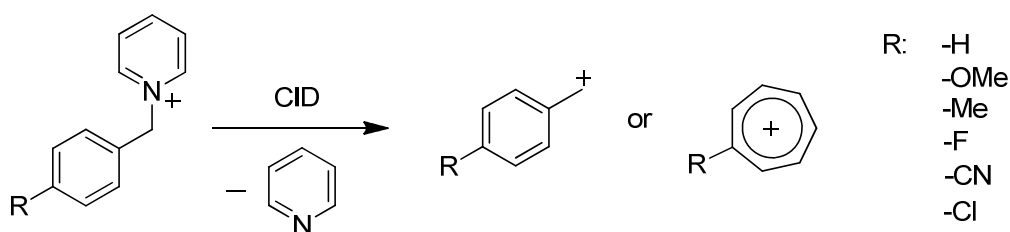


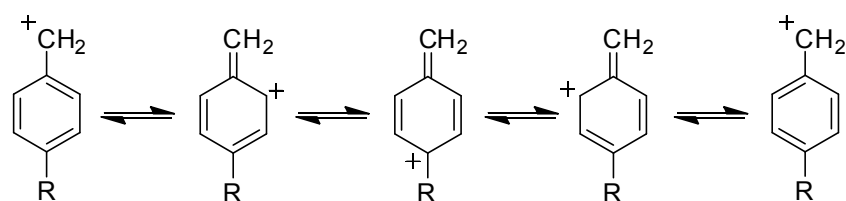
Figure 5: CID appearance curves of the mass-selected complexes **1** (red), **2** (green) and **3** (blue) in the center of mass frame. The dots represent the experimental data, the lines are sigmoid fit functions.

The gradual increase of the collisional activation energy E_{COM} provides CID appearance curves (Fig. 5). These appearance curves of the mass-selected complexes **1**, **2** and **3** show the influence of the side group R on the fragmentation threshold and thereby on the binding energy. For reasons of comparability, we use the center of mass frame.^[5] The observed fragmentation channel is the elimination of HCl (cf. Fig. S1 in the supporting information). Thus, the CID activation energy correlates with the binding energy of HCl. The complexes differ slightly in their fragmentation energies. Complex **2** exhibits the lowest energy needed to eliminate HCl, followed by complex **3** and **1**. The curve of complex **1** exhibits a shallower slope and the sigmoid function does not fit the experimental data points as good as in the cases of complex **2** and **3**. This may be an evidence of passing through a tighter transition state. However, the complexes **2** and **3** reveal a steeper slope than complex **1**.



Scheme 2: Molecular structure of the benzylpyridinium cations, so called “thermometer ions”, with different substituents in the para position of the benzene ring. Collisional activation of the thermometer cations delivers a benzylum cation or after rearrangement a tropylium cation.

Substituted benzylpyridinium cations, so called “thermometer ions”, can be used to calibrate the arbitrary fragmentation amplitude scale of the mass spectrometer towards absolute fragmentation energies. Upon collisional activation, the thermometer ions exhibit a direct C-N bond cleavage and the loss of neutral pyridine is observed (Scheme 2). Two product ions have to be taken into account (i) the benzylum cation as the product of the direct bond cleavage and (ii) the tropylium cation formed via rearrangement. The substitutions R influence the stability of the product ions and also the dissociation energies of the precursor ions.



Scheme 3: Resonance structures to describe the delocalized positive charge within the benzylium cation.

The benzylium cation is stabilized by mesomerism (Scheme 3). However, the rearrangement of the benzylium cation leads to the formation of a tropylium cation, which is also an aromatic species.

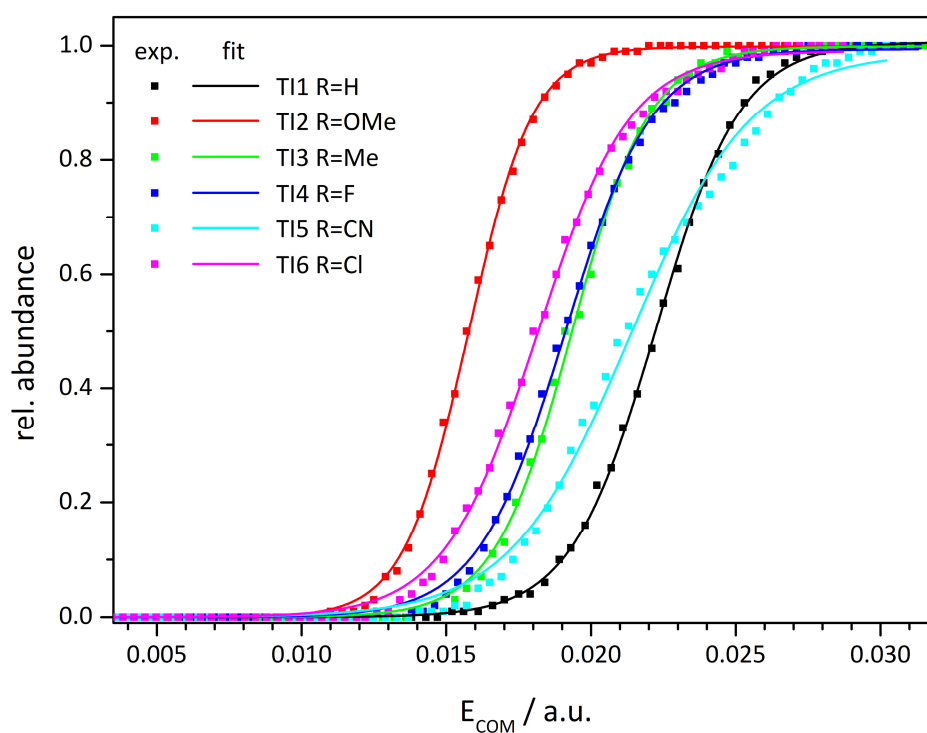


Figure 6: Center of mass transformed fragmentation amplitudes of CID appearance curves of the investigated thermometer ions. The dots represent the experimental data, the lines are sigmoid fit functions.

For the estimation of binding energies, we measured the CID appearance curves of the six thermometer ions **TI1-TI6**. The dots represent the experimental data and the lines are sigmoid fit functions. It shows that the different substitutions influence the dissociation energy of the ions considerably (Fig. 6). The thermometer ion **TI2** exhibit the weakest C-N bond energy followed by **TI6**, **TI4** and **TI3**, **TI5** and **TI1** with the strongest bond energy. Additionally, the curve of **TI5** reveals a shallower slope of the sigmoid fit function than the **TI**'s. This may be an evidence for a tighter transition state, while a steeper rise of the sigmoid fit function indicates a loose entropically favored transition state. This might lead to a kinetic shift in the appearance energy obtained by CID and consequently to an overestimation of the dissociation energy.

Table 1: Computed Gibbs free energies of the dissociation reaction of the thermometer ions at B3LYP/cc-pVTZ level of theory. Both product ions, the benzylium cation and the tropylium cation, are considered.

| substance | R | $\Delta G_{\text{Benzylium}} / \text{kJ/mol}$ | $\Delta G_{\text{Tropylium}} / \text{kJ/mol}$ |
|------------|-----|---|---|
| TI1 | H | 150 | 115 |
| TI2 | OMe | 89 | 84 |
| TI3 | Me | 130 | 109 |
| TI4 | F | 139 | 116 |
| TI5 | CN | 171 | 148 |
| TI6 | Cl | 137 | 120 |

Furthermore, we computed Gibbs free energies of the C-N bond cleavage considering the benzylium cation ($\Delta G_{\text{Benzylium}}$) and the formation of the tropylium cation ($\Delta G_{\text{Tropylium}}$) after rearrangement (Table 1). The direct comparison of the computed $\Delta G_{\text{Benzylium}}$ and $\Delta G_{\text{Tropylium}}$ values reveal a different order in the dissociation energy. On the one hand the order of $\Delta G_{\text{Benzylium}}$ is **TI2 < TI3 < TI6 < TI4 < TI1 < TI5** and on the other hand $\Delta G_{\text{Tropylium}}$ exhibit **TI2 < TI3 < TI4 < TI1 < TI6 < TI5**. The relative order of the computed dissociation energy values of $\Delta G_{\text{Benzylium}}$ and of $\Delta G_{\text{Tropylium}}$ are different from the relative order of the CID thresholds (**TI2 < TI6 < TI4 < TI3 < TI5 < TI1**). This may result from additional stabilizing effects like mesomerism or inductive

effects. Also, we have to admit that transition state entropies and enthalpies and thus ΔG^\ddagger may vary by substituent in deviation from the asymptotic values ΔG .

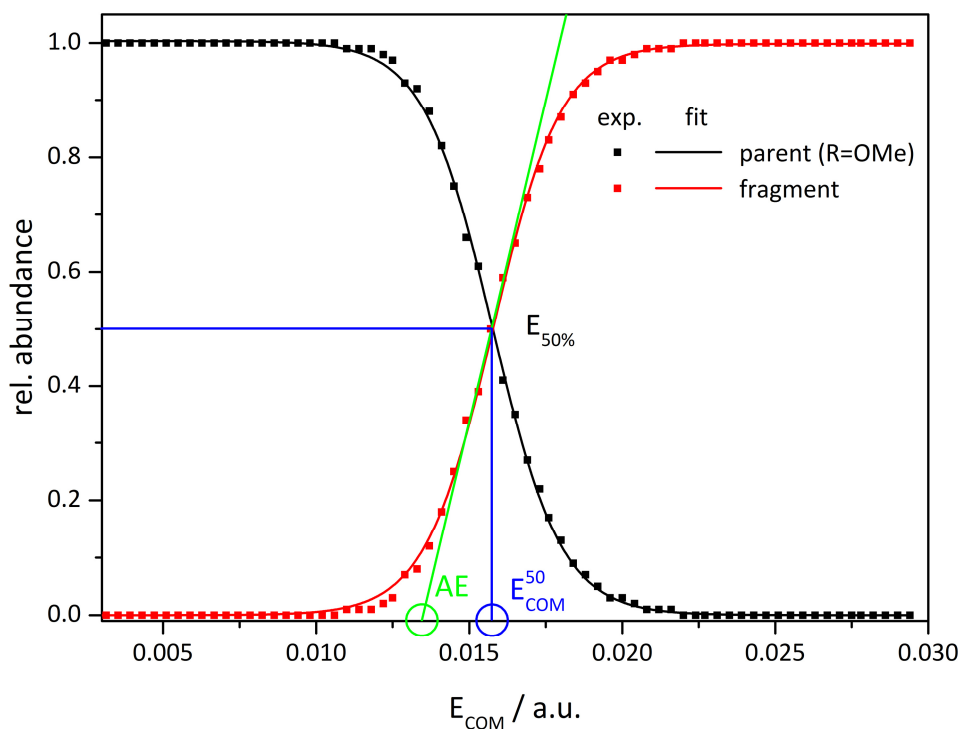


Figure 7: Breakdown diagram of **TI2** ($\text{R}=\text{OMe}$) as a function of the center of mass corrected fragmentation amplitude E_{COM} . The dots represent the experimental data, the black and red lines are sigmoid fit functions used for analysis. The green line was derived from the slope of the sigmoid fit function at E_{COM}^{50} . Positions of the E_{COM}^{50} (blue) and AE (green) values are marked with circles.

Sigmoid fitting of the experimental data points allows for a determination of the phenomenological E_{COM}^{50} values (Fig. 7, blue circle). Furthermore, we derive appearance energies (AE) by linear extrapolation using the slope B of the sigmoid fit function at the E_{COM}^{50} value to the baseline (Fig. 7, green circle). The line passes through $y = E_{50}$ and the corresponding abscissa value.

As shown by *Schroeder et al.*, the phenomenological AE values should deliver better results than the E_{COM}^{50} values.^[11] The consideration of the AE values reduces the influence of kinetic effects on the derivation of the underlying intrinsic thermochemistry. Specifically for a

simple bond cleavage, the rise of the fragment ion from their threshold is determined by the density of states of the precursor ion, which is a size effect. Larger ions should dissociate more slowly thus the resulting CID appearance curve is flatter. Therefore, the E_{COM}^{50} values are shifted to larger values. In the determination of the AE values, the extrapolation to the baseline does not eliminate but lowers the effect of the slope on the energy values derived from E_{COM}^{50} .^[11]

Table 2: Obtained slopes B , E_{COM}^{50} and AE values from modeling the CID appearance curves of the mass-selected thermometer ions **T11-T16** using sigmoid fit functions and linear extrapolations.

| Substance | R | Slope B | E_{COM}^{50} / a.u. | AE / a.u. |
|------------|-----|--------------|------------------------------|-------------|
| T11 | H | 681 ± 6 | 0.0222 | 0.0192 |
| T12 | OMe | 898 ± 9 | 0.0157 | 0.0135 |
| T13 | Me | 746 ± 10 | 0.0193 | 0.0166 |
| T14 | F | 665 ± 9 | 0.0191 | 0.0161 |
| T15 | CN | 482 ± 12 | 0.0214 | 0.0173 |
| T16 | Cl | 623 ± 9 | 0.0182 | 0.0150 |

Table 2 summarizes the characteristic parameters, i.e. the slope B , the E_{COM}^{50} and AE values of the sigmoid fit functions and the linear extrapolations. These values can be correlated to the amount of energy that has to be transferred to an ion during the CID process to get access to the fragmentation channel.

In case of the benzylium cation as product ion, we plotted the DFT derived ΔG_{Benzyl} values in dependence of the experimental E_{COM}^{50} (Fig. 8a, black squares) and AE values (Fig. 8b, black triangles). Both approaches exhibit a linear relationship between the experimental values and theoretical bond energies. We consider three different linear regressions to fit the data points (i) linear fit that crosses the origin^[11] (green line), (ii) linear fit with a free intercept (blue line) and (iii) linear fit with a fixed intercept of 2.7 kJ/mol (black line). The idea of the fixed intercept originates from the assumption, that the temperature of the ion trap within our mass spectrometer and the stored ions resemble each other. The temperature of the ion trap is about 323 K and this corresponds to 2.7 kJ/mol of internal energy of the ions. Due to

the trapping and isolation within the ion trap, we assume that the ions stored a corresponding amount of energy.

However, the linear regression factors of the linear extrapolations are relatively poor (cf. Table S1 in the supporting information). In comparison, the correlation between the experimental and theoretical E_{COM}^{50} values is significantly better than the correlation between the AE values. Unfortunately, these findings do not agree with our assumption that the AE values should deliver better dissociation energy values due to the reduced influence of kinetic effects. Since the linear extrapolations are such defective, the determination of binding energies, i.e. the elimination of HCl, may be under- or overestimated.

Furthermore, we plotted the DFT derived $\Delta G_{\text{Tropylium}}$ values in dependence of the experimental E_{COM}^{50} (Fig. 9a, red squares) and AE values (Fig. 9b, red triangles) for tropylium cation as product ion again. Both approaches exhibit a linear relationship between the experimental values and theoretical bond energies and we consider three different linear regressions to fit the data points (i) linear fit that crosses the origin (green line), (ii) linear fit with a free intercept (blue line) and (iii) linear fit with a fixed intercept of 2.7 kJ/mol (black line). Similar results are obtained compared to the benzylium cation case. The linear regression factors are relatively poor and the use of the E_{COM}^{50} values delivers better results than the use of the AE values.

In summary, the benzylium cation approach delivers more reasonable results than the tropylium cation approach. The linear regression factors are quite better using the E_{COM}^{50} values than the AE values. Hence, we adopt the benzylium cation approach, using the linear extrapolation (intercept=2.7 kJ/mol) to fit the E_{COM}^{50} values. In order to estimate the binding energy needed to eliminate HCl, the projection to the dissociation energy scale of the experimental E_{COM}^{50} (red lines) derived from CID measurements of the complexes **1**, **2** and **3** are used (Fig. 8a). We suppose that the results of the benzylium cation case should lead to results, which are more precise than in the case of the tropylium cation and therefore, we neglect the tropylium cation case.

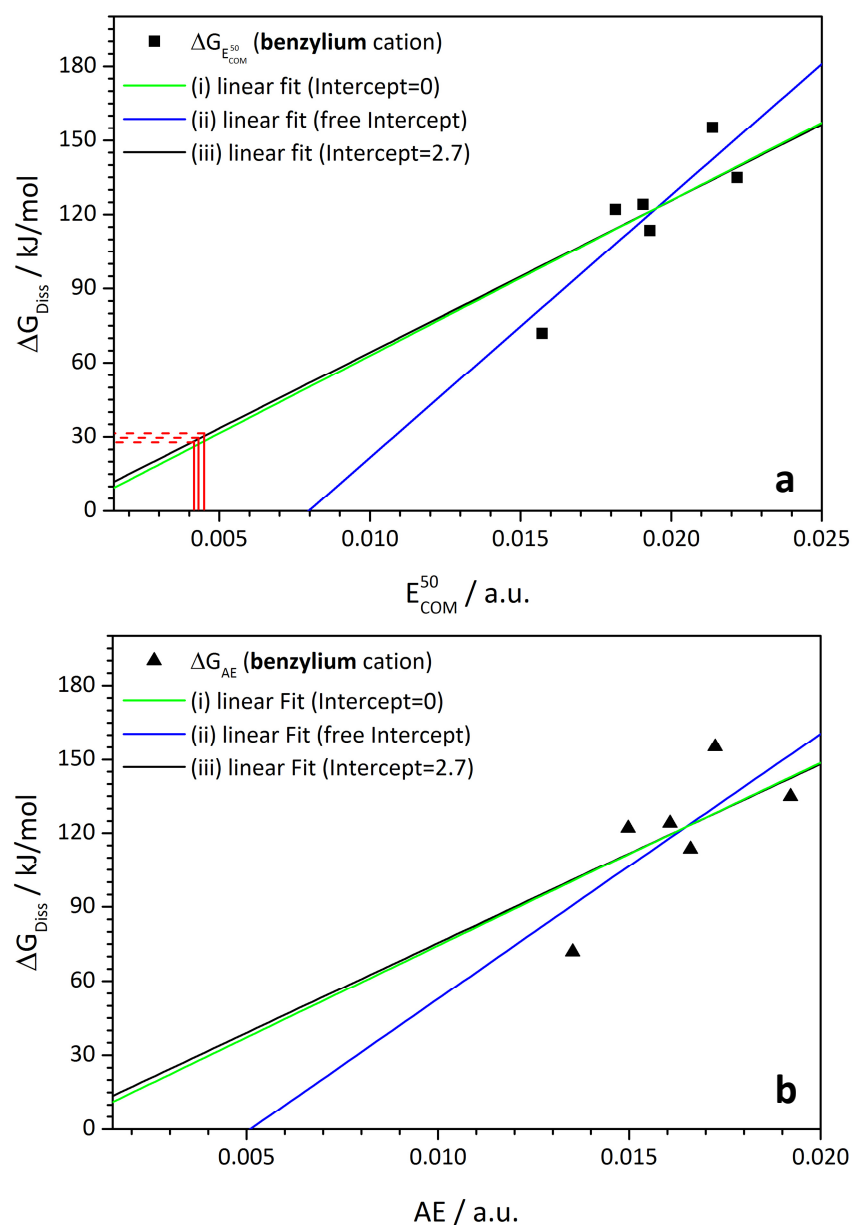


Figure 8: Computed Gibbs free energies derived from DFT calculations for the dissociation of thermometer ions in the case of benzylum cation in dependence of the center of mass (COM) transformed E_{COM}^{50} values (upper graph a, black squares) and in dependence of AE values (lower graph b, black triangles) obtained from CID experiments. The lines (black, blue and green) result from linear fit functions. Measured E_{COM}^{50} values of the complexes **1**, **2** and **3** (solid lines) and their projection to the dissociation energy scale (dashed lines) are shown in red.

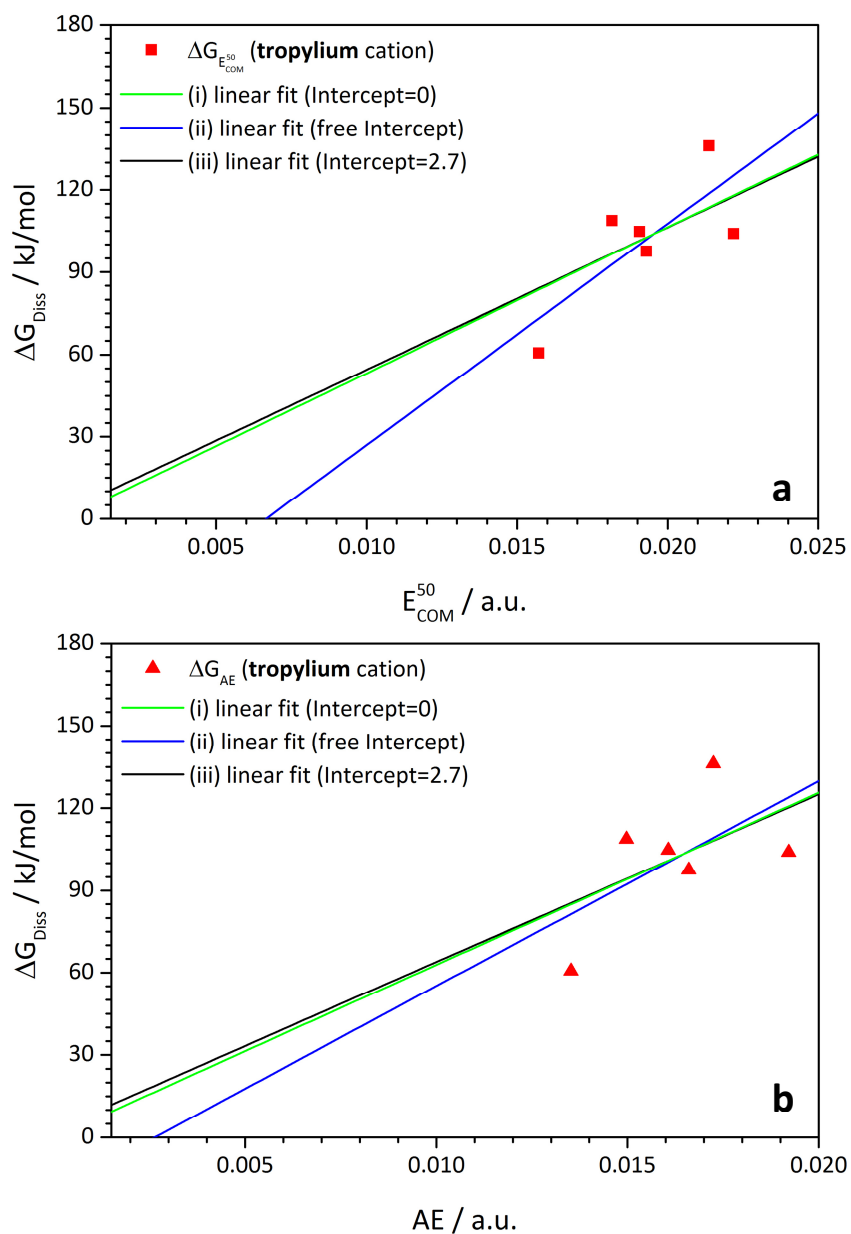


Figure 9: Computed Gibbs free energies derived from DFT calculations for the dissociation of thermometer ions in the case of tropylium cation in dependence of the center of mass (COM) transformed E_{COM}^{50} values (upper graph a, red squares) and in dependence of AE values (lower graph b, red triangles) obtained from CID experiments. The lines (black, blue and green) result from linear fit functions.

The received dissociation energies ΔE_{exp} , obtained by the use of E_{COM}^{50} values, are summarized in Table 3.

Table 3: Experimental E_{COM}^{50} values, AE values and derived dissociation energies of the complexes **1**, **2** and **3** considering the linear extrapolation with an intercept of 2.7 kJ/mol.

| complex | E_{COM}^{50} /a.u. | AE / a.u. | ΔE_{exp} / kJ/mol |
|----------|-----------------------------|-------------|-------------------------------------|
| 1 | 0.0044 | 0.0036 | 33.3 |
| 2 | 0.0042 | 0.0032 | 28.4 |
| 3 | 0.0043 | 0.0035 | 29.9 |

The obtained dissociation energies ΔE_{exp} exhibit that complex **2** needs the lowest energy (28.4 kJ/mol) to eliminate HCl, followed by complex **3** (29.9 kJ/mol). Complex **1** needs the most energy for the abstraction of HCl (33.3 kJ/mol).

Furthermore, we calculated Gibbs free energies ΔG_{Calc} for the dissociation of HCl with different basis sets and plotted them in dependence of the dissociation energies ΔE_{Exp} derived from the CID measurements (Fig. 10). The formation of HCl is the first step in order to eliminate it. DFT computations show that the hydrogen atom needed for the formation of HCl originates from the CH_2 group next to the tertiary amine of the substituted side group. The remaining CH^- group forms a Pd-C bond to guarantee the square planar binding motif of the Pd cation (cf. Scheme S1).

The estimated dissociation energies ΔE_{exp} correspond to the computed Gibbs free energy values. The DFT computations predict complex **2** to be the most unstable complex, followed by complex **3** and complex **1**. These findings are in a good agreement with the findings of the CID measurements. The Gibbs free energy values of the cc-pVDZ basis set in combination with the B3LYP functional comply best with the experimental results. We varied the basis sets and find that the four Pople basis sets, i. e. 6-31G, 6-31++G, 6-311G and 6-311G* overestimate the binding energy of HCl. While the aug-cc-pVDZ and the 6-311++G(3df/3pd) basis sets underestimate the binding energy of HCl. Variation of the DFT functional using a

fixed basis set exhibits B3LYP to give reasonable dissociation energies compared with the CID derived energy values (cf. Table S2-Table S4).

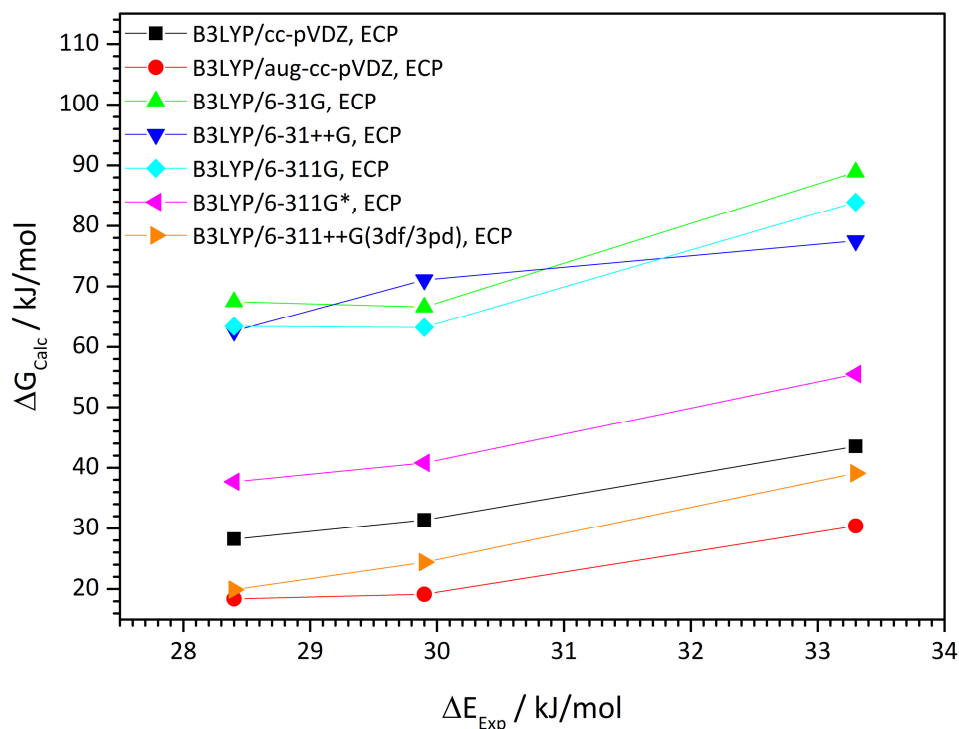


Figure 10: Computed Gibbs free energies ΔG_{calc} for the dissociation of complexes **1**, **2** and **3** as a function of the CID derived dissociation energies ΔE_{exp} .

However, the investigated species are transition metal complexes. In the case of the thermometer ions, the observed fragmentation and the derived dissociation energies are a result of a direct C-N bond cleavage not influenced by a transition metal. Note that the influence of the metal center and the consequent CH bond activation leads to an unpredictable uncertainty due to the catalytic activity of transition metals. Thus, we use CID results of the thermometer ions to derive dissociation energies of a metal catalyzed HCl elimination, which may lead to significant errors. Nevertheless, we obtained reasonable values for the dissociation energy of HCl supported by DFT computations.

5.6 Summary and conclusion

The presented IRMPD spectra in combination with DFT calculations allow for structure determination and give valuable information about the coordination of the transition metal within the complex. The influence of the different side groups on the IRMPD spectrum is small. However, comparison of the experimental IRMPD spectra with the computed linear IR absorption spectra of the most stable isomers found allows for structure determination and reveals a square planar binding motif of the Pd to three chloride ligands and to the nitrogen of the pyrimidine ring.

Furthermore, we measured CID appearance curves of **1**, **2** and **3**. The influence on the activation energy in dependence of the side group is small (< 5 kJ/mol). Complex **1** reveals to be the most stable complex followed by complex **3** and **1**. It is assumed that the CID appearance curves allow for the estimation of binding energies of the different complex ions due to the fact that there is a correlation between the undefined fragmentation voltage and the appearance energies. In order to determine binding energies, we used the so called thermometer ions to calibrate the internal energy scale of the mass spectrometer. We considered two possible fragmentation pathways of the thermometer ions. The direct bond cleavage leads to benzylium cations and to the formation of tropylium cations after rearrangement. Unfortunately, the direct comparison of CID derived activation energies with computed Gibbs free energies reveal different orders in the binding energy. Both the E_{COM}^{50} and AE values exhibit a linear relationship between the experimental values and theoretical binding energies. However, linear extrapolations exhibit relatively poor linear regression factors. The benzylium cation approach with a linear extrapolation using a fixed intercept delivers the best regression factor and is used to determine the dissociation energies. The CID derived dissociation energies correspond to DFT derived Gibbs free energies of **1**, **2** and **3**. Hereby, variation of the basis set and DFT functional reveals that the combination of cc-pVDZ and B3LYP agree the best. All other basis set and DFT functional combinations under- or overestimate the CID derived dissociation energies.

It is important not to overestimate the approach, because the assumption of a sigmoid behavior in general is merely a phenomenological approach to ion dissociation, which is fairly more complex. Additionally, the investigated species **1**, **2** and **3** contain a transition metal and the influence of the metal center on the bond cleavage may lead to an

unpredictable uncertainty due to the catalytic activity of transition metals. This influence may lead to significant errors in the determination of dissociation energies. Computations on transition states on the fragmentation pathway may solve the problem.

Nevertheless, we achieved reasonable energy values for the dissociation energies of the three Pd complexes. The computed Gibbs free energies are in a good agreement with the experimental CID derived dissociation energies. Anyhow, we demonstrate that this procedure may serve as a simple approach to determine dissociation energies of transition metal complexes.

5.7 References

- [1] Y. Nosenko, F. Menges, C. Riehn and G. Niedner-Schatteburg, *Physical Chemistry Chemical Physics*, **2013**, 15, 8171-8178.
- [2] J. Lang, M. Gaffga, F. Menges and G. Niedner-Schatteburg, *Physical Chemistry Chemical Physics*, **2014**, 16, 17417-17421.
- [3] O. Y. Ali and T. D. Fridgen, *Chemphyschem*, **2012**, 13, 588-596.
- [4] J. B. Fenn, *Angewandte Chemie-International Edition*, **2003**, 42, 3871-3894.
- [5] V. Gabelica and E. De Pauw, *Mass Spectrometry Reviews*, **2005**, 24, 566-587.
- [6] J. Naban-Maillet, D. Lesage, A. Bossee, Y. Gimbert, J. Sztaray, K. Vekey and J. C. Tabet, *Journal of Mass Spectrometry*, **2005**, 40, 1-8.
- [7] A. Hoxha, C. Collette, E. De Pauw and B. Leyh, *Journal of Physical Chemistry A*, **2001**, 105, 7326-7333.
- [8] C. Collette, L. Drahos, E. De Pauw and K. Vekey, *Rapid Communications in Mass Spectrometry*, **1998**, 12, 1673-1678.
- [9] P. B. Armentrout, B. Yang and M. T. Rodgers, *Journal of Physical Chemistry B*, **2014**, 118, 4300-4314.
- [10] P. B. Armentrout, C. A. Austin and M. T. Rodgers, *Journal of Physical Chemistry A*, **2014**, 118, 8088-8097.
- [11] E. L. Zins, C. Pepe and D. Schroder, *Journal of Mass Spectrometry*, **2010**, 45, 1253-1260.
- [12] R. A. J. O'Hair, *Chemical Communications*, **2006**, DOI: 10.1039/b516348j, 1469-1481.
- [13] S. Gronert, *Mass Spectrometry Reviews*, **2005**, 24, 100-120.
- [14] C. Collette and E. De Pauw, *Rapid Communications in Mass Spectrometry*, **1998**, 12, 165-170.
- [15] G. H. Luo, I. Marginean and A. Vertes, *Analytical Chemistry*, **2002**, 74, 6185-6190.
- [16] V. Gabelica, E. De Pauw and M. Karas, *International Journal of Mass Spectrometry*, **2004**, 231, 189-195.
- [17] K. V. Barylyuk, K. Chingin, R. M. Balabin and R. Zenobi, *Journal of the American Society for Mass Spectrometry*, **2010**, 21, 172-177.
- [18] E. L. Zins, D. Rondeau, P. Karoyan, C. Fosse, S. Rochut and C. Pepe, *Journal of Mass Spectrometry*, **2009**, 44, 1668-1675.

- [19] E. L. Zins, C. Pepe, D. Rondeau, S. Rochut, N. Galland and J. C. Tabet, *Journal of Mass Spectrometry*, **2009**, 44, 12-17.
- [20] E. L. Zins, C. Pepe and D. Schroder, *Faraday Discussions*, **2010**, 145, 157-169.
- [21] F. Menges, C. Riehn and G. Niedner-Schatteburg, *Zeitschrift Fur Physikalische Chemie-International Journal of Research in Physical Chemistry & Chemical Physics*, **2011**, 225, 595-609.
- [22] N. C. Polfer, *Chemical Society Reviews*, **2011**, 40, 2211-2221.
- [23] J. Roithova, *Chemical Society Reviews*, **2012**, 41, 547-559.
- [24] P. Gruene, C. Trage, D. Schroder and H. Schwarz, *European Journal of Inorganic Chemistry*, **2006**, DOI: 10.1002/ejic.200600587, 4546-4552.
- [25] D. Schroder, M. Engeser, H. Schwarz, E. C. E. Rosenthal, J. Dobler and J. Sauer, *Inorganic Chemistry*, **2006**, 45, 6235-6245.
- [26] C. Trage, M. Diefenbach, D. Schroder and H. Schwarz, *Chemistry-a European Journal*, **2006**, 12, 2454-2464.
- [27] G. Bouchoux, J. Y. Salpin and D. Leblanc, *International Journal of Mass Spectrometry and Ion Processes*, **1996**, 153, 37-48.
- [28] A. D. Becke, *Physical Review A*, **1988**, 38, 3098-3100.
- [29] A. D. Becke, *Journal of Chemical Physics*, **1993**, 98, 5648-5652.
- [30] B. Miehlich, A. Savin, H. Stoll and H. Preuss, *Chemical Physics Letters*, **1989**, 157, 200-206.
- [31] C. T. Lee, W. T. Yang and R. G. Parr, *Physical Review B*, **1988**, 37, 785-789.
- [32] T. H. Dunning, *Journal of Chemical Physics*, **1989**, 90, 1007-1023.
- [33] D. E. Woon and T. H. Dunning, *Journal of Chemical Physics*, **1993**, 98, 1358-1371.
- [34] D. E. Woon and T. H. Dunning, *Journal of Chemical Physics*, **1993**, 99, 3730-3737.
- [35] D. Andrae, U. Haussermann, M. Dolg, H. Stoll and H. Preuss, *Theoretica Chimica Acta*, **1991**, 78, 247-266.
- [36] M. Dolg, U. Wedig, H. Stoll and H. Preuss, *Journal of Chemical Physics*, **1987**, 86, 866-872.
- [37] M. J. T. Frisch, *et al.*, **2009**, Revision D.01 Wallingford CT. 2009.
- [38] NIST Standard Reference Database 101, <http://cccbdb.nist.gov/vibscalejust.asp>.
- [39] R. A. Kendall, T. H. Dunning and R. J. Harrison, *Journal of Chemical Physics*, **1992**, 96, 6796-6806.

- [40] L. A. Curtiss, K. Raghavachari, P. C. Redfern, V. Rassolov and J. A. Pople, *Journal of Chemical Physics*, **1998**, 109, 7764-7776.
- [41] V. A. Rassolov, M. A. Ratner, J. A. Pople, P. C. Redfern and L. A. Curtiss, *Journal of Computational Chemistry*, **2001**, 22, 976-984.
- [42] M. J. Frisch, J. A. Pople and J. S. Binkley, *Journal of Chemical Physics*, **1984**, 80, 3265-3269.
- [43] T. Clark, J. Chandrasekhar, G. W. Spitznagel and P. V. Schleyer, *Journal of Computational Chemistry*, **1983**, 4, 294-301.
- [44] A. D. McLean and G. S. Chandler, *Journal of Chemical Physics*, **1980**, 72, 5639-5648.
- [45] R. Krishnan, J. S. Binkley, R. Seeger and J. A. Pople, *Journal of Chemical Physics*, **1980**, 72, 650-654.
- [46] S. Grimme, *Journal of Computational Chemistry*, **2006**, 27, 1787-1799.
- [47] A. D. Becke, *Journal of Chemical Physics*, **1988**, 88, 2547-2553.
- [48] J. P. Perdew, *Physical Review B*, **1986**, 33, 8822-8824.
- [49] J. P. Perdew and A. Zunger, *Physical Review B*, **1981**, 23, 5048-5079.
- [50] J. P. Perdew, J. A. Chevary, S. H. Vosko, K. A. Jackson, M. R. Pederson, D. J. Singh and C. Fiolhais, *Physical Review B*, **1992**, 46, 6671-6687.
- [51] J. P. Perdew, K. Burke and Y. Wang, *Physical Review B*, **1996**, 54, 16533-16539.

5.8 Supporting Information to The Influence of Side Groups on the Activation Barrier of $[\text{Cl}_3\text{Pd}(\text{MIP})\text{R}]^-$ Complexes: a CID, IRMPD and DFT Study

Maximilian Gaffga, Agnes Fizia, Werner R. Thiel and Gereon Niedner-Schatteburg

*Fachbereich Chemie und Forschungszentrum OPTIMAS, Technische Universität
Kaiserslautern, 67663 Kaiserslautern, Germany*

Table of content

Figure S1: Mass spectra of **1**, **2** and **3**.

Table S1: Linear regression factors of the linear extrapolations in dependence of the different intercepts.

Scheme S1: Illustration of the rearrangement after HCl elimination during the CID process.

Table S2: Computed Gibbs free dissociation energies ΔG_{Diss} by variation of basis set and DFT functional in the case of complex **1**.

Table S3: Computed Gibbs free dissociation energies ΔG_{Diss} by variation of basis set and DFT functional in the case of complex **2**.

Table S4: Computed Gibbs free dissociation energies ΔG_{Diss} by variation of basis set and DFT functional in the case of complex **3**.

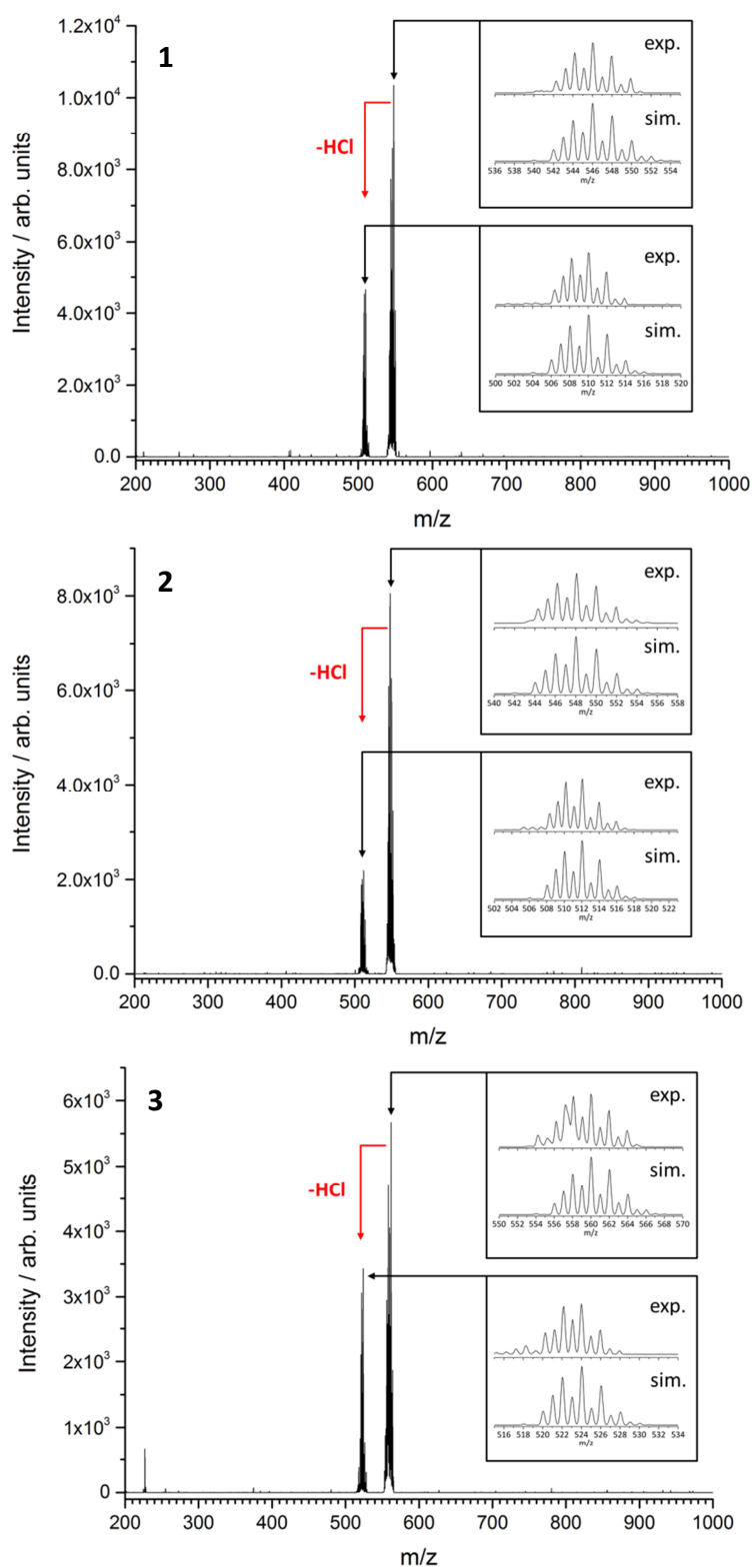
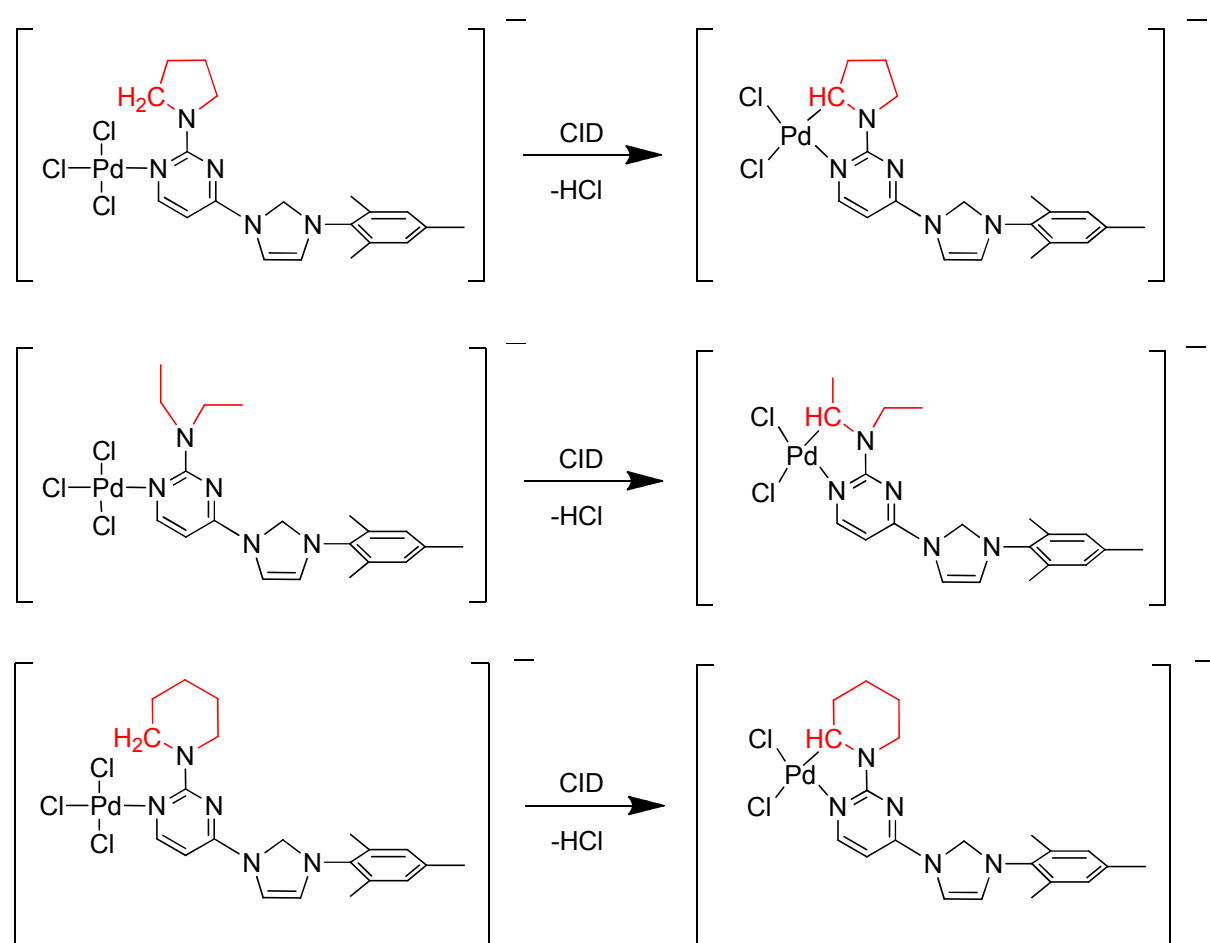


Figure S1: Mass spectra of **1**, **2** and **3** in the negative ion mode, taken at $E_{\text{COM}} = 0.004$ a.u.. Simulations of the isotopic patterns of **1**, **2** and **3** are given as insets. The observed fragmentation channel of all complexes is the loss of HCl.

Table S1: Linear regression factors of the different linear extrapolations in the case of the benzylium cation and in the case of the tropylium cation as product ions.

| intercept | benzylium cation | | tropylium cation | |
|-----------|------------------|------|------------------|------|
| | E_{COM}^{50} | AE | E_{COM}^{50} | AE |
| free | 0.65 | 0.47 | 0.48 | 0.20 |
| 0 | 0.66 | 0.52 | 0.53 | 0.36 |
| 2.7 | 0.73 | 0.51 | 0.51 | 0.35 |



Scheme S1: Dissociation reaction of the HCl elimination during the CID process. Note, that the H atom originates from the CH_2 group of the substituted side group (red). The remaining CH group forms a C-Pd bond and ensures a square planar binding motif of the Pd cation.

Table S2: Computed Gibbs free dissociation energies ΔG_{Diss} for the HCl elimination of complex **1** by variation of the basis sets and the DFT functional. The energy values are given in kJ/mol.

| $\Delta G_{\text{Diss}}(\mathbf{1}\text{-HCl})$ | B3LYP | BLYP | B3P86 | B97D |
|---|--------------|-------------|--------------|-------------|
| cc-pVDZ | 43.48 | 29.89 | 31.49 | 47.84 |
| aug-cc-pVDZ | 30.42 | 20.99 | 27.91 | 35.35 |
| 6-31G | 88.90 | 74.63 | 86.97 | 90.68 |
| 6-31++G | 77.45 | 65.45 | 82.66 | 83.01 |
| 6-311G | 83.86 | 67.10 | 82.26 | 83.55 |
| 6-311G* | 55.50 | 35.85 | 45.23 | 57.35 |
| 6-311G++(3df,3pd) | 39.10 | 25.93 | 37.61 | 31.68 |

Table S3: Computed Gibbs free dissociation energies ΔG_{Diss} for the HCl elimination of complex **2** by variation of the basis sets and the DFT functional. The energy values are given in kJ/mol.

| $\Delta G_{\text{Diss}}(\mathbf{2}\text{-HCl})$ | B3LYP | BLYP | B3P86 | B97D |
|---|--------------|-------------|--------------|-------------|
| cc-pVDZ | 28.19 | 21.39 | 28.23 | 30.24 |
| aug-cc-pVDZ | 18.36 | 17.42 | 17.18 | 22.63 |
| 6-31G | 67.46 | 58.69 | 68.21 | 73.81 |
| 6-31++G | 62.61 | 58.31 | 67.33 | 67.13 |
| 6-311G | 63.36 | 52.67 | 65.84 | 68.42 |
| 6-311G* | 37.70 | 29.67 | 38.35 | 42.60 |
| 6-311G++(3df,3pd) | 19.96 | 14.08 | 5.23 | 26.48 |

Table S4: Computed Gibbs free dissociation energies ΔG_{Diss} for the HCl elimination of complex **3** by variation of the basis sets and the DFT functional. The energy values are given in kJ/mol.

| $\Delta G_{\text{Diss}}(\mathbf{3}\text{-HCl})$ | B3LYP | BLYP | B3P86 | B97D |
|---|-------|-------|-------|-------|
| cc-pVDZ | 31.36 | 14.73 | 22.41 | 28.54 |
| aug-cc-pVDZ | 19.13 | 8.51 | 15.19 | 22.91 |
| 6-31G | 66.57 | 54.91 | 65.14 | 70.92 |
| 6-31++G | 71.10 | 52.42 | 63.43 | 64.50 |
| 6-311G | 63.15 | 59.24 | 58.74 | 64.00 |
| 6-311G* | 40.82 | 27.96 | 34.51 | 35.57 |
| 6-311G++(3df,3pd) | 24.04 | 9.80 | 15.77 | 20.39 |

6. IRMPD Spectroscopy and CID Studies on Iron- / Lanthanide based Single Molecule Magnets

Maximilian Gaffga^a, Annie K. Powell^b and Gereon Niedner-Schatteburg^a

^a*Fachbereich Chemie und Forschungszentrum OPTIMAS, Technische Universität
Kaiserslautern, 67663 Kaiserslautern, Germany*

^b*Institute für Anorganische Chemie, Karlsruher Institut für Technologie
76131 Karlsruhe, Germany*

6.1 Preamble

The following chapter was prepared as a manuscript for publication. It is not submitted so far. All presented measurements, data evaluation, computations and all of the preparation of the manuscript itself were performed by myself. I received experimental support by Joachim Hewer, and I exchanged ideas with my colleagues Matthias Tombers and Johannes Lang. Gereon Niedner-Schatteburg helped by discussions. The complexes were synthesized by the group of Annie K. Powell from the Karlsruher Institute for Technology (KIT).

6.2 Abstract

We present collision-induced dissociation (CID) and infrared multi photon dissociation (IRMPD) investigations on single molecule magnets (SMM) of two different $[\text{Fe}_4\text{Ln}_2]^+$ (Ln = Y, Eu, Gd, Tb, Dy, Ho and Er) coordination types. The CID appearance curves reveal significant changes in the fragmentation thresholds within a given structure type depending on the used Ln metal center. The difference in the dissociation thresholds apparently arises from the ability to form π -backbondings and the occupation of anti-bonding orbitals. Recorded IRMPD spectra exhibit blue and red shifts of OH, sp^3CH , and CO stretching modes depending on the used Ln metal center.

6.3 Introduction

Single molecule magnets (SMM) are a new class of metal-organic compounds exhibiting highly interesting magnetic properties.^[1-3] Recent investigations have led to plenty SMMs containing transition metals such as iron as well as lanthanides with low-temperature magnetism.^[4-6] The given magnetic properties make SMMs a promising class of compounds for several applications, e.g. as data storage devices^[7] and for quantum computing.^[8-10]

The combination of infrared multi photon dissociation (IRMPD) spectroscopy and mass spectrometric analysis has proven to be a powerful tool to investigate the molecular structure of isolated complexes in the gas phase.^[11-14] Gas phase investigations allow for the determination of a system's intrinsic properties without any influences by the surrounding environment. Next to the IRMPD technique, collision-induced dissociation (CID) experiments can be used to obtain insights into binding motifs and provide information about the structural composition of these complexes.^[15, 16] Furthermore, CID studies serve as an approach to estimate stabilities of complexes.^[17-19] In this work, we use the electrospray ionization technique (ESI) to transfer iron and lanthanides containing single molecule magnets of two different $[\text{Fe}_4\text{Ln}_2]^+$ coordination types in the gas phase.^[20, 21] We conduct IRMPD spectroscopy and CID studies to elucidate the influence of the different Ln metal centers on the chemical structure, the dissociation threshold, and the fragmentation behavior of the investigated $[\text{Fe}_4\text{Ln}_2]^+$ complexes.

6.4 Experimental setup and methods

The presented electrospray ionization mass spectrometry (ESI-MS) was performed with two ion trap instruments (Bruker Esquire 6000 for CID and amaZonSL for IRMPD measurements). The investigated cations were produced in the positive electrospray ionization mode. The scan speed was $13000 \frac{m}{z \cdot s}$ in normal resolution scan mode ($0.3 \text{ fwhm} / \frac{m}{z}$). The scan range was at least 70 to $2000 \frac{m}{z}$. All samples were prepared as acetonitrile (MeCN) solutions with concentrations of approximately 1×10^{-4} M. Sample solutions were continuously infused into the ESI chamber at a flow rate of $2 \mu\text{l}/\text{min}$ using an automatical syringe pump. We used nitrogen as a drying gas at a flow rate of 3.0 to 4.0 l/min heated to 220 and 300 °C. We sprayed the solutions at a nebulizer gas pressure of 3 to 4 psi with the electrospray needle held at 4.5 kV. We used Helium as a buffer gas with a partial pressure of about 3×10^{-3} mbar inside the ion trap. BrukerEsquireControl 5.3 (Esquire) and BrukerTrapControl 7.0 (amaZonSL) software controlled the instrument and we performed data analysis using the Data Analysis 4.0 software.

Collision induced dissociation (CID) appearance curves were recorded by varying the excitation magnitude from 0.0 to 1.5 corresponding to an excitation energy scale in the lab frame (E_{LAB}).^[15] These excitation energies were increased in a stepwise fashion until complete dissociation of the ion of interest was observed. Normalized relative and total fragmentation yields were calculated according to:

$$I_{i,norm}^{fr}(E_{LAB}) = \frac{I_i^{fr}(E_{LAB})}{\sum_i I_i^{fr}(E_{LAB}) + \sum_i I_i^p(E_{LAB})} \quad (1a)$$

$$I_{tot}^{fr}(E_{LAB}) = \sum_i I_{i,norm}^{fr}(E_{LAB}) \quad (1b)$$

Center of mass transformed relative excitation energies (E_{COM}) were calculated from the internal amplitudes as following in order to allow for comparability:

$$E_{COM} = \frac{m_{He}}{m_{He} + m_{ion}} \cdot E_{LAB} \quad (2)$$

m_{ion} was chosen according to the most abundant mass peak of the molecule.

An optical parametric oscillator/amplifier (OPO/OPA, LaserVision) laser system pumped with a pulsed injection seeded Nd³⁺:YAG laser (Continuum-PL8000; 10 Hz) was used as a source of

tunable IR radiation ($\delta\bar{\nu} = 0.9 \text{ cm}^{-1}$, $\delta t = 7 \text{ ns}$) to record the vibrational spectra (IR_{scan}). The OPA idler wave ($\leq 10 \text{ mJ}$ per pulse) was used to record spectra within the spectral range of $2600 - 3700 \text{ cm}^{-1}$. The difference frequency (DF) between the OPA signal and idler waves, generated in a AgGaSe_2 crystal was used for the energy range of $1200 - 2100 \text{ cm}^{-1}$ ($\leq 2 \text{ mJ}$ per pulse). After passing through the ion trap chamber, the IR beam was directed onto a power meter sensor to record the laser power during the measurement. The idler beam was focused by a 50 cm CaF_2 lens. The DF radiation was focused tighter by a 90° off-axis parabolic silver mirror with an effective focal length of 15 cm .

The IR spectra were recorded as ion chromatograms while continuously scanning the IR wavelength. The IRMPD yield (Y) was determined as:

$$Y = \frac{\sum_i I_i^{fr}}{\sum_i I_i^{fr} + \sum_i I_i^p} \quad (4)$$

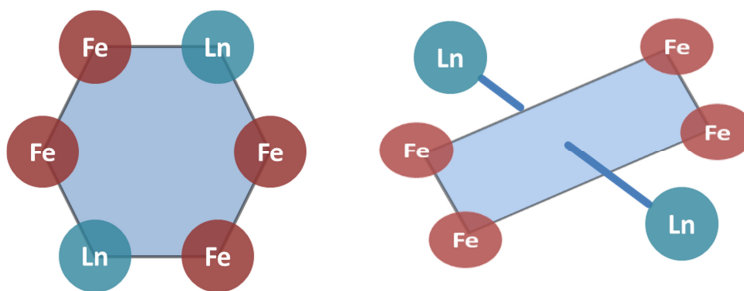
The IR frequency was calibrated by a wavemeter (Bristol Instruments: 821 Pulsed Laser Wavelength Meter) to a theoretical accuracy of $\pm 0.02 \text{ cm}^{-1}$, which is beyond the spectral bandwidth of the utilized IR photon beams by more than one order of magnitude. IRMPD yields scale in an intrinsically nonlinear way with the applied IR photon flux. Therefore, we refrained from any photon flux normalization.

6.5 Results and discussion

6.5.1 Structure type definition

We investigated two types (**I** and **II**) of $[\text{Fe}_4\text{Ln}_2]^+$ complexes differing in their structure and ligand composition. The type **I** complexes reveal an arrangement of the metal centers as a hexagon (Scheme 1). The metal centers represent the edges of this hexagon surrounded by several organic ligands stabilizing the metal array. Thereby, the metal centers follow a special order, namely Ln-Fe-Fe-Ln. One Ln metal center has two adjacent Fe metal centers. In case of type **I**, we investigate complexes with Ln being Y, Eu, Gd, Tb, Dy, Ho, and Er, whereas Y is not a paramagnetic lanthanide but exhibits a diamagnetic species with similar ionic radius. The molecular formula of the compounds is $[\text{Fe}_4\text{Ln}_2(\text{N}_3)_6(\text{N}(\text{C}_2\text{H}_4\text{OH})(\text{C}_2\text{H}_4\text{O})_2)_4$

($\text{C}(\text{CH}_3)_3\text{COO}$) $_4$]. The complexes of type **II** differ in the spatial arrangement of the metal centers. The Fe centers form a plain, while the Ln metals are on a straight line crossing the center perpendicular to the Fe plain. In case of **II**, we investigate compounds with Ln being Y, Dy, Gd, Tb and Dy. The molecular formula is $[\text{Fe}_4\text{Ln}_2\text{O}_2(\text{C}(\text{CH}_3)_3\text{COO})_4(\text{NO}_3)_2(\text{H}_3\text{C}_3\text{N}(\text{C}_2\text{H}_4\text{O})_2)_4]$.



Scheme 1: Metal arrangement within the type **I** (left) and type **II** (right) $[\text{Fe}_4\text{Ln}_2]^+$ complexes.

Mass spectrometric analysis reveal the replacement of one negatively charged ligand, i.e., $\text{C}(\text{CH}_3)_3\text{COO}^-$ for structure type **I** and NO_3^- for structure type **II** with one neutral MeCN molecule during the ESI process. This leads to a singly positive charged complex.

6.5.2 Structure determination by means of the crystal structure

Deprotonated pivalic acid ($\text{C}(\text{CH}_3)_3\text{COO}^-$, Piv), doubly deprotonated triethanolamine (TEA), and azide (N_3^-) ligands coordinate the metal centers of the type **I** complexes (Fig. 1). The oxygen and nitrogen atoms of two TEA ligands coordinate to the Ln metal centers. The Ln metal centers are eightfold coordinated in a cubic arrangement. The deprotonated COOH functions of the pivalic acids act as a bridging ligand between adjacent Fe metal centers. One of the remaining OH groups of a TEA ligand forms a hydrogen bond to the pivalic acid, while the other OH group remains free. The pivalic acids, the azides and the TEAs act as bridging

ligands coordinating the Fe centers in an octahedral manner. Furthermore, the pivalic acids and the azide ligands act as bridging ligands between two Fe metal centers. Note that the oxygen atoms of the TEA ligands connect the Fe with the Ln metal centers and the nitrogen atoms of the azide connect two Fe metal centers. Due to this coordination sphere, the Ln metal centers are not connected to each other by a bridging ligand.

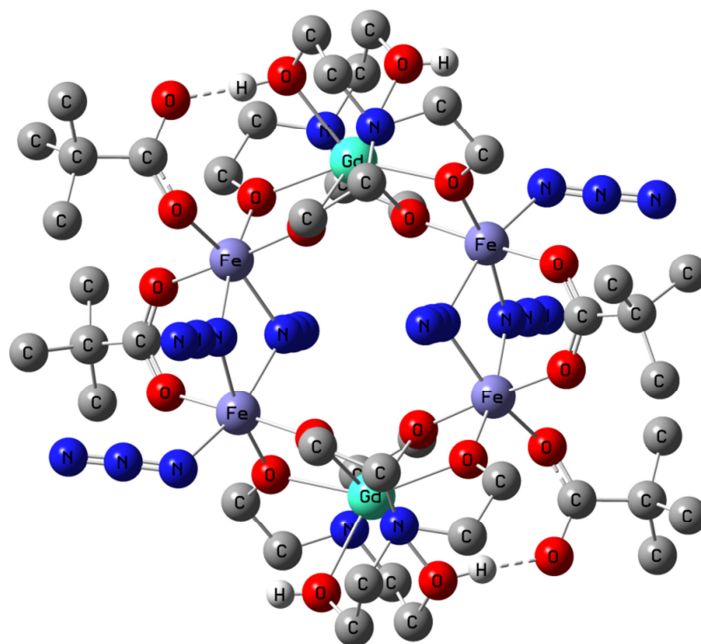


Figure 1: Crystal structures of the type I $[Fe_4Ln_2]$ complexes using the crystal structure of $[Fe_4Gd_2]$ as an example. The aliphatic hydrogen atoms were omitted for purposes of clarity. Note the hydrogen bonds between the TEA ligands and the pivalic acids (dashed lines).

Mass spectrometric investigations exhibit the exchange of a pivalic acid by a MeCN solvent molecule. We suppose that a pivalic acid, revealing a single coordination to a Fe metal and forming a hydrogen bond, is replaced instead of a double coordinating pivalic acid bridging ligand. The replacement leads to a free OH group.

2,2'-[(Prop-2-ynyl)imino] bisethanolate) (PIB), deprotonated pivalic acid, nitrate and O^{2-} ligands coordinate the metal centers of the type II complexes (Fig. 2). The nitrate ligands coordinate the Ln metal centers. Two oxygen anions (O^{2-}) act as bridging ligands between the Ln metal centers. The Ln metal centers are eightfold coordinated in a cubic way. The O^{2-}

anions coordinate the Fe metal centers. The deprotonated pivalic acids, the O^{2-} anions and the PIB ligands coordinate the Fe centers in an octahedral manner. Thereby, the deprotonated COOH functions of the pivalic acids act as a bridging ligand between adjacent Fe metal centers. The PIB ligand coordinates via the nitrogen atom and the two deprotonated oxygen atoms to the Fe metal center. The two deprotonated oxygen atoms coordinate the Ln metal center. The alkyne ($C\equiv C-H$) functions points outwards and remains uncoordinated.

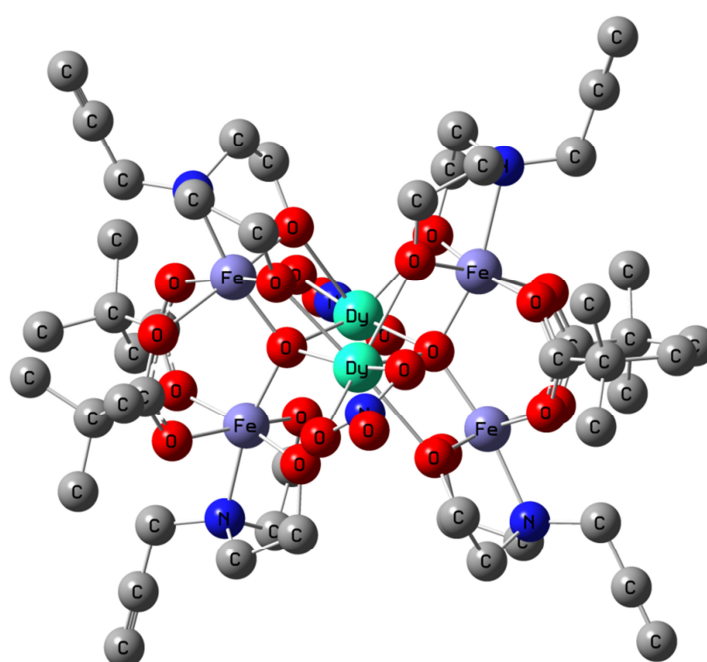


Figure 2: Crystal structures of the type II $[Fe_4Ln_2]$ complexes using the crystal structure of $[Fe_4Dy_2]$ as an example. The aliphatic hydrogen atoms were omitted for purposes of clarity.

Mass spectrometric investigations exhibit the exchange of a nitrate ligand with a MeCN solvent molecule. Note the connections of the Ln metal centers via the two O^{2-} anions instead of the spatial separation of the Ln metal centers in the case of the type I complexes.

6.5.3 Collision-induced dissociation experiments

We performed collision-induced dissociation (CID) studies in order to get insights in the fragmentation behavior of the mass-selected ions of the type I and type II complexes. The main fragmentation channels of the type I complexes are the elimination of [TbTEA], [FePivN₃] and [PivH] units along with H₂. In the case of the type II complexes, the main fragmentation channels are the elimination of [FeNO₃PIB], [FePivPIB] and [FeOPivPIB] units. For both complex types the observed main fragmentation channels remain the same by the variation of the Ln metal centers. Application and stepwise increase of an activation magnitude up to complete depletion of the precursor ions allows for the recording of CID appearance curves.

The CID appearance curves exhibit the complexes' stability in dependence of the different Ln metal centers in the case of the type I complexes (Fig. 3). The dots represent the experimental data points. The curves are sigmoid fit functions. In order to guarantee comparability, we used the center of mass transformation to correct the activation magnitude (E_{COM}). Thereby, the E_{COM}^{50} value represents an amount of energy needed for 50 % depletion of the precursor ion. The comparison of these values allows for the estimation of relative ion stabilities within a given class of compounds. The higher the E_{COM}^{50} value, the more stable the complex. The complexes [Fe₄Er₂]⁺ (red curve) and [Fe₄Eu₂]⁺ (green curve) show similar fragmentation thresholds ($E_{COM}^{50} = 1.06 \cdot 10^{-3}$ a.u. for [Fe₄Er₂]⁺ and $E_{COM}^{50} = 1.07 \cdot 10^{-3}$ a.u. for [Fe₄Eu₂]⁺) and thus, the lowest activation threshold for fragmentation. At higher activation magnitudes the [Fe₄Ho₂]⁺ (cyan curve, $E_{COM}^{50} = 1.15 \cdot 10^{-3}$ a.u.) complex starts to fragment followed by [Fe₄Gd₂]⁺ (blue curve, $E_{COM}^{50} = 1.19 \cdot 10^{-3}$ a.u.) and [Fe₄Tb₂]⁺ (purple curve, $E_{COM}^{50} = 1.21 \cdot 10^{-3}$ a.u.). The [Fe₄Y₂]⁺ (orange curve) complex reveals to be the most stable complex and fragments at the highest activation magnitudes ($E_{COM}^{50} = 1.30 \cdot 10^{-3}$ a.u.). The [Fe₄Dy₂]⁺ (black curve, $E_{COM}^{50} = 1.18 \cdot 10^{-3}$ a.u.) complex exhibits a significantly different curves' shape. Firstly, the slope of the curve is flatter, while the slopes of the other curves are steep. The curves' slope may give indication for entropic effects. At higher activation magnitudes, the dissociation is dominated by the entropy due to the higher value of degrees of freedom which are responsible for the fragmentation pattern.

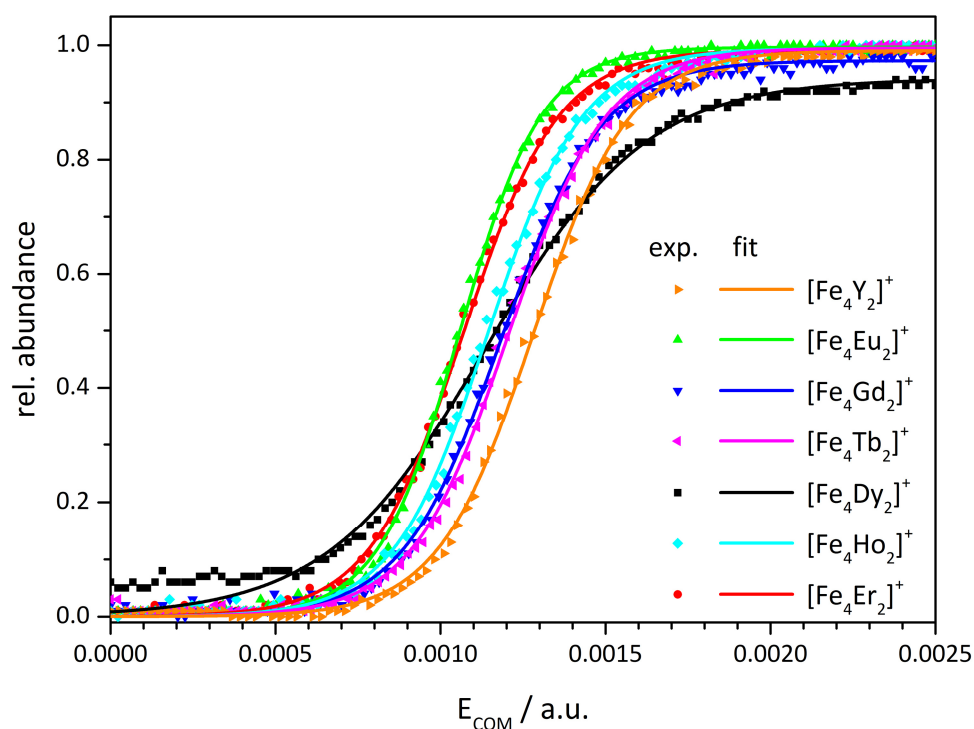


Figure 3: CID appearance curves of type I $[\text{Fe}_4\text{Ln}_2]^+$ complexes. The dots represent the experimental data, the lines are sigmoid fit functions.

A flat slope arises from a tight transition state, while a steep slope points towards a loose transition state. An activated complex with strict steric requirements is referred to as a tight complex, whereas the transition state without such requirements is called a loose complex. The tight complex needs more energy to dissociate and this leads to a flatter slope. Only a few complex ions can overcome the fragmentation threshold. The loose complex forms weak bonds resulting in steep slopes. A higher slope arises with a lower stability due to the fact that a loose transition state favors the fragmentation and thus the stability decreases.^[22, 23] This means that the $[\text{Fe}_4\text{Dy}_2]^+$ complex may have a tighter transition state resulting in the flatter slope of the curve compared to the other CID appearance curves. Secondly, the curve does not reach 100 % fragmentation yield. This indicates that not all complex ions can be fragmented. At this point, we do not have an explanation for this behavior.

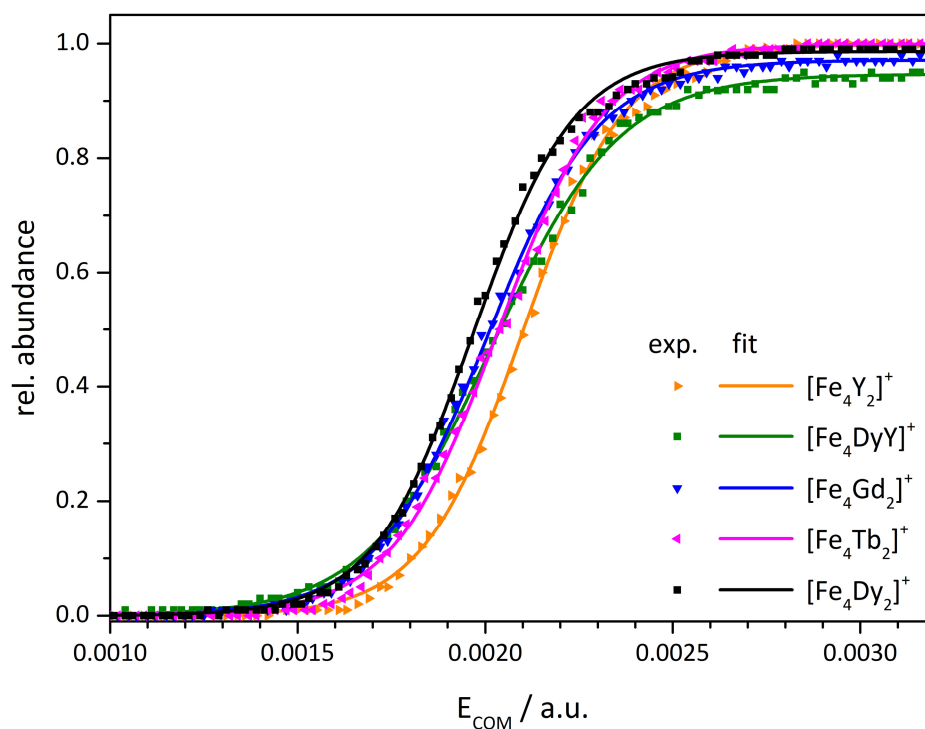


Figure 4: CID appearance curves of type II $[\text{Fe}_4\text{Ln}_2]^+$ complexes. The dots represent the experimental data, the lines are sigmoid fit functions.

In comparison to the CID appearance curves of the type I complexes, the type II complexes do not reveal significant different fragmentation thresholds in dependence of the Ln metal center (Fig. 4). The $[\text{Fe}_4\text{Dy}_2]^+$ (black curve, $E_{\text{COM}}^{50} = 1.97 \cdot 10^{-3}$ a.u.) complex shows the lowest E_{COM}^{50} value. The $[\text{Fe}_4\text{Gd}_2]^+$ (blue curve, $E_{\text{COM}}^{50} = 2.01 \cdot 10^{-3}$ a.u.), $[\text{Fe}_4\text{DyY}_2]^+$ (green curve, $E_{\text{COM}}^{50} = 2.03 \cdot 10^{-3}$ a.u.) and $[\text{Fe}_4\text{Tb}_2]^+$ (purple curve, $E_{\text{COM}}^{50} = 2.04 \cdot 10^{-3}$ a.u.) complexes exhibit moderate fragmentation thresholds. The $[\text{Fe}_4\text{Y}_2]^+$ (orange curve, $E_{\text{COM}}^{50} = 2.10 \cdot 10^{-3}$ a.u.) complex is the most stable complex as seen for the type I complexes. In general, the type II complexes need higher activation magnitudes for fragmentation than the type I complexes. We assume that the type II complexes are more stable due to their different organic ligands and coordination sphere.

The complexes' stability is influenced by the Ln metal centers within the given structure types I and II. The binding strength depends on (i) the bond length, (ii) the bond type (single, double or triple bond), and (iii) the involved atoms. The bond type can be neglected, since it is the same for each complex. However, a possible explanation may be the different ionic

radii of the Ln metal centers influencing the bond length. The ionic radii of the Ln metals are almost similar (Table 1). Starting with Eu (1.07 Å), the ionic radius decreases to Er (1.00 Å) in terms of the lanthanide contraction. Both, the empirical and the calculated atomic radii exhibit the same trend. The radii decrease by higher atomic numbers. Y exhibits a similar ionic radius to the lanthanide radii. Hence, the bond lengths may be not a crucial parameter.

Table 1: Atomic and ionic radii for different metal centers. Ionic radii for complexes with a coordination number of 6 (CN=6) in the case of Fe and a coordination number of 8 (CN=8) in case of Ln (Y - Er). The ionic charge is plus three.

| Metal | Atomic radii / Å empirical ^[24] | Atomic radii / Å calculated ^[25] | Ionic radii ^[26] / Å |
|-------|---|--|---------------------------------|
| Fe | 1.40 | 1.56 | 0.55 |
| Y | 1.80 | 2.12 | 1.01 |
| Eu | 1.85 | 2.31 | 1.07 |
| Gd | 1.80 | 2.33 | 1.06 |
| Tb | 1.75 | 2.25 | 1.04 |
| Dy | 1.75 | 2.28 | 1.03 |
| Ho | 1.75 | 2.27 | 1.02 |
| Er | 1.75 | 2.26 | 1.00 |

Concerning the involved atoms, the different Ln metals may have different affinities to nitrogen or oxygen and thus influences the bond strength. Different metal centers exhibit changes in their metal-ligand coordination strength due to the ability of π -backbonding formation. For π -backbondings, electrons from the metal are used to bond to the ligand and strengthen the metal-ligand bond. The ability to form π -backbondings depends on the ligand field splitting and the orbital occupation of the contributing partners, i.e. the metal and the ligand.^[27] This may be an explanation for the complex stabilities and thus leads to the observed dissociation thresholds of the CID experiments. For the type I, the $[\text{Fe}_4\text{Y}_2]^+$ complex exhibits to be the most stable, while the $[\text{Fe}_4\text{Eu}_2]^+$ and $[\text{Fe}_4\text{Er}_2]^+$ complexes are the most instable ones. Thus, we assume that the Y metal forms the strongest π -backbonding, and the

Eu and Er metals are not able to form π -backbondings. Furthermore, we ascribe the higher fragmentation threshold of the $[\text{Fe}_4\text{Y}_2]^+$ complex to the fact that Y does not belong to the group of lanthanides. The bond formation of Y originates from the 4d orbitals, while the 4f orbitals contribute to the bond formation of the lanthanides. The f orbitals are more diffuse than the d orbitals and this may lead to weaker bonds and results in lower fragmentation thresholds. Gd, Tb and Ho show similar bond strengths. In the case of the type II complexes, the $[\text{Fe}_4\text{Y}_2]^+$ complex reveals a higher dissociation threshold than the $[\text{Fe}_4\text{Gd}_2]^+$, $[\text{Fe}_4\text{Tb}_2]^+$ and $[\text{Fe}_4\text{Dy}_2]^+$ complexes, which is consistent with the findings of the type I complexes. As for the type I complexes, the Tb containing complex exhibits a higher dissociation threshold than the Gd containing complex. Therefore, we assume that Tb forms stronger bonds than Gd. Additionally, the bond formation between electron rich metals and ligands requires the occupation of anti-bonding or non-bonding orbitals which leads to a weakening of the bond strength.^[28] Hence, the electron rich complexes $[\text{Fe}_4\text{Ho}_2]^+$ and $[\text{Fe}_4\text{Er}_2]^+$ exhibit lower fragmentation thresholds than the electron poor complexes $[\text{Fe}_4\text{Gd}_2]^+$ and $[\text{Fe}_4\text{Tb}_2]^+$. Up to now, we were not able to exploit the distinct contribution from π -backbonding and anti- or non-bonding orbital occupation in detail to explain deviations from those general rules, e.g. for the $[\text{Fe}_4\text{Eu}_2]^+$ complex which shows the lowest fragmentation threshold despite having the lowest electron density.

The dissociation thresholds of the type II complexes are higher than the thresholds of the type I complexes. The ligands and the associated structural change of the complex influence the stability of the complexes as well as the Ln metals itself. In the case of the type I complexes the ability to form π -backbondings and the occupation of anti-bonding orbitals have to be taken into account. This has to be done for the type II complexes as well. As seen for the type I Y containing complex, the type II $[\text{Fe}_4\text{Y}_2]^+$ complex reveals the highest fragmentation threshold apparently arising from the used 4d orbitals for the bond formation. The $[\text{Fe}_4\text{Tb}_2]^+$ complex exhibits to be more stable than the $[\text{Fe}_4\text{Gd}_2]^+$ complex which is similar to the findings of the corresponding type I complexes. Once more, these findings can be attributed to different capabilities of π -backbonding and the different degree of occupation for anti- or non-bonding orbitals, a detailed explanation pending. Computations on electron/spin densities (e.g. by the so called broken symmetry approach) may serve to elucidate the influence of π -backbonding and anti- and non-bonding orbital occupation in more detail.

6.5.4 IRMPD spectroscopic investigations

We performed IRMPD spectroscopy within the spectral range from 1200 to 3800 cm^{-1} in order to get insights into the influence of the Ln metal center on the structure of the type I $[\text{Fe}_4\text{Ln}_2]^+$ complexes (Fig. 5).

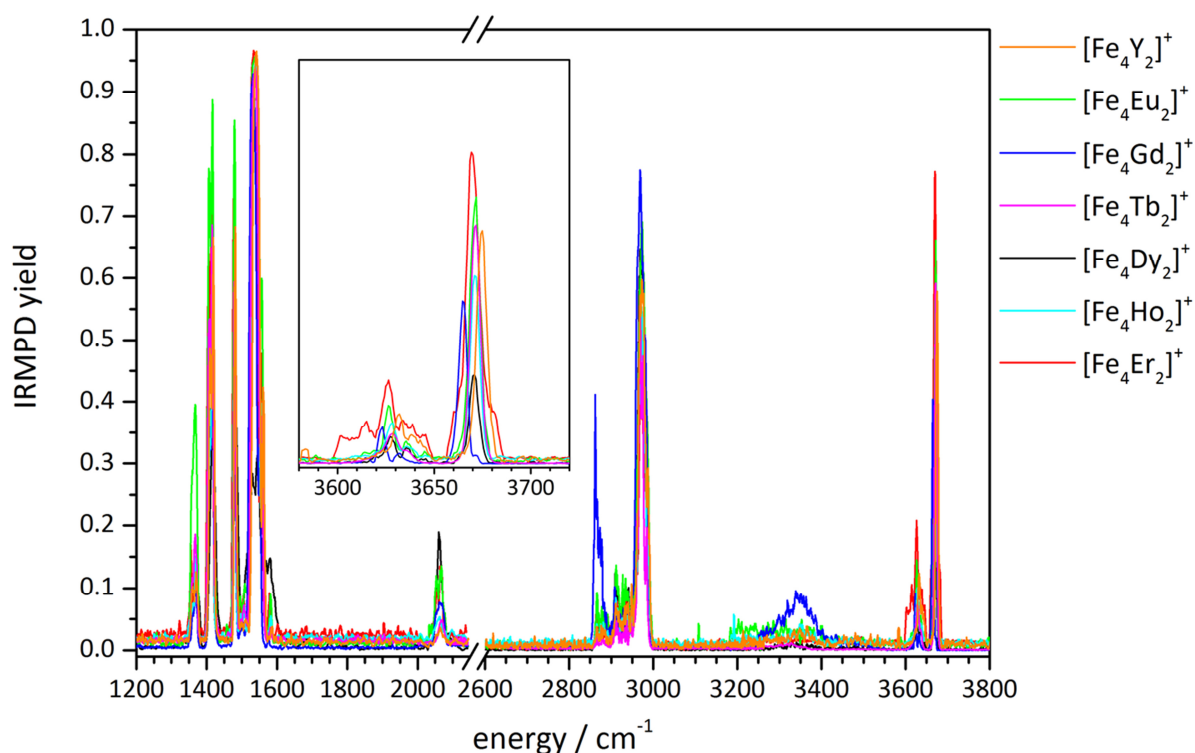


Figure 5: Comparison of the IRMPD spectra of type I $[\text{Fe}_4\text{Ln}_2]^+$ complexes. Note the band shifts of the OH stretching vibration in dependence of the Ln metal centers (inset).

All IRMPD spectra of the type I complexes reveal a sharp strong band at 3670 cm^{-1} as well as a weak band at 3625 cm^{-1} . These vibrations should originate from the free OH groups of the TEA ligands. The weak band at 3625 cm^{-1} may be a result of (i) a second isomer, since in our opinion the vibrations of the free OH groups should be chemically equivalent or (ii) due to the replacement of a pivalic acid ligand by a MeCN solvent molecule, a second OH group is no longer hydrogen bond, and the adjacent MeCN shifts the frequency to higher wavenumbers. The band at 3670 cm^{-1} exhibits an influence of the Ln metal centers. The different metal centers have two effects. The band shifts red or blue in dependence of the Ln

metal. Additionally, the intensity of the band differs in dependence of the Ln metal center. Furthermore, the IRMPD spectra of $[\text{Fe}_4\text{Y}_2]^+$, $[\text{Fe}_4\text{Eu}_2]^+$, and $[\text{Fe}_4\text{Gd}_2]^+$ show a broad band centered at 3340 cm^{-1} which could not be observed in the IRMPD spectra of $[\text{Fe}_4\text{Tb}_2]^+$, $[\text{Fe}_4\text{Dy}_2]^+$, $[\text{Fe}_4\text{Ho}_2]^+$, and $[\text{Fe}_4\text{Er}_2]^+$. Based on this band, the influence of the Ln metal center is significant. The width of this band is an indication for a hydrogen bond. We suppose that this band originates from the hydrogen bond between the OH group of a TEA ligand and the deprotonated COO^- group of the pivalic acid. Between 2850 and 3000 cm^{-1} , there are three more or less intense bands originating from aliphatic CH stretching vibrations. All IRMPD spectra of the type I complexes show a more or less intense band at 2060 cm^{-1} . We ascribe this band to the stretching mode of the azide ligands. In this case, the influence of the Ln metal centers on the complexes' stability and consequently the band intensity is significant. Hereby, the $[\text{Fe}_4\text{Dy}_2]^+$ complex followed by the $[\text{Fe}_4\text{Er}_2]^+$, $[\text{Fe}_4\text{Eu}_2]^+$ and $[\text{Fe}_4\text{Gd}_2]^+$ complexes reveal the highest IRMPD yields. This observation is consistent with the results from the CID chapter (cf. chapter 6.5.3). The IRMPD spectra reproduce the complex stabilities in dependence of the Ln metal center. In the fingerprint region (1300 - 1650 cm^{-1}), there is a strong band at 1535 cm^{-1} , a strong band at 1480 cm^{-1} , two strong bands at 1405 and 1415 cm^{-1} , and a weaker band at 1365 cm^{-1} . We assign the strong band at 1535 cm^{-1} to CO stretching vibrations. One would expect to see typical CO stretching vibrations in the range of 1600 - 1900 cm^{-1} . But the red shift to lower energy values, compared to general CO stretching modes (1600 - 1900 cm^{-1}), results from the coordination of the CO groups to Fe and Ln metal centers. Also this band exhibits small red and blue shifts in dependence of the Ln metal center. The other bands are in the typical range of C-C stretching vibrations and CH bending motions. The band intensities of all complexes are similar except of the $[\text{Fe}_4\text{Dy}_2]^+$ complex. The $[\text{Fe}_4\text{Dy}_2]^+$ complex exhibits the highest IRMPD yield at 2060 cm^{-1} . We do not have a conclusive explanation for this behavior in the presented IRMPD spectrum. Furthermore, it remains unclear why the $[\text{Fe}_4\text{Gd}_2]^+$ complex reveals the highest IRMPD yield at the hydrogen bond band at 3340 cm^{-1} .

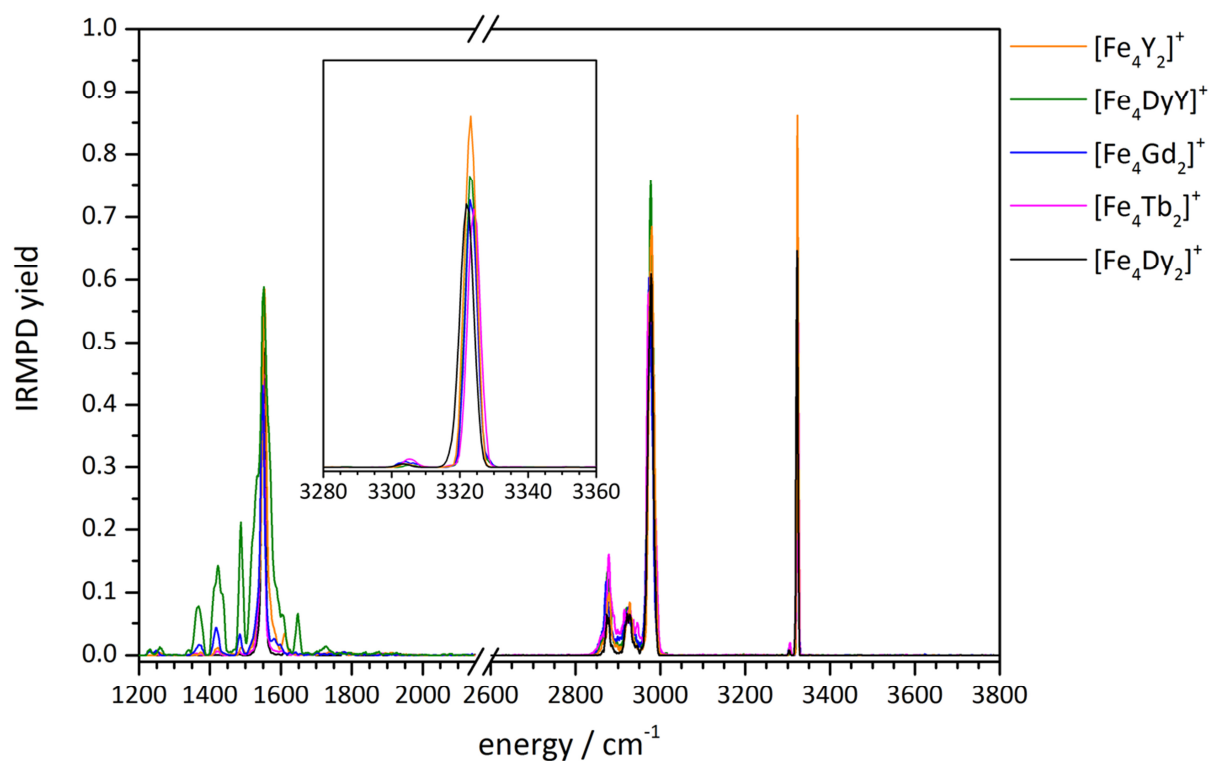


Figure 6: Comparison of the IRMPD spectra of type II $[Fe_4Ln_2]^+$ complexes. Note the Ln metal centers do not influence the *sp* hybridized CH bands (inset).

All IRMPD spectra of the type II complexes reveal a sharp strong band at 3325 cm^{-1} and a weak band at 3305 cm^{-1} (Fig. 6). We assign these bands to the CH stretching vibrations of the $C\equiv C-H$ group of the PIB ligand. One would expect to see one band in this spectral range due to the chemical equivalence of the the $C\equiv C-H$ groups. We suppose that the weak band at 3305 cm^{-1} may originate from a second isomer coexisting at room temperature. In comparison to the OH stretching vibration of the type I complexes, the vibration of the $C\equiv C-H$ group is not influenced by the Ln metal center (cf. inset Fig. 6). The $C\equiv C-H$ groups are not part of the inner coordination sphere, they point outwards. As a consequence, they are not influenced by the Ln metal centers, whereas the OH groups of the type I complexes are in the inner coordination sphere and the influence of the metal center is more pronounced resulting in the observed red and blue shifts. In the spectral range from 2800 to 3000 cm^{-1} , there are three bands, a strong band at 2975 cm^{-1} , and two weak bands at 2925 and 2880 cm^{-1} . These spectral features are quite similar to those of the type I complexes, and we assign those bands to aliphatic CH stretching vibrations. In the fingerprint region ($1300-$

1650 cm^{-1}), there are several bands. All complexes reveal a strong band at 1550 cm^{-1} originating from red shifted CO stretching vibrations due to their coordination to the metal centers as discussed in the case of the type I complexes. The IRMPD spectra of all complexes show weak bands at 1485, 1420, and 1365 cm^{-1} which can be assigned to C-C stretching and C-H bending modes. The trimetallic $[\text{Fe}_4\text{DyY}]^+$ complex (olive curve) exhibits a significant different IRMPD spectrum in this spectral range. There is an additional band at 1650 cm^{-1} which could not be observed for the other complexes. The band at 1550 cm^{-1} is broader and seems to be asymmetric, while the bands of the other complexes are sharp. Additionally, the bands at 1485, 1420, and 1365 cm^{-1} are more intense than the bands of the other complexes. We suppose that the different metals influence the ligand framework leading to an asymmetric geometry distortion of the complex. Due to this distortion, the complex may become unstable and this results in more intense IRMPD yields. Additionally, changes in the geometry may cause changes within the dipole moment. Different transition dipole moments result in different IR absorptions. Note that the IRMPD process is a highly nonlinear process.^[11, 13, 14] This makes comparing IRMPD intensities among themselves and towards CID experiments a difficult task and probably inaccurate. Therefore, IRMPD and CID results are not necessarily redundant, as seen for the type I complexes.

Unfortunately, there are no geometry optimizations and computed linear absorption spectra done so far for the type I and II complexes. Without these computations, we can only speculate about the gas phase structure of the complexes and the metal-metal interactions. Nevertheless we observed changes and shifts in the stretching vibrations but the influence of the metal centers remains unclear.

We plotted the frequencies of the OH (red), the sp^3CH (green), and the CO (blue) bands in dependence of the Ln metal center for the type I complexes (Fig. 7). The Ln metal centers are in the same order as they occur in the periodic table of the elements. The bands reveal red or blue shifts in dependence of the Ln metal centers. Depending on the nature of the band, the shifts are more or less distinct.

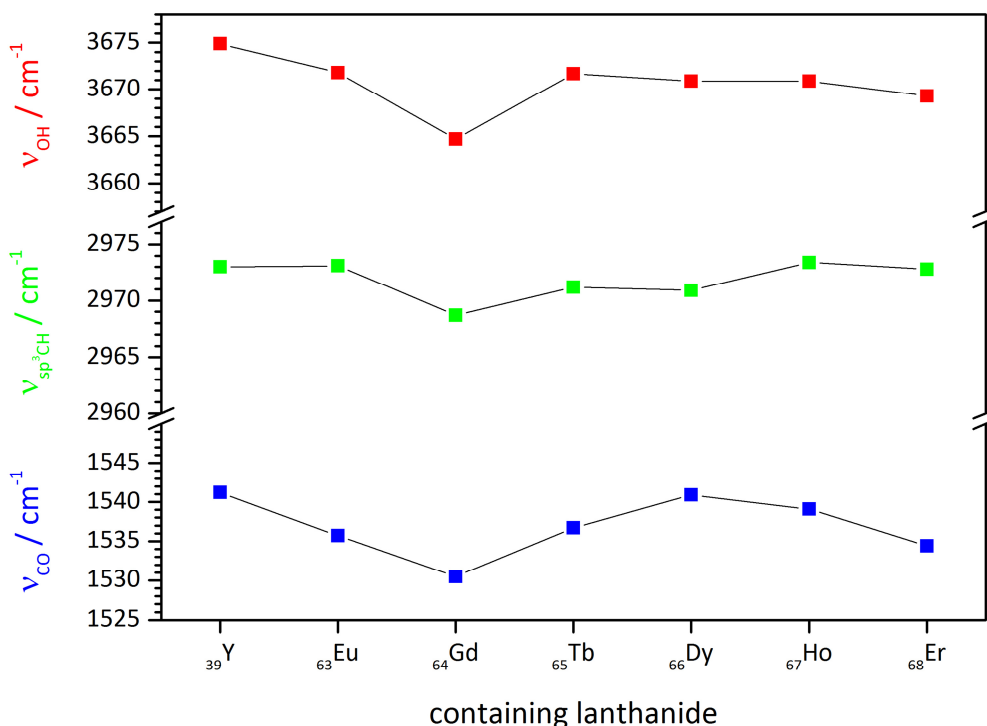


Figure 7: Shifts of the OH, sp^3CH and CO stretching vibration frequencies in dependence of the Ln metal centers within the IRMPD spectra of the type I $[\text{Fe}_4\text{Ln}_2]^+$ complexes.

The OH stretching band reveals a trend. The heavier the Ln metal center, the lower the frequency and thus the bigger the red shift. The complex, containing Gd metal centers, exhibits to be an exception. The OH band of this complex shows the biggest red shift, e.g. 10 cm^{-1} compared to the frequency of the $[\text{Fe}_4\text{Y}_2]^+$ complex. We assume that the different electronic structure of the $[\text{Fe}_4\text{Gd}_2]^+$ complex causes the structural changes. Gd(III) cations reveal a $[\text{Xe}] 5d^0 6s^0 4f^7$ electron shell configuration, i.e. the f-orbitals are half filled. Thus means that the shape of the Gd cations is spherical, while the shape of the electron density of the other Ln metals is oval.^[29] This different electron density shapes affect the complex geometry significantly. The sp^3CH band does not reveal major changes in the frequencies in dependence of the Ln metal centers. There is no obvious trend in dependence of the Ln metal center. Thus the Ln metals do not affect the CH stretching modes in a significant manner. Regarding the CO stretching vibrations, the Ln metals influence the frequencies significantly. Firstly, the frequencies shift red due to the direct coordination of the CO groups to the metal centers. The metal centers weaken the CO bond leading to lower frequencies.

One would expect to see CO stretching vibrations within the range of 1600 - 1900 cm^{-1} . Secondly, the trend follows the trend of the OH band. The frequencies decrease until Gd, rise up to Dy and decrease again. Again, the $[\text{Fe}_4\text{Gd}_2]^+$ complex seems to be an exception due to the biggest red shift of the CO stretching mode. The CO stretching mode reveals a shift of 10 cm^{-1} with respect to the frequency of the $[\text{Fe}_4\text{Y}_2]^+$ complex.

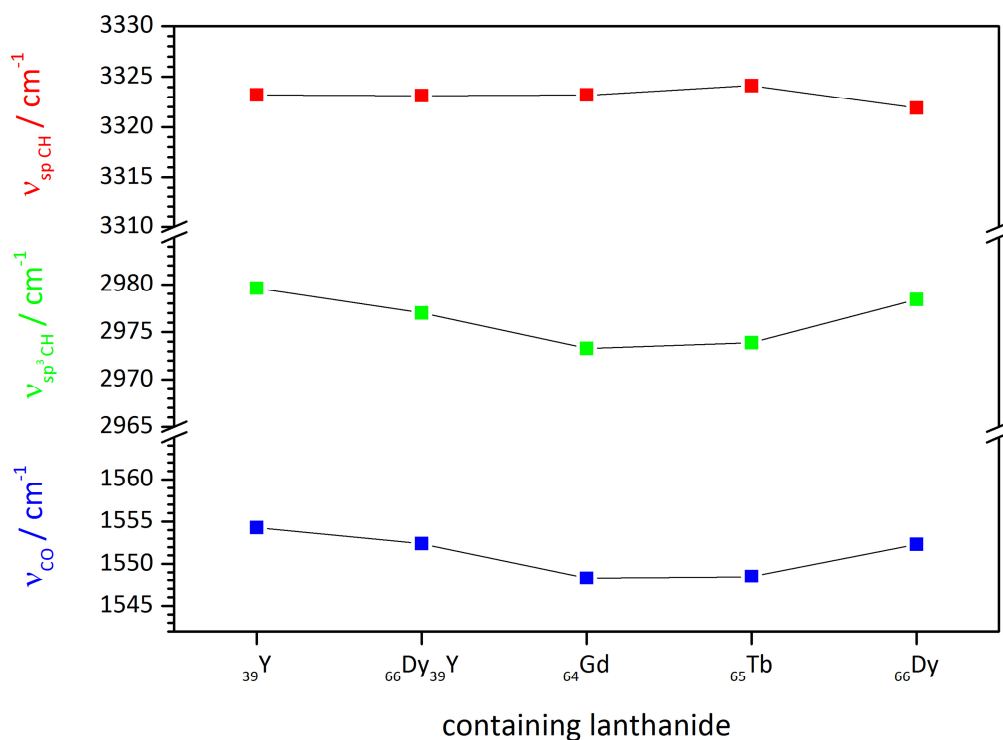


Figure 8: Shifts of the OH, sp^3CH and CO stretching vibration frequencies in dependence of the Ln metal centers within the IRMPD spectra of the type II $[\text{Fe}_4\text{Ln}_2]^+$ complexes.

We plotted the frequencies of the spCH (red), the sp^3CH (green) and the CO (blue) bands in dependence of the Ln metal center for the type II complexes (Fig. 8). The Ln metal centers are in the same order as they occur in the periodic table of the elements. The spCH stretching mode does not reveal significant frequency shifts in dependence of the Ln metal centers. These vibrations are not influenced due to their location in the outer coordination sphere. The influence of the Ln metal center becomes obvious for the sp^3CH and the CO stretching modes. Once more, the CO stretching frequency is red shifted due to the direct

coordination to the Ln metal centers. Both stretching modes exhibit a growing red shift of the frequency up to Gd as a minimum. The frequency rises for Tb and Dy. As seen in the case of the type I complexes, in the $[\text{Fe}_4\text{Gd}_2]^+$ complex the frequency shifts are the largest. Again, we suppose that the electronic structure and thus the shape of the Gd metal center influences the geometry of the complex resulting in the observed band shifts.

6.6 Summary and conclusion

We performed collision-induced dissociation experiments on $[\text{Fe}_4\text{Ln}_2]^+$ complexes of two different types I and II. CID appearance curves reveal significant changes in the fragmentation thresholds in dependence of the used Ln metal center in the case of the type I complexes. Furthermore, the $[\text{Fe}_4\text{Dy}_2]^+$ complex shows a change in the shape of the curve seemingly arising from a tight transition state passed during the fragmentation process. The type II complexes exhibit similar fragmentation thresholds and do not show a significant influence of the Ln metal centers on the fragmentation thresholds. The investigated type II complexes fragment at higher activation magnitudes than the type I complexes. We ascribe the found differences to the ability to form π -backbondings and to the degree of occupation of anti- or non-bonding orbitals weakening metal to ligand bindings. The higher stability of the $[\text{Fe}_4\text{Y}_2]^+$ complex apparently arises from the fact that Y does not belong to the group of lanthanides and uses 4d orbitals instead of 4f orbitals to form bonds to the ligands.

The different Ln metal centers influence the experimental IRMPD spectra of the type I complexes. The OH, sp^3CH and CO stretching modes exhibit blue or red shifts in dependence of the Ln metal centers. The CO stretching mode shifts red significantly due to the direct coordination to metal centers. However, this red shift varies depending on the Ln metal. The OH stretching mode is considerably influenced by the Ln metal and shifts blue or red depending on the Ln metal center. Hereby, the $[\text{Fe}_4\text{Gd}_2]^+$ complex exhibits the biggest red shift, while the $[\text{Fe}_4\text{Y}_2]^+$ reveals the biggest blue shift. In the case of the type II complexes, the sp^3CH and the CO stretching modes show obvious spectral shifts in dependence of the Ln metal centers. The spCH stretching mode is not influenced by the metal centers. Again, the complex, containing Gd metal centers, reveal the biggest red shifts. We assume that the

spherical electron density resulting from a half filled f-shell of the Gd metal centers^[29] induces the observed spectral changes within the IRMPD spectrum of the type **I** and **II** $[\text{Fe}_4\text{Gd}_2]^+$ complex. However, calculations are needed to elucidate the influence of the Ln metal centers on the structure and vibrational frequencies of the type **I** and **II** complexes.

6.7 References

- [1] G. Aromí, Winpenny, R., *Single-Molecule Magnets and Related Phenomena*, Springer Verlag New York, **2006**.
- [2] D. Imanbaew, Y. Nosenko, C. Kerner, K. Chevalier, F. Rupp, C. Riehn, W. R. Thiel and R. Diller, *Chemical Physics*, **2014**, 442, 53-61.
- [3] J. R. Friedman and M. P. Sarachik, in *Annual Review of Condensed Matter Physics, Vol 1*, ed. J. S. Langer, Annual Reviews, Palo Alto, **2010**, vol. 1, pp. 109-128.
- [4] R. Sessoli and A. K. Powell, *Coordination Chemistry Reviews*, **2009**, 253, 2328-2341.
- [5] R. A. Layfield, *Organometallics*, **2014**, 33, 1084-1099.
- [6] J. Tang, Zhang, P., *Lanthanide Single Molecule Magnets*, Springer Verlag New York, **2015**.
- [7] S. T. Liddle and J. van Slageren, *Chemical Society reviews*, **2015**, 44.
- [8] D. Stepanenko, M. Trif and D. Loss, *Inorganica Chimica Acta*, **2008**, 361, 3740-3745.
- [9] L. Ungur, S. Y. Lin, J. K. Tang and L. F. Chibotaru, *Chemical Society Reviews*, **2014**, 43, 6894-6905.
- [10] M. N. Leuenberger and D. Loss, *Nature*, **2001**, 410, 789-793.
- [11] N. C. Polfer, *Chemical Society Reviews*, **2011**, 40, 2211-2221.
- [12] L. MacAleese and P. Maitre, *Mass Spectrometry Reviews*, **2007**, 26, 583-605.
- [13] T. D. Fridgen, *Mass Spectrometry Reviews*, **2009**, 28, 586-607.
- [14] G. von Helden, J. Oomens, B. G. Sartakov and G. Meijer, *International Journal of Mass Spectrometry*, **2006**, 254, 1-19.
- [15] F. Menges, C. Riehn and G. Niedner-Schatteburg, *Zeitschrift Fur Physikalische Chemie-International Journal of Research in Physical Chemistry & Chemical Physics*, **2011**, 225, 595-609.
- [16] R. H. Schultz, K. C. Crellin and P. B. Armentrout, *Journal of the American Chemical Society*, **1991**, 113, 8590-8601.
- [17] P. B. Armentrout, B. Yang and M. T. Rodgers, *Journal of Physical Chemistry B*, **2014**, 118, 4300-4314.
- [18] A. Fedorov, E. P. A. Couzijn, N. S. Nagornova, O. V. Boyarkin, T. R. Rizzo and P. Chen, *Journal of the American Chemical Society*, **2010**, 132, 13789-13798.
- [19] S. Narancic, A. Bach and P. Chen, *Journal of Physical Chemistry A*, **2007**, 111, 7006-7013.

- [20] J. B. Fenn, *Angewandte Chemie-International Edition*, **2003**, 42, 3871-3894.
- [21] M. Yamashita and J. B. Fenn, *Journal of Physical Chemistry*, **1984**, 88, 4451-4459.
- [22] S. Torker, D. Merki and P. Chen, *Journal of the American Chemical Society*, **2008**, 130, 4808-4814.
- [23] M. T. Rodgers, K. M. Ervin and P. B. Armentrout, *Journal of Chemical Physics*, **1997**, 106, 4499-4508.
- [24] J. C. Slater, *Journal of Chemical Physics*, **1964**, 41, 3199-&.
- [25] E. Clementi, D. L. Raimondi and Reinhard.Wp, *Journal of Chemical Physics*, **1967**, 47, 1300.
- [26] W. M. Haynes, *Handbook of Chemistry & Physics*, CRC, **2014-2015**.
- [27] Holleman-Wieberg, *Lehrbuch der anorganischen Chemie*, de Gruyter, **1995**.
- [28] G. L. Miessler, Fischer, P.J., Tarr, D.A., *Inorganic Chemistry*, Prentice Hall: New Jersey, **2013**.
- [29] J. D. Rinehart and J. R. Long, *Chemical Science*, **2011**, 2, 2078-2085.

7. IR Spectroscopic Investigations of Electronic Excited States in a Ruthenium Complex

Maximilian Gaffga, Agnes Fizia, Werner R. Thiel and Gereon Niedner-Schatteburg

*Fachbereich Chemie und Forschungszentrum OPTIMAS, Technische Universität
Kaiserslautern, 67663 Kaiserslautern, Germany*

7.1 Preamble

The following chapter was prepared as a manuscript for publication. It is not submitted so far. All presented measurements, data evaluation, computations and all of the preparation of the manuscript itself were performed by myself. I received experimental support by Joachim Hewer, and I exchanged ideas with my colleagues Matthias Tombers and Johannes Lang. Gereon Niedner-Schatteburg helped by discussions. Agnes Fizia of the Thiels group synthesized the compounds.

7.2 Abstract

We present collision-induced dissociation (CID) and infrared multi photon dissociation (IRMPD) investigations on three derivatives of a ruthenium(II) complex **1**, **2** and **3**. Upon collision-induced dissociation (CID) we found elimination of HCl and cymene along with H₂ units. Electronic and steric effects influence the stability and thus the activation energies of the investigated complexes. IRMPD spectroscopy allows for structure determination in combination with computed linear absorption spectra of the most stable isomers. The IRMPD spectrum of complex **3** exhibits blue shifted bands with respect to the bands of the complexes **1** and **2**. Further IRMPD investigations on “aged” sample solutions show evidence for a rearrangement in solution since bands in the IRMPD spectra vanish in comparison with “fresh” sample solutions. The comparison with computed spectra leads to the assumption that an isomerization from a ruthenium nitrogen bond isomer to a ruthenium carbanion bond isomer takes place. Extension of the measurement range to higher energies reveals broad bands in the range from 4000 to 7500 cm⁻¹ arising from either metal to ligand (MLCT) or ligand to metal (LMCT) charge transfers. Time-dependent (TD) DFT calculations serve to investigate electronic transitions within this spectral range agreeing with the experimental IRMPD spectrum.

7.3 Introduction

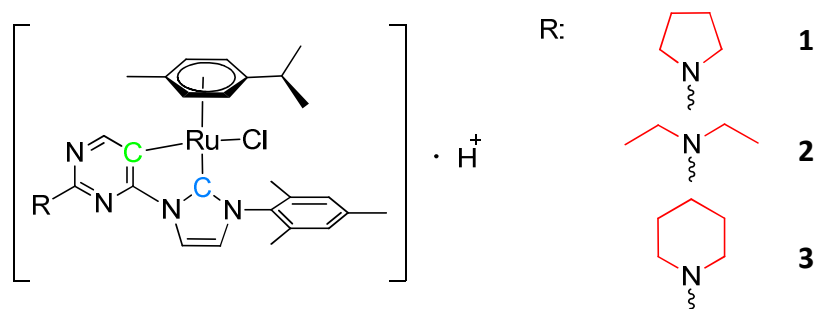
Transition metal based complexes, such as ruthenium complexes, have a versatile range of applications. The catalytic activity of ruthenium containing compounds is well known, e.g. ruthenium may be used to perform transfer hydrogenation reactions and asymmetric transfer hydrogenations.^[1-7] Furthermore, ruthenium-based dyes serve as solar energy converters and can be used for light absorption in dye-sensitive solar cells.^[8, 9]

These dyes serve as photosensitizer.^[10-12] A photosensitizer is a compound that induces a chemical change in adjacent molecules in a photochemical process as a consequence of light absorption in the visible region.^[13, 14] The absorption of light involves a metal to ligand charge transfer (MLCT).^[15] An efficient photosensitizer dye requires an intense absorption of

light providing a sufficient amount of energy. Many different compounds have been investigated and tested for their photosensitive efficiency, and polypyridine ruthenium complexes are proven to be reasonable systems due to intense charge transfer bands.^[9, 16]

Pioneer work on charge transfer investigations was done by *Creutz* and *Taube* and awarded with the Nobel Prize in chemistry.^[17, 18] They showed that mixed-valence ruthenium systems, which comprise pyridine, reveal charge transfer bands in solution. Recent investigations on substituted ruthenium bipyridine complexes exhibit electron charge transfer processes between nitrogen and ruthenium in the near-IR region (between 4000 and 7000 cm^{-1}).^[19]

Herein, we report on the studies of three ruthenium complexes as model systems for gas phase investigations (Scheme 1). Furthermore, the investigated species involve a ruthenium carbon coordination sphere instead of a ruthenium nitrogen binding motif as present in the usual photosensitizers.



Scheme 1: Molecular structure of the three ruthenium complexes **1**, **2** and **3**. Note that the ruthenium(II) coordinates at the carbene (blue) and the carbanion (green) functional group of the NHC ligand. The three derivatives differ in the functional group of the tertiary amine (red). For mass spectrometry analysis, the neutral complex is protonated.

This work is part of our ongoing research on the interaction of transition metal centers with organic ligand systems. The combination of mass spectrometry and infrared multi photon dissociation (IRMPD) spectroscopy serves as a valuable tool for structural analysis of trapped ions in the gas phase.^[20-22] We apply IRMPD spectroscopy for the structural characterization of the three ruthenium complexes in the gas phase. Extension of the IRMPD measurement

range to the mid-IR range allows for the investigation of charge transfer transitions after IR light absorption. We apply time-dependent density functional theory (TD-DFT) computations to support the mid-IR measurements in order to estimate charge transfer transitions and to model electronic excited spectra.^[23, 24] Furthermore, we perform collision-induced dissociation (CID) experiments to get insights into the fragmentation behavior of the ruthenium complexes.^[25, 26]

7.4 Experimental setup and theoretical methods

7.4.1 Experimental setup

The presented electrospray ionization mass spectrometry (ESI-MS) was performed with two ion trap instruments (Bruker Esquire 6000 for CID and amaZonSL for IRMPD measurements). The investigated cations were produced in the positive electrospray ionization mode. The scan speed was $13000 \frac{m}{z \cdot s}$ in the normal resolution scan mode ($0.3 \text{ fwhm} / \frac{m}{z}$). The scan range was at least 70 to $1500 \frac{m}{z}$. Sample solutions of complex **1**, **2** and **3** in acetonitrile (MeCN) at concentrations of approximately 1×10^{-4} M were continuously infused into the ESI chamber at a flow rate of 2 $\mu\text{l}/\text{min}$ using an automatical syringe pump. For our investigations, we measured sample solutions of two different types, called “fresh” and “aged”. The measurements of the “fresh” sample solutions were performed at the day of its preparation, while the measurements of the “aged” sample solutions were performed one day after its preparation. The “aged” sample solution was stored in the air at room temperature. We used nitrogen as a drying gas at a flow rate of 3.0 to 4.0 l/min between 220 and 300 °C. We sprayed the solutions at a nebulizer gas pressure of 3 to 4 psi with the electrospray needle held at 4.5 kV. We used helium as a buffer gas with a partial pressure of about 3×10^{-3} mbar inside the ion trap. BrukerEsquireControl 5.3 (Esquire) and BrukerTrapControl 7.0 (amaZonSL) software controlled the instrument, and we performed data analysis using the Data Analysis 4.0 software.

Collision induced dissociation (CID) appearance curves were recorded by varying the excitation magnitude from 0.0 to 1.5 corresponding to an excitation energy scale in the lab

frame (E_{LAB}).^[27] These excitation energies were increased in a stepwise fashion until complete dissociation of the ion of interest was observed. Normalized relative and total fragmentation yields were calculated according to:

$$I_{i,norm}^{fr}(E_{LAB}) = \frac{I_i^{fr}(E_{LAB})}{\sum_i I_i^{fr}(E_{LAB}) + \sum_i I_i^p(E_{LAB})} \quad (1a)$$

$$I_{tot}^{fr}(E_{LAB}) = \sum_i I_{i,norm}^{fr}(E_{LAB}) \quad (1b)$$

Center of mass transformed relative excitation energies (E_{COM}) were calculated from the internal amplitudes as following:

$$E_{COM} = \frac{m_{He}}{m_{He} + m_{ion}} \cdot E_{LAB} \quad (2)$$

m_{ion} was chosen according to the most abundant mass peak of the molecule.

An optical parametric oscillator/amplifier (OPO/OPA, LaserVision) laser system pumped with a pulsed injection seeded Nd³⁺:YAG laser (Continuum-PL8000, 10 Hz) was used as a source of tunable IR radiation ($\delta\bar{\nu} = 0.9 \text{ cm}^{-1}$, $\delta t = 7 \text{ ns}$) for recording the vibrational spectra. Spectra within the frequency range of 2600 – 3700 cm^{-1} were recorded by application of the OPA idler wave ($\leq 10 \text{ mJ}$ per pulse). Spectra within the frequency range of 3700 – 7500 cm^{-1} were recorded by application of the OPA signal wave ($\leq 10 \text{ mJ}$ per pulse). The difference frequency (DF) between the OPA signal and idler waves, generated in a AgGaSe₂ crystal ($\leq 2 \text{ mJ}$ per pulse) was used for the energy range of 1200 – 2100 cm^{-1} . After passing through the ion trap chamber the IR beam was directed onto a power meter sensor to record the laser power during the measurement. The idler and signal beam were focused by a 50 cm CaF₂ lens. The DF radiation was focused tighter by a 90° off-axis parabolic silver mirror with an effective focal length of 15 cm. The IR pulse energy was recorded by a power meter sensor that obtained the applied photon beam after exiting the ions inside the mass spectrometer through a second window. From the recorded fragment and parent ion intensities, we determine an IRMPD yield (Y) as:

$$Y = \frac{\sum_i I_i^{fr}}{\sum_i I_i^{fr} + \sum_i I_i^p} \quad (3)$$

The applied IR frequencies were calibrated by a wave meter (Bristol Instruments: 821 Pulsed Laser Wavelength Meter) to a theoretical accuracy of $\pm 0.02 \text{ cm}^{-1}$ which is beyond the

spectral bandwidth of the utilized IR photon beams by more than an order of magnitude. Note that IRMPD yields scale in an intrinsically nonlinear way with the applied IR photon flux. Therefore, we refrained from any normalization.

7.4.2 Theoretical methods

We conducted electronic structure calculations at the B3LYP^[28-31]/cc-pVDZ^[32-34] level of theory with the Stuttgart RSC 1997^[35, 36] effective core potential representing the ruthenium atom as implemented in the Gaussian 09 program package.^[37] We performed full geometry relaxation of the molecular structures of the most stable isomers and computed their linear absorption spectra. Standard convergence criteria were applied. Harmonic vibrational frequencies were scaled by a linear lump-sum scaling factor of 0.97 as suggested elsewhere.^[38] Furthermore, we apply time-dependent density functional theory (TD-DFT) computations in order to model electronic excited spectra.^[39, 40]

7.5 Results and discussion

7.5.1 Mass spectrometric analysis and identification

The main peaks of the ESI mass spectra obtained from acidulated MeCN solutions of the complexes **1**, **2** and **3** are located at $\frac{m}{z} = 605$, $\frac{m}{z} = 607$, and $\frac{m}{z} = 619$ (most abundant mass peaks) in the positive ion mode. These peaks correspond to the singly protonated complexes **1** (ClRu(C₂₆H₂₉N₄)C₄H₈N)⁺, **2** (ClRu(C₂₆H₂₉N₄)C₄H₁₀N)⁺, and **3** (ClRu(C₂₆H₂₉N₄)C₅H₁₀N)⁺, respectively (Scheme 1). The elemental composition is unequivocally assigned by their isotopic patterns (cf. Fig. S1 – S3 in the supporting information).

7.5.2 Collision-induced dissociation studies (CID)

We performed collision-induced dissociation studies in order to get insights in the fragmentation behavior of the mass-selected complex ions **1**, **2** and **3**. Application and stepwise increase of an activation magnitude up to complete depletion of the precursor ions allows for the recording of CID appearance curves (Fig. 1).

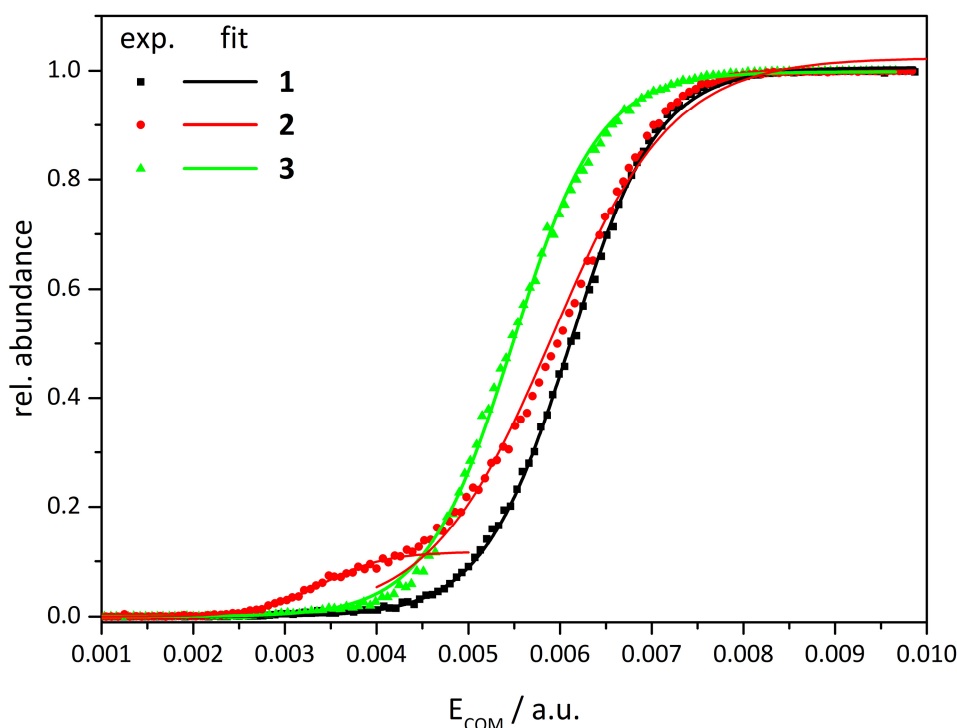


Figure 1: CID appearance curves of the mass-selected ruthenium complexes **1**, **2** and **3**. The dots represent the experimental data points and the lines are sigmoid fit functions. The curve of complex **2** includes two sigmoid fit functions due to the contribution of two coexisting isomers.

Complex **2** (red curve) reveals a significant difference in the curves' shape in comparison to the curves of complex **1** and **3**. The curves' shape indicates a combination of two individual curves. This behavior is evidence for two isomers fragmenting at different activation magnitudes. We suppose that two isomers coexist in solution. The dissociation of the first isomer of complex **2** starts at an activation magnitude of $E_{\text{COM}} = 0.003$ a.u. and the second isomer around $E_{\text{COM}} = 0.004$ a.u.. Due to this two isomer population, the data points of

complex **2** are fitted by two sigmoid fit functions. The rise of the curve is an indication for the tightness of the transition state which is passed during the fragmentation process. The unimolecular decomposition of ions is subject to thermodynamic versus kinetic reaction control: the kinetic product forms faster, whereas the thermodynamic product is more stable.^[41, 42] The more stable a product, the flatter the slope (thermodynamically favored) leading to a tight transition state. In contrast, a steep slope, i.e. a weak bonded product (kinetically favored) indicates a loose transition state. An activated complex with strict steric requirements is referred to be a tight complex, whereas the transition state without such requirements is called a loose complex.^[43-46] The curves' slope for the first isomer is considerably flatter than the curves' slope for the second isomer. This indicates that the first isomer passes through a tighter transition state than the second isomer.

Complex **3** needs an activation magnitude of $E_{\text{COM}} = 0.004$ a.u. to dissociate. Complex **1** appears to be the most stable complex and reveals an activation magnitude of $E_{\text{COM}} = 0.0045$ a.u.. This contradicts the assumption that the higher the energy needed for fragmentation, the higher the heat capacity. Lower heat capacities enable an increase in fragmentation yields even within the same activation magnitude because of less degrees of freedom.^[47, 48] A higher amount of degrees of freedom serve to store more energy during collisional activation. Therefore, the complexes **2** and **3** should reveal higher activation magnitudes due to their higher heat capacity. Indeed, complex **1** shows the highest activation magnitude. Thus electronic or steric effects play a role and affect the fragmentation behavior.

Upon CID, the mass-selected ions show the loss of HCl and the elimination of the cymene ligand (Cym) along with additional H₂ units (Table 1). Recent investigations on ruthenium complexes with analogical structures reveal the loss of H₂ units as well.^[49] The three complexes reveal similar fragmentation patterns. Note that complex **2** reveals additional elimination of ethylene groups.

Table 1: Main fragmentation channels of the complexes **1**, **2** and **3**. Primary neutral losses are HCl and cymene (Cym) along with additional H₂ units.

| species | neutral loss | | | |
|----------|----------------------|---------------------------|----------------------------|----------------------------|
| 1 | -HCl -H ₂ | -HCl -2H ₂ | -Cym -H ₂ | -Cym -HCl -2H ₂ |
| 2 | -HCl | -HCl-H ₂ | -HCl -Et -H ₂ | -HCl -Et -2H ₂ |
| | -Cym -H ₂ | -Cym -HCl -H ₂ | -Cym -HCl -2H ₂ | -Cym -HCl -3H ₂ |
| 3 | -HCl -H ₂ | -HCl -2H ₂ | -Cym -H ₂ | -Cym -HCl -2H ₂ |

Plotting the appearance curves per fragmentation channels exhibits the abstraction of HCl as the main fragmentation channel for all complexes **1**, **2** and **3** (Fig. 2).

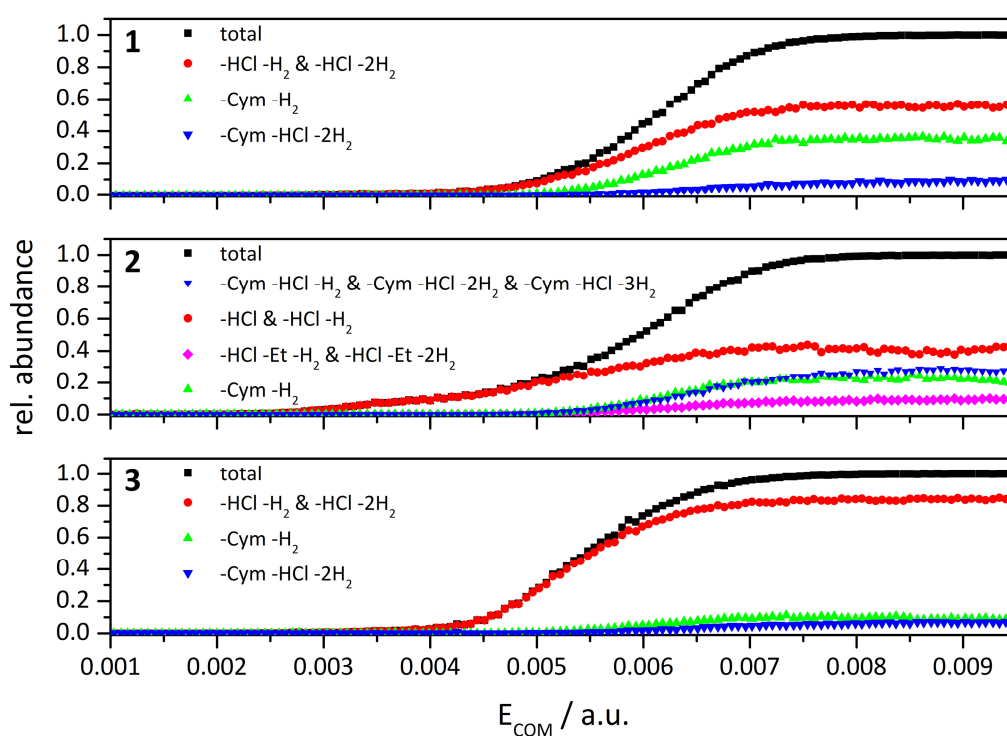


Figure 2: Center of mass transformed fragmentation amplitudes forming the CID appearance curves per single fragmentation channel of the mass-selected complexes **1**, **2** and **3**.

In the following, we neglect to separate the fragmentation channels with and without the abstraction of H₂ units. This separation would not be unambiguous due to their overlapping isotopic patterns. At low activation magnitudes ($E_{\text{COM}} = 0.0045$ a.u.) complex **1** shows HCl abstraction (red dots), while the elimination of the cymene ligand occurs at $E_{\text{COM}} = 0.005$ a.u. (green triangles). The elimination of the cymene ligand along with HCl is less pronounced (blue triangles). The first dissociated isomer of complex **2** exhibits only HCl elimination ($E_{\text{COM}} = 0.003$ a.u., red dots). At an activation magnitude of $E_{\text{COM}} = 0.005$ a.u., the abstraction of the cymene ligand and the simultaneous elimination of cymene along with HCl occurs. At this activation magnitude, the fragmentation arises from the second isomer of complex **2**. The elimination of HCl remains the primary fragmentation channel. In the case of complex **3**, the elimination of HCl dominates the fragmentation pattern (red dots, $E_{\text{COM}} = 0.004$ a.u.). The abstraction of the cymene ligand (green triangles) as well as the elimination of cymene along with HCl (blue triangles) occur at an activation magnitude of $E_{\text{COM}} = 0.0055$ a.u..

7.5.3 IRMPD spectroscopy and structure determination

The experimental IRMPD spectra of the three ruthenium complexes **1**, **2** and **3** show three bands in the range from 2850 to 3000 cm⁻¹. This is the typical spectral range for aliphatic CH stretching vibrations. Furthermore, the spectra exhibit three bands between 1500 and 1650 cm⁻¹. One would expect to see C=C and C-N stretching vibrations as well as CH bending modes in this spectral range. Aromatic CH stretching vibrations should be seen between 3000 and 3200 cm⁻¹. There are weak bands between 3150 and 3170 cm⁻¹ in the experimental IRMPD spectra. Direct comparison of the IRMPD spectra of the three ruthenium complexes **1**, **2** and **3** reveal major spectral changes in the aliphatic CH stretching region (Fig. 3). The variation of the side group induces these observed spectral changes in the experimental IRMPD spectra due to the presence of different CH₂ groups.

On the one hand, a major change arises in the CH stretching vibration range. Complex **1** exhibits a strong band at 2985 cm⁻¹ and two weaker bands at 2935 and 2890 cm⁻¹. Complex **2** shows a strong band at 2990 cm⁻¹, a band at 2940 cm⁻¹ with a medium intensity, and a third very weak band at 2885 cm⁻¹. The intensities for complex **3** are completely different. The

band at 2975 cm^{-1} reveals a weak intensity, while the band at 2955 cm^{-1} is strong. Additionally, this band shifts blue by 20 cm^{-1} and the band at 2875 cm^{-1} shifts red by 15 cm^{-1} with respect to the bands of complex **1**. On the other hand, the IRMPD spectra of all three complexes **1**, **2** and **3** differ in their relative intensities in the range from 1500 to 1650 cm^{-1} . Complex **1** exhibits a strong band at 1615 cm^{-1} , a weak band at 1575 cm^{-1} , and a medium band at 1535 cm^{-1} . Complex **2** reveals three strong bands at 1615 , 1575 , and 1550 cm^{-1} . The band at 1550 cm^{-1} shifts blue by 15 cm^{-1} with respect to the band of complex **1**. The bands of complex **3** have weak intensities compared to the complexes **1** and **2** within this spectral range.

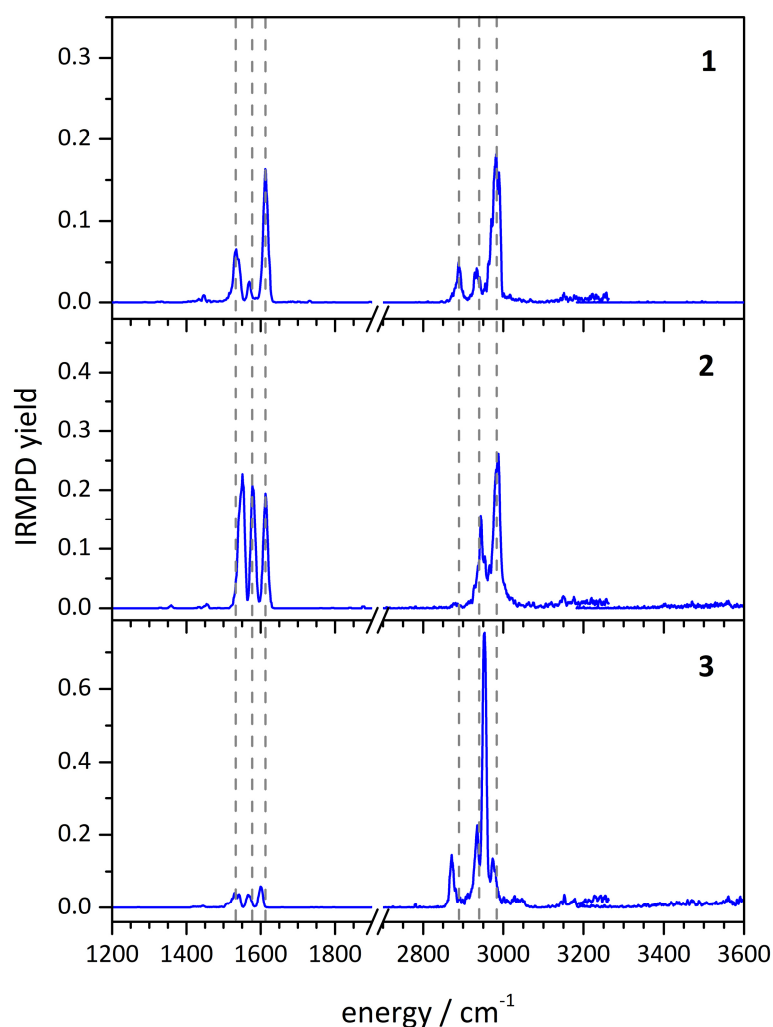


Figure 3: Direct comparison of the IRMPD spectra of the mass-selected complexes **1**, **2** and **3**. The dashed grey lines serve to guide the eye.

Since the IRMPD spectroscopy is an action spectroscopy, the band intensities depend on the laser power and the associated fragmentation. The fragmentation yield depends on the activation barrier, i. e., the nature of the investigated complex ion itself. For the presented IRMPD measurements, the conditions (laser power and irradiation time) were kept the same for each complex to ensure comparability (cf. laser power curves Fig. S6). Furthermore, the IR photon induced fragmentations deliver a similar fragmentation pattern as the collision-induced fragmentations as seen in previous work by ourselves.^[50]

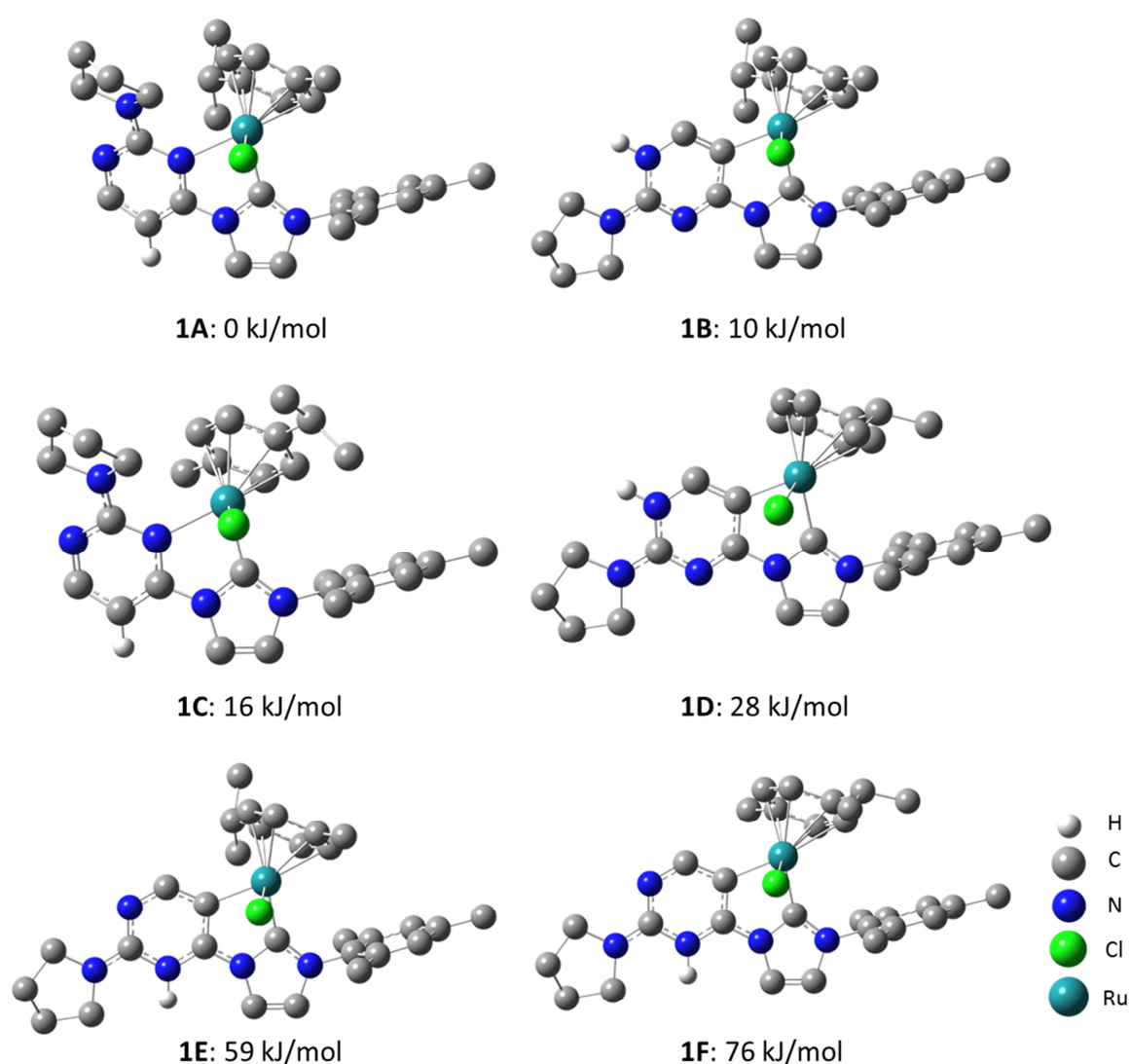


Figure 4: Computed low energy isomers of complex **1**. Relative energies are given with respect to the lowest energy isomer **1A**. Isomers with a relative energy higher than 100 kJ/mol are neglected. Note that hydrogen atoms are omitted for reasons of simplicity except for the protonating hydrogen atom.

The findings from the CID chapter (cf. chapter 7.5.2) reveal complex **2** fragmenting at the lowest activation magnitudes followed by complex **3** and **1**. The IRMPD spectra of the complexes **1** and **2** exhibit similar IRMPD yields. In contrast, the IRMPD spectrum of complex **3** shows more intense bands in the CH stretching vibration region. This may be due to an additional CH₂ group. Furthermore, complex **3** exhibits weaker bands in the region from 1500 to 1650 cm⁻¹. On the one hand, the heat capacity influences the fragmentation yield. The higher the heat capacity, the higher the energy needed for fragmentation.

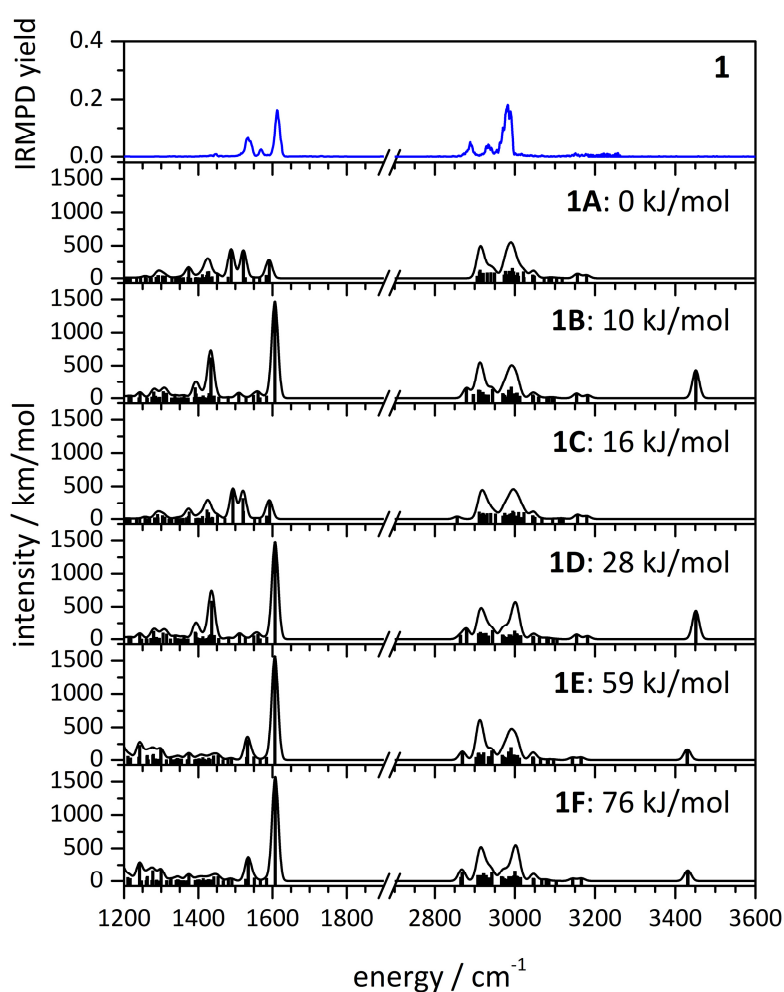


Figure 5: Experimental IRMPD spectrum of complex **1** (blue) and theoretically predicted IR spectra (black, B3LYP/cc-pVDZ and Stuttgart RSC representing the ruthenium, scaled by 0.97) of the six most stable isomers **1A-1F**. The frequency intensities above 2800 cm⁻¹ are multiplied by a factor of 5 for a better visualization. The stick spectra are folded with a Gaussian function (fwhm = 10 cm⁻¹).

Lower heat capacities enable an increase in fragmentation yields by the same given photon flux, since less degrees of freedom serving less energy storage. On the other hand, misalignment may cause the laser not to irradiate the entire ion cloud. This leads to lower fragmentation yields. Additionally, electronic and steric effects affect the fragmentation behavior.

Performing DFT calculations, we found several minimum structures for complex **1**. We selected the six most stable isomers found with relative energies < 100 kJ/mol with respect to the most stable isomer **1A** (Fig. 4). In this isomer **1A**, the ruthenium coordinates to the carbene of the imidazole ring, a nitrogen atom of the pyrimidine ring, to the chlorido ligand and the cymene. The protonation takes place at the carbanion of the pyrimidine ring. Changing the orientation of the cymene ligand results in isomer **1C** and in a relative instability of 16 kJ/mol. If the protonation takes place at a nitrogen atom of the pyrimidine ring, isomer **1B** is obtained. This leads to an instability of 10 kJ/mol. Based on the geometry of isomer **1B**, changing the orientation of the cymene leads to isomer **1D** and a relative instability of 28 kJ/mol. Through protonation of the nitrogen atom isomer **1E** is obtained with a relative instability of 59 kJ/mol. An additional change of the cymene orientation delivers isomer **1F** and a relative instability of 76 kJ/mol.

To determine the structure of complexes **1**, we computed the linear absorption spectra of the six isomers **1A-1F** (Fig. 5). Isomers with NH stretching vibrations can be excluded due to the missing band in the experimental IRMPD spectrum, i.e. the isomer **1B** as well as the isomers **1D-1F** are excluded. The computed spectra of the isomers **1A** and **1C** are in a good agreement with the experimental IRMPD spectrum. Since the structural difference between isomer **1A** and **1C** is the cymene orientation, the IRMPD spectrum does not allow for a separation between these orientations. The computed spectra reveal low intensities of the aromatic CH stretching vibrations, although they are already multiplied by a factor of 5. This observation is consistent with the very weak intensities of these bands in the experimental IRMPD spectrum.

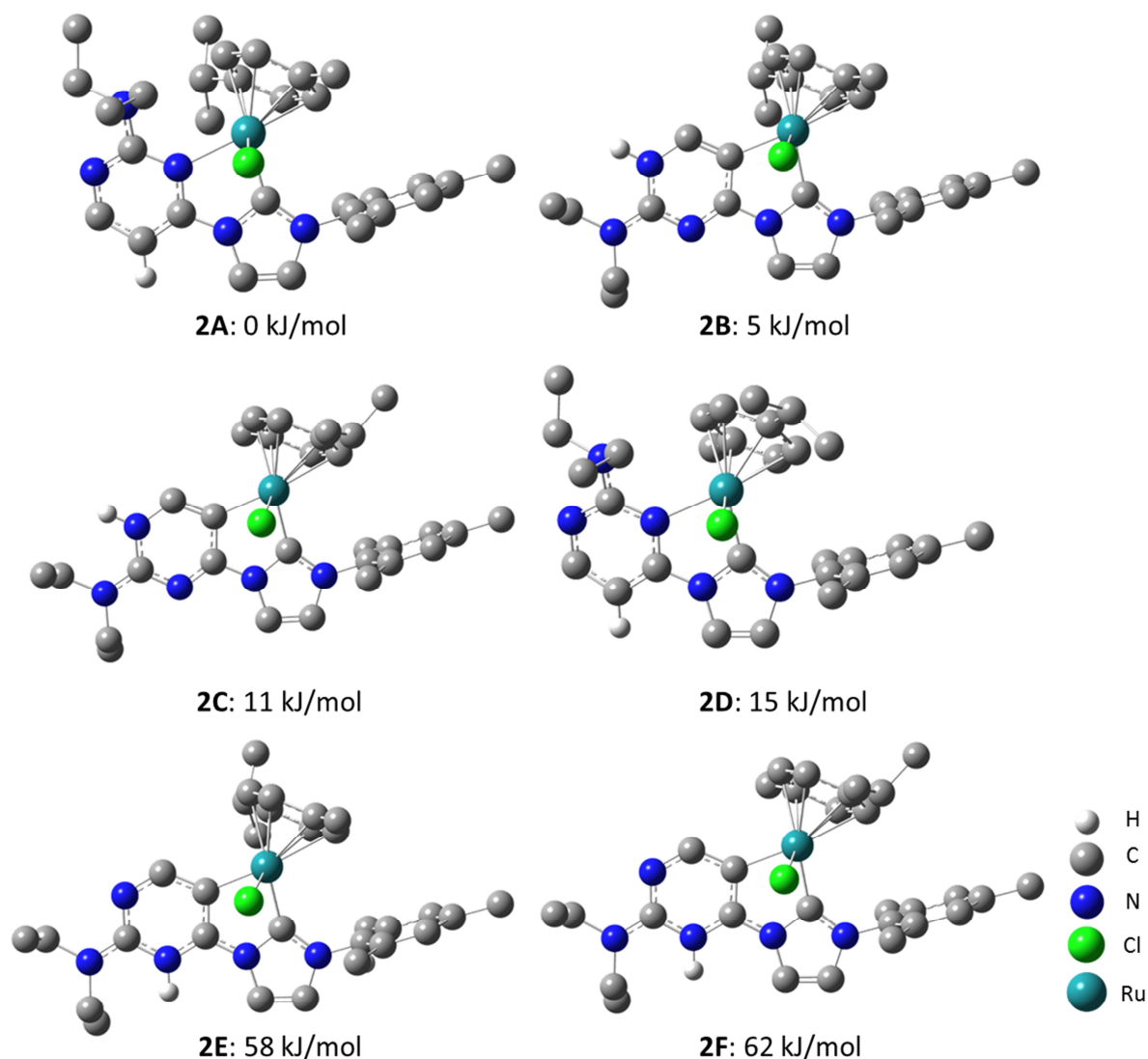


Figure 6: Computed low energy isomers of complex **2**. Relative energies are given with respect to the lowest energy isomer **2A**. Isomers with a relative energy higher than 100 kJ/mol are neglected. Note that hydrogen atoms are omitted for reasons of simplicity except for the protonating hydrogen atom.

We found several minimum structures for complex **2** and selected the six most stable isomers found with relative energies < 100 kJ/mol with respect to the most stable isomer **2A** (Fig. 6). This isomer **2A** reveals a coordination of the ruthenium to the carbene of the imidazole ring, to the nitrogen atom of the pyrimidine ring, to the chlorido ligand and the cymene. The protonation takes place at the carbanion of the pyrimidine ring. Isomer **2D** is obtained by changing the orientation of the cymene ligand. This leads to a relative instability of 15 kJ/mol. Protonation of the nitrogen atom of the pyrimidine ring delivers isomer **2B** and

a relative instability of 5 kJ/mol. Based on this geometry, the change of the cymene orientation leads to isomer **2C** and a relative instability of 11 kJ/mol. To obtain the isomer **1E** with a relative instability of 58 kJ/mol, protonation of the nitrogen atom has to take place. By changing the cymene orientation again, isomer **1F** with a relative instability of 62 kJ/mol is obtained.

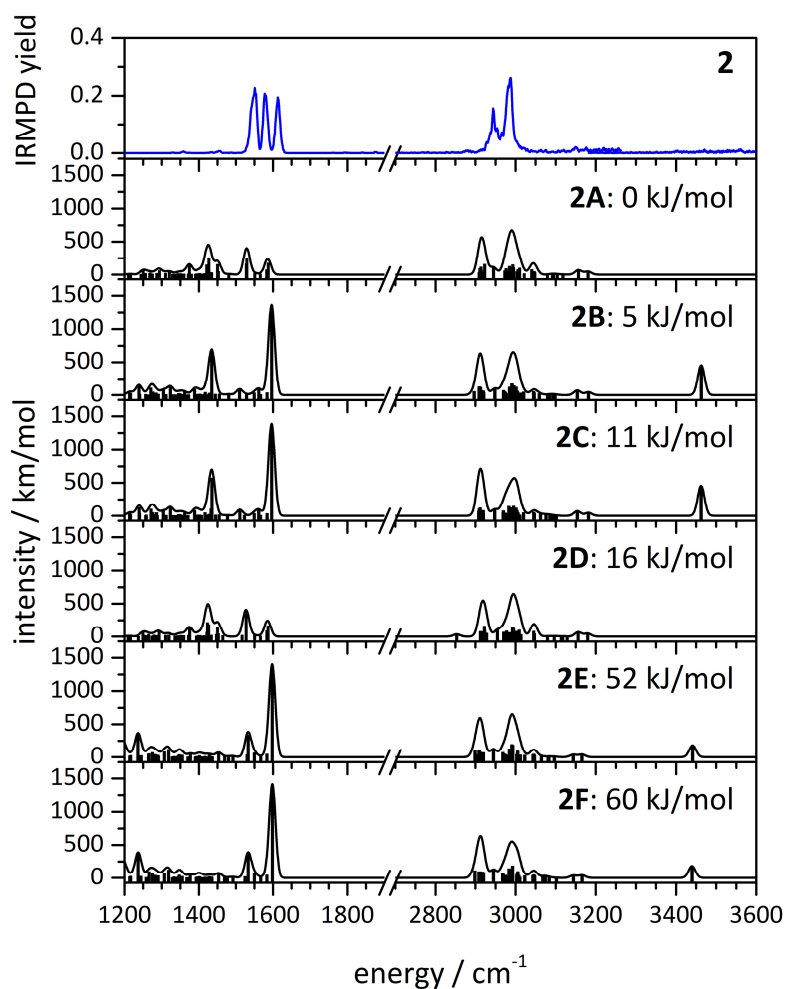


Figure 7: Experimental IRMPD spectrum of complex **2** (blue) and theoretically predicted IR spectra (black, B3LYP/cc-pVDZ and Stuttgart RSC representing the ruthenium, scaled by 0.97) of the six most stable isomers found **2A-2F**. The frequency intensities above 2800 cm⁻¹ are multiplied by a factor of 5 for a better visualization. The stick spectra are folded with a Gaussian function (fwhm = 10 cm⁻¹).

We computed the linear absorption spectra for the six most stable isomers found **2A-2F**. Comparison of these spectra with the experimental IRMPD spectrum allows for structure determination (Fig. 7). As well as in the case of complex **1**, the isomers revealing NH stretching vibrations can be excluded by missing the NH band in the experimental IRMPD spectrum, i.e. the isomer **2B** and **2C** as well as the isomers **2E** and **2F** can be excluded. The experimental IRMPD spectrum is well in line with the computed spectra of the isomers **2A** and **2D**. The geometries of the isomers **2A** and **2D** differ in the orientation of the cymene, and again, it is not possible to distinguish between the different orientations of the cymene with our experimental techniques. These findings are in a good agreement with the CID results. The two isomers found may be responsible for the two isomer specific appearance curve recorded using the collisional activation.

As for the complexes **1** and **2** we found several minimum structures for complex **3** and selected the six most stable isomers found with relative energies < 100 kJ/mol with respect to the most stable isomer **3A** (Fig. 8). Coordination of the ruthenium to the carbene of the imidazole ring, to the nitrogen atom of the pyrimidine ring, to the chlorido ligand and the cymene delivers the most stable isomer **3A**. The protonation takes place at the carbanion of the pyrimidine ring. Changing the orientation of the cymene leads to isomer **3B** and a relative instability of 5 kJ/mol. Variation of the protonation side results in the isomer **3C** and a relative instability of 11 kJ/mol. Isomer **3D** is obtained by the change the cymene orientation based on the geometry of isomer **3C**. This leads to a relative instability of 16 kJ/mol. To obtain the isomers **3E** and **3F**, the protonation takes place at of the pyrimidine ring. The difference between both isomers is the orientation of the cymene. This leads to relative instabilities of 52 kJ/mol for isomer **3E** and of 60 kJ/mol for isomer **3F**.

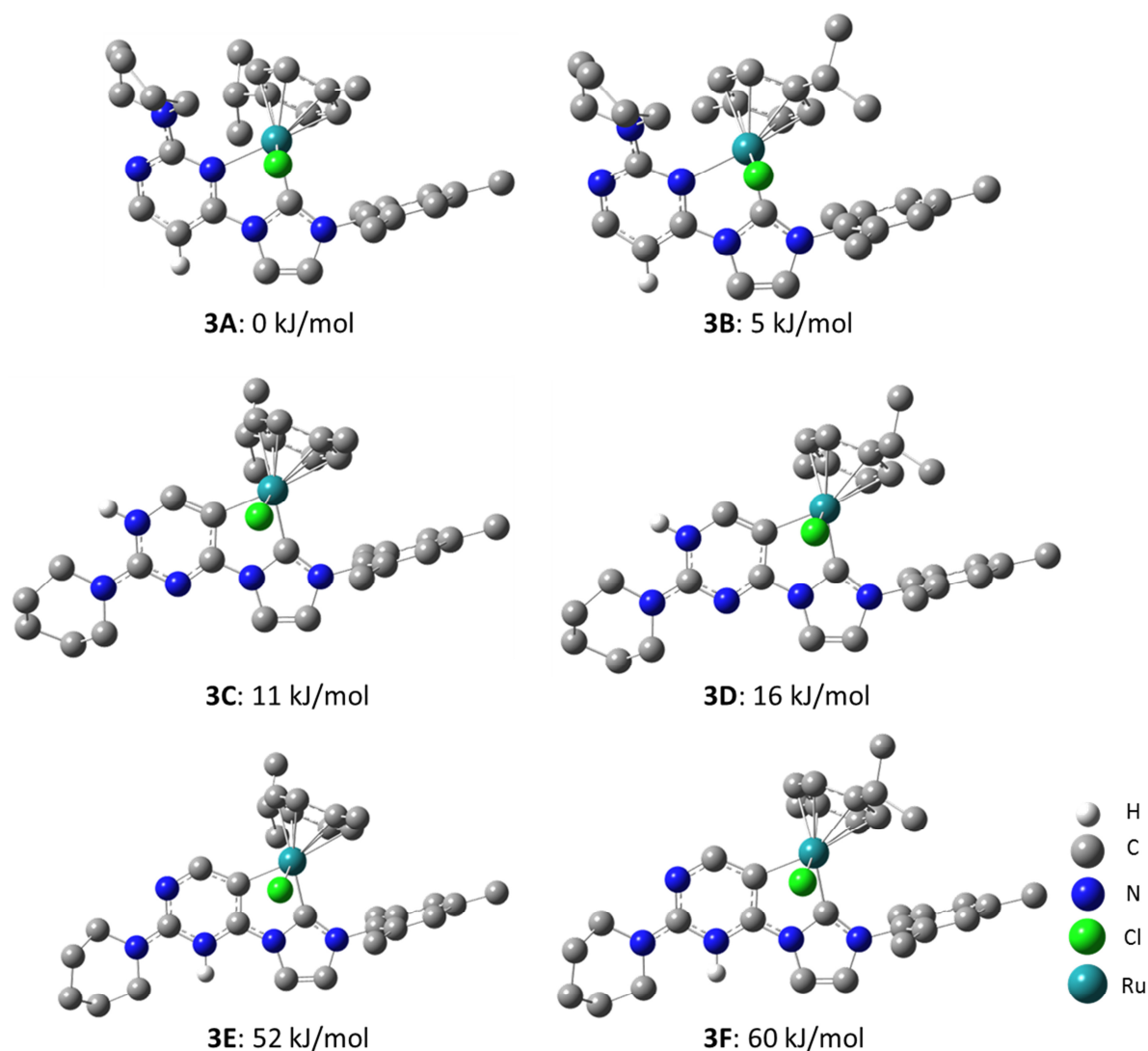


Figure 8: Computed low energy isomers of complex **3**. Relative energies are given with respect to the lowest energy isomer **3A**. Isomers with a relative energy higher than 100 kJ/mol are neglected. Note that hydrogen atoms are omitted for reasons of simplicity except for the protonating hydrogen atom.

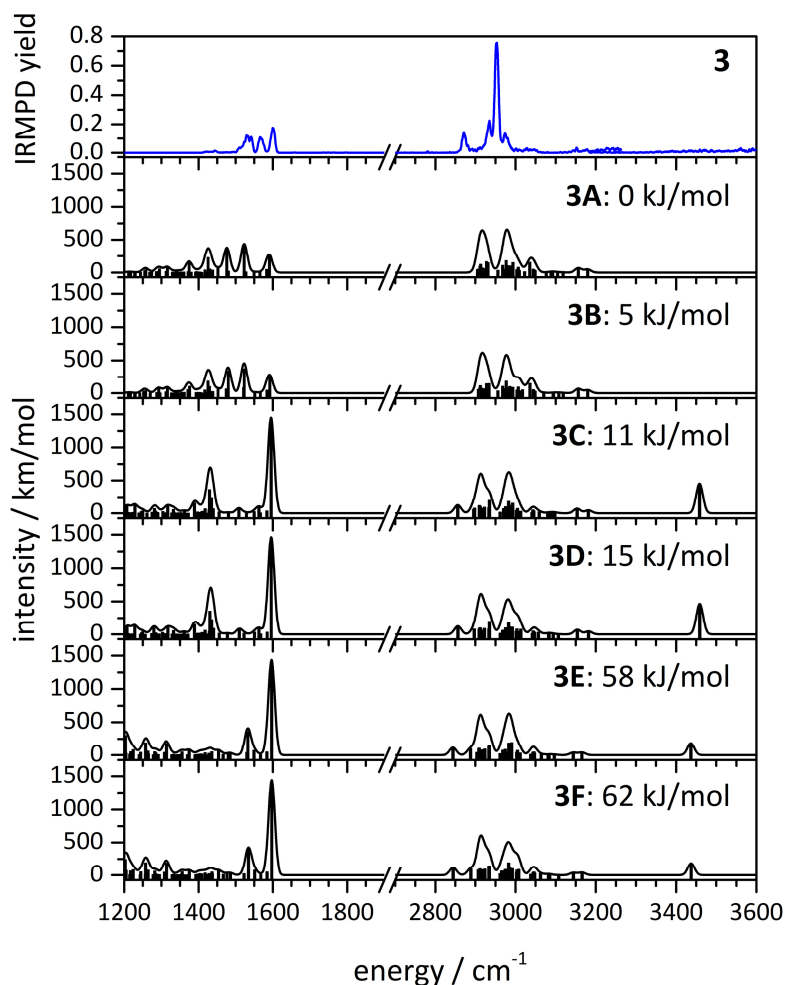


Figure 9: Experimental IRMPD spectrum of complex **3** (blue) and theoretically predicted IR spectra (black, B3LYP/cc-pVDZ and Stuttgart RSC representing the ruthenium, scaled by 0.97) of the six most stable isomers found **3A-3F**. The frequency intensities above 2800 cm^{-1} are multiplied by a factor of 5 for a better visualization. The stick spectra are folded with a Gaussian function ($fwhm = 10\text{ cm}^{-1}$).

We achieve structural determination by direct comparison of the experimental IRMPD spectrum with the computed linear absorption spectra of the found isomers **3A-3F** (Fig. 9). Hereby, the findings are comparable to the findings for the complexes **1** and **2**. The isomers **3C-3F** can be excluded to the nonexistent NH band in the experimental IRMPD spectrum. The spectra of **3A** and **3B** show a good agreement with the experimental IRMPD spectrum. As shown for the complexes **1** and **2**, no discrimination of the cymene orientation is possible.

7.5.4 Identification of coexisting isomers

The IRMPD spectra of the ruthenium complexes **1**, **2** and **3** reveal major spectral changes if we measure the IRMPD spectra of the mass-selected ions of the “aged” sample solutions (Fig. 10).

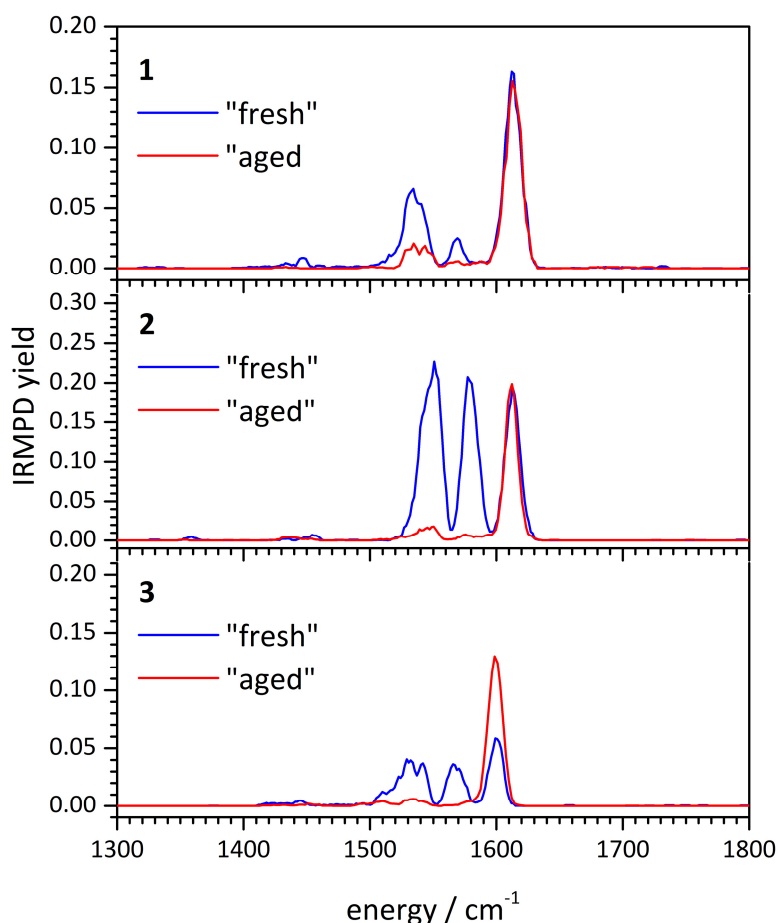


Figure 10: IRMPD spectra of the three complexes **1**, **2** and **3** in the range from 1300 to 1800 cm^{-1} . Spectra are taken from a “fresh” (blue curves) and “aged” (red curves) sample solutions.

The blue curves are the IRMPD spectra measured directly from fresh sample solutions. The blue curves are IRMPD spectra measured from the “aged” solutions. Allowing the sample solutions to stand for one day, the bands around 1540 and 1570 cm^{-1} vanish, while the band at 1600 cm^{-1} stays the same. In the case of complex **3**, the band at 1600 cm^{-1} becomes even more intense. The change in the IRMPD spectra is an evidence for a rearrangement within

the complex ions. As shown, the most stable isomers of all complexes reveal a coordination of the ruthenium to the carbene and to the nitrogen atom of the pyrimidine ring. The protonation takes place at the carbanion position and the computed absorption spectra exhibit three bands in the considered spectral range which are in a good agreement with the experimental IRMPD spectrum (cf. Fig. 5, 7 and 9). The computed spectra of the N-protonated isomers reveal one strong band in this spectral range from 1500 to 1650 cm^{-1} which is in a good agreement with the “aged” IRMPD spectra. It is already known that many ruthenium complexes are used as catalysts for transfer hydrogenation.^[2, 4, 51-53] Recent investigations on structurally similar ruthenium complexes have shown that the ligand undergoes a rearrangement after activation and a Ru-C bond is formed.^[1] Thus, we conclude that the observed change in the IRMPD spectrum originates from a proton migration. The proton rearranges from an isomer with a protonated carbanion to an isomer with a protonated nitrogen atom.

As assumed in chapter 7.5.3 it is questionable that the experimental IRMPD spectrum of the “fresh” sample solution originates from a sole isomer. Due to the assumed CH activation and the associated ligand rearrangement, it is possible that an isomer exhibiting a Ru-C bond also contributes to the experimental IRMPD spectrum.

7.5.5 Electronic Excited States

IRMPD spectra in the mid- to near-IR region (3000 to 7500 cm^{-1}) of the ruthenium complexes **1**, **2** and **3** reveal a very broad band between 3700 and 7300 cm^{-1} (Fig. 11).

Complex **2** exhibits a high fragmentation yield (ca. 70 %) for the near-IR band, while the fragmentation yields of the complexes **1** and **3** are lower (ca. 10-40 %). The intensities of these bands strongly depend on the laser power which varies significantly in the range from 3700 to 4600 cm^{-1} . Between 4800 and 7300 cm^{-1} , the IRMPD spectra of the three complexes differ significantly in their band shapes. The spectrum of complex **1** is rather noisy. The spectrum of complex **2** shows an almost flat curve, while the spectrum of complex **3** exhibits a certain fine structure. This structure suggests three more or less broad bands.

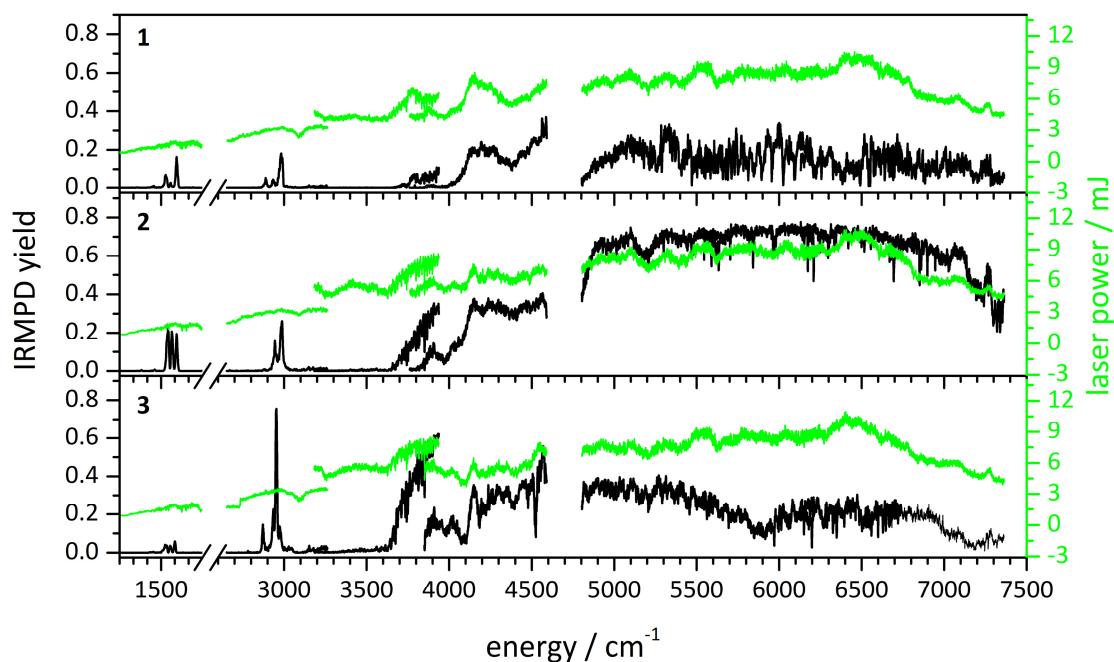


Figure 11: IRMPD spectra of the three complexes **1**, **2** and **3** in the range from 1200 to 7500 cm^{-1} (black curves) including the laser power curves (green curves).

We normalized the IRMPD yields of all three complexes linearly by the laser power. The spectrum of complex **1** after normalization of the IRMPD yields reveals a clearer structured spectrum (Fig. 12). The normalized IRMPD yield spectra of the complexes **2** and **3** are shown in Figure S4 and S5 of the supporting information. Unfortunately, the received spectrum remains noisy and reveals a suboptimal signal to noise ratio. The structure and shape of the bands qualitatively follow the curve of the laser power in the range from 3800 to 4600 cm^{-1} . Nevertheless, between 4800-7400 cm^{-1} , three broad bands emerge centered at 5300 cm^{-1} , 6000 cm^{-1} , and 7000 cm^{-1} . The appearance of these bands as a consequence of the linear power scaling is only an assumption. However, the matter of fact is that there are bands in the near-IR region as shown in the experimental IRMPD spectrum but the linear power scaling should not be overestimated. We assume that the bands may arise from metal to ligand (MTL) or ligand to metal (LTM) charge transfers.

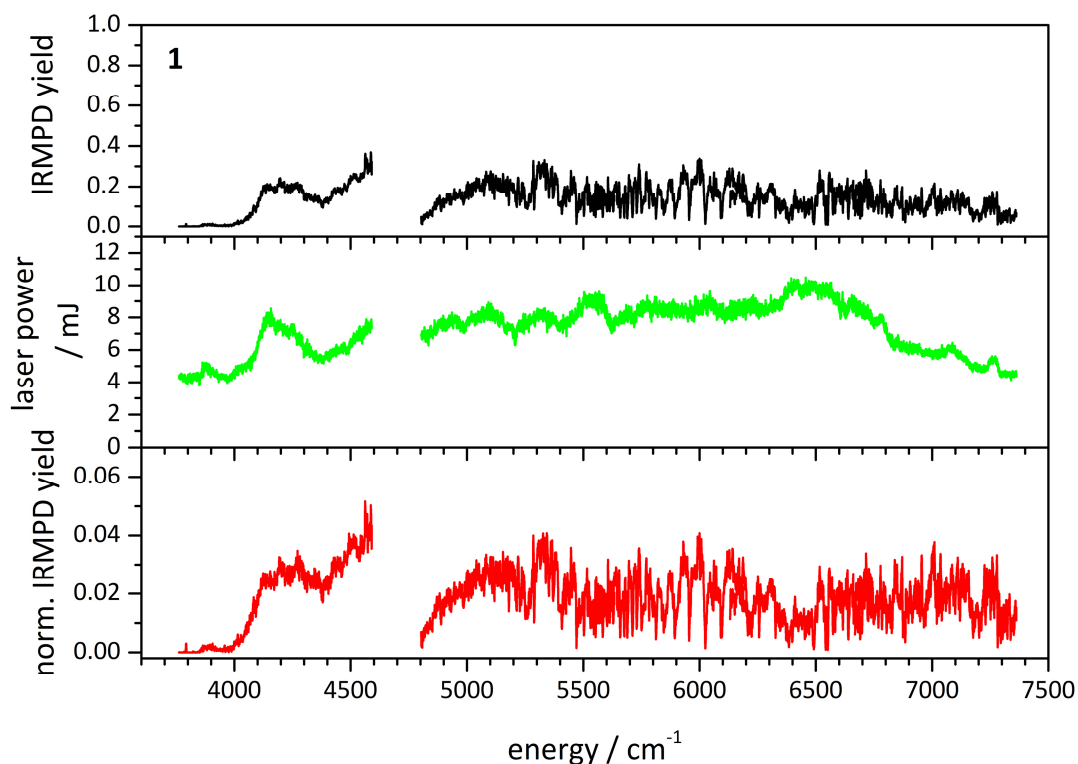


Figure 12: Near IRMPD spectrum of complex **1** (top), laser power curve (middle) and laser power normalized fragmentation yields (bottom).

For further elucidation, we applied time-dependent density functional theory (TD-DFT) to model the near-IR spectra of the complexes **1**, **2** and **3**. Figure 13 shows the comparison of the experimental and the computed spectra using the spectrum of complex **1** as an example. In order to simulate a thermal absorption spectrum, we convert the lines to a Gaussian function with a full width at half maximum (fwhm) of 2000 cm^{-1} .^[54] The computed line spectrum exhibits a good agreement with the experimental IRMPD spectrum. Three computed transitions are in the same region as the broad band of the experimental spectrum. These transitions may be responsible for the recorded resonances. It can be assumed that the position of electronic transitions (MTLCT or LTMCT) crucially depends on an appropriate description of the metal-ligand interaction.

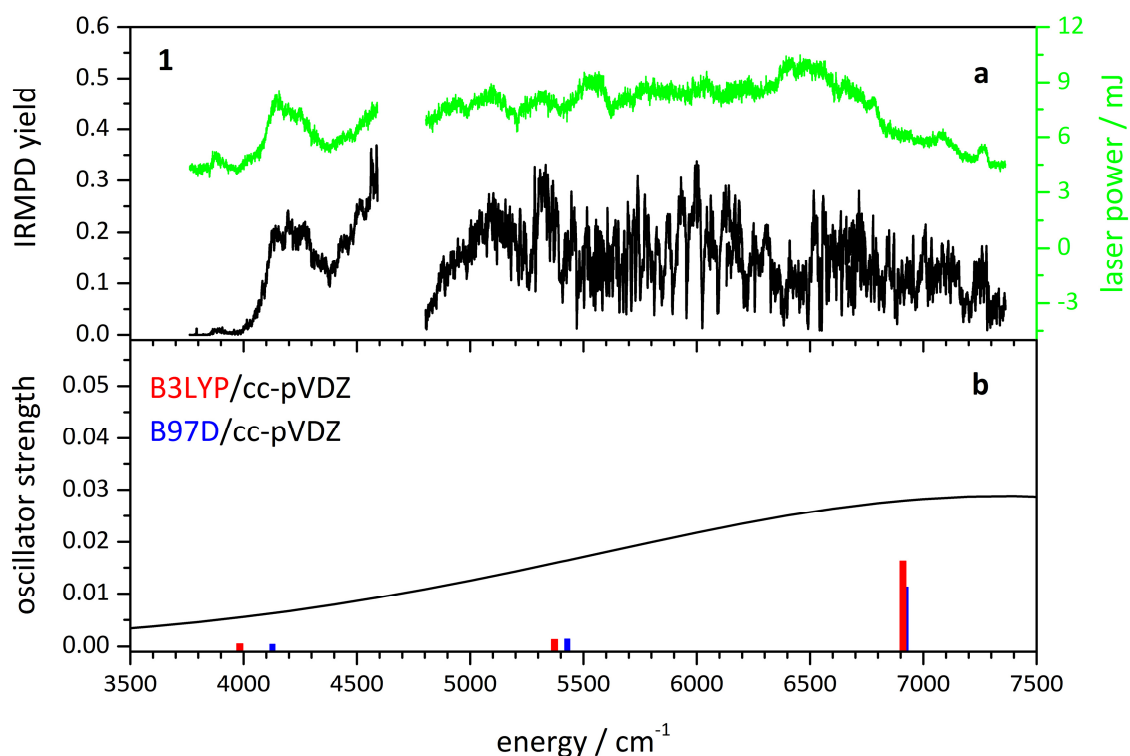


Figure 13: IRMPD spectrum in the range from 3500 to 7500 cm^{-1} including the laser power curve (upper graph a) and the computed TD-DFT spectrum (lower graph b) of complex **1**. The stick spectrum is folded with a Gaussian function ($\text{fwhm} = 2000 \text{ cm}^{-1}$).

We performed TD-DFT calculations for the singlet, triplet, and quintet spin states of the ruthenium metal center at the B3LYP/cc-pVDZ and B97D/cc-pVDZ level of theory (Table S1). It is evident that a change in the multiplicity has a strong influence on the position of the transitions. However, the triplet and quintet spin state computations reveal transitions in the mid- to near-IR range. The computed transitions are located in the same spectral region as the experimental obtained transitions. The computed transitions of the singlet spin state reveal higher energies and do not agree with the experimental IRMPD spectrum. This indicates ruthenium seemingly being in a high spin state instead of the low spin state. The spin states depend on the ligand field splitting. The splitting induced by chloride ligands is rather smaller than the splitting of cymene and pyrimidine ligands.^[55] Due to this fact, it is difficult to estimate the ligand field splitting and thus high spin states are questionable. Nevertheless, these computations should not be overestimated due to the matter of simple TD-DFT calculations. Further calculations are needed varying the DFT functionals or basis sets especially for ruthenium.

7.6 Summary and conclusion

We presented CID and IRMPD investigations on three ruthenium complexes. The three complexes reveal a similar fragmentation behavior upon collisional activation. At low activation magnitudes HCl elimination along with H₂ units takes place. The increase in activation magnitude, shows the abstraction of cymene or the concomitant loss of HCl and cymene. The elimination of HCl remains the main fragmentation channel. The three complexes exhibit similar activation energies for dissociation due to comparable heat capacities. However, complex **1** shows the highest activation energy and the lowest heat capacity. Hence, electronic and steric effects influence the stability and thus the activation energies of the complexes. Complex **2** reveals a CID appearance curve which shows evidence for two different isomers. Comparison of the IRMPD spectrum of complex **2** with computed linear absorption spectra confirms this assumption.

The IRMPD spectra of the three complexes exhibit vibrations in the same spectral range. Bands of complex **3** shift blue with respect to the other two complexes. Additionally, the IRMPD spectrum of complex **3** reveals less intense bands in the region from 1500 to 1650 cm⁻¹. These band shifts and less intense bands may originate from electronic and steric effects. The comparison with computed linear absorption spectra of the most stable isomers reveals a ruthenium coordination sphere to the chlorido ligand, to the carbene, to the cymene and to a nitrogen atom of the pyrimidine ring. The protonation takes place at the carbanion function. Two isomers have to be taken into account to explain the experimental IRMPD spectra. The difference between these two isomers is the orientation of the cymene ring. Protonation of a nitrogen atom of the pyrimidine ring and the associated ruthenium carbanion bond can be neglected due to missing NH stretching vibrations in the experimental IRMPD spectrum.

Additional IRMPD investigations on “aged” sample solutions show evidence for a structural rearrangement. Bands in the IRMPD spectra of “aged” solutions vanish in comparison with “fresh” sample solutions. Comparison with computed spectra leads to the assumption that an isomerization from a ruthenium nitrogen bond isomer to a ruthenium carbanion bond isomer takes place.

Extension of the IRMPD range reveals broad bands in the range from 4000 to 7500 cm^{-1} . These bands are rather noisy and their shape follows the shape of the laser power curve. We suppose that these bands seemingly originating from either metal to ligand or ligand to metal charge transfers. Linear normalization of the IRMPD yields by the laser power does not deliver clear band structures and seems to fail. However, TD-DFT calculations provide for several electronic transitions within this spectral range. The received Gaussian function agrees with the experimental IRMPD spectrum in the range from 4000 to 7500 cm^{-1} . Variation of the DFT functional leads to similar results. These findings should not be overestimated and further studies are needed to elucidate metal to ligand or ligand to metal charge transfers. Nevertheless, the TD-DFT computations reproduce the experimental findings.

7.7 References

- [1] L. T. Ghoochany, C. Kerner, S. Farsadpour, F. Menges, Y. Sun, G. Niedner-Schatteburg and W. R. Thiel, *European Journal of Inorganic Chemistry*, **2013**, 2013, 4305-4317.
- [2] T. Naota, H. Takaya and S. I. Murahashi, *Chemical Reviews*, **1998**, 98, 2599-2660.
- [3] E. Peris and R. H. Crabtree, *Coordination Chemistry Reviews*, **2004**, 248, 2239-2246.
- [4] M. Yamakawa, H. Ito and R. Noyori, *Journal of the American Chemical Society*, **2000**, 122, 1466-1478.
- [5] S. Gladiali and E. Alberico, *Chemical Society Reviews*, **2006**, 35, 226-236.
- [6] G. Zassinovich, G. Mestroni and S. Gladiali, *Chemical Reviews*, **1992**, 92, 1051-1069.
- [7] T. Ikariya and A. J. Blacker, *Accounts of Chemical Research*, **2007**, 40, 1300-1308.
- [8] A. Hagfeldt and M. Gratzel, *Accounts of Chemical Research*, **2000**, 33, 269-277.
- [9] K. Kalyanasundaram and M. Gratzel, *Coordination Chemistry Reviews*, **1998**, 177, 347-414.
- [10] A. S. Polo, M. K. Itokazu and N. Y. M. Iha, *Coordination Chemistry Reviews*, **2004**, 248, 1343-1361.
- [11] M. Gratzel, *Journal of Photochemistry and Photobiology C-Photochemistry Reviews*, **2003**, 4, 145-153.
- [12] M. Gratzel, *Accounts of Chemical Research*, **2009**, 42, 1788-1798.
- [13] A. W. Girotti, *Photochemistry and Photobiology*, **1983**, 38, 745-751.
- [14] G. J. Kavarnos and N. J. Turro, *Chemical Reviews*, **1986**, 86, 401-449.
- [15] N. Robertson, *Angewandte Chemie-International Edition*, **2006**, 45, 2338-2345.
- [16] N. Murakami Iha, Garcia, C.G., Bignozzi, C.A., *Handbook of Photochemistry and Photobiology*, American Scientific Publishers, Los Angeles, **2003**.
- [17] H. Taube, *Angewandte Chemie-International Edition*, **1984**, 23, 329-339.
- [18] C. Creutz and H. Taube, *Journal of the American Chemical Society*, **1969**, 91, 3988-&.
- [19] J. H. Tang, S. H. Wu, J. Y. Shao, H. J. Nie and Y. W. Zhong, *Organometallics*, **2013**, 32, 4564-4570.
- [20] N. C. Polfer, *Chemical Society Reviews*, **2011**, 40, 2211-2221.
- [21] L. Sleno and D. A. Volmer, *Journal of Mass Spectrometry*, **2004**, 39, 1091-1112.
- [22] J. S. Brodbelt and J. J. Wilson, *Mass Spectrometry Reviews*, **2009**, 28, 390-424.
- [23] A. Rosa, G. Ricciardi, O. Gritsenko and E. J. Baerends, *Principles and Applications of Density Functional Theory in Inorganic Chemistry I*, **2004**, 112, 49-115.

- [24] A. Vlcek and S. Zalis, *Coordination Chemistry Reviews*, **2007**, 251, 258-287.
- [25] B. Biri, L. Nagy, A. Kuki, E. R. Toke, G. Deak, M. Zsuga and S. Keki, *Journal of Mass Spectrometry*, **2013**, 48, 16-23.
- [26] J. M. Wells and S. A. McLuckey, in *Biological Mass Spectrometry*, ed. A. L. Burlingame, Elsevier Academic Press Inc, San Diego, **2005**, vol. 402, pp. 148-185.
- [27] F. Menges, C. Riehn and G. Niedner-Schatteburg, *Zeitschrift Fur Physikalische Chemie-International Journal of Research in Physical Chemistry & Chemical Physics*, **2011**, 225, 595-609.
- [28] A. D. Becke, *Physical Review A*, **1988**, 38, 3098-3100.
- [29] A. D. Becke, *Journal of Chemical Physics*, **1993**, 98, 5648-5652.
- [30] B. Miehlich, A. Savin, H. Stoll and H. Preuss, *Chemical Physics Letters*, **1989**, 157, 200-206.
- [31] C. T. Lee, W. T. Yang and R. G. Parr, *Physical Review B*, **1988**, 37, 785-789.
- [32] T. H. Dunning, *Journal of Chemical Physics*, **1989**, 90, 1007-1023.
- [33] D. E. Woon and T. H. Dunning, *Journal of Chemical Physics*, **1993**, 98, 1358-1371.
- [34] D. E. Woon and T. H. Dunning, *Journal of Chemical Physics*, **1993**, 99, 3730-3737.
- [35] D. Andrae, U. Haussermann, M. Dolg, H. Stoll and H. Preuss, *Theoretica Chimica Acta*, **1991**, 78, 247-266.
- [36] M. Dolg, U. Wedig, H. Stoll and H. Preuss, *Journal of Chemical Physics*, **1987**, 86, 866-872.
- [37] M. J. T. Frisch, *et al.*, **2009**, Revision D.01 Wallingford CT. 2009.
- [38] NIST Standard Reference Database 101, <http://cccbdb.nist.gov/vibscalejust.asp>.
- [39] C. Garino and L. Salassa, *Philosophical Transactions of the Royal Society a-Mathematical Physical and Engineering Sciences*, **2013**, 371.
- [40] T. Liu, B. H. Xia, Q. C. Zheng, X. Zhou, Q. J. Pan and H. X. Zhang, *Journal of Computational Chemistry*, **2010**, 31, 628-638.
- [41] J. A. Hipple and E. U. Condon, *Physical Review*, **1945**, 68, 54-55.
- [42] E. V. Anslyn, Dougherty, D.A., *Modern Physical Organic Chemistry*, Macmillan Education, **2005**.
- [43] S. Torker, D. Merki and P. Chen, *Journal of the American Chemical Society*, **2008**, 130, 4808-4814.

- [44] S. Narancic, A. Bach and P. Chen, *Journal of Physical Chemistry A*, **2007**, 111, 7006-7013.
- [45] M. T. Rodgers, K. M. Ervin and P. B. Armentrout, *Journal of Chemical Physics*, **1997**, 106, 4499-4508.
- [46] C. Lifshitz, Laskin, J., *Principles of Mass Spectrometry Applied to Biomolecules*, John Wiley & Sons, **2006**.
- [47] K. Vekey, *Journal of Mass Spectrometry*, **1996**, 31, 445-463.
- [48] N. Vinokur and V. Ryzhov, *Journal of Mass Spectrometry*, **2004**, 39, 1268-1274.
- [49] D. Imanbaew, Y. Nosenko, C. Kerner, K. Chevalier, F. Rupp, C. Riehn, W. R. Thiel and R. Diller, *Chemical Physics*, **2014**, 442, 53-61.
- [50] Y. Nosenko, F. Menges, C. Riehn and G. Niedner-Schatteburg, *Physical Chemistry Chemical Physics*, **2013**, 15, 8171-8178.
- [51] S. E. Clapham, A. Hadzovic and R. H. Morris, *Coordination Chemistry Reviews*, **2004**, 248, 2201-2237.
- [52] A. Fujii, S. Hashiguchi, N. Uematsu, K. J. Haack, T. Ikariya and R. Noyori, *Abstracts of Papers of the American Chemical Society*, **1996**, 211, 158-ORGN.
- [53] A. Fujii, S. Hashiguchi, N. Uematsu, T. Ikariya and R. Noyori, *Journal of the American Chemical Society*, **1996**, 118, 2521-2522.
- [54] S. Hirabayashi, M. Ichihashi, Y. Kawazoe and T. Kondow, *Chemical Physics Letters*, **2010**, 490, 19-23.
- [55] Holleman-Wieberg, *Lehrbuch der anorganischen Chemie*, de Gruyter, **1995**.

7.8 Supporting Information to IR Spectroscopic Investigations of Electronic Excited States in a Ruthenium Complex

Maximilian Gaffga, Agnes Fizia, Werner R. Thiel and Gereon Niedner-Schatteburg

*Fachbereich Chemie und Forschungszentrum OPTIMAS, Technische Universität
Kaiserslautern, 67663 Kaiserslautern, Germany*

Table of content

Figure S1: CID mass spectrum of complex **1** including simulations of the isotopic patterns.

Figure S2: CID mass spectrum of complex **2** including simulations of the isotopic patterns.

Figure S3: CID mass spectrum of complex **3** including simulations of the isotopic patterns.

Figure S4: Near IRMPD spectrum of **2** including the laser power curve and laser power normalized fragmentation yields.

Figure S5: Near IRMPD spectrum of **3** including the laser power curve and laser power normalized fragmentation yields.

Figure S6: Laser power curves recorded behind the ion trap.

Table S1: TD-DFT predicted transitions and oscillator strength (OS) at the B3LYP/cc-pVDZ and B97D/cc-pVDZ level of theory.

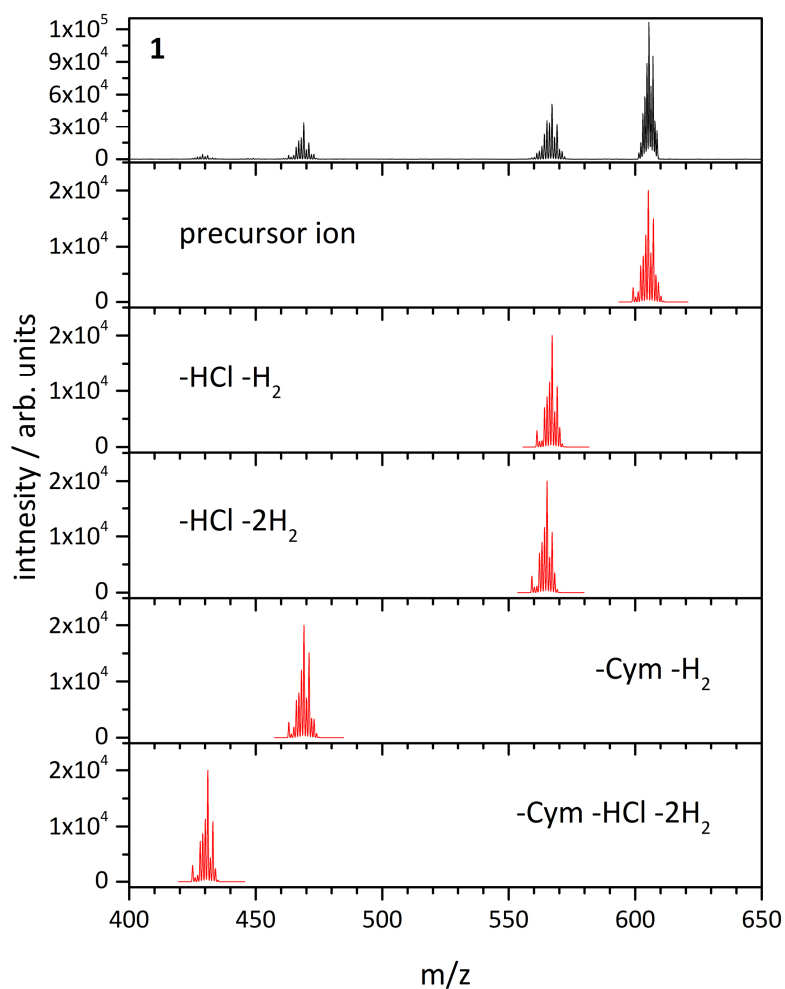


Figure S1: CID mass spectrum of the complex ion **1** (black curve) taken at $E_{COM} = 0.006$ a.u. and simulations of the isotopic pattern of the resulting fragment ions (red curves). Note that the main fragmentation channels are the elimination of HCl and cymene (Cym) along with additional H₂ units.

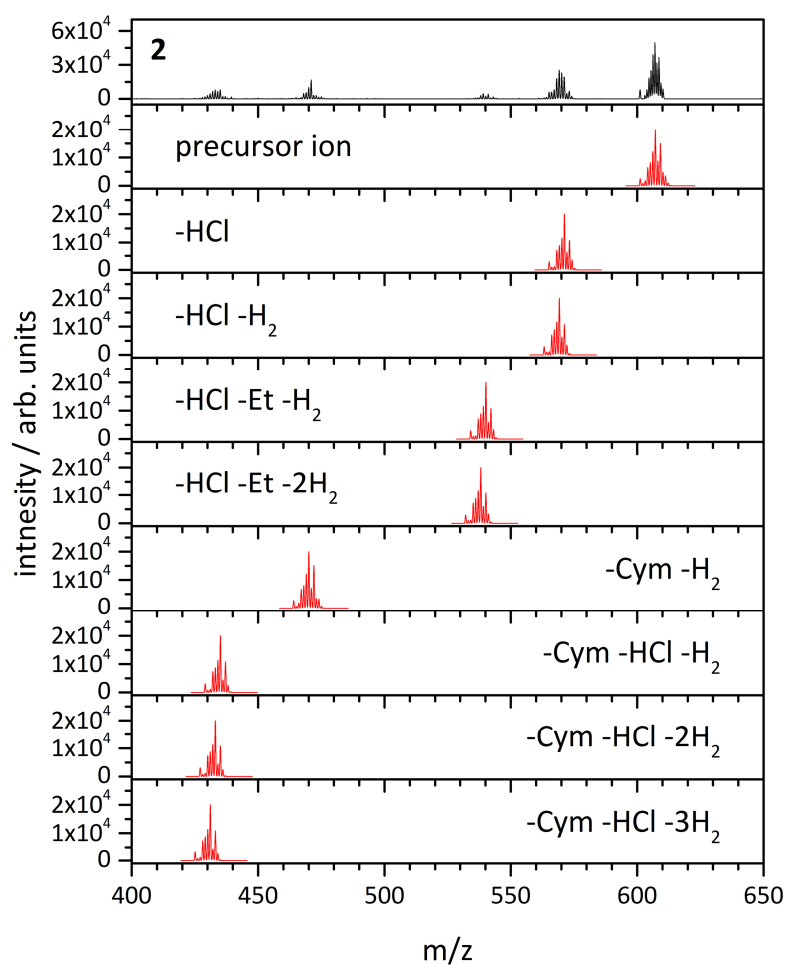


Figure S2: CID mass spectrum of the complex ion **2** (black curve) taken at $E_{COM} = 0.006$ a.u. and simulations of the isotopic pattern of the resulting fragment ions (red curves). Note that the main fragmentation channels are the elimination of HCl and cymene (Cym) along with additional H₂ units.

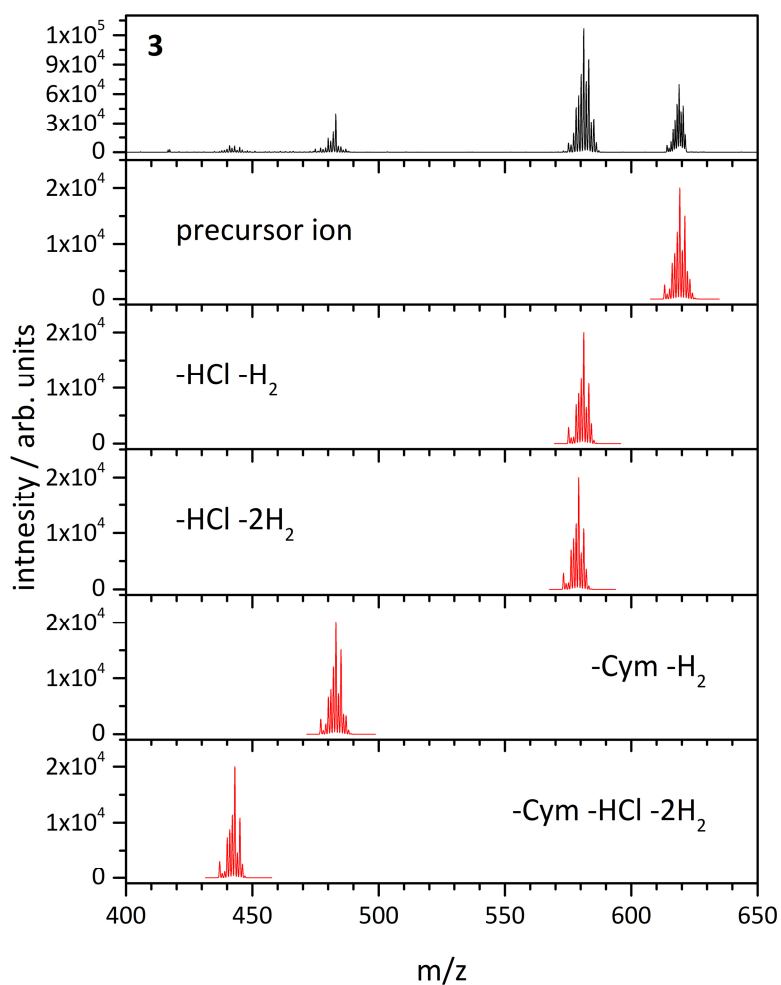


Figure S3: CID mass spectrum of the complex ion **3** (black curve) taken at $E_{COM} = 0.006$ a.u. and simulations of the isotopic pattern of the resulting fragment ions (red curves). Note that the main fragmentation channels are the elimination of HCl and cymene (Cym) along with additional H₂ units.

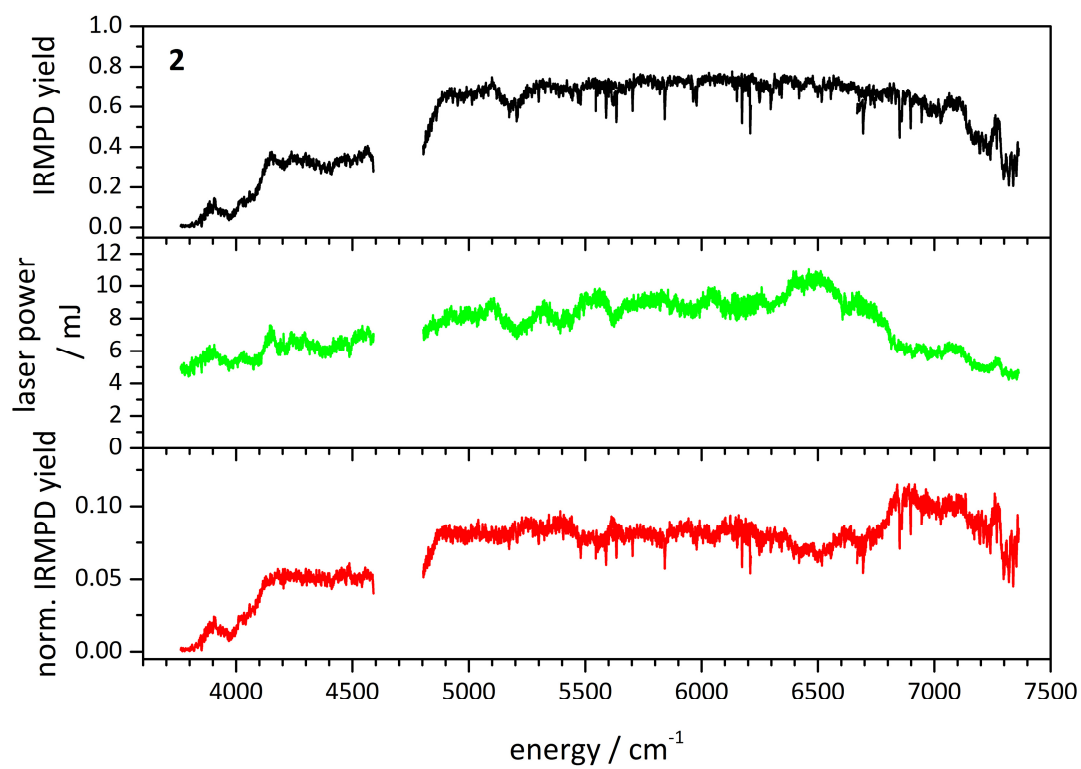


Figure S4: Near IRMPD spectra of complex **2** (top), laser power curve (middle) and laser power normalized fragmentation yields (bottom).

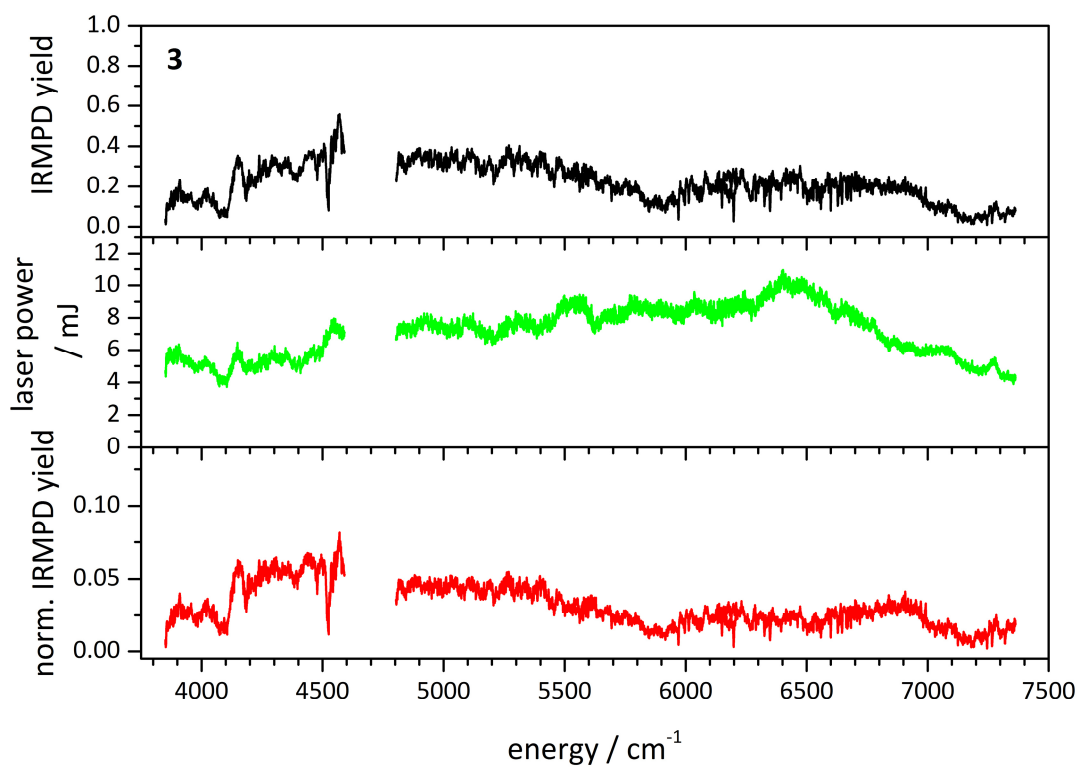


Figure S5: Near IRMPD spectra of complex **3** (top), laser power curve (middle) and laser power normalized fragmentation yields (bottom).

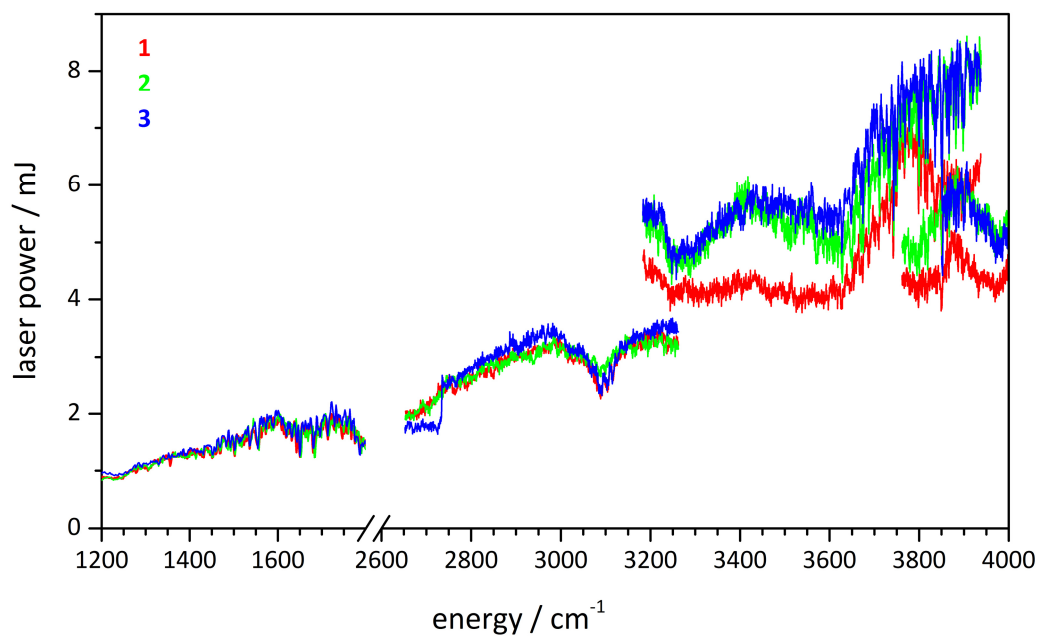


Figure S6: Laser power curves recorded behind the ion trap. The red curve represents the laser power during the measurement of complex **1**, the green curve of complex **2**, and the blue curve of complex **3**.

Table S1: TD-DFT predicted transitions and oscillator strength (OS) at the B3LYP/cc-pVDZ and B97D/cc-pVDZ level of theory of the complexes **1**, **2** and **3** for the singlet, triplet, and quintet spin state of the ruthenium.

| | C4N | | | | Et2N | | | | C5N | | | |
|-----|-----------------------------|----------|----------------------------|----------|-----------------------------|----------|----------------------------|----------|-----------------------------|----------|----------------------------|----------|
| | B3LYP / cm ⁻¹ | OS | B97D / cm ⁻¹ | Os | B3LYP / cm ⁻¹ | OS | B97D / cm ⁻¹ | Os | B3LYP / cm ⁻¹ | OS | B97D / cm ⁻¹ | Os |
| M=1 | 18858 | 5.30E-03 | 18888 | 5.40E-03 | 18994 | 4.80E-03 | 19019 | 4.80E-03 | 18842 | 5.60E-03 | 18866 | 5.70E-03 |
| | 20866 | 7.00E-04 | 20963 | 7.00E-04 | 21179 | 8.00E-04 | 21270 | 8.00E-04 | 20954 | 7.00E-04 | 21044 | 6.00E-04 |
| | 24792 | 1.20E-03 | 24851 | 1.20E-03 | 24695 | 1.30E-03 | 24748 | 1.20E-03 | 24644 | 1.50E-03 | 24700 | 1.30E-03 |
| | 26197 | 1.10E-03 | 26413 | 1.20E-03 | 25981 | 3.40E-03 | 26293 | 3.70E-03 | 26309 | 2.90E-03 | 26534 | 2.90E-03 |
| | 27355 | 1.33E-02 | 27611 | 1.60E-02 | 27461 | 1.84E-02 | 27631 | 1.37E-02 | 27257 | 2.37E-02 | 27468 | 2.54E-02 |
| M=3 | 2648 | 3.00E-04 | 2658 | 3.00E-04 | 2777 | 4.00E-04 | 2786 | 3.00E-04 | 2745 | 4.00E-04 | 2754 | 3.00E-04 |
| | 6127 | 6.00E-04 | 6103 | 6.00E-04 | 5830 | 6.00E-04 | 5811 | 6.00E-04 | 5980 | 6.00E-04 | 5960 | 6.00E-04 |
| | 9008 | 2.00E-03 | 8991 | 2.00E-03 | 9087 | 2.10E-03 | 9075 | 2.10E-03 | 9127 | 2.00E-03 | 9109 | 2.00E-03 |
| | 12271 | 3.70E-03 | 12521 | 3.70E-03 | 11478 | 2.00E-03 | 11720 | 2.00E-03 | 12281 | 2.20E-03 | 12526 | 2.00E-03 |
| | 12584 | 7.00E-03 | 12828 | 7.40E-03 | 12959 | 8.90E-03 | 13204 | 9.20E-03 | 12484 | 1.10E-02 | 12703 | 1.15E-02 |
| M=5 | 3952 | 3.00E-04 | 3899 | 3.00E-04 | 3455 | 3.00E-04 | 3061 | 2.30E-03 | 3705 | 3.00E-04 | 3367 | 2.20E-03 |
| | 4278 | 3.00E-04 | 4287 | 3.00E-04 | 3905 | 4.00E-04 | 4287 | 4.40E-03 | 4162 | 3.00E-04 | 3536 | 3.00E-04 |
| | 7023 | 2.10E-03 | 7263 | 2.10E-03 | 6323 | 2.20E-03 | 4756 | 2.70E-03 | 7008 | 2.20E-03 | 5746 | 1.31E-02 |
| | 10405 | 1.30E-03 | 10636 | 1.40E-03 | 10602 | 1.30E-03 | 5786 | 4.70E-03 | 10491 | 1.30E-03 | 5936 | 5.00E-04 |
| | 12066 | 2.80E-03 | 12251 | 2.70E-03 | 12213 | 1.50E-03 | 7022 | 4.10E-03 | 12022 | 5.30E-03 | 7523 | 1.39E-02 |

8. Summary and Conclusion

In the presented work transition metal complexes were investigated. The combination of gas phase collision-induced dissociation (CID) studies and infrared multi photon dissociation (IRMPD) spectroscopy served to investigate the molecular structure and the metal to ligand interactions of mono- and bifunctional Pd catalysts, lanthanide based single molecule magnets and Ru containing complexes. CID studies provide for relative stabilities and fragmentation thresholds within a given class of compounds. The IRMPD spectroscopy combined with density functional theory (DFT) computations enabled a structural elucidation and the characterization of coexisting isomers. Two different mass spectrometers were used for the presented CID studies (Bruker Esquire 6000) and the IRMPD spectroscopy (Bruker amZon SL). The Bruker amaZon SL mass spectrometer is combined with a OPO/OPA laser system, which generates the necessary infrared light.

Mass spectrometric investigations on a novel bifunctional Fe-Pd catalyst revealed solvent attachment. Computed structures show a coordination change of the Pd atom in favour of solvent attachment. Upon collisional excitation the solvent attached complexes may loose the attached solvent, may loose HCl, may loose both in concert, or may loose – most notably – FeCl₂ and solvent in concert. A solvent modulated Fe-Pd proximity coincides, and seems to favor, FeCl₂ elimination. Gas phase IRMPD experiments reveal competing HCl/FeCl₂ elimination with branching ratios much alike the CID ones. The solvent modulated formation of NH-Cl hydrogen bonds help to verify computed structures and isomers. The identified *syn* and *anti* isomers favor and disfavor FeCl₂ elimination, respectively. DFT computations reveal a multitude of stationary points along the multistep reaction coordinates of the three conceivable spin states. The quintet spin state shows a static Jahn-Teller type relaxation by a tilt away of the Cp ligand at the iron center. Thereby, the quintet stabilizes below the triplet state and admits the rearrangements towards FeCl₂ elimination. This quintet state steeply drops below the initially most stable singlet state -namely by further enhancing the Cp ligand tilt at the iron center. The remainder of rearrangements likely proceed by the quintet state, allowing for chlorido and Cp ligand exchange amongst the metallic centers in opposite directions in a concerted, ballet like manner. The assumption of an adiabatic progression along the reaction path would thus imply a direct singlet-quintet spin cross over - seemingly without a direct involvement of the higher triplet state. The concomitant spin flips of two

electrons (likely d electrons at Fe) need to occur in concert. The elucidated coordination change upon solvent attachment at the Pd center nicely reveals a likely structure with conceivable catalytic activity. Electron rich hydrocarbon molecules may easily swap for the solvent and proceed towards further steps of activation. The elimination of FeCl_2 would result in a deactivation of the catalytic activity of the complex.

CID studies on three derivatives of protonated Pd complexes, containing Pd-carbene, Pd-carbanion and Pd-MeCN coordination, reveal evidence of two coexisting isomers, which are both populated at room temperature. Experimental IRMPD spectra and computed linear absorption spectra of the most stable isomers identify the likely structures of the two coexistent isomers. Protonation takes place at the carbanion function or at the nitrogen atoms of the pyrimidine ring. Depending on the position of the protonation, Pd either coordinates to the carbanion or to the nitrogen atom of the pyrimidine ring. Mass spectrometric analysis of the single fragment channels exhibits the contributions of the individual fragments to the resulting IRMPD bands. Hereby, the band at 1535 cm^{-1} exclusively reveals HCl elimination and no concomitant loss of HCl and MeCN followed by water attachment, in a remarkable contrast to the other recorded IRMPD bands. Computed structures of the resulting fragments exhibit a rearrangement that hinders the attachment of water. A methylene group of the mesitylene takes the vacant Pd coordination site. Two-color IRMPD investigations show isomer selective hole burning in dependence on the time delay between the two laser pulses. According to the time delay, enhancement or decrease of bands assigned to certain isomers are observed. Photon-induced isomerization is likely taking place. The replacement of the MeCN ligand by pyridine reveals a remarkably different fragmentation behavior. The IRMPD spectra as well as the CID appearance curves do not show any evidence of two coexisting isomers. The comparison of the experimental IRMPD spectra with computed linear absorption spectra allows for structure determination and identifies the likely sole isomer prevailing. According to the findings of the MeCN containing complexes two possible protonation sites have to be considered. However, the IRMPD spectra of the pyridine containing complexes reveal that the protonation of the carbanion can be neglected. The pyrimidine protonated isomers show a good agreement with the experimental IRMPD spectra. These isomers are stabilized by π -stacking due to the interaction of the pyridine with the mesitylene. Moreover, the considerably size of the

pyridine leads to steric hindrances. These two effects inhibit the formation of a second isomer.

The presented IRMPD spectra of three negatively charged Pd complexes, differing in their side group, in combination with DFT calculations allow for structure determination and give valuable information about the coordination of the transition metal within the complex. The influence of the different side groups on the IRMPD spectrum is small. However, comparison of the experimental IRMPD spectra with the computed linear IR absorption spectra of the most stable isomers found allows for structure determination and reveals a square planar binding motif of the Pd to three chloride ligands and to the nitrogen of the pyrimidine ring. The influence on the activation energy in dependence of the side group is small (< 5 kJ/mol). The CID appearance curves allow for the estimation of binding energies of the different complex ions. In order to determine binding energies, the so called thermometer ions are used to calibrate the internal energy scale of the mass spectrometer. Two possible fragmentation pathways of the thermometer ions are considered. A direct C-N bond cleavage leads to benzylium cations and to the formation of tropylium cations after rearrangement. The direct comparison of CID derived activation energies with computed Gibbs free energies reveal different orders in the binding energy. Both the E_{COM}^{50} and AE values exhibit a linear relationship between the experimental values and theoretical binding energies. Linear extrapolations exhibit relatively poor linear regression factors. The benzylium cation approach with a linear extrapolation using a fixed intercept delivers the best regression factor and is used to determine the dissociation energies. The CID derived dissociation energies correspond to DFT derived Gibbs free energies. Hereby, variation of the basis set and DFT functional reveals that the combination of cc-pVDZ and B3LYP agree the best. All other basis set and DFT functional combinations under- or overestimate the CID derived dissociation energies. Note that the assumption of a sigmoid behavior in general is merely a phenomenological approach to ion dissociation, which is fairly more complex. Additionally, the investigated species contain a transition metal and the influence of the metal center on the bond cleavage may lead to an unpredictable uncertainty due to the catalytic activity of transition metals. This influence may lead to significant errors in the determination of dissociation energies. Computations on transition states on the fragmentation pathway may solve the problem. Nevertheless, the achieved energy values for the dissociation energies of the three Pd complexes are reasonable. The computed Gibbs

free energies are in a good agreement with the experimental CID derived dissociation energies. Anyhow, this procedure may serve as a simple approach to determine dissociation energies of transition metal complexes.

Upon collisional excitation, single molecule magnets (SMM) of two different $[\text{Fe}_4\text{Ln}_2]^+$ ($\text{Ln} = \text{Y}, \text{Eu}, \text{Gd}, \text{Tb}, \text{Dy}, \text{Ho}$ and Er) types **I** and **II** reveal significant changes in the fragmentation thresholds in dependence of the used Ln metal center. Y is not a paramagnetic lanthanide but exhibits a diamagnetic species with similar ionic radius. The $[\text{Fe}_4\text{Dy}_2]^+$ complex shows a change in the curves' shape of the CID appearance curve seemingly arising from a tight transition state passed during the fragmentation process. The investigated type **II** complexes fragment at higher activation magnitudes than the type **I** complexes. The found differences are ascribed to the ability to form π backbondings and to the degree of occupation of anti- or non-bonding orbitals weakening metal to ligand bindings. The higher stability of the $[\text{Fe}_4\text{Y}_2]^+$ complex seemingly arises from the fact that Y does not belong to the group of lanthanides and uses 4d orbitals instead of 4f orbitals to form bonds to the ligands. The different Ln metal centers influence the experimental IRMPD spectra of the type **I** complexes. The OH, sp^3CH and CO stretching modes exhibit blue or red shifts in dependence of the Ln metal centers. The CO stretching mode shifts red significantly due to the direct coordination to metal centers. However, this red shift varies depending on the Ln metal. The OH stretching mode is significantly influenced by the Ln metal and shifts blue or red depending on the Ln metal center. Hereby, the $[\text{Fe}_4\text{Gd}_2]^+$ complex exhibits the biggest red shift, while the $[\text{Fe}_4\text{Y}_2]^+$ reveals the biggest blue shift. In the case of the type **II** complexes, the sp^3CH and the CO stretching modes show significant spectral shifts in dependence of the Ln metal centers. The spCH stretching mode is not influenced by the metal centers. Again, the complex containing Gd metal centers reveals the biggest red shifts. The spherical electron density, resulting from a half filled f-shell of the Gd metal centers may induce the observed spectral changes within the IRMPD spectrum of the type **I** and **II** $[\text{Fe}_4\text{Gd}_2]^+$ complex. However, calculations are needed to elucidate the influence of the Ln metal centers on the structure and vibrational frequencies of the type **I** and **II** complexes in more detail.

Investigations on three protonated Ru complexes reveal a similar fragmentation behavior upon collisional activation for all three complexes. At low activation magnitudes, HCl elimination along with H_2 units takes place. The increase in activation magnitude shows the

abstraction of cymene or the concomitant loss of HCl and cymene. The elimination of HCl is the main fragmentation channel for all three complexes. The three complexes exhibit similar fragmentation thresholds due to comparable heat capacities. However, the complex with the lowest heat capacity shows the highest fragmentation threshold. Hence, electronic and steric effects influence the stability and thus the activation energies of the complexes. The Et₂N-substituted complex reveals a CID appearance curve, which shows evidence for two different isomers confirmed by the comparison of the IRMPD spectrum with computed linear absorption spectra. The IRMPD spectra of the three complexes exhibit vibrations in the same spectral range as well as variance in their frequencies, i.e. blue and red shifted bands. The comparison with computed linear absorption spectra of the most stable isomers found reveals a Ru coordination to the chlorido ligand, to the carbene, to the cymene and to a nitrogen atom of the pyrimidine ring. The protonation takes place at the carbanion function. Two isomers have to be taken into account to explain the experimental IRMPD spectra. The difference between these two isomers is the orientation of the cymene ring. Unfortunately, the used experimental techniques do not allow for the distinction between these two isomers. Protonation of a nitrogen atom of the pyrimidine ring and the associated Ru-carbanion bond can be neglected due to missing NH stretching vibrations in the experimental IRMPD spectrum. Additionally, IRMPD investigations on “aged” sample solutions show evidence for a structural rearrangement. Bands in the IRMPD spectra of “aged” solutions vanish in comparison with “fresh” sample solutions. Comparison with computed spectra leads to the conclusion that an isomerization from a Ru-N bond isomer to a Ru-carbanion bond isomer takes place. Extension of the IRMPD range reveals broad bands in the range from 4000 to 7500 cm⁻¹. We suppose that these bands seemingly originate from either metal to ligand or ligand to metal charge transfers (MLCT or LMCT). Linear normalization of the IRMPD yields by the laser power does not deliver clear band structures and seems to fail. However, TD-DFT calculations provide for several electronic transitions within this spectral range. The received Gaussian function agrees with the experimental IRMPD spectrum in the range from 4000 to 7500 cm⁻¹. Variation of the DFT functional leads to similar results. Further studies are needed to elucidate metal to ligand or ligand to metal charge transfers in more detail. Nevertheless, the TD-DFT computations reproduce the experimental findings.

The combination of the presented techniques (CID and IRMPD) serves for a comprehensive characterization and understanding of interactions between transition metals and organic ligands. The presented investigations on the different transition metal complexes reveal manifold effects for each species leading to valuable results. A fundamental understanding of metal to ligand interactions is mandatory for the development of new and better organometallic complexes with catalytic, optical or magnetic properties.

9. Zusammenfassung und Schlussfolgerung

Die vorliegende Arbeit umfasst Gasphasenuntersuchungen ein- und zweikerniger palladiumhaltiger Katalysatoren, lanthanoidbasierter Einzelmolekülmagnete sowie rutheniumhaltiger Komplexe. Die Kombination aus stoßinduzierter Dissoziation (*collision-induced dissociation*, CID) und Infraroter Multiphotonen Dissoziation (*infrared multi photon dissociation*, IRMPD) Spektroskopie dient zur Strukturanalyse und zur Aufklärung von Metall-Ligand Wechselwirkungen. CID-Studien geben hierbei Aufschluss über relative Stabilitäten und das Fragmentierungsverhalten innerhalb einer Substanzklasse. Die Strukturaufklärung und die Charakterisierung koexistenter Isomere gelang mittels einer Kombination aus IRMPD-Spektroskopie und Dichtefunktionaltheorie (*density functional theory*, DFT) Berechnungen. Die CID-Experimente wurden an einem Bruker Esquire 6000 Massenspektrometer, die IRMPD-Messungen an einem Bruker amaZon SL Massenspektrometer durchgeführt. Ein OPO/OPA-Lasersystem diente zur Erzeugung des für die IR-Spektroskopie notwendigen IR-Lichtes.

Die massenspektrometrische Analyse eines bifunktionellen Fe-Pd-Katalysators zeigte eine Lösungsmittelanlagerung. Bedingt durch die Anlagerung des Lösungsmittels an das Pd-Zentrum erfolgt eine Änderung der Koordinationssphäre. Dies konnte anhand von Computersimulationen aufgezeigt werden. Unter stoßinduzierter Anregung können die Komplexe mit dem koordinativ gebundenen Lösungsmittelmolekülen das Lösungsmittelmolekül, HCl, beides gleichzeitig oder FeCl₂ in Kombination mit dem Lösungsmittelmolekül, verlieren. Die Fe-Pd-Nähe wird durch das Lösungsmittel bestimmt und begünstigt die FeCl₂-Eliminierung. Gasphasen IRMPD-Experimente zeigen die konkurrierende HCl/FeCl₂-Eliminierung mit den CID-Messungen entsprechenden Verteilungen. Die durch das Lösungsmittel hervorgerufene Ausbildung einer NH-Cl-Bindung hilft bei der Identifizierung der berechneten Strukturen und Isomere. Die identifizierten *syn* und *anti* Isomere bevorzugen oder benachteiligen die FeCl₂-Abspaltung. DFT-Berechnungen zeigen eine Vielzahl an stationären Punkten entlang der mehrstufigen Reaktionskoordinate der drei vorstellbaren Spinzustände. Der Quintett-Zustand zeigt eine Jahn-Teller-Verzerrung durch Neigung des Cp-Liganden weg vom Fe-Zentrum. Dabei stabilisiert sich der Quintett-Zustand unterhalb des Triplett-Zustandes und lässt eine Umlagerung in Richtung FeCl₂-Abspaltung zu. Dieser Quintett-Zustand fällt unter den anfangs stabileren Singulett-Zustand – durch

stärkere Neigung des Cp-Liganden am Fe-Zentrum. Der Rest der Umlagerung verläuft entlang des Quintett-Zustandes und erlaubt den Austausch des Cp-Liganden mit den Cl-Liganden an den Metallzentren in entgegengesetzter Richtung. Die Vermutung eines adiabatischen Prozesses entlang des Reaktionsweges würde somit einen Singulett-Quintett-Spinübergang beinhalten – wahrscheinlich ohne direkte Involvierung des Triplett-Zustandes. Der gleichzeitige *spin flip* von zwei Elektronen (d-Elektronen des Fe) muss gleichzeitig vonstattengehen. Die Koordinationssänderung durch die Anlagerung eines Lösungsmittels an das Pd-Zentrum zeigt eine Struktur mit denkbarer katalytischer Aktivität. Elektronenreiche Kohlenwasserstoffe können leicht mit dem Lösungsmittelmolekül austauschen und eine weitere Aktivierung folgen. Die Abspaltung von FeCl_2 resultiert dann in einer Desaktivierung der katalytischen Aktivität.

CID-Experimente an drei Derivaten eines protonierten Pd-Komplexes, welche eine Pd-Carben, Pd-Carbanion und Pd-MeCN Koordination beinhalten, lassen das Vorhandensein zweier koexistenter Isomere erkennen. Der Vergleich von experimentellen IRMPD-Spektren und theoretisch berechneten linearen Absorptionsspektren der energiegünstigsten Isomere dient zur Identifizierung dieser. Die berechneten Strukturen zeigen, dass die Protonierung entweder an der Carbanion-Funktion oder an einem Stickstoff des Pyrimidinringes erfolgen kann. Abhängig von der Protonierungsstelle konkurriert Pd-Carbanion- oder Pd-N-Koordination. Die massenspektrometrische Analyse der Einzelfragmentkanäle zeigt den Anteil der einzelnen Fragmente zu den resultierenden IRMPD-Banden. Hierbei zeigt nur die Bande bei 1535 cm^{-1} HCl-Abspaltung, während alle anderen Banden die gleichzeitige Eliminierung von HCl und MeCN gefolgt von Wasseranlagerung zeigen. Theoretisch berechnete Strukturen der Fragmente nach HCl-Abspaltung zeigen, dass innerhalb eines Isomers eine Umlagerung stattfindet. Diese Umlagerung inhibiert die Anlagerung von Wasser auf Grund einer Bindungsausbildung zwischen der Methylen-Gruppe des Mesityls an das Palladium. In Abhängigkeit des Zeitdelays zwischen zwei Laserpulsen zeigen zweifarbige IRMPD-Untersuchungen isomerelektives Lochbrennen. Abhängig von diesem Zeitdelay wird bei den Isomeren zugeordneten Banden eine Signalverstärkung oder Intensitätsabnahme beobachtet. Der Austausch des MeCN-Liganden durch Pyridin ändert das Fragmentierungsverhalten. Sowohl die IRMPD- als auch die CID-Spektren zeigen keinen Anhaltspunkt für koexistente Isomere. Der Vergleich der experimentellen IRMPD-Spektren mit berechneten linearen Absorptionsspektren erlaubt die Strukturbestimmung des

beitragenden Isomers. Gemäß den Ergebnissen der MeCN beinhaltenden Komplexe müssen wieder zwei Protonierungsstellen berücksichtigt werden. Allerdings zeigen die IRMPD-Spektren, dass die Protonierung der Carbanion-Funktion vernachlässigt werden kann. Die am Pyrimidin-Stickstoff protonierten Isomere zeigen eine gute Übereinstimmung mit den experimentellen IRMPD-Spektren. Dabei übt die Wechselwirkung zwischen den π -Systemen des Pyridins und Mesitylens eine stabilisierende Funktion aus. Eine zusätzliche sterische Hinderung resultiert aus der Größe des Pyridins. Diese zwei Effekte inhibieren die Bildung eines weiteren Isomers.

Die IRMPD-Spektren dreier negativ geladener Pd-Komplexe, die sich in ihrer Seitengruppe unterscheiden, in Kombination mit DFT-Berechnungen erlauben die Strukturbestimmung und geben nützliche Informationen über die Koordinationssphäre des Metalls innerhalb des Komplexes. Der Einfluss der Seitengruppe auf das IRMPD-Spektrum ist klein. Der Vergleich der experimentellen IRMPD-Spektren mit den berechneten linearen Absorptionsspektren der energiegunstigsten Isomere zeigt eine quadratisch planare Koordination des Pd an drei Cl und ein N des Pyrimidins. Der Einfluss der Seitengruppe auf die Aktivierungsenergie fällt gering aus (< 5 kJ/mol). Die CID *appearance curves* erlauben die Abschätzung von Bindungsenergien der Komplexionen. Bei deren Bestimmung wurden die sogenannten „Thermometerionen“ benutzt, um die interne Energieskala des Massenspektrometers zu kalibrieren. Hierbei werden zwei mögliche Fragmentierungswege der „Thermometerionen“ berücksichtigt. Eine direkte C-N-Bindungsspaltung führt zu Benzylumkationen, während eine nachfolgende Umlagerung zu Tropyliumkationen führt. Der direkte Vergleich der CID abgeleiteten Aktivierungsenergien mit berechneten Gibbs'schen freien Enthalpien zeigt eine unterschiedliche Reihenfolge innerhalb der Energien. Die E_{COM}^{50} und AE Werte zeigen eine lineare Beziehung zwischen den experimentellen und den berechneten Bindungsenergien. Eine lineare Extrapolation führt zu eher mittelmäßigen Regressionsfaktoren, wobei der Benzylumkationen Ansatz bei festem y-Achsenabschnitt die besten Regressionsfaktoren liefert und zur Bestimmung der Dissoziationsenergien benutzt wird. Die CID abgeleiteten Dissoziationsenergien entsprechen den DFT abgeleiteten Gibbs'schen freien Enthalpien. Die Variation des Basissatzes und des DFT Funktionals zeigt, dass die Kombination aus cc-pVDZ und B3LYP am besten übereinstimmt. Alle anderen Kombinationen unter- oder überschätzen die CID abgeleiteten Dissoziationsenergien. Es ist zu beachten, dass die Annahme eines sigmoidalen Verhaltens im Allgemeinen lediglich ein phänomenologischer Ansatz für die

Ionendissoziation ist, welcher allerdings komplexer ist. Zusätzlich beinhalten die untersuchten Spezies ein Übergangsmetall und der Einfluss des Metallzentrums auf die Bindungsspaltung kann auf Grund der katalytischen Aktivität des Metalls zu wesentlichen Fehlern in der Bestimmung der Dissoziationsenergien führen. Berechnungen von Übergangszuständen innerhalb des Fragmentierungsweges können diese Probleme eventuell lösen. Dennoch sind die erzielten Energiewerte für die Dissoziationsenergien der drei Pd-Komplexe passend. Die berechneten Gibbs'schen freien Enthalpien stimmen mit den experimentell ermittelten Dissoziationsenergien überein. Dieses Verfahren bietet einen simplen Ansatz zur Bestimmung von Dissoziationsenergien von Übergangsmetallkomplexen.

Zwei verschiedene Typen I und II Einzelmolekülmagnete der Art $[\text{Fe}_4\text{Ln}_2]^+$ ($\text{Ln} = \text{Y}, \text{Eu}, \text{Gd}, \text{Tb}, \text{Dy}, \text{Ho}$ and Er) zeigen in Abhängigkeit vom benutzten Ln-Metallzentrum nach stoßinduzierter Anregung wesentliche Änderungen in ihren Fragmentierungsgrenzwerten. Y ist kein paramagnetisches Lanthanoid, weist allerdings ein diamagnetisches Verhalten und einen ähnlichen Ionenradius auf. Der $[\text{Fe}_4\text{Dy}_2]^+$ -Komplex zeigt eine Änderung im Kurvenverlauf der CID *appearance curve*, die wahrscheinlich durch einen engeren, während des Fragmentierungsprozesses durchlaufenen, Übergangszustand hervorgerufen wird. Die Komplexe des Types II fragmentieren bei höheren Aktivierungsenergien als die des Types I. Dieser Unterschied wird der Fähigkeit der Ausbildung von π -Rückbindungen und dem Besetzungsgrad von anti- und nichtbindenden Orbitalen zugeschrieben. Letzteres führt zu einer Schwächung der Metall-Ligand-Bindung. Die höhere Stabilität des $[\text{Fe}_4\text{Y}_2]^+$ -Komplexes kommt wahrscheinlich durch die Tatsache zu Stande, dass Y nicht zur Gruppe der Lanthanoide gehört und 4d-Orbitale anstelle von 4f-Orbitalen zur Bindungsausbildung zu den Liganden benutzt werden. Die IRMPD-Spektren der Typ I-Komplexe werden durch die verschiedenen Ln-Metallzentren beeinflusst. In Abhängigkeit des Ln-Metallzentrums zeigen die OH-, sp^3CH - und CO-Streckschwingungen Rot- und Blauverschiebungen. Auf Grund der direkten Koordination an das Metallzentrum verschiebt die CO-Streckschwingung wesentlich rot. Bei den OH-Streckschwingungen zeigt der $[\text{Fe}_4\text{Gd}_2]^+$ -Komplex die größte Rotverschiebung, während der $[\text{Fe}_4\text{Y}_2]^+$ -Komplex die größte Blauverschiebung zeigt. Im Falle der Typ II-Komplexe zeigen die sp^3CH - und die CO-Streckschwingungen einen wesentlichen Einfluss des Ln-Metallzentrums und spektrale Verschiebungen. Die sp^3CH -Streckschwingung wird nicht durch das Metallzentrum beeinflusst. Erneut zeigt der Gd-haltige Komplex die größte Rotverschiebung. Die aus einer halb gefüllten f-Schale resultierende sphärische

Elektronendichte mag die beobachteten spektralen Änderungen innerhalb des IRMPD-Spektrums der Typ I- und II-Komplexe hervorrufen. Um diesen Einfluss des Metallzentrums auf die Struktur und die Schwingungsfrequenzen im Detail aufzuklären, werden theoretische Berechnungen benötigt.

Untersuchungen an drei protonierten Ru-haltigen Komplexen zeigen nach stoßinduzierter Anregung ähnliches Fragmentierungsverhalten. Bei geringen Aktivierungsenergien beobachtet man HCl-Eliminierung einhergehend mit der Abspaltung von H₂-Einheiten. Eine Erhöhung der Aktivierungsenergie zeigt die Abspaltung von Cymol oder die gleichzeitige Eliminierung von HCl und Cymol. Für alle drei Komplexe ist die HCl-Abstraktion der Hauptfragmentierungskanal. Auf Grund von vergleichbaren Wärmekapazitäten ähneln sich die Fragmentierungsgrenzwerte der drei Komplexe. Jedoch besitzt der Komplex mit der niedrigsten Wärmekapazität den höchsten Fragmentierungsgrenzwert. Die Stabilitäten und damit die Aktivierungsenergien der Komplexe werden von elektronischen und sterischen Effekten beeinflusst. Die CID *appearance curve* des Et₂N-substituierten Komplexes zeigt Anzeichen für zwei koexistente Isomere, was durch Vergleich der IRMPD-Spektren mit berechneten linearen Absorptionsspektren bestätigt wird. Die IRMPD-Spektren der drei Komplexe zeigen sowohl Schwingungen im gleichen Spektralbereich als auch Veränderungen in ihren Frequenzen, d.h. rot und blau verschobene Banden. Der Vergleich der berechneten linearen Absorptionsspektren der energiegünstigsten Isomere zeigt eine Koordination von Ru an den Cl-Liganden, an die Carben-Funktion, an das Cymol und an ein N-Atom des Pyrimidins. Die Protonierung findet an der Carbanion-Funktion statt. Zwei Isomere müssen in Betracht gezogen werden, um die experimentellen IRMPD-Spektren zu erklären. Dabei unterscheiden sich die beiden Isomere in der Orientierung des Cymolringes. Leider erlauben die von uns benutzten Techniken nicht die Unterscheidung der beiden Isomere. Auf Grund der fehlenden NH-Bande kann die Protonierung eines der N-Atome des Pyrimidins und die damit verbundene Ru-Carbanion-Bindung vernachlässigt werden. Weitere IRMPD-Untersuchungen an „gealterten“ Probelösungen lassen auf eine strukturelle Umlagerung schließen. Im Vergleich zu „frischen“ Probelösungen verschwinden Banden der „gealterten“ Lösung in den IRMPD-Spektren. Der Vergleich mit berechneten Spektren lässt darauf schließen, dass eine Umisomerisierung von einem Ru-N-Isomer zu einem Ru-C-Isomer stattfindet. Eine Erweiterung des IRMPD-Messbereiches führt zu breiten Banden zwischen 4000 und 7500 cm⁻¹. Vermutlich sind diese Banden Folge von Metall zu Ligand oder Ligand zu

Metall *charge transfer* Vorgängen (MLCT oder LMCT). Eine lineare Normalisierung der IRMPD-Intensität mit Hilfe der Laserenergie führt nicht zu einer klareren Bandenstruktur und scheint fehlzuschlagen. TD-DFT-Berechnungen zeigen einige elektronische Übergänge in diesem Spektralbereich. Die erhaltene Gaussfunktion stimmt mit den experimentellen IRMPD-Spektren im Bereich von 4000 bis 7500 cm^{-1} überein. Weitere Untersuchungen sind notwendig, um die Metall-Ligand-Wechselwirkung und die resultierenden *charge transfer* Vorgänge im Detail zu verstehen. Dennoch werden die experimentellen Spektren durch die TD-DFT-Berechnungen reproduziert.

Die Kombination der präsentierten Techniken (CID und IRMPD) dient der umfassenden Charakterisierung und dem Verständnis der Wechselwirkungen zwischen Übergangsmetall und organischem Ligand. Die vorgestellten Untersuchungen der verschiedenen Übergangsmetallkomplexe zeigen eine Vielzahl an Effekten für jede Spezies und führen zu wertvollen Resultaten. Ein fundamentales Verständnis der Metall-Ligand-Wechselwirkungen ist zwingend notwendig im Hinblick auf die Entwicklung neuer und besserer metallorganischer Komplexe mit katalytischen, optischen oder magnetischen Eigenschaften.

10. Publications and Contributions to Conferences

PUBLICATIONS / VERÖFFENTLICHUNGEN

1. "Multi State Mediated Rearrangements and FeCl₂ Elimination in Dinuclear FePd Complexes"
Gaffga M., Munstein I., Müller P., Thiel W.R. and Niedner-Schatteburg G.
submitted, Journal of Physical Chemistry. A, (2015)
2. "Mechanistic Investigation on Ru(II) catalyzed base-free Transfer Hydrogenation of Ketones and Reductive Amination of in-situ Generated Imines through a CH Activation Step"
Kerner C., **Gaffga M.**, Sun Y., Niedner-Schatteburg G. and Thiel W.R.
in preparation
3. "Investigations on the CH-Activation by roll-over Mechanism of 2,2'-pyrimidinyl-pyridine Ligands at d9 Metals"
Kerner C., Neu J.P., **Gaffga M.**, Lang J., Sun Y., Niedner-Schatteburg G. and Thiel W.R.
in preparation
4. "Infrared spectroscopy of N₂ adsorption on size selected cobalt cluster cations in isolation"
Dillinger S., Mohrbach J., **Gaffga M.**, Hewer J. and Niedner-Schatteburg G.
Physical Chemistry Chemical Physics, 17, 10358, DOI: 10.1039/C5CP00047E (2015)
5. "A Novel Bifunctional Ligand for the Synthesis of Polynuclear Alkynyl Complexes"
Wilhelmi C., **Gaffga M.**, Sun Y., Niedner-Schatteburg G. and Thiel W.R.
Zeitschrift für Naturforschung Section B-A Journal of Chemical Sciences, 69, 1290, DOI: 10.5560/ZNB.2014-4164 (2014)
6. "Two-color delay dependent IR probing of torsional isomerization in a [AgL₁L₂](+) complex"
Lang J., **Gaffga M.**, Menges F. and Niedner-Schatteburg G.
Physical Chemistry Chemical Physics, 16, 17417, DOI: 10.1039/C4CP02045F (2014)
7. "Mono- vs. Dinuclear Gold-Catalyzed Intermolecular Hydroamidation"
Serrano-Becerra J.M., Maier A., Gonzalez-Gallardo S., Moos E., Kaub C., **Gaffga M.**, Niedner-Schatteburg G., Roesky P.W., Breher F. and Paradies J.
European Journal Of Organic Chemistry, 21, 4515, DOI: 10.1002/EJOC.201402068 (2014)
8. "Heterobimetallic Cuprates Consisting of a Redox-Switchable, Silicon-Based Metallo-ligand: Synthesis, Structures and Electronic Properties"
Styra S., Gonzalez-Gallardo S., Armbruster F., Ona-Burgos P., Moos E., Weis P., Hampe O., Schmitt Y., Gerhards M., Menges F., **Gaffga M.**, Niedner-Schatteburg G. and Breher F.
Chemistry-A European Journal, 19, 8436, DOI: 10.1002/CHEM.201300586 (2013)

PRESENTATIONS / EINGELADENE VORTRÄGE

- 23.-27.03.2015 *Microsolvation and coordination changes in a dinuclear iron-palladium complex in isolation*
DPG-Frühjahrstagung, Heidelberg
- 28.-29.03.2014 *Characterisation of dinuclear transition metal complexes by collision-induced dissociation studies and IRMPD spectroscopy*
PhD meeting des Sonderforschungsbereiches SFB/TRR88 3MET, Karlsruhe
- 17.-21.03.2014 *Characterisation of dinuclear transition metal complexes by collision-induced dissociation studies and IRMPD spectroscopy*
DPG-Frühjahrstagung, Berlin
- 05.-07.08.2013 *Two color enhanced IR spectroscopy of transition metal complexes*
PhD meeting des Sonderforschungsbereiches SFB/TRR88 3MET, Bad Bergzabern
- 09.-11.05.2013 *Two color enhanced IR spectroscopy of oligonuclear transition metal complexes*
112th Bunsentagung of the German Chemical Society (GdCh), Karlsruhe

POSTERS / POSTERBEITRÄGE

- 14.-16.05.2015 114th Bunsentagung of the German Chemical Society (GdCh), Bochum
- 03.-04.06.2014 3nd International Conference on Bimetallic Complexes Sonderforschungsbereich SFB/TRR88 3MET, Karlsruhe
- 29.-31.05.2014 113th Bunsentagung of the German Chemical Society (GdCh), Hamburg
- 02.-04.03.2014 10th Koordinationschemie-Tagung, Kaiserslautern
- 23.-25.09.2013 2nd International Conference on Bimetallic Complexes, Karlsruhe

Mein Dank gilt...

- ... Herrn Prof. Dr. Gereon Niedner-Schatteburg für die Ermöglichung der Promotion, die Betreuung, die gute Zusammenarbeit und die stete Diskussionsbereitschaft.
- ... Herrn Prof. Dr. Markus Gerhards für die Übernahme des Zweitgutachtens und Herrn Prof. Dr. Werner R. Thiel für die Übernahme des Prüfungsvorsitzes.
- ... Joachim Hewer für die überaus schöne Zeit, die gemeinsame Laborarbeit und Messzeiten und das Bekämpfen von Lasertechnikproblemen.
- ... Anke Stamm für Ihre Unterstützung jeglicher Art, nicht nur während den Prüfungsphasen. Danke für deine Aufmunterungen und dass du immer ein offenes Ohr für mich hast!
- ... meinen Arbeitskollegen/innen Matthias Tombers, Sebastian Dillinger, Jennifer Mohrbach, Dr. Thomas Kolling, Johannes Lang und Dimitri Imanbaew. Es war nie langweilig mit Euch! Weiterhin danke ich allen ehemaligen Kollegen für die Einarbeitung in bestehende Forschungsprojekte, die produktive Zusammenarbeit und die immer angenehme Arbeitsatmosphäre.
- ... allen anderen Freunden und Kollegen des 5. Stockes der Physikalischen Chemie in besonderer Weise für viele lustige Stunden und die tolle Arbeitsatmosphäre!
- ... unseren beiden Sekretärinnen Hilde Seelos und Sybille Heieck für die jahrelange Hilfe.
- ... den Kollegen/innen aus anderen Arbeitsgruppen für die gute Zusammenarbeit und Kooperation, mit denen ich viele Projekte erfolgreich bearbeiten konnte.
- ... Isabel, die stets an meiner Seite war, mir den Rücken gestärkt und mich in einer schwierigen Zeit durchweg unterstützt hat. Danke, dass es dich gibt und du immer für mich da bist!
- ... meiner Familie, ohne die Vieles nicht möglich gewesen wäre und durch die ich mein Studium überhaupt erst realisieren konnte. Herzlichen Dank für jegliche Unterstützung!
- ... meinen Freunden, für tolle Stunden abseits der Uni und die Ablenkung vom Promotionsstress.

Lebenslauf

MAXIMILIAN GAFFGA

AUSBILDUNG

- seit 10/2012 **Promotion** in Physikalischer Chemie
Prof. Dr. Gereon Niedner-Schatteburg, TU Kaiserslautern
Titel: *Characterization of Mononuclear and Oligonuclear Transition Metal Complexes in Isolation*
- 10/2012 **Diplom** in Chemie
Prof. Dr. Gereon Niedner-Schatteburg, TU Kaiserslautern
Titel: *Darstellung isolierter oligonuklearer Metallkomplexe via Elektrospray Ionisation (ESI-MS) und deren Charakterisierung mittels stoßinduzierter Dissoziation (CID) und infrarot induzierter Multiphotonendissoziation (IRMPD)*
- 10/2007 - 10/2012 **Studium der Chemie**, TU Kaiserslautern
Diplomarbeit: *Physikalische Chemie*
Vertiefungsrichtung: *Physikalische Chemie*
- 07/2007 - 10/2007 **Ferienjob**, Ursapharm - Arzneimittel GmbH, Saarbrücken
- 07/2006 - 07/2007 **Militärdienst**, 1. Fallschirmjägerbataillon 263, Zweibrücken
- 06/2006 **Abitur**, Gymnasium am Steinwald Neunkirchen / Saar

Eidesstattliche Erklärung

Hiermit bestätige ich, Maximilian Gaffga, dass die vorliegende Arbeit gemäß der Promotionsordnung des Fachbereichs Chemie der Technischen Universität Kaiserslautern selbständig und nur unter Verwendung der angegebenen Quellen und Hilfsmittel angefertigt wurde.

Kaiserslautern, im Dezember 2015

